CORROSION PROTECTION AND COMPOSITE REPAIR OF STEEL COMPONENTS AND FATIGUE LIFE PREDICTION OF PIPELINE

By

MILAD SALEMI

A dissertation submitted to the

School of Graduate Studies

Rutgers, The State University of New Jersey

In partial fulfillment of the requirements

For the degree of

Doctor of Philosophy

Graduate Program in Civil and Environmental Engineering

Written under the direction of

Hao Wang

And approved by

____

____

____

____

New Brunswick, New Jersey

January 2020

ABSTRACT OF THE DISSERTATION

Corrosion protection and repair of steel components using inorganic coating and carbon fiber reinforced polymer and fatigue life prediction of pipeline

by MILAD SALEMI

Dissertation Director

Hao Wang

Pipeline is one of most important transportation infrastructures in the U.S. Many of pipe structures are old and have been in service in for decades. Effective maintenance is needed to keep pipeline infrastructure in serviceable condition and prevent catastrophic failure against corrosion and fatigue. This research investigates application of inorganic coating for corrosion protection and composite repair of steel pipeline. First, a customized accelerated corrosion procedure was developed to induce rapid degradation in coated steel specimens with organic and inorganic coatings. Bonding strengths of the coatings with steel substrate were examined using the modified lap shear test. Inorganic coating matrix was fabricated with various nano-materials to investigate the effectiveness of nano-modification. Furthermore, Carbon fiber reinforced polymer (CFRP) laminates were tested on coated and uncoated steel specimens to evaluate their repair capabilities. Laboratory test results from shear and tension coupons were then used as baseline inputs for finite element modeling (FEM) of pipeline structure. The FE models were used to calculate stress intensity factor (SIF) of pipeline with crack defects and composite repair. Finally, the fatigue life of pipeline was calculated using a backward-forward Bayesian inference methodology based on the observed crack growth measurements and cycle data that predicts the probability density of failure after initially estimating the equivalent initial flaw size (EIFS). The study results show that composite repair with inorganic coating can be an effective method for steel pipeline repair and service life extension.

Dedication

To my beloved parents.

Acknowledgements

At first I want to thank my brother, Mahrad, for his help to kick start my journey at Rutgers.

I would like to extend my special gratitude to my advisor, Prof. Wang, for his guidance on every step of the way, and to Prof. Balaguru for all the insightful conversations, and the committee members, Prof. Najm, and Dr. Vankeetila for their encouraging and supporting comments. This research was in part supported by Pipeline and Hazardous Materials Safety Administration (PHMSA). The support is gratefully acknowledged.

I also would like to thank my friends and colleagues whose help made this research work possible: Muralee Balaguru, Jinhao Liang, Wei Huang, David Caronia, Pengyu Xie, Yangmin Ding, and all others who helped me. Thank you all!

And finally a special thanks to my khargoosh for her love and support!

December 2019

Table of Contents

ABSTRACT OF THE DISSERTATION ii

Dedication iii

Acknowledgements iv

Table of Contents v

List of Figures...x

1 Introduction 1

1.1 Background 1

1.2 Problem Statement 2

1.3 Objectives and Methodology 4

2 Literature Review 7

2.1 Steel Structure Repair.. 7

2.2 Fiber Reinforced Polymer (FRP) 8

2.2.1 Environmental degradation and aging effect 9

2.2.2 Surface Preparation Effect 10

2.2.3 Bond performance... 10

2.3 Steel Bridge Repair with CFRP 14

2.3.1 Laboratory Studies 14

2.3.2 Field Studies.. 17

2.4 FRP Applications in Pipeline 20

2.4.1 Composite Repair Methods 20

2.4.2 Standards in Pipeline repair using FRP Wraps 21

2.4.3 Laboratory Studies 24

2.4.4 Numerical Studies 27

2.5 Coating for Steel Corrosion Protection 32

2.5.1 Current Practice of Coating 32

2.5.2 Geopolymer Coating 35

2.6 Fatigue Life Prediction of Pipeline 40

3 Coating for Corrosion Protection 44

3.1 Accelerated Corrosion Test 44

3.1.1 Existing Corrosion Test Procedures 44

3.1.2 Test Chamber design and build 45

3.1.3 Corrosion cycle 48

3.1.4 Corrosion resistance indicator 49

3.2 Test procedure 50

3.2.1 Surface Preparation 51

3.2.2 Coating preparation 51

3.2.3 Coating Thickness Control 53

3.2.4 Adhesive Bond Evaluation 54

3.3 Accelerated Corrosion Test Results 57

3.3.1 Batch-1 ... 57

3.3.2 Batch-2 ... 61

3.3.3 Batch – 3 ... 65

3.4 Geopolymer Coating with Nano-Additives ... 73

3.4.1 Calculation of Nano-Additives Content ... 74

3.4.2 Batch-4 ... 75

3.4.3 Batch-5 ... 81

3.4.4 Coating Thickness and its effect on shrinkage cracking ... 85

4 CFRP-Substrate bond behavior ... 89

4.1 Modified Lap Shear Test Setups ... 89

4.1.1 SETUP 1- Single Lap Shear ... 89

4.1.2 SETUP 2 – Double Lap Shear (Double Strap) ... 90

4.2 CFRP-Coating Interfacial properties ... 91

4.2.1 Pull Off Test (Mode-I Failure) ... 91

4.2.2 Lap-Shear Tests (Mode-II Failure) ... 97

4.3 Finite Element Analysis ... 101

4.3.1 Model Geometry ... 101

4.3.2 Cohesive Zone Model ... 102

4.3.3 Comparison between 2D and 3D Models ... 105

4.3.4 Effect of Bonding Length ... 107

4.3.5 Yielding Effect of Steel ... 108

4.3.6 Comparison between Measurement and Modeling ... 112

4.3.7 Bond Stress Distribution ... 116

5 Effect of Nano-additives on Lap-shear and steel coupon specimens ... 122

5.1 Lap-shear specimens ... 122

5.1.1 Specimen Preparation ... 122

5.1.2 Testing and results ... 123

5.2 Steel Coupon Specimens ... 130

5.2.1 Linear damage ... 132

5.2.2 Through Thickness Hole Damage ... 134

5.2.3 Patch Damage ... 134

5.2.4 Test results ... 135

6 Finite Element Analysis Pipeline with Defect and Repair ... 140

6.1 Finite Element (FE) Modeling ... 140

6.1.1 Two Dimensional FE Model ... 140

6.1.2 Three-Dimensional FE Model ... 143

6.2 Surrogate Function of Stress Intensity Factor ... 150

6.2.1 Polynomial Surface Fitting ... 150

6.2.2 Gaussian Process Fitting ... 151

6.3 Effect of Patch Repair on Stress Intensity Factor ... 155

7 Fatigue Life Prediction of Pipeline...162

7.1 Equivalent Initial Flaw Size (EIFS) Concept.. 163

7.2 Base Model Development – Steel Plate 165

7.2.1 EIFS Direct Probability Density Inference - $\boldsymbol{p(\theta)}$ 167

7.2.2 EIFS Probability Density Inference with Hyper parameters- $\boldsymbol{p(c|\alpha)}$ 171

7.2.3 Estimating probability and cycle of the failure.. 176

7.3 Pipe Model Development.. 184

7.3.1 EIFS Direct Probability Density Inference 184

7.3.2 Estimating probability and cycle of the failure.. 187

8 Conclusions and Recommendations...190

8.1 Conclusions 190

8.2 Recommendation for Future Work 193

9 References..196

List of Figures

Figure 2-1 Details of repair using steel plates with welding (left), and combination of welding and bolting (right) (Shanafelt et al. 1984). 7

Figure 2-2 Double strap Lap Shear Joint (after Zhao et. al, 2007). 11

Figure 2-3 Failure modes of adhesively bonded FRP to adherends (after Zhao et al. 2007). 11

Figure 2-4 Bilinear bond-slip model (after Zhao et. al ,2007). 12

Figure 2-5 Comparison of pre- and post-retrofit tension strain field test (After Miller et al. 2001) 16

Figure 2-6 Lab test setup (left), Comparison to of response to analytical model (After Miller et al. 2001) 16

Figure 2-7 Comparison of damaged, undamaged, and FRP repaired pipes. Ultimate internal pressure (left), circumferential stress (right) (After Toutanji et. al, 2001) 26

Figure 2-8 Stress distribution along thickness of repaired pipe for different defect geometries (after Duell et al. 2008) 28

Figure 2-9 Mixed mode traction separation law (top left); Tests to calibrate Mode I failure (top right); and Mode II failure or direct shear (bottom) (after Mazurkiewicz et al. 2017). 30

Figure 2-10 Maximum burst pressure results for different cases (top left), pressure vs radial displacement curve (bottom left), Failed pipe (a) – circumferential stress before failure (b) and after failure (c) in the simulation for damaged pipe (top right) and repaired pipe (bottom right) (After Mazurkiewicz et al. 2017). 31

Figure 2-11 Geopolymer structure. 37

Figure 2-12 Room temperature viscosity of geopolymer resin over time after mixing (left), Extent of cure and viscosity of geopolyer over time (right) (After Lyon et a. 1997). 38

Figure 2-13 Fatigue result of a low ally steel (After Schijve, 2003). 41

Figure 3-1 Corrosion Chamber (Top), Spray nozzle (bottom). 46

Figure 3-2 UV light. 47

Figure 3-3 Hydraulic manual pull off test machine. 50

Figure 3-4 Coating preparation and application procedure. 52

Figure 3-5 Thickness measurement device. 54

Figure 3-6 Pull off dolly (left), Cutting tool for isolating dolly (right). 55

Figure 3-7 Dolly grip (top right) and its schematics (top left), and dolly after failure (bottom). 56

Figure 3-8 Quad sample coated with four various coatings (up), Dual sample (bottom). 58

Figure 3-9 Batch-1 Pull-off test before (Top), and after accelerated corrosion cycle (Bottom). 61

Figure 3-10 Batch-2 Pull off strength test results after corrosion cycle. 65

Figure 3-11 Pull Off test performed on Batch-3 specimens before corrosion cycle. 67

Figure 3-12 Batch-3 Pull Off test samples after one month of accelerated corrosion cycle. 68

Figure 3-13 Pull off test performed after two month, Batch-3. 72

Figure 3-14 Nano-Additives used in the coating mix. 73

Figure 3-15 Freshly coated specimens using foam brush. 77

Figure 3-16 Foam brush trace on the coted specimen with Nano-Silica Additive (Right), Dolly glued to the specimen with uneven surface (left). 77

Figure 3-17 Back of a specimen coated with organic coating 79

Figure 3-18 Batch-4 after one week corrosion cycle. 79

Figure 3-19 Batch-4 after one month corrosion cycle. 80

Figure 3-20 Macroscopic images of Batch-4 Coatings before corrosion. 80

Figure 3-21 Macroscopic images of Batch-4 Coatings after corrosion. 81

Figure 3-22 Fresh coated specimens using 1.4mm nozzle tip HVLP spray gun. 82

Figure 3-23 Cured Nano-Added specimens coated with spray gun. 83

Figure 3-24 Control withWt11.76% with 204μm average thickness – Coated Specimen(Top), Cracks are clear in macroscopic image of the coated surface(Bottom Left), Thickness measurement distribution over coated area(Bottom Right). 84

Figure 3-25 Control withWt%9.1 with 165μm average thickness – Coated Specimen(Top), Macroscopic image of the coated surface(Bottom Left), Thickness measurement distribution over coated area(Bottom Right). 85

Figure 3-26 Control withWt11.76% with 204μm average thickness – Coated Specimen(Top), Cracks are clear in macroscopic image of the coated surface(Bottom Left), Thickness measurement distribution over coated area(Bottom Right). 86

Figure 3-27 Batch-2 Specimens before Corrosion (Top), and after one month Accelerated Corrosion (Bottom). 87

Figure 4-1 ASTM original specimen(top), SETUP 1 CFRP lap shear modified specimen (bottom).. 90

Figure 4-2 ASTM original type-B specimen(top), SETUP2 CFRP-STEEL lap shear test. coated and uncoated samples and Specimen details (bottom). 91

Figure 4-3 Thickness frequency distribution of coated samples for Resin-Coating bond evaluation. 93

Figure 4-4 Resin Saturant applied and cured on coated samples..................................... 93

Figure 4-5 Resin thickness measurement distribution on coated samples. 95

Figure 4-6 Pull off strength performed on geopolymer coated steel specimen topped with DowAksa CarbonBond 300H Saturant. P2 (Top), P3 (Bottom)...................................... 96

Figure 4-7 Load-Displacement Curve for Lap-Shear Specimens. 98

Figure 4-8 Performing tension test in MTS machine.. 99

Figure 4-9 Modified Lap-Shear specimens before tension test (left), Specimens after Failure from left to right: Coated-20-2, Coated-20-3, Uncoated-20-1, Uncoated-20-2, Uncoated-20-3.. 100

Figure 4-10 Comparison of uncoated experimental results with 20mm and 40mm bond lengths. 101

Figure 4-11 Traction-Separation Behavior (After Dassault Systémes, 2015). 103

Figure 4-12 BK Failure Criterion (After Dassault Systémes, 2015)........................... 104

Figure 4-13 Comparison of 2D vs 3D simulation for a modified Lap-Shear test for uncoated steel sheet with 20mm Bond length.. 105

Figure 4-14 2D FE Model. Interface shear stress distribution at the onset of damage (Top Section). 3D FEM simulation. Mesh (top), Mises Stress (Middle), Interface stress distribution at the onset of damage (Bottom). 106

Figure 4-15 Bond Strength and Ultimate Load predictions using elastic 2D simulation. 108

Figure 4-16 Yield occurred in the steel coupon tension simulation. 109

Figure 4-17 Comparison of ABQUS simulation for steel coupon tension test and Lab test. 109

Figure 4-18 2D FE model results with elastic behavior assumption for steel. 110

Figure 4-19 2D simulation of modified Lap-Shear test with plastic behavior for steel sheet. 111

Figure 4-20 Elastic behavior versus Elastic-Plastic behavior for 20mm bond length Lap-Shear specimen simulation. 111

Figure 4-21 Comparison of FE simulation with Lab results for 40mm bond length...... 113

Figure 4-22 2D simulation of modified Lap-Shear test with full range plastic behavior for steel sheet. 114

Figure 4-23 Comparison of uncoated steel lap shear test results for 20mm bond length between FE simulation and lab test. 115

Figure 4-24 Shear and slip variations along 20mm bond length. 117

Figure 4-25 Shear and slip variations along 25mm bon length. 118

Figure 4-26 Shear and slip variations along 30mm bond length. 118

Figure 4-27 Shear and slip variations along 35mm bond length. 119

Figure 4-28 Shear and slip variations along 40mm bond length. 119

Figure 4-29 Shear and slip variations along 45mm bond length. 120

Figure 4-30 Shear and slip variations along 50mm bond length. 120

Figure 4-31 Simulation results for strain along bond lengths for modified single lap shear specimens. 121

Figure 5-1 Specimen fabrication. Alignment and mark ups pf specimens where black lines show the extend of overlap on both ends of the specimen (top), laying CFRP in place (bottom). 124

Figure 5-2 Water source effect on strength performance of geopolymer. 125

Figure 5-3 Bond failure at the end with coated steel sheet of the lap shear specimens.. 125

Figure 5-4 Bond strength trend versus Nano-additive concentration in the coating mixture. 128

Figure 5-5 Summary of lap shear load-displacement test on coated specimens with various Nano-modifications. 128

Figure 5-6 Summary of lap shear load-displacement test on coated specimens with SiO_2 129

Figure 5-7 Summary of lap shear load-displacement test on coated specimens with Graphene oxide. 129

Figure 5-8 Summary of lap shear load-displacement test on coated specimens with Ti powder 130

Figure 5-9 Schematics of steel coupon samples as per recommendations in ASTM E8/E8M. 131

Figure 5-10 Scribes in the steel coupon. The damage is the filled red area. 133

Figure 5-11 Figure 1.2 CFRP Repaired steel sheet specimen. 133

Figure 5-12 Patch section loss (top), and through thickness hole (bottom). Red dots indicate the damaged area. 135

Figure 5-13 Types of damages (top) shown in the specimens, repaired specimens with CFRP. 136

Figure 5-14 Load-Displacement curves for specimens tested with hole damage. 137

Figure 5-15 Load-Displacement curves for specimens tested with linear damage. 138

Figure 5-16 Load-Displacement curve for patch damaged specimens. 139

Figure 6-1 Example of calculated SIF for mode I fracture for a 1mm deep crack. (a) schematics of crack location, (b) SIF calculated at 5 counter integration points, (c) 5 contours shown at the crack tip, and (d) stress at the crack tip. 141

Figure 6-2 Variations of K1 SIF with increasing crack depth through pipe thickness for 5 different contour integration groups. 142

Figure 6-3 SIF values for Mode-I fracture at 3.6mm crack depth for 2D plane strain pipe model (blue square is 1st contour). 143

Figure 6-4 Mesh size sensitivity analysis results for an elliptical crack with length of $L = 10mm$ and depth of $a = 1mm$. 144

Figure 6-5 3D pipe model with three different representations for modeling. 145

Figure 6-6 Verification of model size reduction by symmetry. Comparison of all three model results shows full accordance. 146

Figure 6-7 All FE modeled crack length-depth combination considered. 147

Figure 6-8 Comparison of SIF results from simulation. (a) results for crack length $L = 10mm$ along the length, (b) results for crack length $L = 10mm$ along the crack perimeter , (c) results for crack length $L = 40mm$ along the length, and (d) results for crack length $L = 40mm$ along the crack perimeter. 148

Figure 6-9 This figure shows variations of stress intensity along crack front in 6 scenarios of length-depth. 149

Figure 6-10 comparison of data fitting functions for SIF along crack depth with various training data sizes. Gaussian process fit (left), polynomial fit(middle), and R square score and fitting error distribution (right). (a) models fit with 13 training data, (b) model fit with 26 training data, and (c) model fit with 42 training data. Crack lengths are in mm and SIF in MPa.mm-1. 153

Figure 6-11 comparison of data fitting functions for SIF along crack length with various training data sizes. Gaussian process fit (left), polynomial fit(middle), and R square score and fitting error distribution (right). (a) models fit with 13 training data, (b) model fit with 26 training data, and (c) model fit with 42 training data. Crack lengths are in mm and SIF in MPa.mm-1. 154

Figure 6-12 Comparison of SIF results from simulation for patch repaired pipe model. (a) results for crack length $L = 10mm$ along the length, (b) results for crack length $L = 10mm$ along the crack perimeter , (c) results for crack length $L = 40mm$ along the length, and (d) results for crack length $L = 40mm$ along the crack perimeter. 157

Figure 6-13 Symmetrical quartile model of patch repaired pipe. 158

Figure 6-14 comparison of data fitting functions for SIF along crack depth with various training data sizes for patch-repaired pipe model. Gaussian process fit (left), polynomial fit(middle), and R square score and fitting error distribution (right). (a) models fit with 13 training data, (b) model fit with 26 training data, and (c) model fit with 42 training data. Crack lengths are in mm and SIF in MPa.mm-1. 159

Figure 6-15 comparison of data fitting functions for SIF along crack length with various training data sizes for patch-repaired pipe model. Gaussian process fit (left), polynomial fit(middle), and R square score and fitting error distribution (right). (a) models fit with 13 training data, (b) model fit with 26 training data, and (c) model fit with 42 training data. Crack lengths are in mm and SIF in MPa.mm-1. 160

Figure 7-1 Flowchart of proposed model.. 162

Figure 7-2 EIFS and IFS concept. Top: (a) Concept of crack growth with origination vs. crack existence and growth from day one, (b) Demonstration that how EIFS distribution affects distribution of number of cycles (time) at failure, (after Johnson 2010);Bottom: (c) crack growth behavior with growth rate, (d) equivalency of final cycle Nf with area under inverse growth functions,(after Liu et al. 2009). 164

Figure 7-3 Schematics of plate with edge crack under uniform remote tensile stress.... 165

Figure 7-4 Simpson's quadratic integration rule is estimating $f(x)$ with $P(x)$ to perform integration from $x = a$ to $x = b$... 168

Figure 7-5 Synthetically generated data in plate model. (a) (N, a) pair data set sample, (b) True N versus noisy N, and (c) Comparison of inferred EIFS distribution and True EIFS distribution. 170

Figure 7-6 Box plot illustrating EIFS distribution for individual data points............... 171

Figure 7-7 (a) Initialization of likelihood array. For a normal distribution the hyper parameters $\alpha 1$ and $\alpha 2$, are mean and standard deviation. For each pair of hyper-parameters an $EIFS$ distribution which are indicated by long gray blocks are generated , shown with θ. (b) Bayes structure with hyper parameters. 172

Figure 7-8 Flowchart of estimating the likelihood of $EIFS$ distribution hyper parameters. 174

Figure 7-9 Joint likelihood of mean and standard deviation ($\boldsymbol{\alpha}$ parameters) of EIFS distribution for all 20 data points.. 174

Figure 7-10 (a) Joint probability density function of mean and standard deviation of EIFS, (b) Marginal probability density of mean of EIFS, (c) Marginal probability density of standard deviation of EIFS. (d) Estimated EIFS density vs. True assumed density for EIFS. 175

Figure 7-11 Flow chart that shows derivation of number of cycles for at failure depth in generating synthetic data.. 178

Figure 7-12 An illustrative example of possible distribution of number cycles to failure for a steel plate with thickness of 7mm. assumptions: $EIFS \sim N(1.5,0.12)$, and $af \sim N(6,0.1)$. 180

Figure 7-13 Flowchart of deriving estimated distribution for number cycles for final (or failure) crack size distribution. 181

Figure 7-14 Estimating the distribution for number of cycles to reach final crack size. Inferring $\boldsymbol{N_{range}}$ likelihood density directly for various sample sizes(left), Inferring $\boldsymbol{N_{range}}$ hyper parameters’ joint likelihood (middle), and likelihood densities of $\boldsymbol{N_{range}}$ for various sample sizes (right)... 183

Figure 7-15 Synthetic data points generated for 2 dimensional crack growth in pipe wall. Crack depth vs. cycle(left), crack length vs. cycle (middle), and true cycle vs. noise added cycle (right). 185

Figure 7-16 Comparison of estimated and true marginal $EIFS$ likelihood distributions. Joint likelihood distribution of crack length and depth (left), Crack depth distribution (middle), crack length (right). for 30 data points. 185

Figure 7-17 Estimating the distribution for number of cycles to reach final crack size. Inferring $\boldsymbol{N_{range}}$ likelihood density directly for various sample sizes(top), Inferring $\boldsymbol{N_{range}}$ hyper parameters' joint likelihood (bottom left), and likelihood densities of $\boldsymbol{N_{range}}$ for various sample sizes (bottom right). 189

List of Tables

Table 2-1 Mechanical properties of geopolymer-carbon fiber composites (Lyon et a. 1997). 39

Table 3-1 FHWA test cycle (after Kodumuri et al. 2012). 45

Table 3-2 Batch-1 Coating systems. 57

Table 3-3 Batch-1 Coating systems and Thicknesses. 58

Table 3-4 Failure Type keyword glossary for pull off strength test. 59

Table 3-5 Batch-1 pull off strength results. 60

Table 3-6 Batch-1 Coating systems. 61

Table 3-7 Spot coating thickness measurements, Batch-2 62

Table 3-8 Pull off strength test results for Batch-2 specimens. 64

Table 3-9 Coating systems in Batch-3. 66

Table 3-10 Coating thickness measurements, Batch-3. 66

Table 3-11 Pull off strength for Batch-3 samples. 70

Table 3-12 Batch-4 coating mix constituents – Original water Content 76

Table 3-13 Batch-5 coating Mix constituents – increased water content 84

Table 4-1 Thickness data of coated samples for Resin-Coating bond evaluation. 92

Table 4-2 Resin thickness measurement data on the coated samples. 94

Table 4-3 Pull-Off strength of Saturant Resin on Geopolymer coated specimen............ 95

Table 4-4 Ultimate Load for coated and uncoated specimens... 97

Table 4-5 Steel Properties used in the FE model.. 107

Table 5-1 Summary of test results on all lap-shear specimens...................................... 126

Table 7-1 Material and model parameters used in the plate model............................... 170

Table 7-2 Comparison of EIFS inference results using discussed methods.................. 176

Table 7-3 Comparison of direct inference of $\boldsymbol{N_{range}}$ on different sample sizes. 183

Table 7-4 Comparison of inference of $\boldsymbol{N_{range}}$ with hyper parameters on different sample sizes... 183

Table 7-5 Estimated vs. true distribution values for $EIFS$ along depth and length........ 187

Table 7-6 Comparison of direct inference of $\boldsymbol{N_{range}}$ on different sample sizes. 187

Table 7-7 Comparison of inference of $\boldsymbol{N_{range}}$ with hyper parameters on different sample sizes... 189

1 Introduction

1.1 Background

Maintenance of civil infrastructures is an important task to ensure safe and optimized serviceability of these facilities. Steel as one of the major construction materials used in many structures such bridges, pipelines, and power transmission towers (pylons) is susceptible to environmental degradation without proper coating protection and recoating maintenance. On the other hand， many older structures need to be repaired as design codes are updated and reinforced, or loading considerations for those structures changes.

Most extensively developed applications of polymer composites are in repair and upgrading of bridge beams and girders and building structures. Due to variety of reasons such as marginal design, use of inferior materials, poor construction and management, and/or design errors the desired factor of safety maybe breached in those structures. On the other hand, the increase of service loads such as traffic, safety requirements, and the change of serviceability may require upgrade in design of the present structure. In addition, the deterioration of materials in load bearing elements of the structure as a result of aging, corrosion compromises the serviceability and safety of those structures.

Many lab scale and field studies have been cried out to investigate composite repair application on steel. Tavakolizadeh et al. (2001) showed increase of 144% and 63% on load bearing of an I-beam with 80% and 40% loss of tension flange with drawback of loss of ductility among others. The bond strength between CFRP and metal surfaces which transfers load from metal substrate to CFRP is an important property to be appropriately quantified. A number of studies have investigated the relationship between bond length and bond strength, and predicting fatigue failure and ultimate load using Single lap joint (ASTM D1002) tests and FEM using fracture mechanics concepts.

Larger scale tests (beam tests) have been also carried out to come up with expressions for minimum required bond length and stiffness increase. Miller et al. (2001) reported an increase of 1%-37% in steel girder stiffness. Sen et al. (2001) reported an increase of 21% and 52% for 2 and 5 mm CFRP laminates for 310Mpa wide flange shape girders. To investigate cylindrical reservoir shells, Teng et al. (2007) studied the confined steel tube with CFRP to investigate elephant foot buckling. They reported enhancement of ductility but not considerable compressive load bearing increase.

1.2 Problem Statement

The conventional repair of steel structures involves the use of steel plates in form of welding, bolting, adhesive attachment and clamping. These methods introduce new challenges such as additional dead weight to the structure, minimum length and thickness restrictions (5mm minimum thickness and 6-8m minimum length) to satisfy welding and blasting requirements. In addition, they need for more comprehensive surface preparation and more labor intensive fitting and sizing procedure. Also the conventional method cannot change the fact of susceptibility to corrosion of the strengthening elements.

As a desired alternative for steel repair, Carbon Fiber Reinforced Polymer (CFRP) composites have the flexibility of shape and fitting convenience. Fiber content and carbon fiber density can be selected based on application specifics. The imposed weight on the structure would be a fraction of the case of reinforcement with steel plates. They also project lower cost in the combined initial and maintenance costs and require minimal traffic interruptions in the case of bridge repairs.

CFRP is one of the best performing polymer composites because of high modulus of carbon fibers. Light, medium, and heavy weight carbon fabrics with different modulus are available for various applications. One of the challenges of using carbon fibers is to prevent induction of galvanic corrosion (Tavakkolizadeh et al. 2001) in steel pipelines due to presence of cathodic protection currents. Common practice is to use Glass FRP as the barrier layer prior to CFRP wrap. Other practice recommends application of thicker adhesive layer as base layer.

Organic coatings are the major products used for corrosion control in different industries such as pipelines. Despite the general good performance of these coatings they have some major draw backs. Most of these materials are toxic to human health in long term exposures during applications and need full protective masks and suits during the process. They are susceptible to gouge and dents which occur frequently during transportation of pipe sections.

Alternatively, an inorganic coating system such as geopolymer could be used as standalone coating system or a hybrid system along with organic coating and reduce these risks. Geopolymers coatings have zero Volatile Organic Components (VOCs) and no special waste management is required for the excess material. They have high abrasion resistance will not be peeled compared to organic systems.

In an aging pipeline network fatigue is one of the failure scenarios that increases the risk of failure in the pipe structure. Crack initiation and growth is a complex stochastic phenomenon. Timely maintenance is the key to keep the pipeline in serviceable and safe condition. Previously collected crack inspection data can be used to infer statistics of different variables of interest and propose suitable times to do repairs. Bayesian inference is an effective method to estimates parameters especially when available data is limited.

1.3 Objectives and Methodology

The objective of the proposed research is to evaluate the feasibility and applicability of using inorganic coating with CFRP for steel repair and corrosion protection. It is expected that inorganic coating could work as an effective barrier between carbon fabric and steel for corrosion protection and at the same time provide better load transfer from steel to carbon fabric. It could replace GFRPs or thick adhesive layers that are the common practice.

The following tasks are conducted to fulfill the study objectives.

1. Compare corrosion protection performance of different inorganic coating systems and organic coatings using accelerated corrosion test. The inorganic coating will be prepared using different nano-additives, layer thicknesses, water contents, and preparation procedures.

To study the effect of environmental induced degradation such as corrosion, freezing, and UV deterioration, samples from both Pull off and Lap shear tests will be put in an accelerated corrosion chamber. In this chamber the samples will be exposed to harsh conditions of freezing, UV an Infrared exposure and salt water spray in 24h cycle. The samples will be tested at different exposure times to study the performance under long time environmental exposure of rain and moisture, deicing agents, freezing cold, and sun’s UVB and infrared rays.

2. Evaluate mechanical strength of CFRP-geopolymer interface when using inorganic coating as an intermediate layer between steel and CFRP using laboratory experiments and finite element modeling.

The pull-off test measures the failure stress to debond a coating or epoxy from a substrate surface (adhesive failure) under direct tension. The resin used to impregnate the Carbon Fabric will be spread on the designated specimen surface to achieve same thickness as in application of CFRP. Pull off test will be performed on both sets of specimens (with and w/o inorganic coating) to study adhesive failure and compare epoxy-steel and epoxy-coating interface behavior.

A modified Lap shear test was designed to study direct shear stress and shear strength of epoxy resin under similar shearing stress regime as in CFRP repaired structural section working in tension. Like pull off test, the lap shear test would be performed both on coated and uncoated steel to investigate role of inorganic coating on failure load and bond length and consequently the average bond strength. The following tasks are conducted to fulfill the study objectives.

3. Evaluate mechanical performance of strengthened steel component with inorganic coating and CFRP using laboratory experiments and finite element modeling.

Steel sheet stripes with different types of damages will be repaired using CFRP wrap. Laboratory experiments similar to lap shear tests will be performed to evaluate integrity of repaired element under various loading condition. Plastic behavior of steel during failure and bond length effect on the ultimate load capacity of repaired element will be investigated using FE analysis. Damage initiation and evolution within the steel and/or CFRP-Steel bond are investigated.

4. Develop a backward-forward application of a Bayesian network to infer probability density function (PDF) of the equivalent initial crack (flaw) size (EIFS) and subsequently infer the respective PDF for number of cycles to failure.

The model was first developed based on single dimensional crack growth problem in plate with edge crack. Then wit was expanded to 2-dimenssional crack growth problem in pipe wall. Stress intensity factors (SIF) at the crack tip in pipe model were computed using finite element (FE) analysis at various combinations of crack length and depths, and extended to intermediary point using fitted surrogate models. Accurate inferred results for PDF of both EIFS and number of cycles to failure in both plate and pipe models were demonstrated.

2 Literature Review

2.1 Steel Structure Repair

Primary guidelines recommended to repair steel girders are flame straightening, hot mechanical straightening, cold mechanical straightening, welding, bolting, partial replacement, and complete replacement (Shanafelt et al. 1984). Welding may be used to repair defects or cracks. In addition, welding a replacement segment into place, and adding strengthening plate by welding are other options.

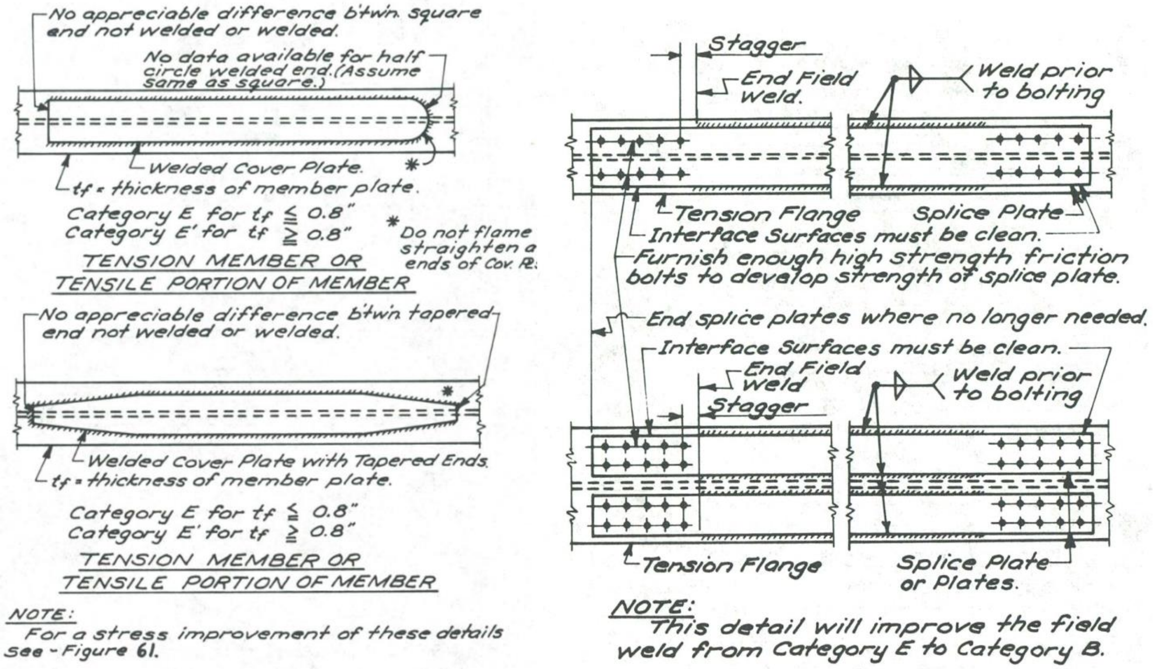
No appreciable difference b'twn. square end not welded or welded.
No data available for half circle welded end. (Assume same as square.)
Welded Cover Plate.
*
t_f = thickness of member plate.
Category E for $t_f \leq 0.8''$
Category E' for $t_f \geq 0.8''$
* Do not flame straighten a ends of Cov. P
TENSION MEMBER OR TENSILE PORTION OF MEMBER
No appreciable difference b'twn. tapered end not welded or welded.
*
Welded Cover Plate with Tapered Ends.
t_f = thickness of member plate.
Category E for $t_f \leq 0.8''$
Category E' for $t_f \geq 0.8''$
TENSION MEMBER OR TENSILE PORTION OF MEMBER
NOTE: For a stress improvement of these details see - Figure 61.
Stagger
End Field Weld.
Weld prior to bolting
Tension Flange
Splice Plate
Interface Surfaces must be clean.
Furnish enough high strength friction bolts to develop strength of splice plate.
End splice plates where no longer needed.
Interface Surfaces must be clean.
End Field Weld
Stagger
Weld prior to bolting
Tension Flange
Splice Plate or Plates.
NOTE: This detail will improve the field weld from Category E to Category B.

Figure 2-1 Details of repair using steel plates with welding (left), and combination of welding and bolting (right) (Shanafelt et al. 1984).

Not all grades of steel are recommended for welding and welding in tensile areas can be dangerous and counterproductive measure such as welding fracture-critical members (members whose failure would induce structural collapse). Welding should not be performed on low Charpy impact value steels or in very cold weather where this value is reduced.

Bolting can be used as a single or supplemental repair method. A damaged element will be replaced and fastened with high strength bolts and is considered one of the safest methods of repair. Damaged riveted elements may be considered to be replaced with bolted material. Adding bolted splice material to bolted members are difficult. A combination of welding and bolting at plate ends would be a suitable solution for weldable steel. Fracture critical members, A-514 and A-517 steel grades, and members that do not meet flame straightening criterial should be repaired by bolting. Some details of repair methods are shown in Figure 2-1.

In cases of excessive damages to the steel members such as wrinkled, reared, extreme deformation, and cracks, partial replacement is used as the repair method. This includes removal of defective member, and placing new welded insert or bolted splice. In terms of durability, any chosen method of repair should have equivalent or better durability than that of the original undamaged member.

2.2 Fiber Reinforced Polymer (FRP)

Advanced Polymer Composites (APCs) are made of reinforcing fibers or fabrics and adhesive resin. Common fibers include carbon fiber, aramid fibers, glass fibers, and basalt fibers. The composite product would be manufactured in a factory in the form of pultruded plates and delivered to the site, or from pre-impregnated fabric sheets with resin for in situ lamination. The last method is performed on site by wetting the fabrics with resin and laid-up process. Properties of the polymer composites depend on fabric volume fraction and fiber orientation. Epoxies are most common adhesives used in civil engineering applications for bonding polymer composite plates. Due to curing condition on construction sites it is desirable to use epoxies that are compatible for curing at ambient temperature rather than elevated temperature curing (Hollaway, et al. 2002).

According to CIRIA report, throughout the world there are a large number of metallic structures dating back to 19th century including railway bridges, underground tunnel lining, jack arch decks, and cast iron framed industrial buildings. Common materials include grey cast iron, wrought iron, ductile cast iron, and most recently carbon steel. Upgrading design and procedure would be different for each of these metals as they have different mechanical properties.

The gap Analysis for durability of fiber Reinforced Polymer Composites in Civil Engineering conducted by Civil Engineering Research Federation (CERF) of the ASCE in 2001 has reported substantial advantages of FRPs over convention materials in applications such as pipelines, storage thanks, and architectural components. The report indicates six areas where further research in long term durability performance data is required: alkaline environment, thermal effects, creep and relaxation effects, ultra violet effects, fatigue performance, and fire performance (Tavakolizadeh et al. 2001)

2.2.1 Environmental degradation and aging effect

Environmental degradation is an important issue in design consideration for CFRP plates, as mechanical properties of the resin such as strength and stiffness may change due to long-time exposure to harsh service environments such as moisture, temperature, chlorides from salt water, de-icing agents used during winter, and ultra violet (UV) exposure from sun. Additionally, edges at the bond area which are the primary and critical load transfer zones are first to be affected by environmental adverse effects.

Durability of adhesive joint is greatly affected by the presence of water or high humidity. Water affects the adhesive bond by plasticization of adhesive, irreversible change of properties, and attacking the interface through capillary action within cracks.

2.2.2 Surface Preparation Effect

Surface preparation for metal adherents is an important step to ensure formation of chemical bonds between adherents and adhesive. These chemical links (mainly covalent and some ionic, also hydrogen bonds may exist) transfer the load from metal to the polymer composites. Degreasing, surface abrasion to provide fresh metal surface that promotes chemical bond, and chemical modification of surface to produce a hydration resistant interface. One of the best methods of practice is grit blasting.

Galvanic interaction between CFRP and metal adherent in electrolyte such as sea water is another undesirable phenomenon that should be controlled. A corrosion barrier (usually glass fabric layer) and an adhesive resistant to chlorides, moisture, and freeze-thaw should be utilized (Hollaway, et al. 2002; Tavakkolizadeh et al. 2001).

2.2.3 Bond performance

Adhesion between CFRP and the adherent is the critical part of repaired or strengthened structure with CFRP. This yearns for deep understanding of bond behavior at the interface. Zhao et al. (2007) conducted extensively reviews bond between steel and FRP, strengthening of hollow section members, and fatigue crack propagation. Four types of bond test methods were categorized. To investigate bond performance a modified double strap lap shear joint is recommended, as shown in Figure 2-2.

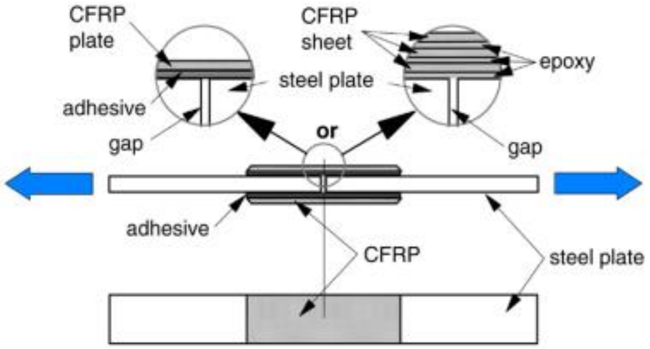
CFRP plate
adhesive
gap
CFRP sheet
steel plate
epoxy
or
gap
adhesive
CFRP
steel plate

Figure 2-2 Double strap Lap Shear Joint (after Zhao et. al, 2007).

The possible failure modes in the CFRP strengthened system subject to tensile force are: steel and adhesive interface failure, cohesive failure (adhesive layer failure), CFRP delamination (separation of carbon fibers and resin), CFRP rupture, steel yielding (Figure 2-3).

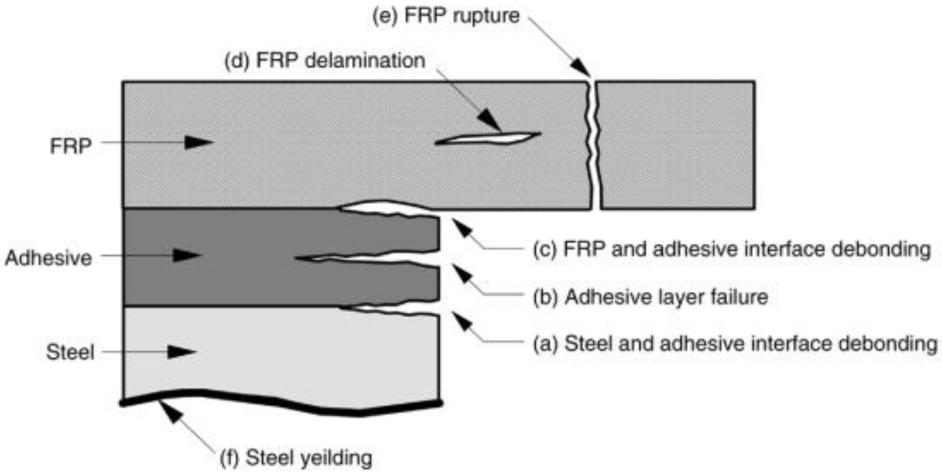
(e) FRP rupture
(d) FRP delamination
FRP
Adhesive
Steel
(c) FRP and adhesive interface debonding
(b) Adhesive layer failure
(a) Steel and adhesive interface debonding
(f) Steel yeilding

Figure 2-3 Failure modes of adhesively bonded FRP to adherends (after Zhao et al. 2007).

The common failure modes for normal modulus (100-250GPa) CFRP plates are CFRP delamination and steel interface deboning. But for high modulus (greater than 640GPa) the failure mode is CFRP rupture (Zhao et al. 2007).

Three bond strength prediction methodologies were categorized. First, stress distribution method, which is based on equilibrium and deformation compatibility with close form solutions for maximum shear strength. The calculated bond strength is function of material properties and geometry of the bond such as adhesive thickness, Young's modulus and shear modulus of adhesive, adhesive shear strength, Young's modulus of CFRP, and Poisson's ratio of adhesive.

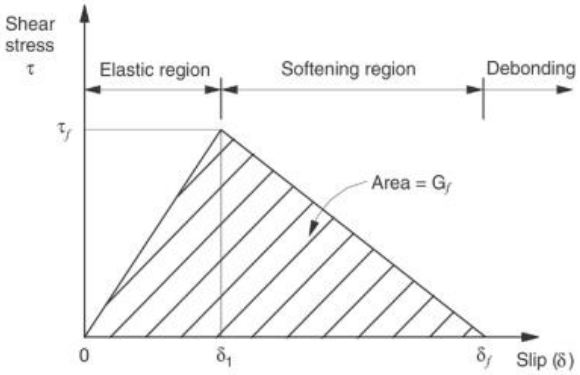

Figure 2-4 Bilinear bond-slip model (after Zhao et. al ,2007).

Second, the bond-slip relationship, which is similar to existing analytical model in CFRP-Concrete bond system. This model assumes a thin CFRP plate glued to a bulk size adherent (high rigidity compared to the CFRP plate). The predicted strength is function of elastic modulus and stiffness of CFRP plates (section dimensions), and interfacial fracture energy (G_f) can be calculated using tensile stress-displacement (bond-slip) relationship (Figure 2-4). An accurate model is required to capture accurate properties. A simplified bi-linear bond-slip model can be defined by three variables, local bond strength (τ_f), slip at peak shear stress (δ_1), and slip at the fracture (δ_f).

Fatigue crack propagation in steel FRP interface is not significant (less than 10%) if the cyclic load is less than 35% of ultimate static load and the exposure is less than 6 million cycles. Normal modulus bonded CFRP are deemed to be more sensitive to fatigue cycles while high modulus bonded CFRP show more sensitivity to applied load ranges. Use of very stiff CFRP does not contribute to effectiveness of reinforcement. Thin adhesive layer reduces reinforcement effectiveness. It is recommended to apply CFRP reinforcement directly on the defective tensile element such as cracked section, hole in section or area of loss in the section. Better performance may be achieved by pre-tensioning of CFRP plates (Zhao et al. 2007).

Analytical solutions are reliable tools to predict failure and verify numerical simulations. Wu et al. (2002) proposed an analytical solution for interfacial stress transfer with a bilinear and linear bond-slip behavior for pull-pull and pull-push FRP-adhrent setup and showed satisfactory comparison of results with numerical solutions. Yuan et al. (2004) extended the analytical solution to capture full debonding propagation process employing bond-slip model. Their work has two objectives. The first is to establish a rigorous FRP-to-Adherent (focused on concrete but applicable to steel and aluminum) theoretical basis for full range of load-displacement behavior. The second is to determinate of interfacial property using load displacement behavior. It was assumed that adherent has only uniform axial stresses and bending, pure shear behavior, and Mode-II failure of adhesive layer were neglected. The bond length is assumed to be strictly infinite or considerably longer than effective bond length.

2.3 Steel Bridge Repair with CFRP

Repair of concrete structural elements such as concrete columns are more common than steel structures. Primary reasons for this practice are lower modulus of concrete compared to steel and galvanic corrosion of steel in proximity to carbon. Applications of FRPs to steel structures are becoming more popular as higher modulus carbon fabrics are becoming more available and practical.

2.3.1 Laboratory Studies

Many lab scale and field studies have been cried out to investigate CFRP repair application on steel. Tavakolizadeh et al. (2001) showed increase of 144% and 63% on load bearing of an I-beam with 80% and 40% loss of tension flange with drawback of loss of ductility among others (Tavakkolizadeh et al. 2003; Bambach et al. 2009). Sen et al (2001) investigated CFRP laminates used to reinforce composite bridge girders. Two variations of yield strength of 310MPa (3 beams) and 370Mpa (2 beams) and two CFRP laminate thicknesses of 2mm and 5mm were combined to study different repair scenarios. Two of 310MPa yield beams were reinforced with 5mm laminates and last one was reinforced by 2mm laminate. Both 370MPa yield beams were reinforced by 2mm laminates. Surface preparation prior to CFRP bonding was performed by sand blasting the tension flange.

Composite beams were preloaded past yielding point of steel tension flange before repair to simulate service damage. To curtail peel stress at the ending edges of CFRP laminate a steel clamp was utilized. The reported increase in the ultimate strength ranged from 9% (for 2mm laminates) to 52% for 5mm laminates. The stiffening effect of the laminates, which affected deflection of the beams was shown to be negligible due to the lower modulus of CFRP laminates compared to steel. Reported failure was due to shear of CFRP by bolts in case of 5mm laminates and excessive deflection for cases strengthened with 2mm laminates.

Miller et al. (2001) used Pultruded CP laminates with 5.25mm thickness to reinforce bridge girder. The application process included grinding and sand blasting to reveal clean bare steel. Steel surface was pre-treated with adhesion promoter prior to applying adhesive layer. Glass FRP was used as the intermediary layer to prevent galvanic corrosion between steel and carbon. A static 3-point bending test was conducted on four 21ft. long S24X80 beams obtained from a bridge that has been in service. Due to corrosion, stiffness loss determined to be from 13% to 32%. A single layer Glass FRP was applied to prevent galvanic corrosion. Stiffness increase observed in the girder was from 10% to 37%. The reported strength increase compared to the corroded samples was from 17% to 25%. Field application of plates was followed by a jointed application of laminates along the girder according to selected development length. Plated endings were beveled at 45° to reduce peel stress. Tests were performed before and after truck load to investigate performance of strengthened girder. The load test data showed 11.6% increase in the stiffness. The strain response is shown in Figure 2-5.

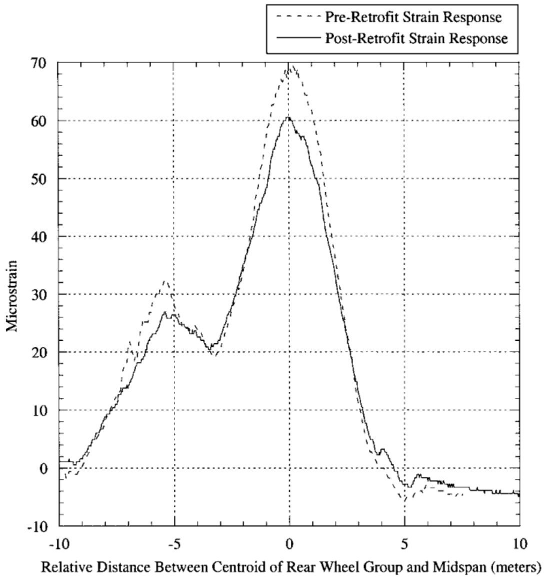

Figure 2-5 Comparison of pre- and post-retrofit tension strain field test (After Miller et al. 2001)

.

To study force transfer between steel substrate and CFRP plates a test setup according to the Figure 2-6 (left) was presented.

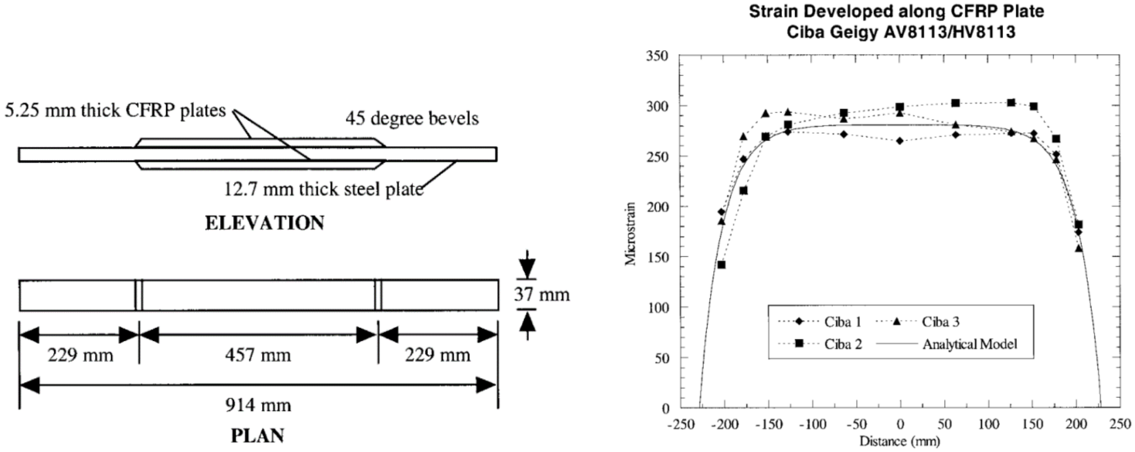
5.25 mm thick CFRP plates
45 degree bevels
12.7 mm thick steel plate
ELEVATION
37 mm
229 mm
457 mm
229 mm
914 mm
PLAN
Strain Developed along CFRP Plate
Ciba Geigy AV8113/HV8113
Microstrain
350
300
250
200
150
100
50
0
-250
-200
-150
-100
-50
0
50
100
150
200
250
Distance (mm)
Ciba 1
Ciba 2
Ciba 3
Analytical Model

Figure 2-6 Lab test setup (left), Comparison to of response to analytical model (After Miller et al. 2001)

Eighteen foil strain gauges were used to log the longitudinal strain along the bond. An elastic 1-Dimmenssional analytical method was used to compare with test results:

$$\tau_a(y) = -\frac{\frac{P}{E_S t_S} + (\alpha_{SS} - a_p)\Delta T}{\left(\frac{1}{E_p t_p} + \frac{2}{E_S t_S}\right)} \lambda \frac{\sinh(\lambda y)}{\cosh(\lambda l)} \tag{2.1}$$

$$\sigma_p(y) = \left(\frac{\frac{P}{E_S t_S} + (\alpha_{SS} - a_p)\Delta T}{t_p\left(\frac{1}{E_p t_p} + \frac{2}{E_S t_S}\right)}\right)\left(1 - \frac{\cosh(\lambda y)}{\cosh(\lambda l)}\right) \tag{2.2}$$

$$\sigma_s(y) = 2\left(\frac{\frac{P}{E_S t_S} + (\alpha_{SS} - a_p)\Delta T}{t_s\left(\frac{1}{E_p t_p} + \frac{2}{E_S t_S}\right)}\right)\frac{\cosh(\lambda y)}{\cosh(\lambda l)} + \left(\frac{\frac{P}{E_p t_p} + 2(\alpha_{SS} - a_p)\Delta T}{t_s\left(\frac{1}{E_p t_p} + \frac{2}{E_S t_S}\right)}\right) \tag{2.3}$$

$$\lambda_{shear-lag\ correction} = \sqrt{\frac{\left(\frac{1}{E_p t_p} + \frac{2}{E_S t_S}\right)}{\left(\frac{1\,t_S}{4G_S} + \frac{t_a}{G_a} + \frac{3\,t_p}{8G_p}\right)}} \tag{2.4}$$

A fatigue test was performed on seven of the same type test specimens at 82.7MPa stress range. All samples could reach 2.55 million cycles without falling and stayed fully bonded (Miller et al. 2001).

2.3.2 Field Studies

Some of the case studies of restoration of older metallic structures are reviewed. Tickford Bridge in Newport Pagnell UK, where the world's oldest operational cast iron highway bridge (Built in 1810) was strengthened by CFRP wet lay-up system to eliminate the imposed 3-tonne gross weight restriction. A combination of ambient curing and elevated temperature cuing for critical areas was implemented. A total 120m^2 of carbon fabric up to 14 layers was applied. To prevent galvanic corrosion, a continuous filament polyester veil was used at the interface of carbon fabric and prepped metal surface. The maximum thickness of 10mm demonstrated that strengthening was achieved with the minimal effect on aesthetics of the bridge. This work was completed in 10 weeks.

A principal beam on Boots building in Nottingham, UK was strengthened with a low temperature curing advanced polymer composite. A combination of unidirectional for flexural strengthening and bidirectional for shear and torsional strengthening Ultra High Modulus (UHM) carbon fabric was used in this project. In addition to the proper surface preparations, silica gel packs were used to dry the application surface.

King Street Railway Bridge was updated to be able to carry heavy vehicles. This cast iron bridge was preloaded initially with struts to support the dead weight and it was released of the preload after CFRP application which enforces partially pre stressed conditions on the strengthened system. Cast iron is notorious for having defects such as voids which projects unpredictable brittle failure in the material comped to the modern ductile steel. Unidirectional UHM carbon fabric with 360GPa elastic modulus and 1.1GPa tensile strength were selected for this project and glass fibers were used as base layer for galvanic action prevention and provided transverse strength. The thickness of the laminates was limited to 10mm with adhesive layer of 2 to 10mm.

The I-704 Bridge in Newark Delaware, USA, was strengthened with CFRP to study CFRP bonding to steel structure and failure of the CFRP would not have had compromised the integrity of the bridge. The girder under highest stress range was selected to be treated with CFRP plates with 1.5m length and 300mm staggered joints. Adhesive thickness was measured to be 1.5 mm. Load test after strengthening showed

CFRP plates resulted in 1.6% stiffness increase and strain decrease of 10% (Tavakkolizadeh et al. 2001; Miller et al. 2001).

The Bid Bridge in Kent, UK, was strengthened by UHM CFRP plates. This bridge was built in 1876 with brick jack arch supported beams in need of restoration. Twelve 6m-ling UHM CFRP pre-impregnated plates was used to seven of the nine cast iron beams to enhance the strength required to allow 40 tonne and 5-Axle vehicle passage. Plates were 0.5mm thick and were stacked for each case to achieve required thickness. Tapers and localized reinforcements were provided to control stress concentration at the end edge of plates.

The Slatocks canal Bridge in Rochdale, UK, an historic steel bridge, constructed in 1935 had been restricted to 19tonnes since 1996. In 2000 it was upgraded to 40 tonne by plate bonding of 8mm thick, 100 mmm wide unstressed CFRP plates. An elastic-plastic design was implemented where the steel was allowed to become plastic while CFRP plates were working in elastic limits.

The Bow Road Bridge, East London UK, built in 1850 with cast iron beams, was strengthened with eleven 170mm wide, 20mm thick, 5m long unstressed CFRP plates.

London underground Railway system was constructed mainly in 19th century with cut-and-cover technique. Cast iron beams spaced at 2.4 meters were designed sitting on the lined brick walls. Due to ageing of cast iron over the years and significant increase in building and traffic loads, structure was deemed to have weakened. CFRP plates were chosen for strengthening.

2.4 FRP Applications in Pipeline

2.4.1 Composite Repair Methods

Several different methods are practiced to repair in service pipes in the industry. Grinding and recoating is a method in which shallow surface defects (up to 10% of pipe thickness), such as corrosion and micro-cracks are grinded to achieve a smooth surface. This method is performed while pipeline is in service. During the repair period the service pressure is reduced 20%. Non-destructive methods are used to examine grinded surface to verify a smooth and non-defective finish is achieved.

Steel reinforcement sleeve is another method of repair. This method has two main sub-categories of Type A and Type B. In Type A two half circle steel sections are covered the damaged area. These half circles are not welded to the pipe itself. They recover mechanical strength of the pipe section and are not intended to contain leaks. Type B on the other hand is designed to contain leaks and circumferentially oriented defects. Another type of steel reinforcement is use of half circles clamps coupled together using bolts. Improper application method and corrosion of bolts are reported as potential drawbacks of this method.

Composite sleeve repair is an innovative and proven technology to restore structural capacity of damaged pipes (Toutanji et al. 2001; Alexander et al. 2006; Freire et al. 2007; Duel et al. 2008; Farrag 2012; Shamsuddoha et al. 2013). Research in application of composites as repair alternative in pipeline industry was initiated by Gas Research Institute (GRI) from mid-1980’s to the late 1990’s. Several testing programs were established and performed by manufacturers and different research agencies to study composite physical properties, long term adhesive creep. Other performance indicators such as cyclic fatigue, lap shear tests, and long term perm performance were performed (Farag 2013). Commonly accepted techniques were documented in a manual developed by Pipeline Research International Council (PRIC) (Jaske et al. 2006). Wide spread use of composite repair systems for pipeline repairs in the United States urged the industry to develop standard codes (Alexander et al. 2006).

2.4.2 Standards in Pipeline repair using FRP Wraps

ASME considers two main repair scenarios: component is not leaking and needs reinforcement (Type-A), and component is leaking and needs reinforcement (Type-B).

For Type-A repair three design approaches are recommended. The component being repaired as load bearing member in the reinforcement design could be allowed yielding or prevented from yielding. In the latter case the minimum repair thickness required is chosen as maximum of calculated thicknesses from hoop stress and axial stress expressions below (American Society of Mechanical Engineers, 2015) :

$$t_{min} = \frac{D}{2s} \cdot \left(\frac{E_s}{E_c}\right) \cdot (P - P_s) \tag{2.5}$$

$$t_{min} = \frac{D}{2s} \cdot \left(\frac{E_s}{E_c}\right) \cdot \left(\frac{2F}{\pi D^2} - P_s\right) \tag{2.6}$$

For the former case where yielding is allowed for original component the expression are:

$$\epsilon_c = \frac{PD}{2E_c t_{repair}} - s\frac{t_s}{E_c t_{repair}} - \frac{P_{live}D}{2(E_c t_{repair} + E_s t_s)} \tag{2.7}$$

For zero live pressure we would have:

$$t_{repair} = \frac{1}{\epsilon_c E_c} \left(\frac{PD}{2} - st_s\right) \tag{2.8}$$

The assumption made in these expressions assume that steel is elastic-perfectly plastic (no strain hardening occurs in the substrate component) and after yield all the load is carried by repair component. For axial load considering yield expression is as follows:

$$t_{repair} = \frac{1}{\epsilon_c E_a} \left(\frac{PD}{4} - st_s\right) \tag{2.9}$$

Similarly, maximum of two calculated thicknesses from hoop stress and axial stress will be selected as minimum required thickness for design.

If the contribution of original component is neglected, the design would be based on laminate allowable strains. Similar to the previous methods larger value of the calculated minimum thickness for hoop stress and axial stress is selected as the design thickness. For hoop stress the expression is as follows:

$$t_{min} = \frac{1}{\epsilon_c} \left(\frac{PD}{2} \frac{1}{E_c} - \frac{F}{\pi D} \frac{\upsilon_{ca}}{E_c}\right) \tag{2.10}$$

For Axial stress:

$$t_{min} = \frac{1}{\epsilon_a} \left(\frac{F}{\pi D} \frac{1}{E_a} - \frac{PD}{2} \frac{\upsilon_{ca}}{E_c}\right) \tag{2.11}$$

Allowable circumferential and axial laminate strains can be derived from:

$$\epsilon_c = f_T\, \epsilon_{co} - \Delta T\, (\alpha_s - \alpha_c) \tag{2.12}$$

$$\epsilon_a = f_T\, \epsilon_{ao} - \Delta T\, (\alpha_s - \alpha_a) \tag{2.13}$$

If performance test data is available ASME design suggests a service factor based on length of performance study. If the contribution from original component is not considered in the design the following expression is recommended:

$$t_{min} = \frac{PD}{2} \cdot (\frac{1}{f \cdot s_{lt}}) \tag{2.14}$$

If the contribution from original component is considered:

$$t_{repair} = (\frac{PD}{2} - t_s s) \cdot (\frac{1}{f \cdot s_{lt}}) \tag{2.15}$$

For axial stress previous expressions are still valid.

For Type-B repair in addition to the discussed methods for Type-A other consideration is required. A component is considered leaking if the thickness at the defect site is reduced to less than 1mm at the end of its life. Other considerations for repair include impact, axial length of repair application and cyclic loading. The reader is referred to ASME PCC2 paragraph 3.4.6 for further details.

It is important that standards are kept updated and improved with continuous research to have the most optimized guidelines in the practice. Saeed et al. (2014) suggested an equation to calculate hoop strain which is not influenced by live pressure in the pipe as ASME PCC2 and ISO 24827 suggest in their equations. For the case where live pressure in the pipe is not zero suggested equation estimates correct composite thickness for combination of different thickness reduction percentages and percentages of designed pressure. The ASME PCC2 for various thickness reduction percentages at higher percentages of design pressure and ISO 24827 for larger thickness reduction and higher percentage pressure cases estimate inadequate composite thickness.

2.4.3 Laboratory Studies

Damages incurred to pipelines such as loss of pipe thickness due to corrosion, dents and gouges during transportation are increasingly being repaired using FRPs. Proper load transfer from pipe to composite is one of the important factors to be addressed. Yielding of steel pipe transfers the load to the composite sleeve (Alexander et al. (2006); Freire et al. 2007). Wet lay-up application procedure makes repair of elbow and T fittings possible. Alexander et al. (2006) reported 15% and 50% burst pressure increase for T fittings and elbow fitting, respectively. They were six-inch diameter pipes with 50% emulated corrosion damage. To investigate effectiveness of composite repair systems for pipes, Freire et al. 2007 tested 14 steel pipe sections with 70% loss of thickness repaired with three composite repair systems. They reported that important part of pressure loading was carried out by composite sleeve.

Mechanical damage is responsible for large number of pipe failures (Dahlberg et al. 1985; Alexander et al. 2006). Traditionally mechanically damaged pipes were required to be repaired by welded sleeves or removal of the pipe altogether. Alexander et al. (2006) studied repair of dented or gauged pipes with composites for pipes with diameter to wall thickness ratios of 34 to 68 inches. Fatigue under cyclic water pressure for dent damage, indented grinded dent, and composite wrap repair after indentation of dent were investigated. Fatigue life was increased by the factor of nine times and 21 times for diameter to wall thickness ratios of 34 to 68 inches, respectively. Toutanji et al. (2001) investigated performance of carbon FRP, glass FRP, and aramid FRP in pipeline repair. Undamaged pipe, damaged pipe, and FRP repaired pipes were compared under soil, traffic and internal pressure loading. A superimposed equation for maximum circumferential tensile stress in the pipe wall was introduced considering hoop stress, stress due to soil weight, and traffic above the buried pipe. The effect of thickness reduction in the wall of the pipe due to corrosion was taken into account by a power law reduction factor for wall thickness derived empirically. Strengthening with FRP was taken into account by increasing the reduced thickness of pipe wall by a coefficient derived from relative stiffness ratio of the FRP patch to the thickness reduced area.

Undamaged pipe stress calculation formula (Toutanji et al. 2001):

$$\sigma_m = \sigma_f + \sigma_s + \sigma_t \tag{2.16}$$

$$\sigma_m = \frac{pr}{t} + \frac{6k_m C_d \gamma B_d^2 Etr}{Et^3+24k_d pr^3} + \frac{6k_m I_c C_t FEtr}{A(Et^3+24k_d pr^3)} \tag{2.17}$$

Defect depth:

$$d = kT^n \tag{2.18}$$

Modified expressions for damaged pipe:

$$\sigma_f = \frac{pr}{t-d} \tag{2.19}$$

$$\sigma_s = \frac{6k_m C_d \gamma B_d^2 E(t-d)r}{E(t-d)^3+24k_d pr^3} \tag{2.20}$$

$$\sigma_t = \frac{6k_m I_c C_t FE(t-d)r}{A(E(t-d)^3+24k_d pr^3)} \tag{2.21}$$

$$\sigma_m = \sigma_f + \sigma_s + \sigma_t \tag{2.22}$$

Thickness increase factor after FRP application:

$$t_t = (t_s - d)\left[1 + \frac{E_{FRP} t_{FRP}}{E_s(t_s-d)}\right] \tag{2.23}$$

$$\sigma_f = \frac{pr}{(t_s - d)\left[1 + \frac{E_{FRP}t_{FRP}}{E_s(t_s - d)}\right]} \tag{2.24}$$

$$\sigma_s = \frac{6k_m C_d \gamma B_d^2 E_s t_t r}{E{t_t}^3 + 24k_d p r^3} \tag{2.25}$$

$$\sigma_t = \frac{6k_m I_c C_t F E t_t r}{A\left(E{t_t}^3 + 24k_d p r^3\right)} \tag{2.26}$$

Where $t_t = (t_s - d) + nt_{FRP}$.

$$\sigma_m = \sigma_f + \sigma_s + \sigma_t \tag{2.27}$$

The comparisons between undamaged, damaged, and different FRP repairs are shown in Figure 2-7.

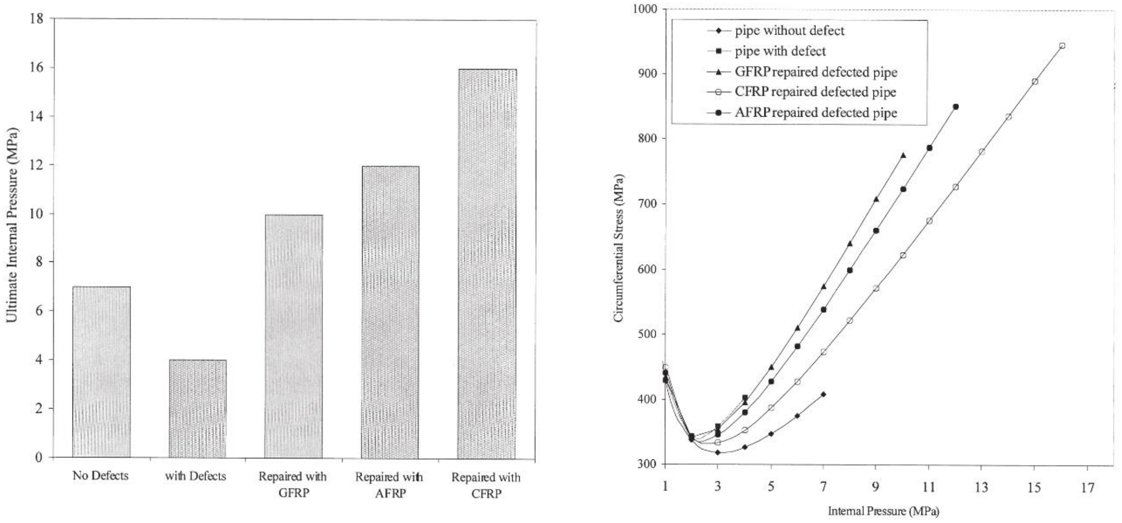

Figure 2-7 Comparison of damaged, undamaged, and FRP repaired pipes. Ultimate internal pressure (left), circumferential stress (right) (After Toutanji et. al, 2001)

According to the charts in Figure 2-7 CFRP performs best regarding increase in internal pressure capacity of the pipe. Also it can be seen that for the same magnitude of internal pressure CFRP repaired pipe is under less circumferential stress compared to GFRP and AFRP repaired pipes.

Patch repair of pipes with small cracks and holes were studied by Ayaz et al. (2016). Small pipe specimens of 170mm length 33.7mm outer diameter galvanized piped were used. Specimens were pressurized up to failure using hand stroke hydraulic pump. Woven carbon fabrics were used in the repair and due to the brittle characteristics of these fabrics, thicker lay-up results in higher internal pressure capacity. It was reported that 35mm overlap is adequate and longer overlap lengths will not add to the capacity.

2.4.4 Numerical Studies

Finite Element (FE) simulation is a powerful tool to predict repair performance of pipes and closely estimate burst pressure with correct assumptions. Many research studies have applied FE analysis for performance predictions for pipelines. Duel et al. (2008) studied four different defect geometries (1×6, 3×6, 6×6 inches, and an axisymmetric patch) representing thickness loss due to corrosion using FEM analysis (Figure 2-8).

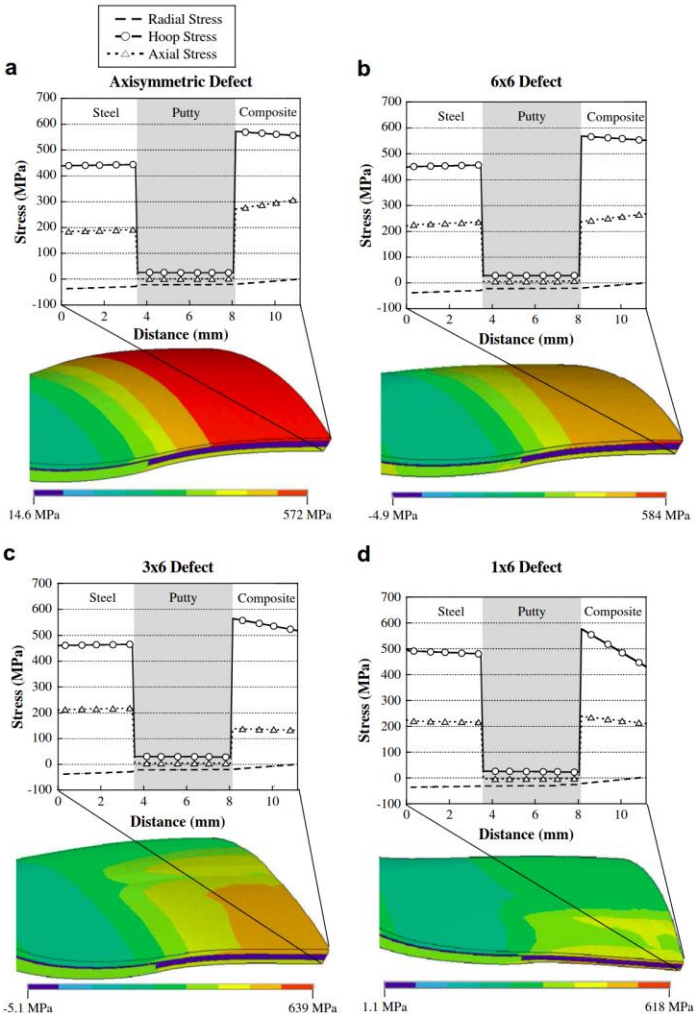

Figure 2-8 Stress distribution along thickness of repaired pipe for different defect geometries (after Duell et al. 2008)

Simulations were compared with field tests. Studied pipe had 5 ft. (1.52m) length with welded end caps, nominal diameter of 6 in., and 0.28 in. (7.11mm) wall thickness. Pipe wall was subjected to 50% thickness loss. Epoxy putty was used to fill even the defect area with undamaged surrounding.

A bilinear elastic behavior was considered for modeling the putty. Six layers of CFRP wrap was applied to the defect patch with total thickness of 3.1 mm. Failure was observed as Mises stress exceeding ultimate strength of steel, or principal stress in composite or putty exceeding tensile or compressive strength of these materials. In all cases failure occurred in the CFRP wrap at the putty interface. Predicted burst pressure had 2.2% variation among all defect geometries. Defects with smaller area show larger variation of hoop stress along CFRP thickness. In addition, the hoop stress in the steel is greater for smaller patches, which cause this defect to be more susceptible to fatigue failure.

Predicted burst pressure was about 44Mpa for repaired pipe, and the unrepaired burst pressure was reported to be 22.4 MPa 26.2 MPa following ASME B31G and RSTERENG criteria. The ASME PCC2 method of calculating required thickness for FRP repair suggests 4.57mm thickness which is conservative and it is due to simplifying assumptions made, such as omission of strain hardening of steel pipe after yielding. In more advanced tiers of simulation, damage can be incorporated into the Finite Element model. Fracture, delamination, and yielding, and plastic deformations are common factors that can be considered. Although these elements can complicate model definition, they simulate the behavior more closely and accurately. Similar FE simulation along repaired defective pipe section was performed by (Freire et al. 2007). (Mazurkiewicz et al. 2017) studied simulation of pipe burst pressure with consideration of damage in the model. A defect of 60% thickness loss with a rectangular area of 133mmx102mm filleted at corners was studied. The pipe considered had a 6mm wall thickness, 219mm outside diameter, and 1m length.

Finite element simulation results were compared to performed lab test results on the actual pipe segment pressurized with water pump. Four cases of undamaged (case 1), damaged (case2), wrapped undamaged pipe (case 3), and repaired damaged pipe (case4) segments were compared. The defective area was filled and evened with epoxy material prior to be wrapped with up to 24 layers of unidirectional glass fabric with 0.75mm thickness and 200mm length. Epoxy filler was assumed to have elasto-plastic constitutive behavior. Adhesive behavior was modeled with traction-separation law with quadratic mixed mode delamination failure criteria. Mode I and Mode II adhesive fracture properties were obtained from experimental tests and corresponding simulation calibrations (Figure 2-9).

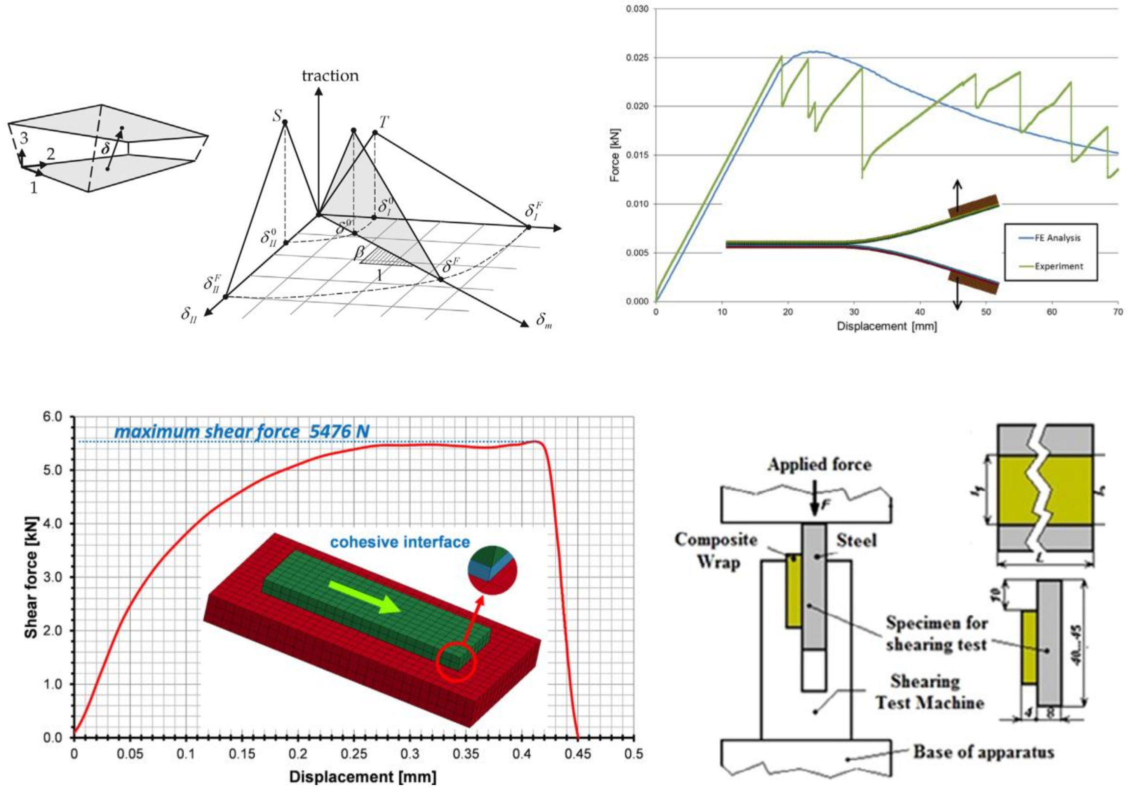

3
2
1
δ
traction
S
T
δ_{II}^0
δ^0
δ_I^0
δ_I^F
β
1
δ^F
δ_{II}^F
δ_{II}
δ_m
0.030
0.025
0.020
0.015
0.010
0.005
0.000
Force [kN]
0
10
20
30
40
50
60
70
Displacement [mm]
FE Analysis
Experiment
6.0
5.0
4.0
3.0
2.0
1.0
0.0
Shear force [kN]
maximum shear force 5476 N
cohesive interface
0
0.05
0.1
0.15
0.2
0.25
0.3
0.35
0.4
0.45
0.5
Displacement [mm]
Applied force
F
Composite Wrap
Steel
Specimen for shearing test
Shearing Test Machine
Base of apparatus
t_1
t_2
L
10
40...45
4
8

Figure 2-9 Mixed mode traction separation law (top left); Tests to calibrate Mode I failure (top right); and Mode II failure or direct shear (bottom) (after Mazurkiewicz et al. 2017).

Burst pressure for undamaged pipe shows close accordance between experiment, simulation, and analytical results. The same trend is observed for the undamaged part. However, both simulation and analytical methods overestimate maximum burst pressure which can be reasoned due to material craftsmanship and defect preparation. For the cases of repaired undamaged and damaged pipe with FRP good experimental and simulation agreement was reported (Figure 2-10).

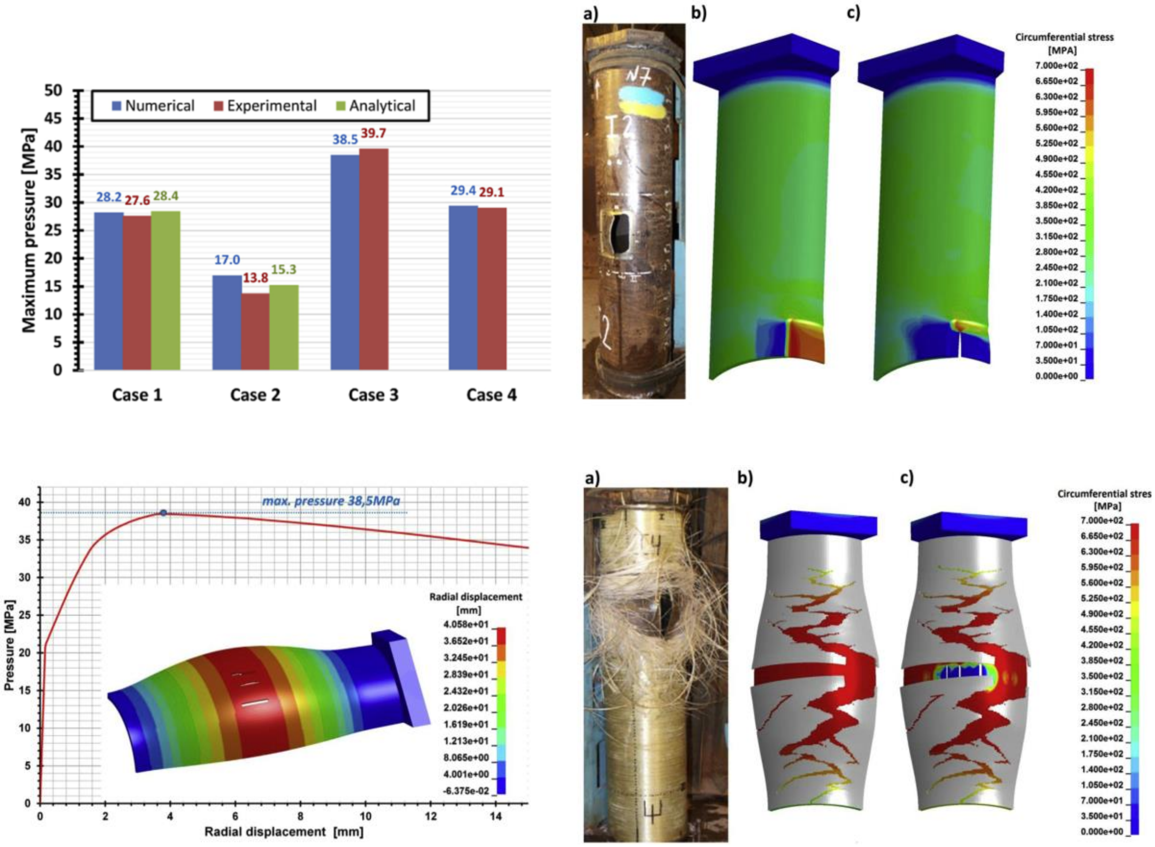

Figure 2-10 Maximum burst pressure results for different cases (top left), pressure vs radial displacement curve (bottom left), Failed pipe (a) – circumferential stress before failure (b) and after failure (c) in the simulation for damaged pipe (top right) and repaired pipe (bottom right) (After Mazurkiewicz et al. 2017).

2.5 Coating for Steel Corrosion Protection

Protecting pipelines from mechanical damages, ultraviolet rays of sun, extreme operating temperatures, and finally and most importantly corrosion are the main concern of stakeholders of oil and gas pipeline industry. Practice of coating application in pipeline industry debut with asphalt mastic and coal tar enamel (CTE).

2.5.1 Current Practice of Coating

Fusion-bonded epoxy (FBE), coal tar coat, 2-layer/3-layer Polypropylene (PP)/ Polyethylene (PE) are commonly used in oil and natural gas pipeline. Various performance factors are considered when selecting external coating for steel pipes: physical and chemical stability, resistance to soil stress, adhesion and resistance to impact, and most importantly resistance to corrosion and cathodic disbandment (Romano et al. 2005; Roche et al. 2006; Papavinasam et al. 2006; Bahadori 2015; Osai et al. 2015).

2.5.1.1 Coal Tar

Coal tar is a high viscosity liquid which production comes from the distillation of coal usually on a coke gas oven. This material has many diverse applications and has been used for pipe coating for over the last 80 years having its popularity peak on the 1970's, being one of the first successful coatings applied in a plant. Coal tar is also used as pavement sealcoat, in the industry as part of steel and iron fabrication, as well as in the medical supply commerce.

The coating procedure consist of a layering mechanism being the primer. The first layer is followed by the first coat of coal tar, then a thin glass fiber wraps the pipe with a consecutive second layer of glass fiber wrap, and finished with an external coating of coal tar epoxy. The two layers of coal tar and two layers of fiber glass or mineral felt are expected to work as one compound coating. Before the primer is applied the pipe is heated to prepare the surface for the sand blasting and to ensure well adherence between the pipe and primer.

2.5.1.2 Fusion-Bonded Epoxy (FBE)

Fusion-bonded epoxy is excellent coating to provide long-term protection for steel pipes from corrosion. FBE is an epoxy based powder coating, which were used commercially to protect steel pipelines in pipeline construction since 1960s. Constituents include epoxy resin, hardeners, pigment, flow control additives, and stabilizers.

One-layer and dual-layer FBE powder coating are commonly used in oil and natural gas industry. Besides, FBE can be used as primary coating for two-layer or three-layer PP/PE coatings. The thickness of FBE coating is in range of 300-400µm. In order to improve specific properties, pipeline stake holders occasionally designate increased coating thickness of 1000µm.

2.5.1.3 2-Layerand 3-Layer Polypropylene Coating

Polypropylene (PP) is one of the fastest growing polymers nowadays, and much of this growth is due to polypropylene’s ability to displace conventional materials (wood, glass, metal) and other thermoplastics at lower cost. Polypropylene has a wide variety of applications including packaging, labeling, textiles, stationery, plastic parts and reusable containers of various types, laboratory equipment, automotive components, etc. At the same time, polypropylene is attracting increasing attention as a highly desirable component in oil and gas pipeline coating systems.

Limitation exists in terms of these systems because placement of PP or PE for long-term in ground or underwater environment is to be discussed; however, actual completed projects was found in the field since 1986.

Corrosion is a big problem for the coating materials and pipeline industry, and the earliest anti-corrosion coatings for buried pipelines were bitumen-type coatings, specifically, asphalt mastic, enamel, as well as coal tar enamel. The asphalt coatings absorb water to a greater degree than the coal tar enamel coating, but both are subject to cracking, leading to contact of water with the pipe, and coating disbandment. Later, epoxy-based coatings were used; although it was found that these epoxy materials provided good adhesion to the steel pipe, but they suffered from poor impact and abrasion resistance. Therefore, polyethylene and polypropylene were adopted for coatings. They are considered as an excellent outer coating and can offer highly desirable qualities, and the difference between these two is polyethylene has high temperature limitations.

When polypropylene is used in the coating system, the coating type is similar to 2-layer or 3-layer polyethylene except that polypropylene is more temperature resistant than high density polyethylene, which becomes a major factor on pipelines operating at temperatures greater than 80°C. These types of pipelines may be typical of flow or gathering lines in an oil field where the resource is drawn from deep reservoirs and flows at very high temperatures (100°C-140°C).

Another reason for selecting polypropylene is its superior hardness and abrasion resistance. This can be important for use in remote oil fields, where pipe handling will traverse rocky terrain, for directional drilling applications or for offshore pipelines where a damage-free coating will save time and money during pipeline construction.

2.5.2 Geopolymer Coating

Inorganic cementitious coatings are resistant to UV exposure and compatible with concrete surfaces. Drawbacks of these coatings are fluidity for application with low water content, long curing period, and high permeability. An inorganic matrix called geopolymer with varying degrees of permeability capable of releasing vapor pressure was developed.

Different variations of geopolymer are processed and prepared with materials such as fly-ash, slag, or Metakaolin exist and depending on the application they can be modified (Zhang et al. 2010; Liyana et al. 2013; Salwa et al. 2013). Geopolymers are considered a green material due to their zero VOC residuals. Prominent mechanical properties of geopolymers are high compressive strength and elastic modulus an excellent acid and fire resistance (Balaguru 1998; Lyon et a. 1997; Salwa et al. 2013).

According to Davidovits (1991), the synthesis of geopolymer consist of three steps. The first step is dissolution of alumino-silicate under strong alkali solution which includes 8 pathways. In thermodynamic, different pathway can create different ion clusters that directly determine the final properties of geopolymers. Thus, it is very important to understand the actual pathway in order to gain insight into the mechanism of geopolymerization process. The second step is reorientation of free ion cluster and followed by polycondensation process. Up until now, these studies are not done yet. This is because the forming rate of geopolymer is very rapid. As a result, these three steps take place almost at the same time which makes the kinetics of these steps inter-dependent.

From here on geopolymer is referred to the geopolymer used in this study which is patented (Balaguru 2012). Geopolymer is a water based potassium alumina-silicate matrix with properties similar to cement concrete. With particles smaller than 0.5µm it can have low viscosity and be applied in thin layers. Applications in automobiles, aerospace, and infrastructure have been investigated (Lyon et al. 1997; Balaguru 1998; Wasserman 2012).

- It is water based and unused residuals can be disposed of safely without any toxicity concerns.
- Good bonding behavior to concrete, wood, and steel with average bond strength of 11MPa (1.6ksi).
- Improved properties using added carbon, glass, steel, and ceramic fibers in the mix design.
- Excellent interfacial bond properties due to chemical bond with concrete surface.
- High durability similar to bricks as both materials have alumina-silicate.
- Capable of developing hard finished surface which is scratch resistant.
- Fire resistant as it can withstand temperatures up to 1000°C.
- Graffiti resistant by achieving a glossy finish configuration.
- Compressive strength of 34 MPa (5ksi)
- Modulus of rupture of 8 MPa (1.2ksi) which can be improved to 104 MPa (15ksi) by adding discrete fiber. If Continuous fiber is used Modulus of rupture would increase to 483 MPa (70ksi).

The geopolymer matrix is composed of liquid components, silica fumes, fillers, activator, fiber, water repellent agent, and organic polymers. Types of silica fume are associated with cost factors and color preferences. Fillers provide hardness and also work as an economical cost factor. Activators engage in a curing period which could be rapid or slow. Organic fibers help with the ductility of the geopolymer. Fiber content is less than 0.5 percent. Organic polymer additives are used to help with early strength gain and water resistance. Geopolymer composition requires protection from rain and running water for 3 days.

The geopolmer can be cured in room temperature or elevated temperatures of 80°C or 150°C. At 150°C the curing is 99% complete in 3 hours while 3 hours provide 92% curing at 80°C. The geopolymer matrix is a potassium aluminosilicate, or poly (silate-silox) with the formula of $Si_{32}O_{99}H_{24}K_7Al$. The geopolymer element structure is shown in Figure 2-11.

$$K_n\{-(SiO_{2z} - AlO_2)_n\}gwH_2O$$

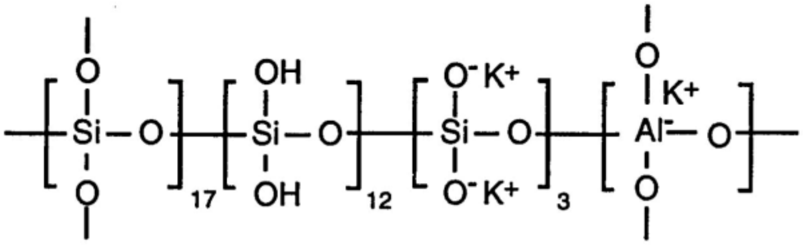

Figure 2-11 Geopolymer structure.

Where Z>>n.

It hardens to an amorphous or glassy material at moderate temperatures with density of 2.14 g/cm^3. Main ingredients of Geopolymer matrix are aqueous silica +

potassium oxide solution, silica powder having SiO_2/AlO_2 in mole ratio of 27/1. Ingredients are mixed with a high shear mixer (minimum of 1500rpm) for one minute to form a thick liquid. A dynamic rheometer with 25mm steel plates was used to determine the viscosity of the fresh matrix at room temperature (20°C). The viscosity measurements vs time at room temperature is shown in Figure 2-12 left. The Geopolymer matrix remains workable for 4-5 hours. Figure 2-12 right shows extent of reaction (cure) in geopolymer and viscosity versus curing time at 80°C. Onset of sudden viscosity increase is equivalent to about 50% of curing completion.

After one hour, geopolymer is 99% cured, tensile properties were measured according to ASTM D3039, in-plane shear properties were measured according to ASTM D3518, and inter-laminar shear properties were measured according to ASTM D3846 at different temperatures for gopolymer-carbon fabric laminates. In room temperature the In-plane and inter-laminar shear modulus are 30.5 and 14.1 MPa respectively.

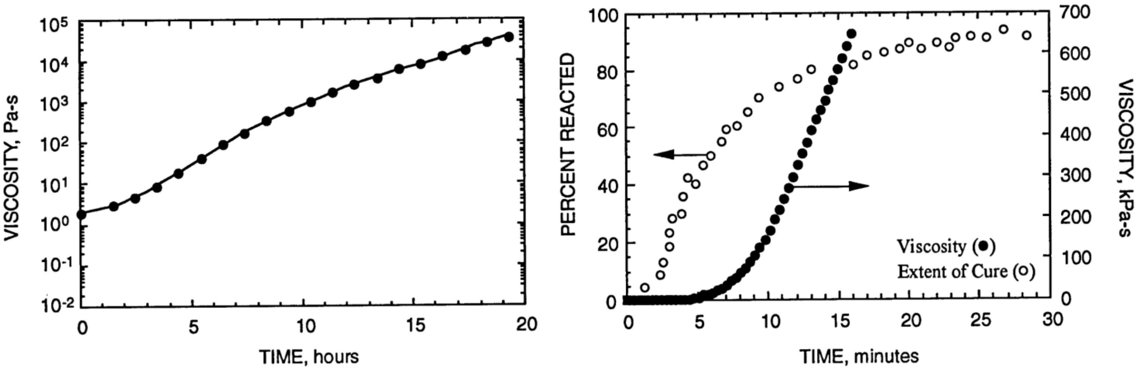

Figure 2-12 Room temperature viscosity of geopolymer resin over time after mixing (left), Extent of cure and viscosity of geopolyer over time (right) (After Lyon et a. 1997).

Differential scanning calorimetry studies were performed (Lyon et a. 1997) to determine extent of reaction of geopolymer components over 3 hours at 80°C. Samples of approximately 50mg were prepared for this study. Energy released during hydration of geopolymer in form of heat was determined to be 16.42±0.49 J/g. various mechanical properties of geopolemer-carbon fiber composites at different temperatures are presented in Table 2-1.

Table 2-1 Mechanical properties of geopolymer-carbon fiber composites (Lyon et a. 1997).

Property	Max Temp (°C)	Number of samples Tested	Modulus (GPa)	Strength (MPa)
In-plane Shear	22	3	4 ± 0.1	30.5 ± 1.2
Inter-laminar Shear	22	5		14.1 ± 0.6
	200	5		12.5 ± 0.3
	400	5		6.8 ± 0.4
	600	5		4.6 ± 0.1
	800	5		4.6 ± 0.2
	1000	5		5.6 ± 0.5
Wrap Tensile	22	5	79 ± 0.2	343 ± 31
Flexure	22	5	45.3 ± 0.9	245 ± 8
	200	5	36.5 ± 4.0	234 ± 10
	400	5	27.5 ± 2.5	163 ± 6
	600	5	18.3 ± 1.4	154 ± 24
	800	5	12.3 ± 0.5	154 ± 9

The geopolymer provides flexibility in terms of application for large and small areas to be coated. Depending on the actual composition of the geoplymer being used (where it may include discrete fibers) foam and bristle brushes can be used to coated the desire surface. While paint sprayers perform the best in terms of final finished surface and uniform thickness, they need to be used with larger tip size sprayers and additional water content to perform flawlessly.

Inorganic matrices with polymer additives where used by Balaguru et al. (2001) to have sealing capabilities while it has enough permeability to release vapor pressure in concrete structures. Reinforced inorganic matrices were used to repair concrete elements and steel beams. Due to inorganic nature of matrices it had better results for concrete than steel. Modified inorganic coating was successfully tested as protective coating against deicing salt and freeze-thaw cycles for concrete structures.

2.6 Fatigue Life Prediction of Pipeline

In the 19th century according to (Schütz, 1996) Albert a civil servant for mines published the first fatigue test results. He performed tests on the chains used in operating conveyers used Clausthal mines that had failed while in service. One of the more prominent accidents that contributed to the fatigue research was the Versalles disaster. A locomotive axle broke and took lives of more than 60 people (Schütz, 1996; Smith, 1990). Wohler developed a deflection gauge to measure loads of the train axle. By finding the largest axle deflection, Wohler then calculated the corresponding dynamic load. By comparing that load with the static load he arrived at a factor of 1.33 or the impact factor in present day literature. Later works of Wohler were plotted by his colleague, which formed S-N curves aka *Wohler curves*.

The Wohler curves show the relationship between number of load cycles with respect to a certain stress in a material before it fails. The stress has tensile strength as the higher bound which corresponds to very low number of load cycles, and fatigue limit at the lower stress bound which is asymptotic to infinite cycles. In other words, for certain stress range no fatigue will occur (see Figure 2-13)(Schijve, 2003). The next millstone in fatigue was Bauschinger effect which addressed change of elastic limit due to repetitive loading. In 1921 Griffith established the fracture mechanics by his research on brittle materials and glass and relationship between the surface energy and initiation of crack

(Griffith, 1921). Irwin followed up on Griffith's work and determined stress intensity factor (SIF) in static crack state. He proposed that there exists a critical value for SIF that cause instant fracture. This was called fracture toughness and is the basis of linear elastic fracture mechanics (LEFM) (Irwin, 1958). And perhaps the most notable and frequently used equation is the one proposed by Paris in 1963 which captures full crack propagation process (Paris, 1963). Paris's equation relates the rate of crack growth to SIF. For further in detail discussions of fatigue history refer to (Schütz, 1996; Schijve, 2003). And most recently with the advent of computers and use of finite elements, Newman et al. (1981, 1984) introduced empirical equations for calculating SIF in in three dimensional plate with ellipse shape cracks.

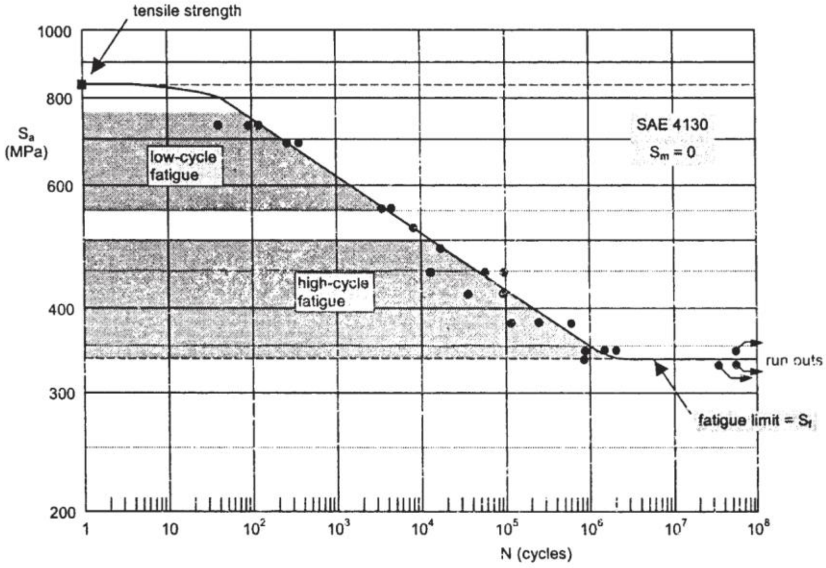

Figure 2-13 Fatigue result of a low ally steel (After Schijve, 2003).

Fatigue cracking is an inherently stochastic problem affected by various sources of variability and uncertainty. In the particular case of oil and gas pipeline fatigue-induced cracks, it is important to effectively and efficiently monitor and inspect pipelines. Due to the old age and large size of pipeline transmission network maintaining these infrastructures within safe and serviceable conditions is not an easy task. As a result, it is important to contentiously improve and update efficiency of means and interval of monitoring and maintenance by use of innovative scientific methodologies. Such methodologies should be able to account for probabilistic nature of fatigue process, such as uncertainties in material properties, variability of internal pressure within the pipe, and reliability and accuracy of inspection data about the condition of pipe structure.

On one hand, traditionally probabilistic models within the *classical statistic*s scope deal with analyzing statistics of the error due to differences between model predictions and measurement/observation data. The accuracy of such models rely upon the quality and quantity of available observation data. On the other hand, *Bayesian statistics* view on model definition quantifies the extent to which the model represents the data and determines the probability of the model being correct itself. This makes Bayesian models suitable for cases in which the relevant data is limited.

In recent years there has been a great focus on data driven solutions with help of machine learning methods in detecting patterns and performance prediction in various fields of science and engineering. Aeronautical engineering and aircrafts structural failures has been the major front for doing research related to fatigue in various metallic alloys (Fujii et al. 1996; Makeev et al. 2007; Cross et al.2007; Sankararaman et al. 2010; Liu et. al 2009; Sankararaman et al. 2011; Xie et al. 2011 ;Zarte et al. 2012).

Knowledge about equivalent initial flaw size (EIFS) in material is key to estimate crack initiation and progression process. Different authors have conducted research in various aspects of the Bayesian inference applications in fatigue modeling. Makeev et al.

(2007) investigated Bayesian inference of EIFS using Weibull and log-normal distribution. In a follow up work, Cross et al. (2007) extended the inference of Makeev's work to multivariable inference of other crack growth parameters in addition to EIFS using Markov Chain Monte Carlo (MCMC) method.

Fujii et al. (1996) proposed a Bayesian neural network based method characterize significance of various variables contributing to a crack growth regime. Their results showed crack growth rate, rack size, and loading as the most important variable in a crack growth regime which again shows conformity with Paris' equation. Liu et al. (2009) used a fracture-mechanics based approach to estimate Equivalent Initial Flaw Size (EIFS) based fatigue limit of the material and compared the results with available SEM data of the material and subsequently presented prediction on fatigue life.

Sankararaman et al. (2010, 2011) performed detailed inference of multiple parameters involved in crack growth model in conjunction with FE simulations under variable amplitude loading. Xie et al. (2011) used Bayesian inference to infer parameters of crack growth model in addition to fatigue life. They tested their model with pipeline field data and reported desirable results. Johnson (2010) used data collected from C-130 aircraft and gas turbine to predict EIFS in their structure. Fawaz et al. (2002) replicated lap-splice joints commonly used in aircrafts and experimental performed fatigue test and compared EIFS.

3 Coating for Corrosion Protection

One of the most important properties of protective coatings is their performance over time and under influence of environmental hazards such as corrosion, freezing and high temperatures, moisture, and Ultra Violet (UV) exposure from sunlight. It is of interest to predict long term performance of coatings by conducting short term accelerated environmental degradation tests.

3.1 Accelerated Corrosion Test

3.1.1 Existing Corrosion Test Procedures

Several codes (ASTM B117, D6675, G8, G95) exist to conduct these tests which mainly concerns exposure to corrosive environments or electrochemical induced corrosion such as cathodic disbandment.

One of the required factors of an accelerated corrosion test is to have good performance accordance and correlation in the short term with degradation and corrosion due actual environmental exposure in long term service. Chong (1997) compared performance of different accelerated (1000 to 3000 hours) coating degradation tests to actual long term (28 months) environmental degradation. Different coating systems were evaluated for creepage growth (from an initial scribe into the coating) during the tests. It was shown that salt fog test alone had the most accelerated creep growth (highest severity) while freeze/UV-condensation/cyclic salt fog had the best correlation with long term environmental degradation.

A 360-hour (15 days) cycle was proposed by FHWA HRT-12-044 report (Kodumuri et al. 2012). The cycle is as follows: 24-hour freeze at -10°F (-23.3°C) followed by 7 days of UVA/B (350nm nominal wave length) /condensation (4 hours UV - 4 hours condensation). UV temperature was 140°F (60°C) and condensation temperature 104°F (40°C). Prohesion cycle was 168 hours (7 days). Prohesion is the non-continuous salt spray exposure which correlates better with outdoor conditions. Table 2 shows the cycle components.

Table 3-1 FHWA test cycle (after Kodumuri et al. 2012).

Item	Freeze Exposure (Hours)	UV Condensation Exposure (Hours)	Prohesion Exposure (Hours)	Total Exposure (Hours)
Each cycle	24	168	168	360
Target Duration (20 Cycles)	480	3360	3360	7200

3.1.2 Test Chamber design and build

To evaluate geopolymer performance as corrosion protective coating and compare the performance with organic coatings a test chamber was designed and built. Several environmental emulators were considered such as salt water spray system, UV exposure, heat source, and freezing. Test cycle combinations can be chosen according to the region were coating will be used to emulate climate and exposure conditions. The cycles were finally chosen in a customized fashion adopted from previously mentioned long term studies and codes. Performance data was collected before and during the cycle at different times. Main performance indicators were corrosion creepage growth, emerge of blisters, and adhesive strength between coating and steel substrate.

A custom corrosion chamber was built to achieve an accelerated corrosion process. The components of the chamber are the following:

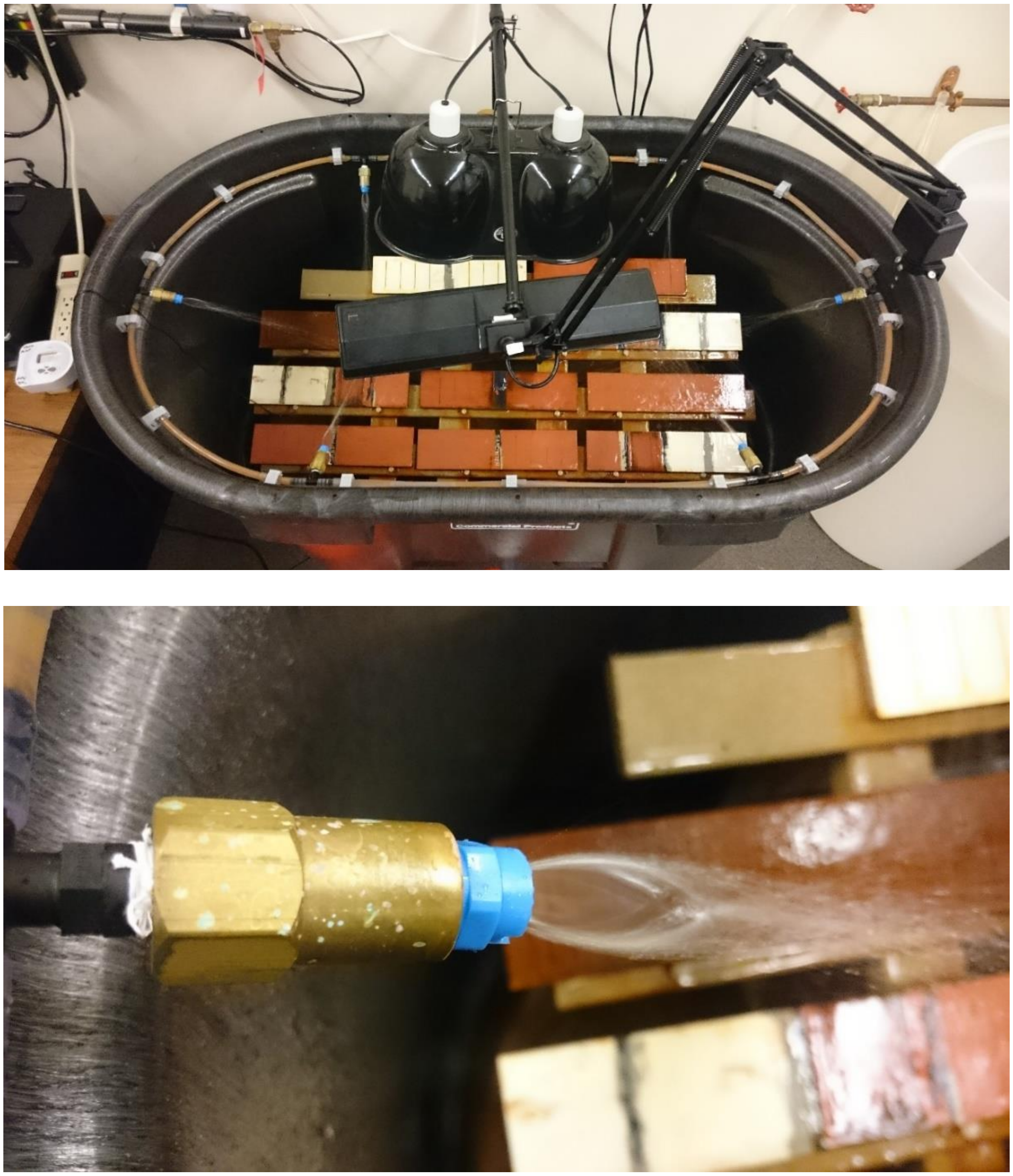

Figure 3-1 Corrosion Chamber (Top), Spray nozzle (bottom).

1- A 100 Gallon chamber (tank): This tank provides the housing and installation foundation for specimen rack, tubing, and UV lamp handle base. It contains the sprayed saltwater and prevents spread of saltwater. Saltwater is then discharged from the tank and then collected in bucket where the feeding piping into system is located.

2- Nozzles installed on the perimeter of the chamber to spray salt water. Selected nozzles provide a 60° flat spray pattern (Figure 3-1 , bottom).

3- A pump that feeds the salt water into the tubing system (Add picture)

4- Infrared light casing containing two 250W infrared bulbs. To provide elevated temperature exposure to the samples Infrared bulbs were used along with UV bulb to emulated sunlight exposure.

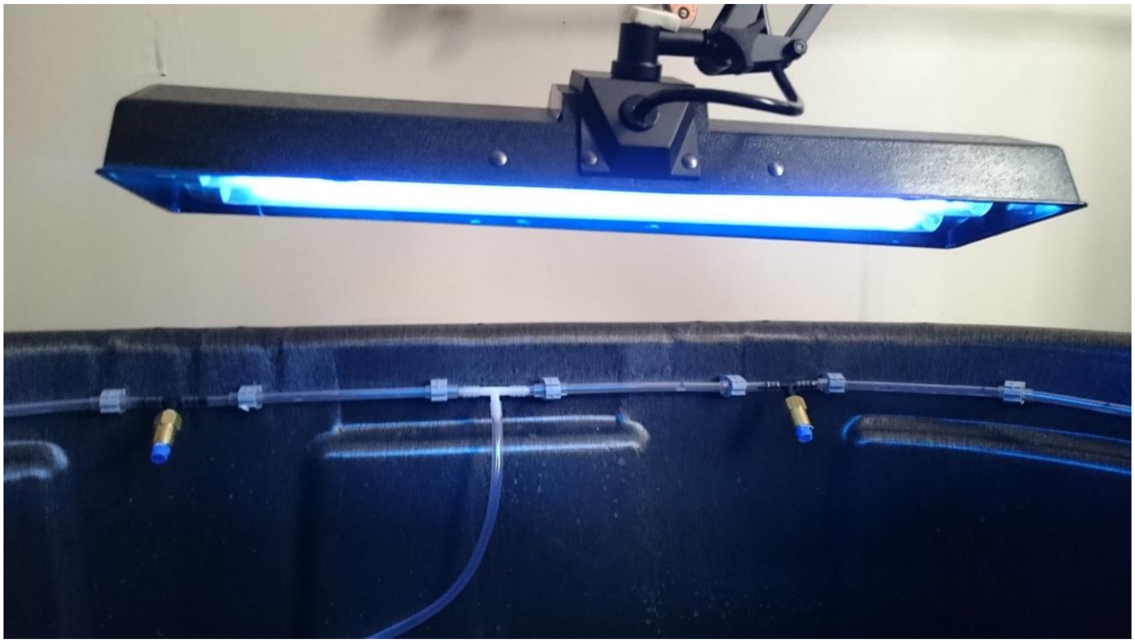

Figure 3-2 UV light.

5- Ultra Violet light casing containing two 15W tubes. Black lamps which radiate UVB-A rays in the range of 350nm wavelength range were used. In some instances UVC germicidal lamps with 250nm wavelength range were used (Figure 3-2).

6- An inclined rack to hold the steel coupons. The rack was custom built into the chamber and the inclination slope was achieved to accord the ASTM – B1117 recommendation which states the specimens should be placed in 15 to 30-degree inclination. Synthetic wood was used to build the rack and nylon screws were used to provide leaning support for specimens placed on the rack.

7- Timer switch to control the cycles of the UV, heat and salt spray actions. To provide automatic cycle programs timer switches were used to start and end UV, infrared lights, and water pump.

8- Temperature and humidity meter. A temperature meter was used to measure average temperature rise on the elevation where specimens are placed on. The measured temperatures on specimen surface varied from 40 to 60°C at different positions on the rack. Humidity meter was mainly used to compare humidity inside uncovered chamber and humidity in the room.

3.1.3 Corrosion cycle

As mentioned before a cycle was adopted based on previous studies and available accelerated corrosion test codes. The test cycle was customized to have an appropriately harsh environment to achieve accelerated corrosion and deterioration of the coating surface and steel. The procedure and cycle was developed based on four major references: FHWA-HRT-12-044, Chong Cycle (Chong, 1997), ASTM- B1117, and ASTM – D4587.

The cycle was designed to need the least operator presence. Only session that needs the operator to be present is to place the specimens into the freezer from the chamber and vice versa. New salt water is made on the latter session.

The cycle was selected as follows:

1- 12 hours of freezing, 4 hours UVB-A radiation + Infrared heating, 8 hours of saltwater spray. Freezing at -23°C (-10°F), infrared induced temperature on black surface probe up to 60°C. This constitutes one cycle per day.
2- Target duration: 15 weeks

A rotation scheme according to ASTM B117 was followed for all the specimens to be exposed in similar conditions in different locations of the inside the chamber over the course of the test cycle.

3.1.4 Corrosion resistance indicator

The indicator of corrosion resistance used in this study is the adhesive strength between the coating and the steel substrate after exposure to the corrosive environment. A pull off strength test according to ASTM D7234 is performed on multiple coated specimens before and after exposure to investigate possible drop in adhesive strength between coating and the steel due to corrosion or coating degradation due to harsh environment exposure. Pull-off device is shown in Figure 3-3.

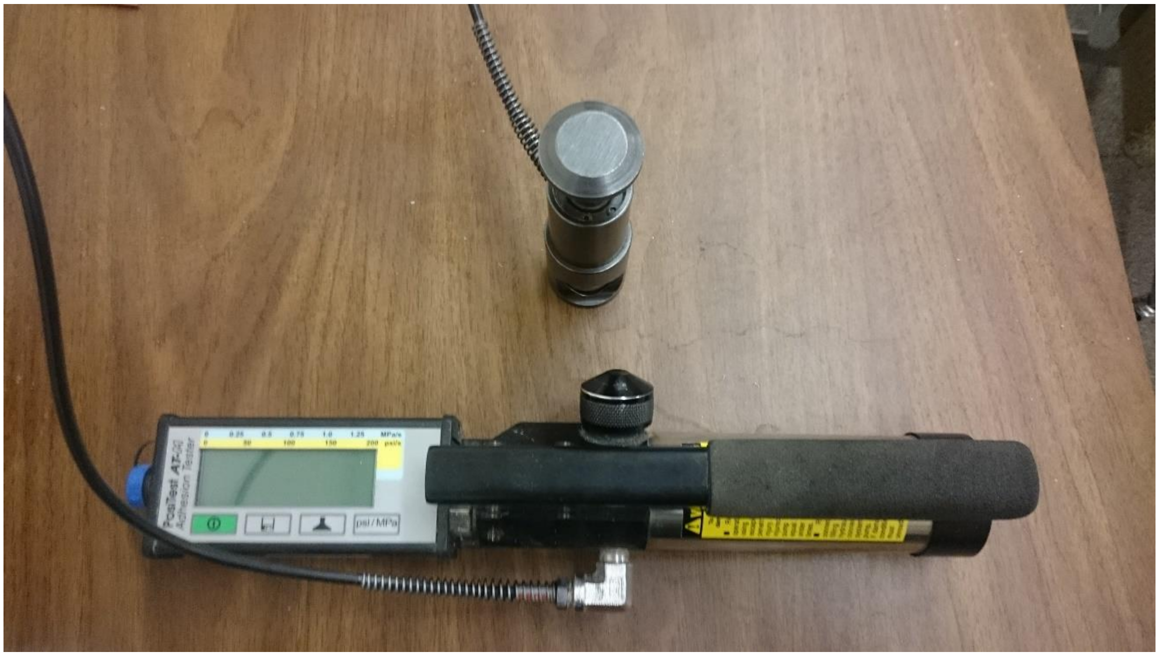

Figure 3-3 Hydraulic manual pull off test machine.

3.2 Test procedure

The test has four major steps of surface preparation of steel specimens, coating specimens, performing accelerated corrosion cycle, and evaluation of performance indicators. Steel plates (coupon) to be used in the test need to undergo surface preparation procedure. Then two part geopolymer coating is prepared and applied on the coupon surface. After coating steel specimens, they are cured either in room temperature or in the oven. Main components of the test probes are outlined here:

- The steel coupons that were used in the accelerated corrosion test were chosen to have 12×4×0.5 inches dimensions.
- The coating thickness was measured using PosiTest DFT Ferrous thickness meter.
- The scratches scribed on the surface of the coating to measure creepage over time were performed according to the ASTM-D1654 procedure.

- Coating adhesion strength was evaluated according to ASTM – D7234 procedure and PosiTest–M adhesion tester by Deflesko was used to perform the test.

3.2.1 Surface Preparation

It is important for the steel surface to be free of any contaminant, rust, and grease prior to coating application. Steel plates that were purchased for the test were usually treated oil to protect them from corrosion in storage. A decontamination cleaning foam was used to clean the grease oil from steel plates. Acetone also could be used to clean the contaminants off the steel surface. To expose a fresh layer of steel, all plates were grit blasted or sand blasted prior to coating application. It is important to note that after blasting, steel surface becomes very susceptible to corrosion even in room condition. In case of the need to store the sand blasted specimens they should be stored in airtight plastic bags in small group of numbers.

3.2.2 Coating preparation

The geopolymer coating is two-part component mix plus water. Part A is Potassium Silicate solution and Part B is the powder component plus additional water which increases workability of the coating to be brushed or sprayed. To mix the geopolymer designated amounts of Part A, Part B, and water are added into the mixing container. A mixing drill bit can be used with a high revolution drill with at least 1500 RPM frequency. Components are mixed for one minute untill thick liquid is achieved. A spatula could be used to scrap excess unmixed powder from the container wall and bottom and redo the mix for another one minute. A food processor also could be used to do the mixing task. Caution should be taken while using food processor as they tend to leave more unmixed component that needs to be tended manually with spatula as noted earlier. Prepared coating will have 45 minutes to an hour of workable time (pot life). If the geopolymer is being sprayed it is advised to use prepared coating at earlier time of pot life to prevent clogging in the spray components. Figure 3-4 shows the process of coating preparation and application.

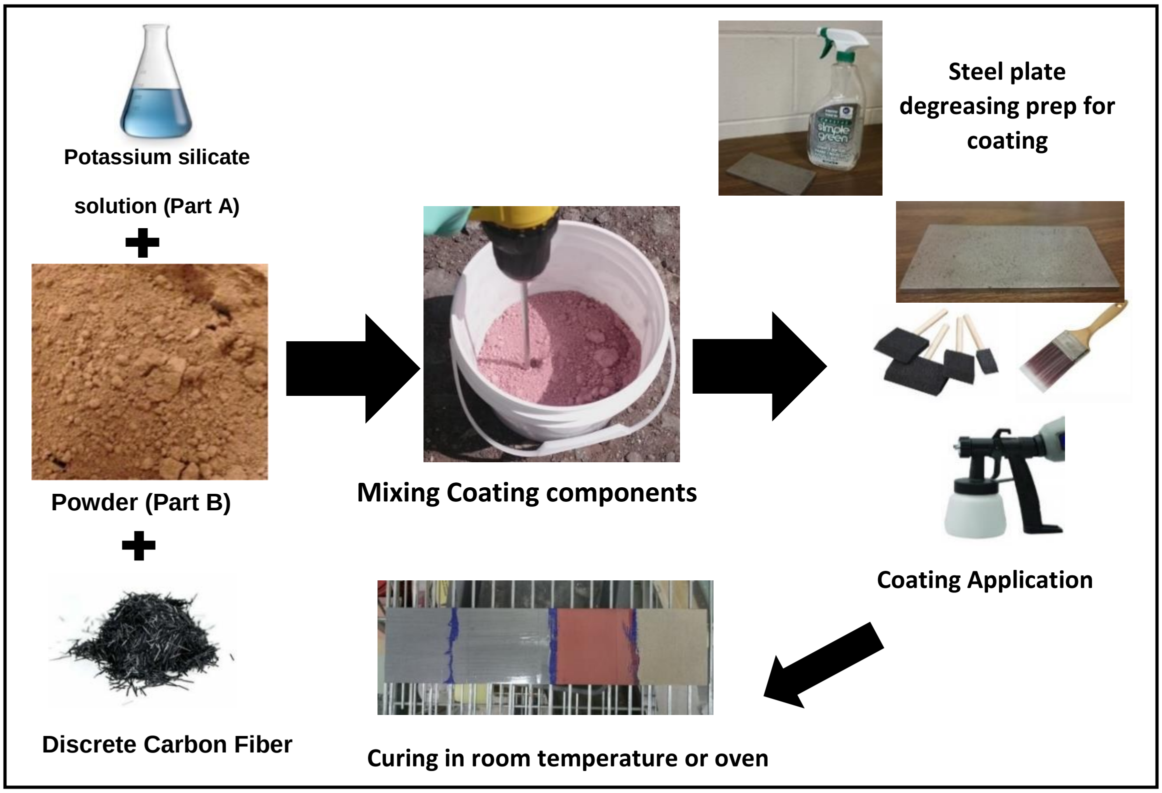
Potassium silicate
solution (Part A)
+
Powder (Part B)
+
Discrete Carbon Fiber
Mixing Coating components
Steel plate degreasing prep for coating
Coating Application
Curing in room temperature or oven

Figure 3-4 Coating preparation and application procedure.

3.2.2.1 Using brush or roller

Depending on the designated components in a geopolymer mix, coated surface could have very good finish using bristle, foam, and roller brushes, or it may have a mediocre finish. Simple tips while using brush in general is to avoid over saturating the brush and release the excess coating in the tray or container. Applying the coating using brush is recommended to follow a single direction such as consistently left to right or up down motion. Back and forth motions should be avoided as they tend to form a bumpy finish.

3.2.2.2 Using Spray Gun

Spraying results in smooth surface and the most even finish for coating applications. The challenge of using sprayers is making a workable mix for the coating amount required. Two major types of spray guns are available in the market. Siphon-fed (vacuumed) spray guns and gravity fed spray guns. For higher volumes the Siphon spray guns work fine but they become a problem for lower volumes. Gravity-fed guns are better choice for applications of coating in lower volumes as they waste the least coating material. Finding the right pressure and spray pattern and distance for gropolymer coating is a bit different than the more common organic coatings used with the sprayers. To avoid overspray one should follow the gun’s manual closely and practice using geopoymer coating on some trial work before coating actual work.

Geopolymer was cured in room temperature for two weeks or in the oven for 24 hours in 80°C (175°F) after one day of coating application. Relative humidity is required for the coating to cure faster in room temperature.

3.2.3 Coating Thickness Control

Geopolymer similar to cement-based mixes undergoes shrinkage during curing phase. It has been observed that keeping the thickness of the coating under 200µm prevents incurring micro-cracks on the finished surface after full curing has achieved. For coatings to have consistent performance they are required to have uniform thickness distribution over the coated area. A digital thickness meter with accuracy of ±(2 + 3%) was used to measure coating thickness (see *Figure 3-5*). Several points of the coated area of the specimens were measured and the average thickness was reported as coating thickness for respective specimens.

PosiTest®DFT

Figure 3-5 Thickness measurement device.

3.2.4 Adhesive Bond Evaluation

To evaluate the bonding properties of the geopolymer coating to the substrate steel, pull-off tests are performed to investigate bonding strength of coating to the steel substrate. To perform this test a manual hydraulic pump (PosiTest AT-M) is used. Aluminum dollies with 14mm diameter were selected as the adhesive probe. The pull-off test procedure is as follows:

- A medium sand paper is used to make dolly surface rough enough to be glued to the coated surface properly.
- A two-part high-strength adhesive is used to glue the dolly to the coated surface. The dolly is pressed to the coated surface to make sure no air bubble is formed at the adhesive interface and the excess adhesive should be cleaned at the edges using

cotton swabs. A tape or weight can be used to maintain pressure for first initial hours after application of adhesive, although this was not found to be a critical requirement. It is recommended to let the adhesive cure for at least 24 to 48 hours with the latter having shown best results according to the writer’s experience.

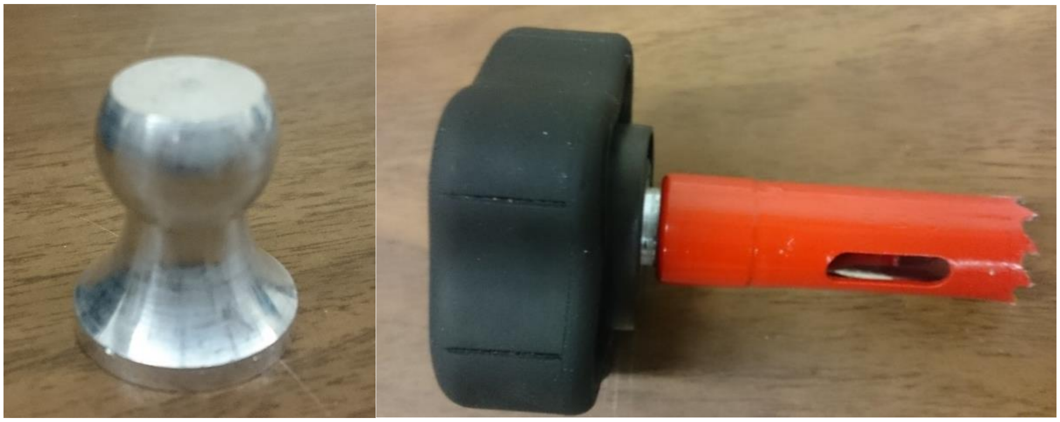

Figure 3-6 Pull off dolly (left), Cutting tool for isolating dolly (right).

- Using the cutting tool provided with the test tool a cut is performed around the dolly to isolate that area from whole coated surface (see Figure 3-6).
- The grip is adjusted over the glued dolly on the coated surface to perform the test. Pressure is then applied at a constant rate using the stroke handle on the pull off machine till deboning occurs. It should be noted that the dolly size should be given as an input before performing the test. Figure 3-7 shows the grip and a dolly interface after test is performed and failure occurred.
- This test is performed before and after exposure of specimen in the accelerated corrosion chamber.

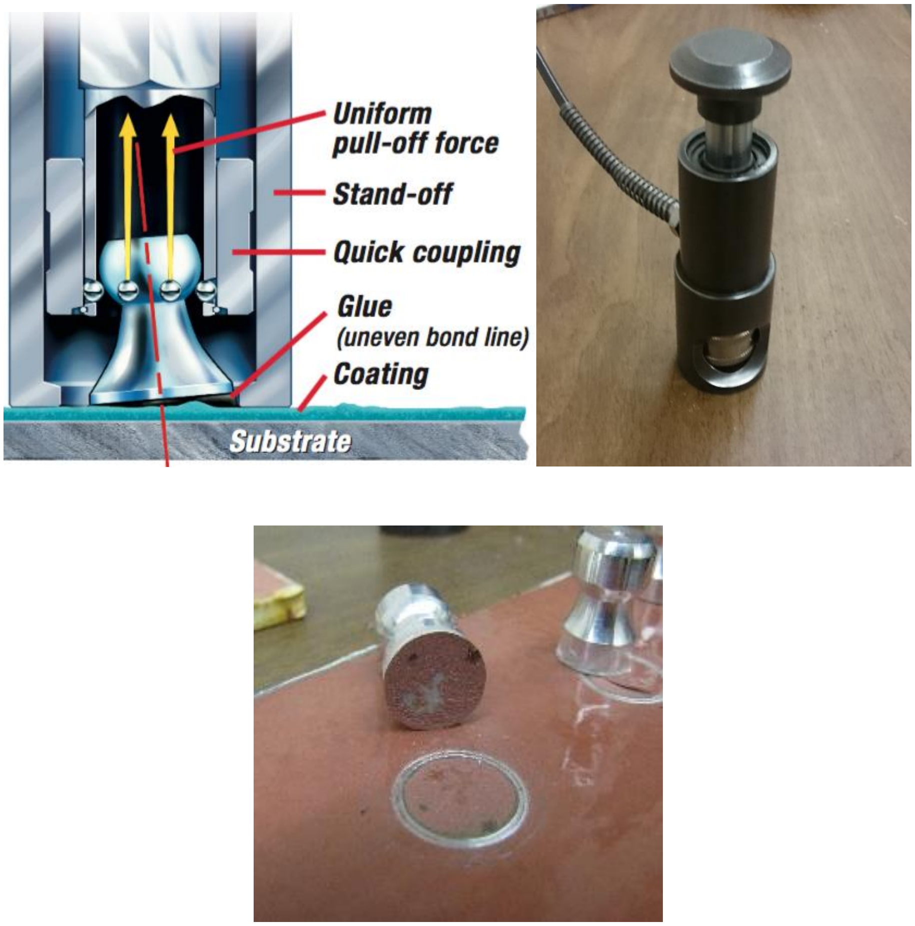
Uniform pull-off force
Stand-off
Quick coupling
Glue
(uneven bond line)
Coating
Substrate

Figure 3-7 Dolly grip (top right) and its schematics (top left), and dolly after failure (bottom).

3.3 Accelerated Corrosion Test Results

In total, five batches of specimens were prepared to be tested in accelerated corrosion chamber. Minimum duration of the test for each batch was one month.

3.3.1 Batch-1

The first batch of tested specimens were prepared on 3/8 ×3 × 12-inch steel plates without sand blasting. Two inorganic coating systems and two organics coating systems were evaluated. Table 1 shows all prepared specimens and respective coating thicknesses.

Table 3-2 Batch-1 Coating systems.

Coating system		Description
Inorganic	3-Layer Geo	Sandwich coating with Geopolymer base layer + Nano sealant in the middle + Geopolymer top layer
	Geo + Fiber	Geopolymer with added discrete carbon fibers.
Organic	Organic-Gloss	2-Layer system - Sherwin Williams Epoxy Mastic Aluminum II (B60 V 100) Base + Hi Solid Polyurethane (B65W 311) Top
	Organic Semi-Gloss	2-Layer system - Sherwin Williams Epoxy Mastic Aluminum II (B60 V 100) + Hi Solid Polyurethane (B65W 351) Top

In this batch, four of the plates were divided into four approximate equal section separated by tape to be used for pull off strength test at different time pints after start of the corrosion cycle. Each section was coated with one of the coating systems using foam brush. This sample group was called Quad Sections. A sample of Quad section is shown in Figure 3-8 up.

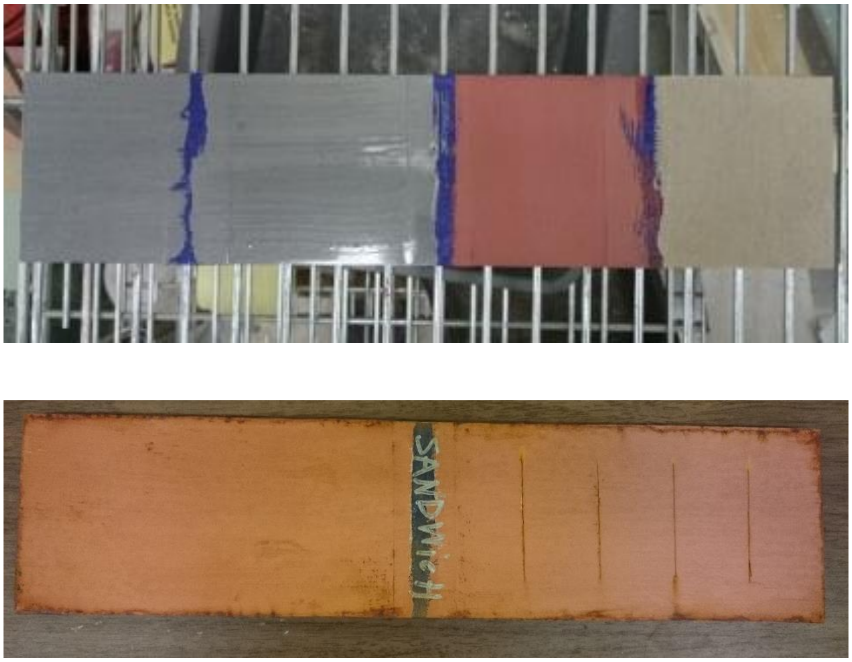

Figure 3-8 Quad sample coated with four various coatings (up), Dual sample (bottom).

An additional five dual section specimens were prepared. Similar to Quad sections the plate was divided into two section with tapes. The purpose of a Dual section was to have the same coating system on both section, while one of the section would have scribes to study creepage with exception for organic systems which shared a Dual section only to have scribes. Each of organic coating systems had two dual sections. Dual section sample is shown in Figure 3-8 bottom.

Table 3-3 Batch-1 Coating systems and Thicknesses.

Sample Type	Average coating thickness (µm)			
Pull Off samples (Quad sections)	3 - Layer Geo	Geo + Fiber	Organic - Gloss	Organic - Semi Gloss

PULL - OFF - 1	177	69	181	156
PULL - OFF - 2	175	73	158	178
PULL - OFF - 3	181	73	150	157
PULL - OFF - 4	298	81	137	200
Mean	207.8	74.0	156.5	172.8
Standard Deviation	60.2	5.0	18.5	20.8

3.3.1.1 Evaluation of Pull off strength

Pull off strength test was performed using 14mm diameter dollies. Table (…) shows the keyword definitions used to describe failure type for each test.

Results of the pull off test before accelerated corrosion and after month of corrosion cycle are shown in Table 6. Corresponding images are shown in Figure 3-9. It can be seen that organic coatings have higher pull off strength in general. The 3-Layer Geopolymer coating consistently fails at the interface where the Nao-film is applied, before and after corrosion. Although Pull off strength shows an average reduction of 27% after corrosion cycle. Nao-Modified Geopolymer has closed pull off strength to organic systems before corrosion cycle.

Table 3-4 Failure Type keyword glossary for pull off strength test.

Failure Type Keyword	Description
CF	Cohesive failure in the coating

AF-CS	Adhesive failure (coating-steel)
AF-GD	Adhesive failure (glue-dolly)
AF-GC	Adhesive failure (glue-coating)

Table 3-5 Batch-1 pull off strength results.

Corrosion System	Pull Off Strength (MPa) and Coating Failure Status								
	Before Corrosion Cycle					After One Month of Corrosion Cycle			
	A	B	C	D	E	A	B	C	D
3 - Layer Geo	9.61	6.28	8.06	7.07	4.14	6.59	5.18	3.65	5.06
	CF	CF	CF	CF	CF	CF	CF	CF	CF
Inorganic Geo	11.58	11.56	12.06	10.5	5.06	9.66	8.9	NA	NA
	AF-GD	AF-GD	AF-GD	AF-GD	AF-GC	CF	CF		
Organic - Gloss	13.33	10.27	12.65	13.38	7.65	16.13	18.29		
	AF-GD	AF-CS	AF-GD	AF-GD	AF-CS	AF-GC	AF-GC		
Organic - Semi Gloss	17.74	15.08	12.52	12.65	13.63	17.27	15.07		
	CF	CF	CF	AF-GD	CF	CF	CF		

Observed failure modes show that Nano Geopolymer did not show cohesive failure within the coating or adhesive failure from the steel substrate. An average strength reduction of 8% in pull-off test was observed for Nano Modified Geopolymer coating after accelerated corrosion testing. Organic coatings show increase in pull off strength after corrosion cycle which is believed to be caused by weak adhesion of epoxy glue to the coated surface on the tested specimens before corrosion cycle exposure.

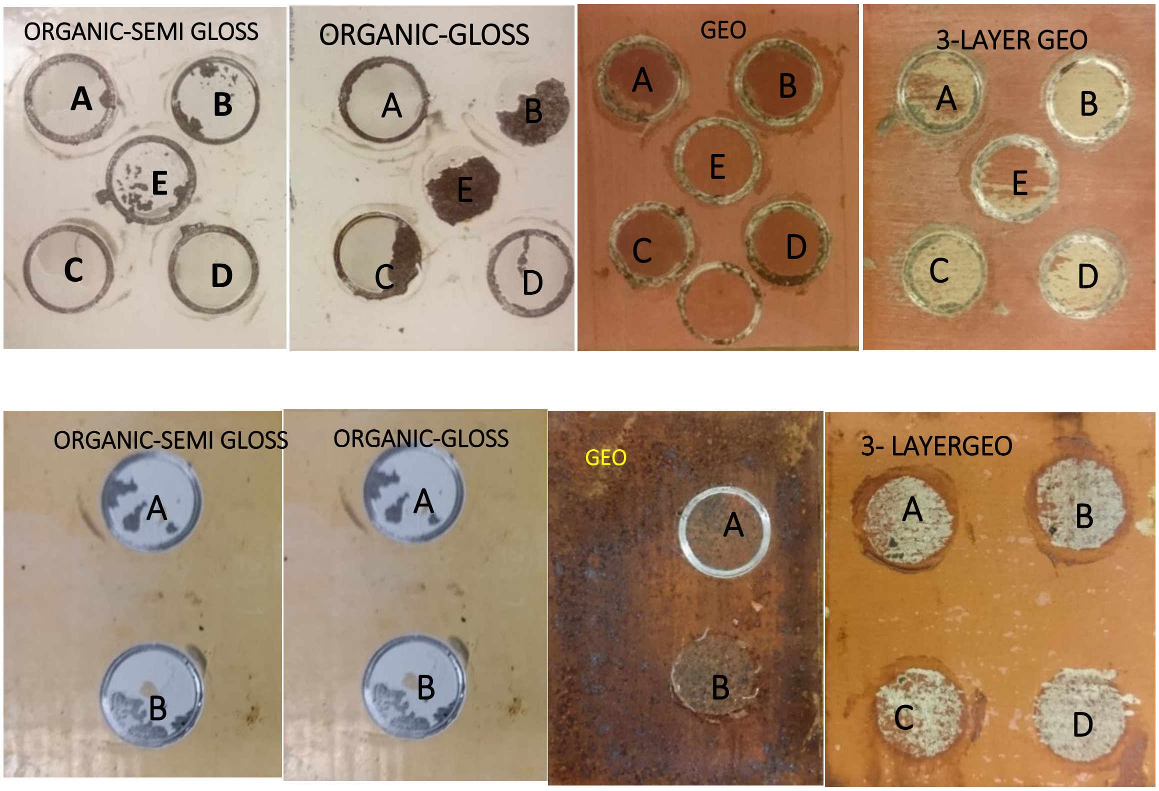
ORGANIC-SEMI GLOSS
A
B
E
C
D
ORGANIC-GLOSS
A
B
E
C
D
GEO
A
B
E
C
D
3-LAYER GEO
A
B
E
C
D
ORGANIC-SEMI GLOSS
A
B
ORGANIC-GLOSS
A
B
GEO
A
B
3- LAYERGEO
A
B
C
D

Figure 3-9 Batch-1 Pull-off test before (Top), and after accelerated corrosion cycle (Bottom).

3.3.2 Batch-2

In this batch three coating systems were evaluated for pull off strength before and after corrosion. Table 3-6shows description for coating systems used in this batch.

Table 3-6 Batch-1 Coating systems.

Coating system		Description
Inorganic	3-Layer Geo	Sandwich coating with Geopolymer base layer + Nano sealant in the middle + Geopolymer top layer
	Nano Film on Top	Geopolymer with added discrete carbon fibers and Nano Film on Top.

Hybrid	Semi-Gloss Finish	2-Layer system – Inorganic Geopolymer as base layer + Hi Solid Polyurethane (B65W 351) Top

Thickness measurements for Batch-2 specimens are presented inTable 3-7. This batch has higher average coating thickness compared to Batch-1 specimens.

Table 3-7 Spot coating thickness measurements, Batch-2.

Trials	Coating Thickness, µm				
	Hybrid - Inorganic Base + Organic top coat		Geo + Nano film on top		
	Sample1	Sample2	Sample1	Sample2	Scribed
1	289	227	156	195	260
2	370	256	130	237	305
3	288	284	137	227	258
4	275	243	158	216	302
5	274	246	140	248	279
6	251	309	210	276	293
7	276	267	156	240	218
8	370	311	140	280	219
9	317	349	135	305	249
10	264	245	136	338	270
Mean	297.4	273.7	149.8	256.2	265.3
Standard deviation	42.0	38.7	23.4	43.4	31.0
Trials	Coating Thickness, µm				
	3 – Layer Geo (Sandwich)				
	Sample1	Sample2	Sample3	Sample4	Scribed
1	428	397	363	Defective (Already Warped - delaminated)	Defective (Already Warped - delaminated)
2	452	388	304		
3	444	418	295		
4	475	500	306		

5	466	400	305		
6	522	436	292		
7	422	338	346		
8	445	378	318		
9	454	364	325		
10	467	408	316		
Mean	457.5	402.7	317		
Standard deviation	28.2	44.0	22.5		

Failure type keyword glossary for batch-2 specimens is shown in Table 3-4. An additional consideration was imposed for Batch-2 corrosion cycle compared to Batch-1; uncoated back side and edges of steel plates were coated with organic coating to prevent contamination of saltwater spray reservoir with rust. This improved investigation of specimens after cycle to eliminated rust residue in the saltwater that otherwise could have been accumulated on the specimen surface.

Cycle was run for one month for Batch-2 specimens. Major performance indicator to investigate was pull off strength after corrosion cycle between three in organic coating systems. Summary of test results is presented in Table 3-8. Nano top and hybrid coating systems shown no sign of coating degradation on the coated surface at the end of cycle, while 3-Layer coating system developed powdery surface which would leave residue on touch. This made performing pull off test on the 3-Layer sample not possible or yielding low pull off strength values.

Table 3-8 Pull off strength test results for Batch-2 specimens.

Coating System	Pull Off Strength (MPa) and Coating Failure Status				
	After Corrosion Cycle				
	A	B	C	D	Average
3 - Layer	NA	3.3	NA	4.8	4.1
	CF	CF	CF	CF	
Nano film Top	8.13	9.1	10.72	NA	9.3
	CF	AF-GC	AF-GC	NA	
Hybrid	7.15	7.95	9.08	NA	8.1
	CF	CF	CF	NA	

Nano top sample showed an excellent condition after corrosion cycle with average pull off strength of 9.3MPa. Two Failure type was observed. Failure in the base layer and failure at Nano film interface with dolly adhesive. Hybrid system showed good pull off strength with average of 8.1 MPa. Failures occurred in the inorganic base layer. This means that the organic top layer had established good bonding with the base layer. Figure 3-10 shows Pull Off failures for Batch-2.

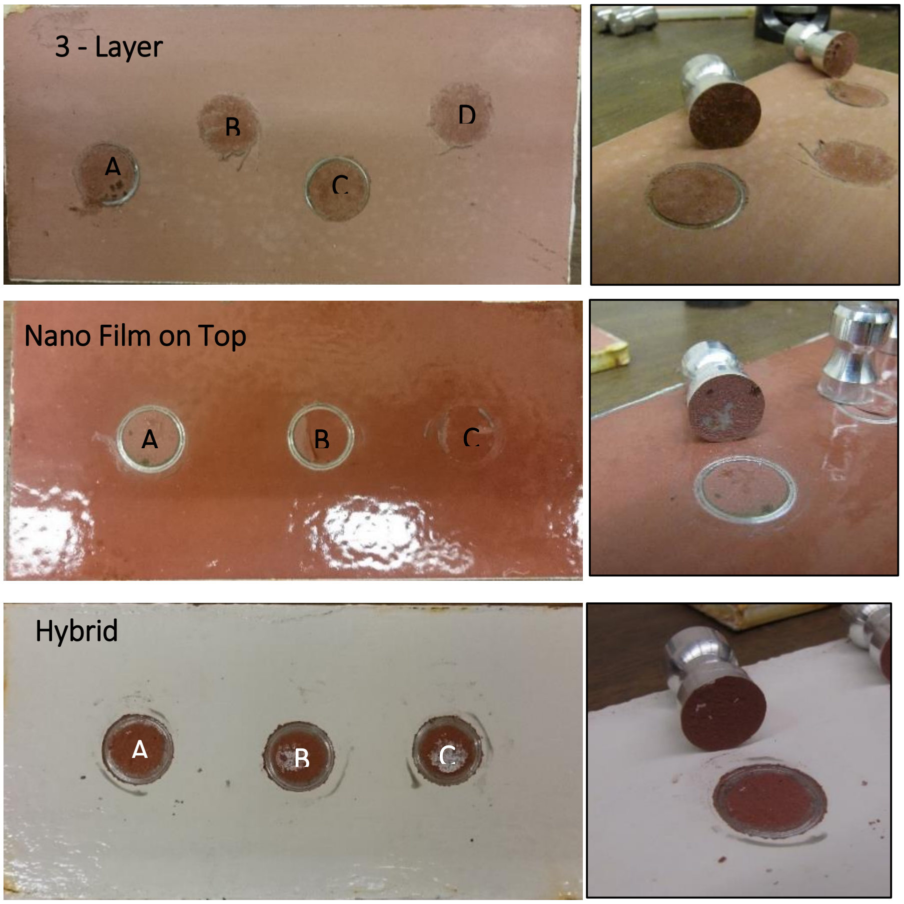

Figure 3-10 Batch-2 Pull off strength test results after corrosion cycle.

3.3.3 Batch – 3

The Nano-Film top coating system which outperformed the other systems in Batch-2 was investigated in thin and thick finishes. An additional geopolymer sample with 3M sole gel adhesive promoter as top layer was prepared to compare with Nano film on to specimens. Table 3-9 describes coating systems in the Batch-3. Accelerated corrosion cycle was conducted for two months. A set of three specimens for each coating system was prepared to be test before, one month after, and two months after corrosion cycle. Coating was applied with vacuum fed spray gun same as in Batch-2.

Coating thickness was measured at 10 spots on each specimen. Table 3-10 shows spot measurements and average coating thickness for each specimen.. These measurements are for specimens undergoing corrosion cycle. Similar to Batch-2 specimens, back of the samples was coated with organic coating to prevent rust contamination of saltwater cycle system.

Table 3-9 Coating systems in Batch-3.

Coating system	Description
Geopolymer base + 3M Sole Gel on Top	Geopolymer base layer + 3M sole gel
Geoplymer + Nano Film on Top	Geopolymer with added discrete carbon fibers and Nano Film on Top. (Separate Thick and Thin Finish)

Table 3-10 Coating thickness measurements, Batch-3.

Trials	Thickness (μm)					
	NANO Film - Thin		NANO Film - Thick		3M Sole Gel	
	Sample 1	Sample 2	Sample 1	Sample 2	Sample 1	Sample 2
1	118	142	185	219	142	238
2	120	165	190	186	190	213
3	136	177	233	204	183	230

4	162	129	214	205	171	231
5	168	172	196	232	169	198
6	168	152	220	243	155	220
7	148	191	207	198	262	204
8	136	173	196	236	2.14	273
9	153	163	221	226	183	205
10	151	178	194	253	187	222
Mean	146	164.2	205.6	220.2	164.41	223.4
Standard deviation	18.1	18.5	15.8	21.5	65.3	21.7

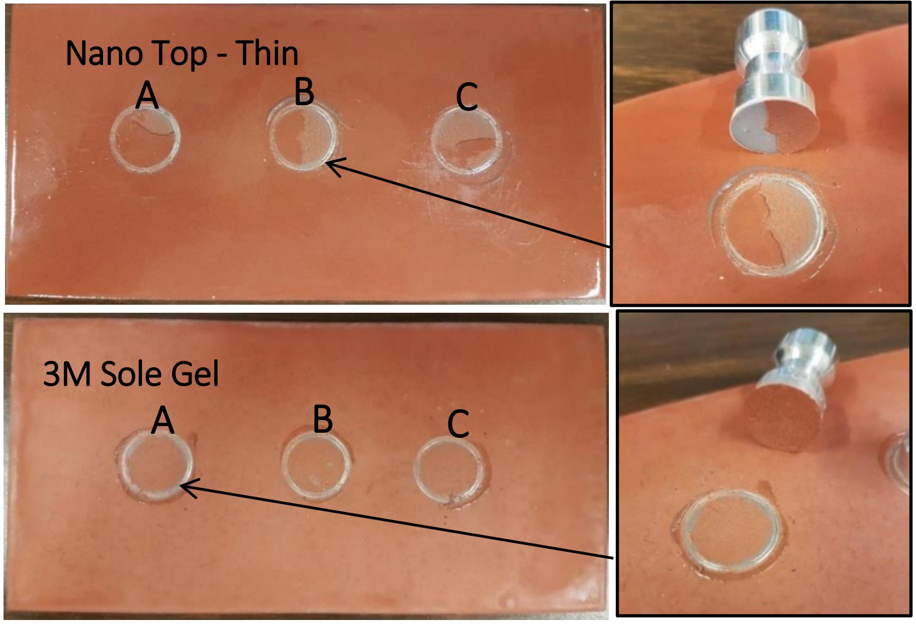

Figure 3-11 Pull Off test performed on Batch-3 specimens before corrosion cycle.

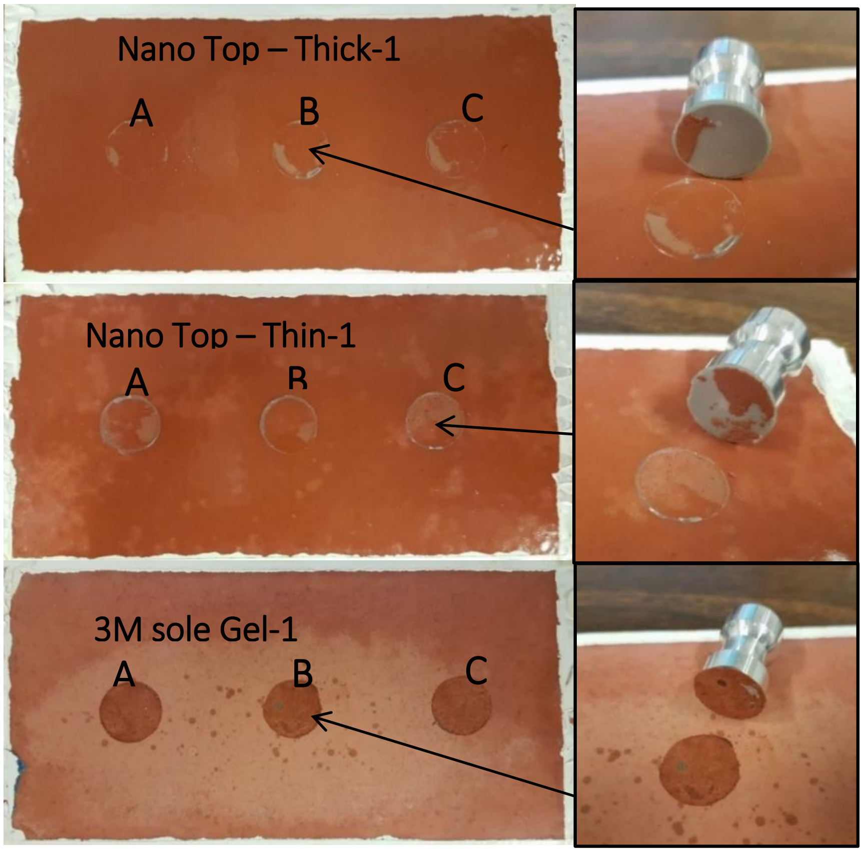

Figure 3-12 Batch-3 Pull Off test samples after one month of accelerated corrosion cycle.

Pull-off strength test was performed before, after one month, and after two months of accelerated corrosion. Results are presented in Table 3-11. Failure Keywords follow Table 3-8

Figure 3-11, Figure 3-12, and Figure 3-13 show failures observed. Investigating the values in Table 3-11 it can be seen that Pull Off strengths observed in the samples before corrosion cycle are smaller than those after corrosion cycle. This is because the coating has continuous curing after application and getting dried. As these samples were not oven-cured, they were still curing even during the corrosion cycle phase. As a result, the Pull Off strength increase is true for all coating systems after one month of corrosion cycle. This trend is reversed again for two-month exposure results.

Pull Off test results before corrosion shows consistent CF failure type for all tested dollies. Nano Film-to coating in thin layer Also is mainly CF failure typ. Finally, thick layered Nano Film top samples are also showing CF failure type.

After one-month cycle 3M Sole Gel sample, Thin Layered Nano Film on top, and Thick layered Nano Film on Top have 130%, 75%, and 233% increase in pull off strength. More than three times strength increase for Thick Layered Nano Film Top sample can be reasoned based on the fact that greater thickness of a coating would require longer time to attain maximum strength and curing. This is also true for 3M Sole Gel Sample which has similar thickness range and showed more than twice increase gain after one month of corrosion. The difference between these two also can be explained to be as the results of stronger insulating feature of Nano Film which delays curing of geopolymer base.

After two-month cycle 3M sole Gel specimen has shown surface decomposition and has developed powdery residue on the top surface. Consequently, this made dolly adhesion for the test too delicate and not usable. The Thick layered Nano Film Top specimen suffers 48% reduction in the pull off strength, while Thin layered Nano Film Top sample loses only 18% of the Pull Off strength. This observation again bolsters the fact that geopolymer coating will have optimum performance at thinner layers. Principal underlying caused for this phenomenon is relatively long time required for geopolymer in room temperature and shrinkage which can be reduced by limiting coating thickness below 200μm for this particular geopolymer formulation.

Table 3-11 Pull off strength for Batch-3 samples.

Coating System	Pull Off Strength (MPa) and Coating Failure Status		
	Before Corrosion Cycle		
	A	B	C
3M Sole Gel	3.73	4.26	4.17
	CF	CF	CF
Nano film Top - Thin	9.75	9.04	8.8
	AF-GC	CF	CF
Nano film Top - Thick	4.74	4.46	4.15
	CF	CF	CF
Coating System	After Corrosion Cycle - 1 Month		
	A	B	C
3M Sole Gel	9.01	8.13	10.92
	CF	CF	CF
Nano film Top – Thin-1	17.85	15	15.36
	AF-GC	AF-GC	CF
Nano film Top – Thick-1	16.47	13.85	13.99

	AF-GC	AF-GC	AF-GC
Coating System	After Corrosion Cycle - 2 Months		
	A	B	C
3M Sole Gel	NA - Powdered surface		
Nano film Top – Thin-2	16.47	14	8.9
	AF-GC	AF-GC	AF-GC
Nano film Top – Thick-2	8.56	7.32	7.29
	AF-CS	AF-CS	AF-CS

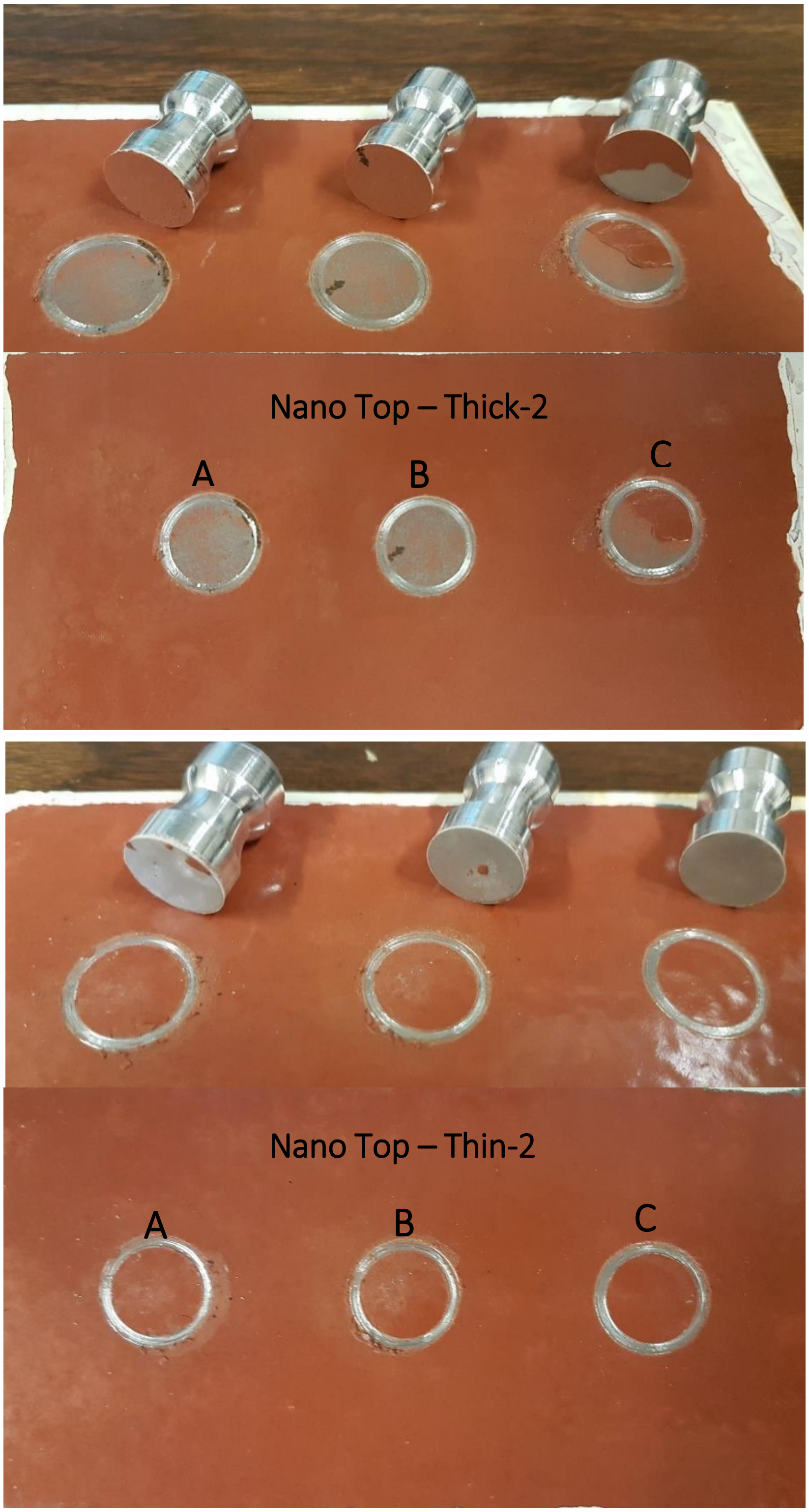
Nano Top – Thick-2
A
B
C
Nano Top – Thin-2
A
B
C

Figure 3-13 Pull off test performed after two month, Batch-3.

3.4 Geopolymer Coating with Nano-Additives

In this section three nano-additives were evaluated for their performance as corrosion inhibitors in geopolymer coating mix. Nano Additives are diluted in water. Iron oxide with 20wt%, Titanium Oxide with 30-37 wt%, and silica with 30wt% additives were used (Figure 3-14). To offset the water content from Nano-Solutions so that total water content in the mix remains unchanged. Direct water content in the mixture is offset to avoid excessive water in the coating mixture.

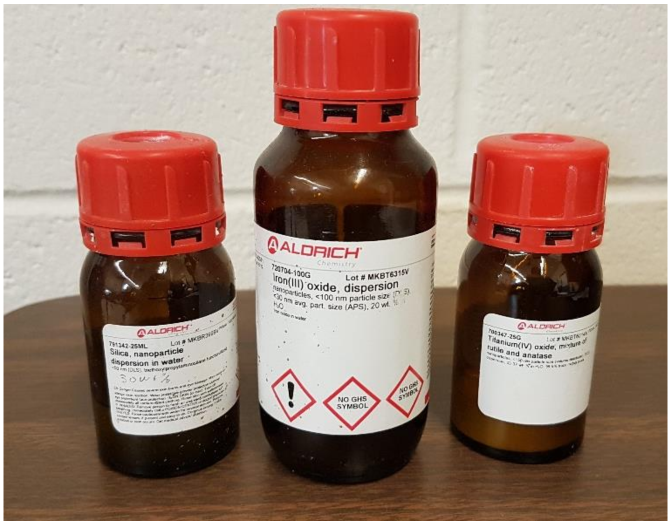

ALDRICH
Silica, nanoparticle dispersion in water
ALDRICH
Iron(III) oxide, dispersion
NO GHS SYMBOL
ALDRICH
Titanium(IV) oxide, mixture of rutile and anatase

Figure 3-14 Nano-Additives used in the coating mix.

Two coated specimen for each nano-additive sample and a two specimens as control (in total 8 specimens) were prepared in two separate batches. In batch-4 geopolymer coating was applied using foam brush, while in batch-5 geopolymer was diluted with additional water to be able to be sprayed.

3.4.1 Calculation of Nano-Additives Content

It was selected to add each Nano-additive equal to %1 weight of the coating mixture. Calculations for addition of *%1 weight of coating mixture* Nano Additive to account for the water that additives are diluted in are as follows:

$\text{Part A weight} = \mathrm{W_A}$

$\text{Part B weight} = \mathrm{W_B}$

$\text{Total water content} = \mathrm{W_T}$

$\text{Added Water} = \mathrm{W_1}$

$\text{Water content in the additive} = \mathrm{W_2}$

$\text{Nano Additive solution weight} = \mathrm{X}$

$\text{Nano Additive weight} = \mathrm{W_N}$

$\text{Nano Additive concentration (wt\%)} = \mathrm{C}$

For total water content we have:

$$W_T = W_1 + W_2 \tag{3.1}$$

For Nano solution weight we have:

$$X = W_N + W_2 \tag{3.2}$$

$$W_N = CX \tag{3.3}$$

$$W_2 = (1 - C)X \tag{3.4}$$

We want to have %1 of Nano additive in whole coating mixture,

$$\frac{W_N}{W_A+W_B+W_T} = 0.01 \tag{3.5}$$

$$W_N = 0.01(W_A + W_B + W_T) \tag{3.6}$$

$$X = \frac{W_N}{C} = \frac{0.01}{C}(W_A + W_B + W_T) \tag{3.7}$$

$$W_2 = \frac{0.01(1-C)}{C}(W_A + W_B + W_T) \tag{3.8}$$

$$W_1 = W_T - W_2 \tag{3.9}$$

X and W_1 in grams are the values required to make the coating mixture with Nano-Additives.

Surface preparation before coating application in each test batch was performed. A decontamination cleaning foam was used to clean the grease oil from steel plates. Acetone also could be used to clean the contaminants off the steel surface. To expose a fresh layer of steel, all plates were grit blasted or sand blasted prior to coating application.

3.4.2 Batch-4

In this batch the water content was kept the same as original in coating mixture which results in a thick viscose coating. Foam brushes were used to coat the steel specimens (Figure 3-15). Table 3-12 shows the constituents required for Batch-4 by their weights. It can be seen that the Part A and Part B of geopolymer in control sample are same as Nano-Modified samples and only water content is modified.

Table 3-12 Batch-4 coating mix constituents – Original water Content

Constituent	Content in grams (% of Mixture)			
	Control (C)	Iron Oxide	Titanium Oxide	Silica
Part A (Powder)	42 (65.6%)	42 (65%)	42 (65%)	42 (65%)
Part B (Fluid)	18 (28.1%)	18 (28%)	18 (28%)	18 (28%)
Water	4 (6.25%)	1.5 (2.32%)	2.8 (4.33%)	2.5 (3.87%)
Nano Additive	-	3.1 (5.26%)	1.83(4.38%)	2.13(3.3%)

The coated finish on cured samples showed signs of foam brush passes on the which created an uneven surface (Figure 3-16). As a result pull off test was not successfully performed on these set of samples. Examining the surface texture of the specimens showed that Silica added specimen has better finish which was least porous and glossier. This is because of densification property that Silica adds to the geopolymer mix.

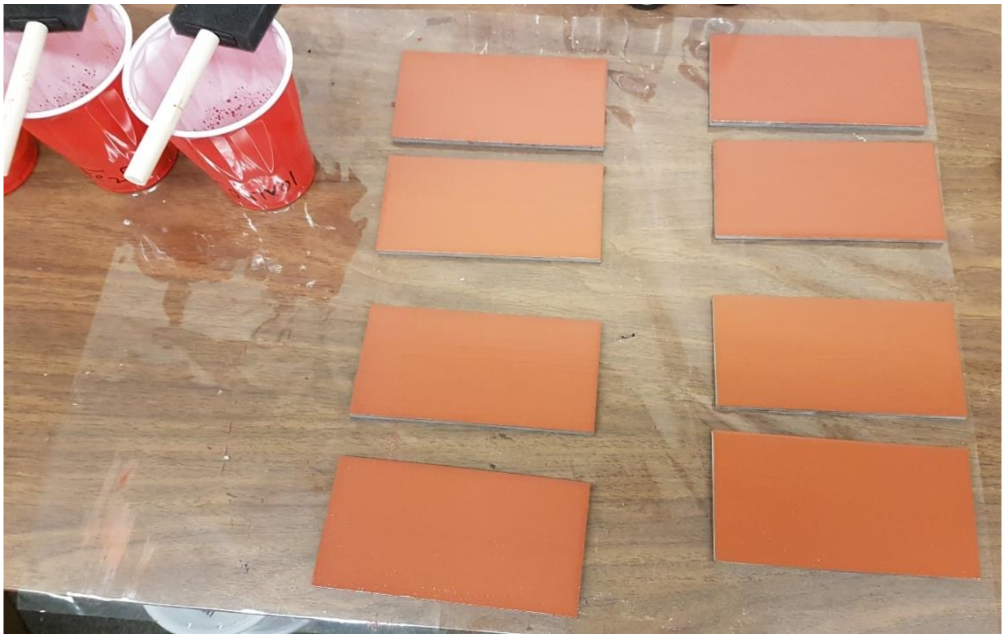

Figure 3-15 Freshly coated specimens using foam brush.

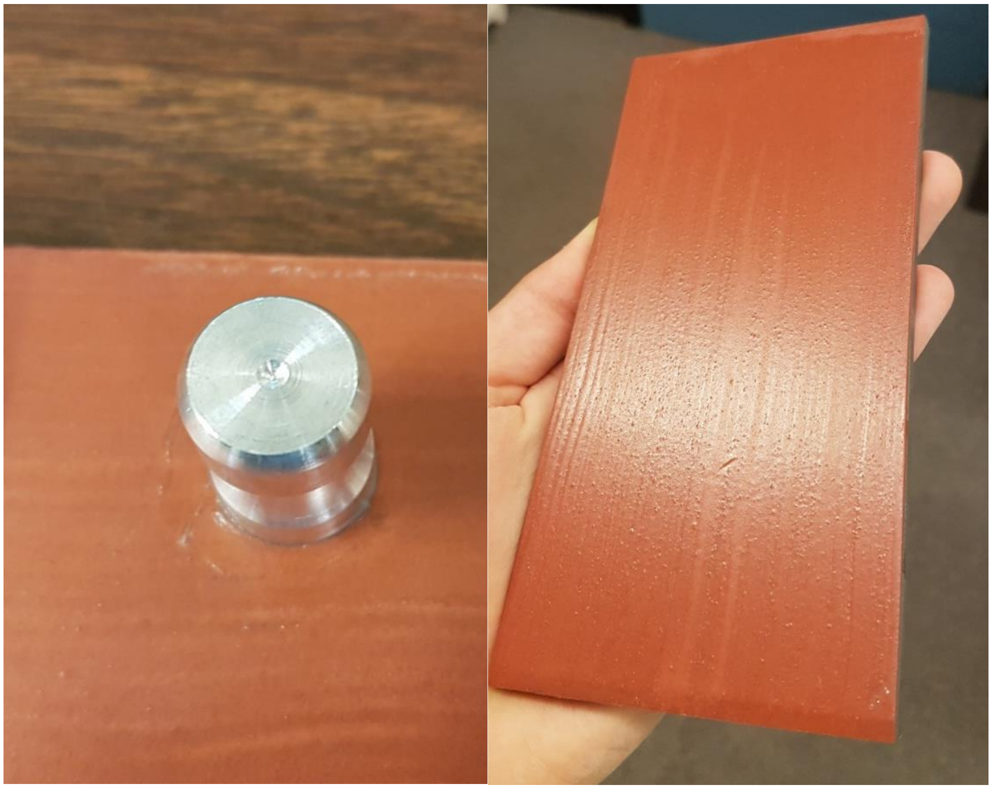

Figure 3-16 Foam brush trace on the coted specimen with Nano-Silica Additive (Right), Dolly glued to the specimen with uneven surface (left).

Specimens were left in the accelerated corrosion chamber for one month. To control ingress of rust into salt water reservoir circulation system, back of the four samples in the chamber were also coated with organic coating (Figure 3-17). The appearance of specimen after placing in the corrosion chamber for one week and one month are shown in Figure 3-19, respectively.

Examination and observation of specimens during the accelerated corrosion test and at the end concluded the following remarks:

1- It was clear that Control specimen developed the signs of blistering before other specimens. This was followed by Iron Oxide added specimen, Titanium Oxide added specimen, and finally Silica added specimen which showed the best performance.
2- In general Control specimen and Iron oxide added specimen were more severely affected by corrosion than Titanium Oxide added and Silica added specimens.
3- Foam brush left a groove like pattern on the surface of the specimens which caused concentration of corrosion within these grooves. This suggest coating with brush is more susceptible to result in uneven finish especially because of existence of discrete fibers in the coating.
4- Comparison macroscopic images of surface of specimens before and after corrosion cycle shows micro-cracks which were not present before corrosion are visible in all specimens. In addition, rust developed within micro-cracks. Figure 3-20Figure 3-21 show macroscopic images of specimens before and after corrosion cycle.

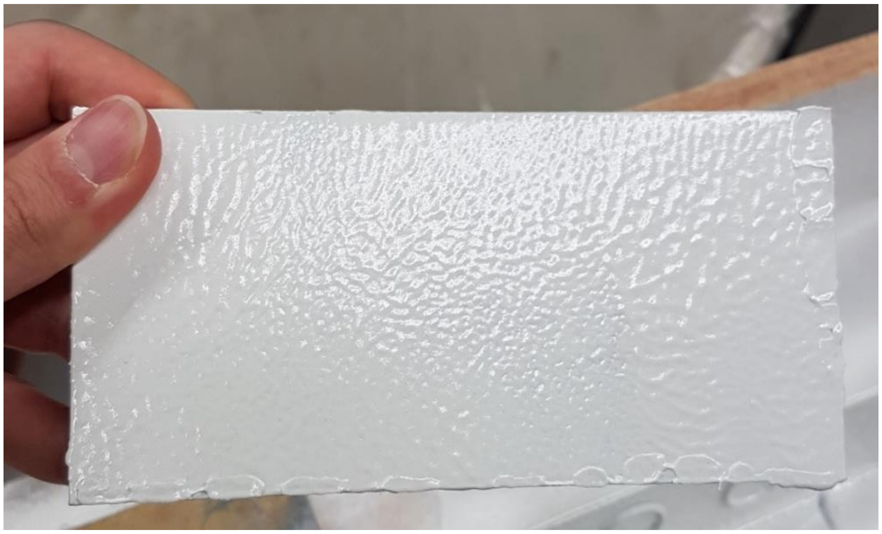

Figure 3-17 Back of a specimen coated with organic coating

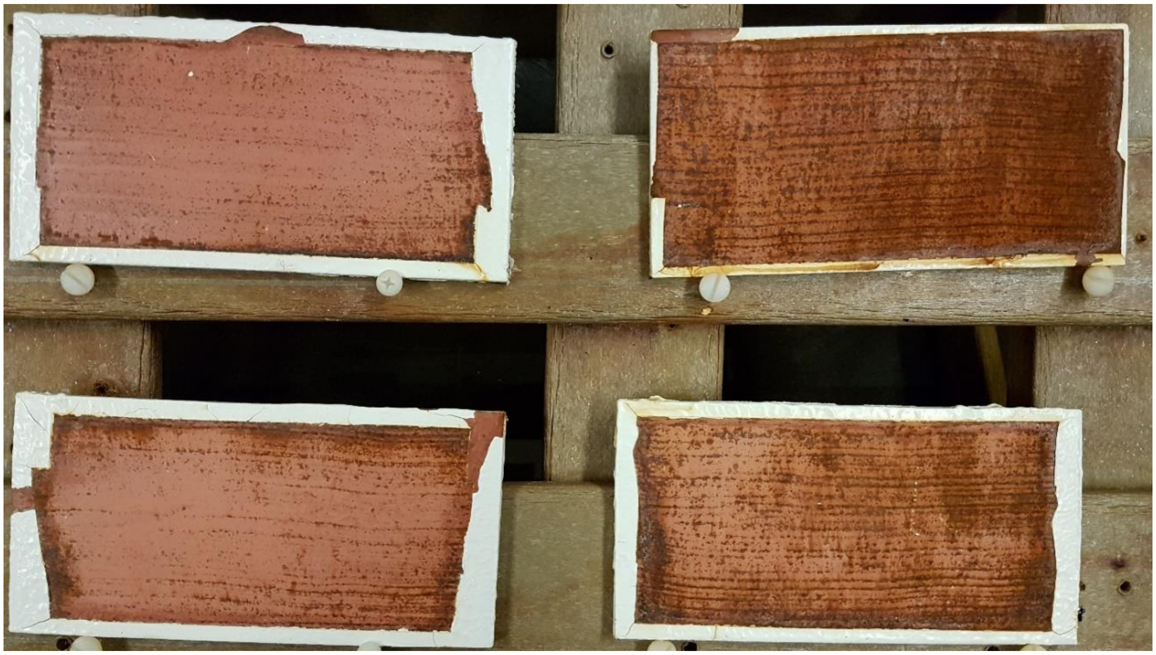

Figure 3-18 Batch-4 after one week corrosion cycle.

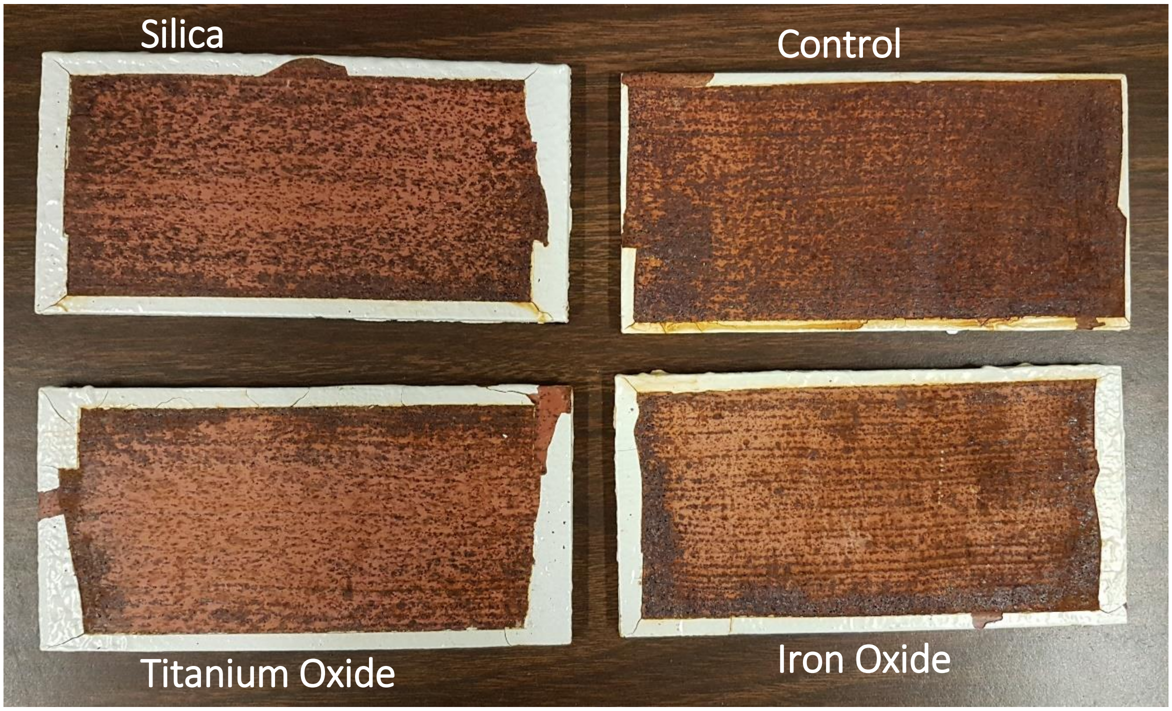
Silica
Control
Titanium Oxide
Iron Oxide

Figure 3-19 Batch-4 after one month corrosion cycle.

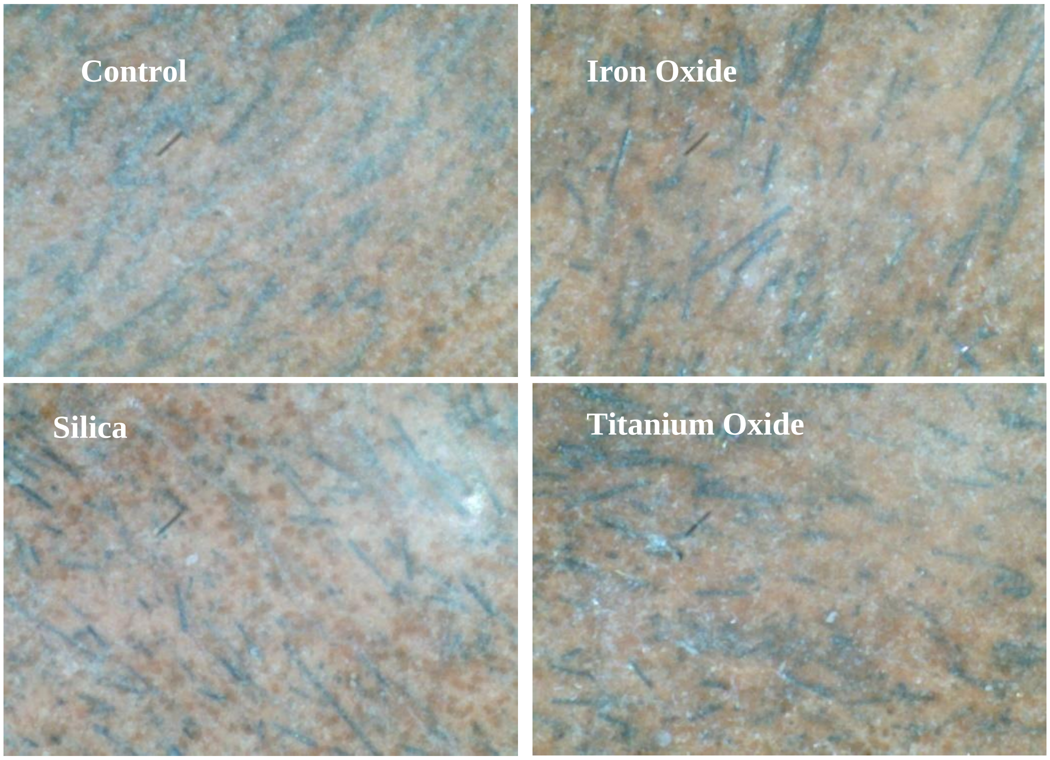
Control
Iron Oxide
Silica
Titanium Oxide

Figure 3-20 Macroscopic images of Batch-4 Coatings before corrosion.

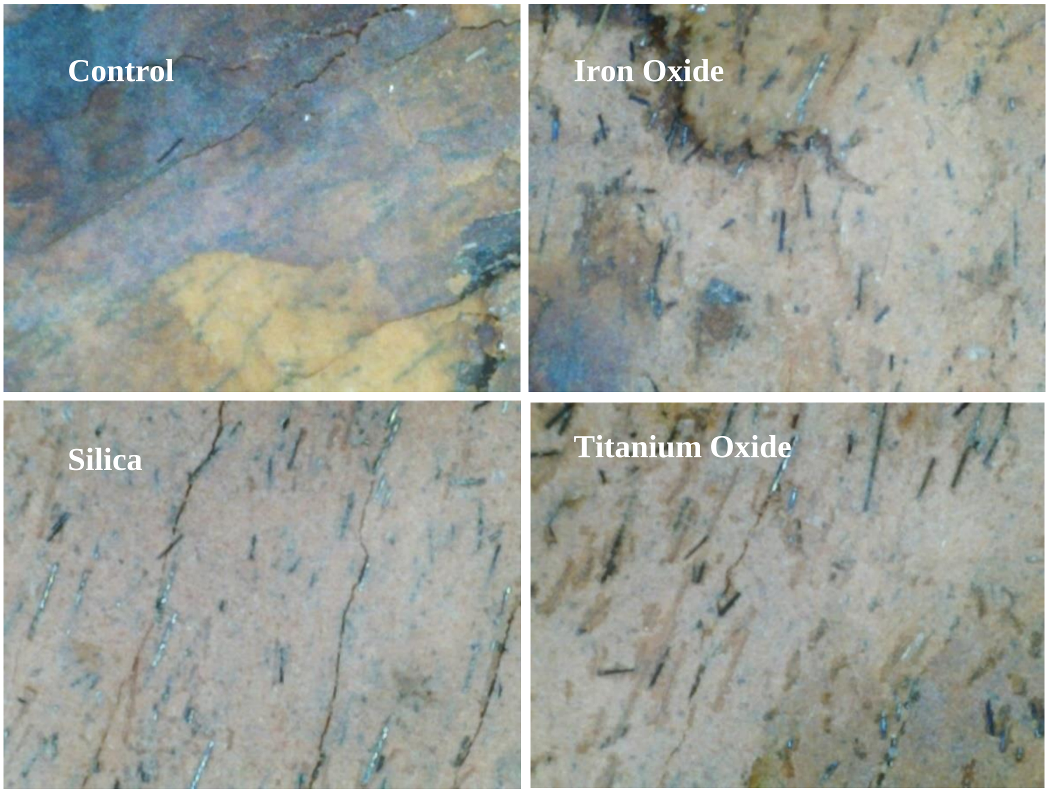

Figure 3-21 Macroscopic images of Batch-4 Coatings after corrosion.

3.4.3 Batch-5

In this batch to avoid problems with using brush for coating sprayers were used to have a better and even coated finish. This also means that the water content needed to be adjusted to be able to spray the coating using spray gun. To achieve a uniformly coated surface, steel coupons were coated using 1.4mm nozzle tip High Volume Low Pressure (HVLP) spray gun (see Figure 3-22). Original water content in the coating mixture proved to be incompatible with this spray gun and coating mixture could not be properly sprayed or sprayed at all. This is contributed by relatively higher viscosity and lower surface tension of the mixture (which makes flow of coating mixture over surfaces and container’s walls more difficult).

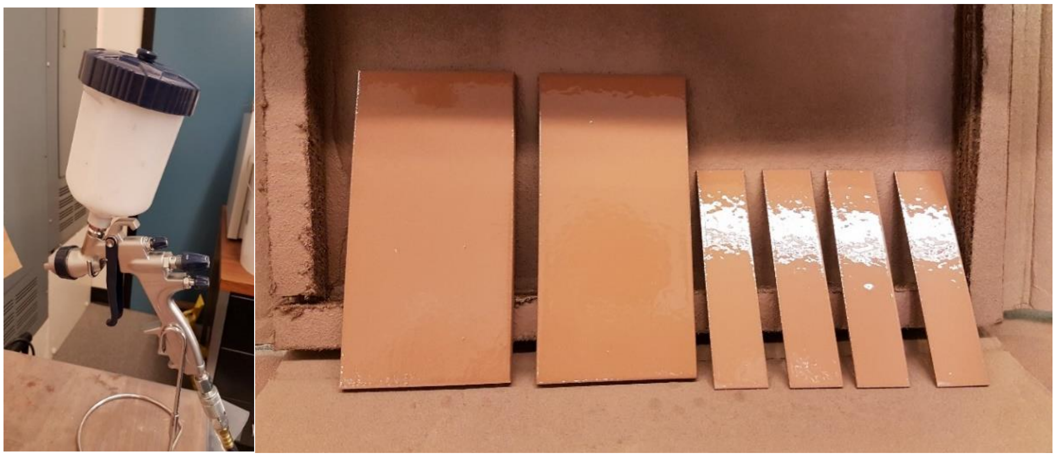

Figure 3-22 Fresh coated specimens using 1.4mm nozzle tip HVLP spray gun.

To fix this issue two separate approaches were tested:

1) Using 2.5mm nozzle tip HVLP spray gun: Although this larger nozzle spray gun was able to spray original coating mixture, the results were far from satisfactory. Because of the thick mixture even at most concentered pattern of spray gun, coating would be spattered in droplets on the surface and won't achieve a smooth finish. Frequent clogging of gun nozzle was also happened.
2) Diluting mixture by increasing water content: First the water content was increased from %6.25 of mixture weight to %9.1 of mixture weight. This water content increase enables the 2.5mm nozzle tip gun to be able to spray coating mixture. The finish from this mixture had considerable improvements but still could not achieve completely smooth finish and some degree of uneven-ness was observed on the coated surface. By increasing water content from 6.25% of mixture weight to 11.76% of mixture weight, coating mixture was successfully coated using 1.4mm nozzle tip gun with

desired smooth finish (Figure 3-23). Table 3-13 shows the mix constituents for Batch-5 specimens. Figure 3-23 shows the Nano-Added coated samples after curing.

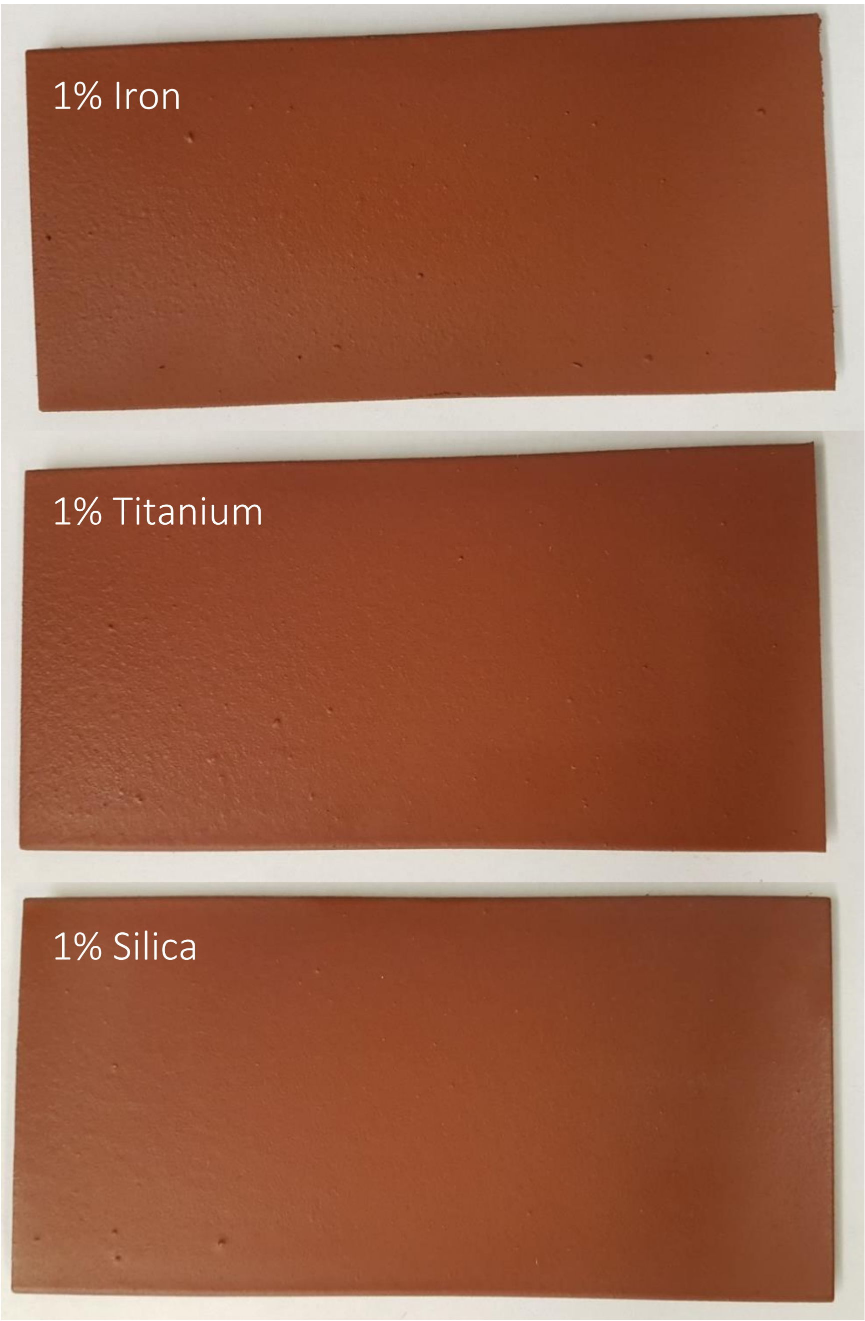
1% Iron
1% Titanium
1% Silica

Figure 3-23 Cured Nano-Added specimens coated with spray gun.

Table 3-13 Batch-5 coating Mix constituents – increased water content

Constituent	Content in grams (% Mixture)			
	Control (C)	Iron Oxide	Titanium Oxide	Silica
Part A (Powder)	42 (61.76%)	42 (61.15%)	42 (64.98%)	42 (61.76%)
Part B (Fluid)	18 (26.47)	18 (26.2%)	18 (27.85%)	18 (26.47)
Water	8 (11.76%)	6.74 (9.81)	2.8 (4.33%)	6.41 (3.87%)
Nano Additive	-	1.94 (5.26)	1.83(4.38%)	2.27(3.3%)

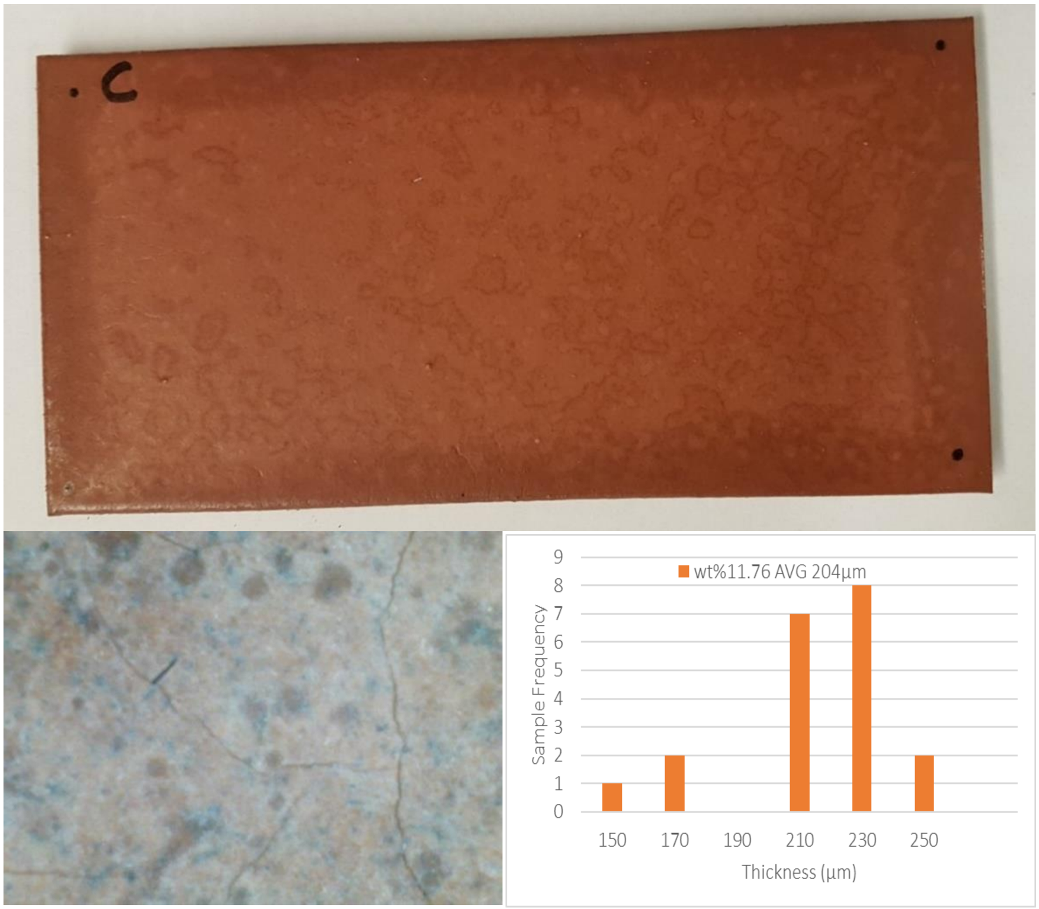
.C
wt%11.76 AVG 204μm
Sample Frequency
0
1
2
3
4
5
6
7
8
9
150
170
190
210
230
250
Thickness (μm)

Figure 3-24 Control withWt11.76% with 204μm average thickness – Coated Specimen(Top), Cracks are clear in macroscopic image of the coated surface(Bottom Left), Thickness measurement distribution over coated area(Bottom Right).

3.4.4 Coating Thickness and its effect on shrinkage cracking

Examination and observations were made to evaluate effect of thickness and water content on shrinkage process and macro crack formation. At 11.76% water content the coating becomes more susceptible to cracking. At average thickness of 204nm after curing, coated surface shows traces of micro-cracks (Figure 3-24).

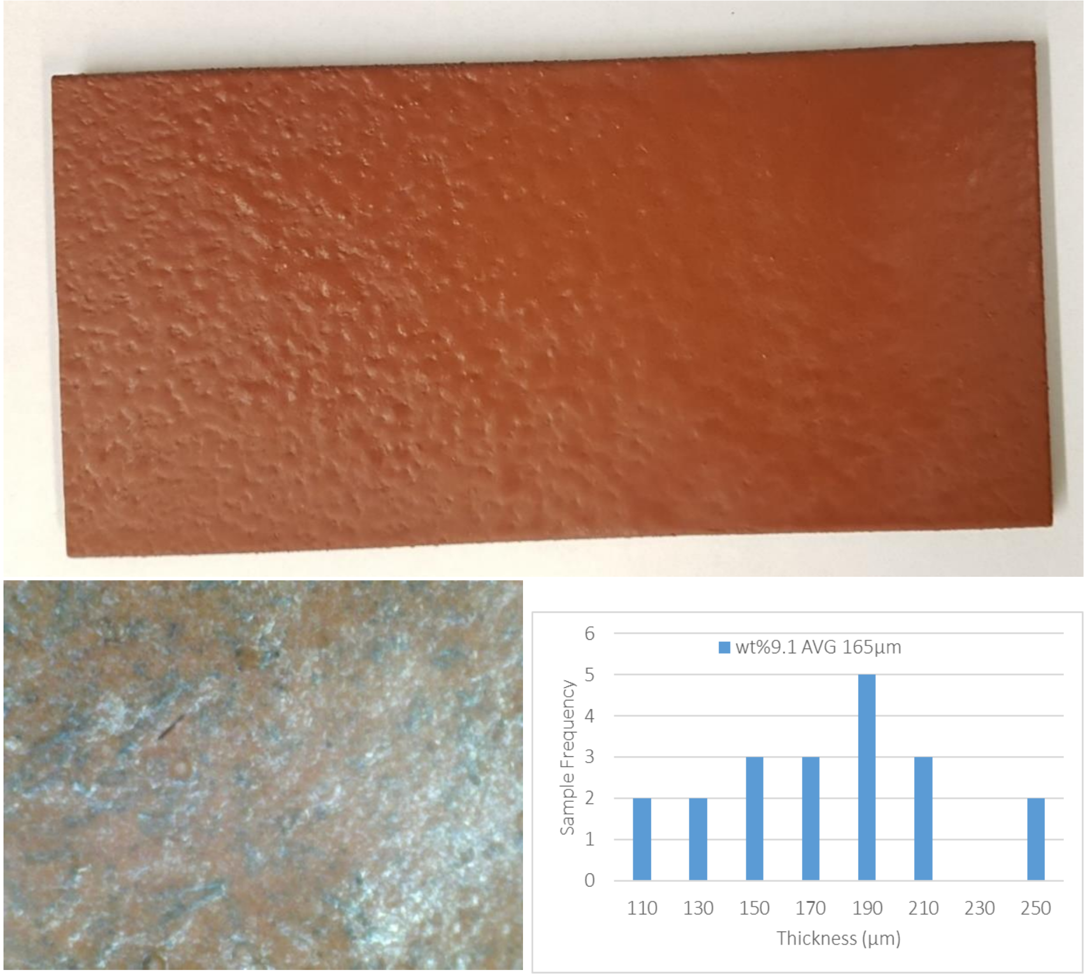
6
5
4
3
2
1
0
■ wt%9.1 AVG 165µm
Sample Frequency
110
130
150
170
190
210
230
250
Thickness (µm)

Figure 3-25 Control withWt%9.1 with 165µm average thickness – Coated Specimen(Top), Macroscopic image of the coated surface(Bottom Left), Thickness measurement distribution over coated area(Bottom Right).

At 9.1% water content the coated surface, although not smooth shows no sign of cracks at an average thickness of 165μm (Figure 3-25). At 11.76% water content coated surface with an average thickness of 106μm shows no sign of cracks (Figure 3-26).

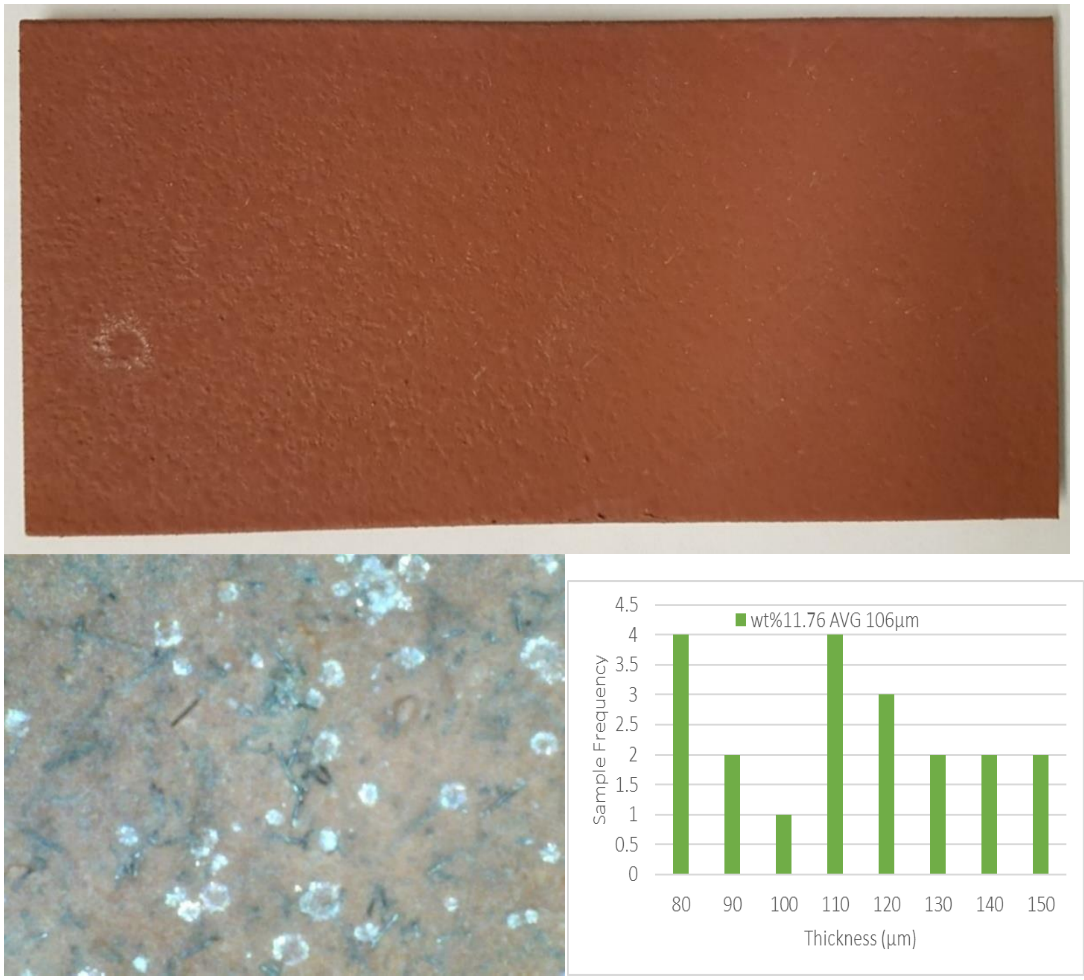
wt%11.76 AVG 106μm
Sample Frequency
0
0.5
1
1.5
2
2.5
3
3.5
4
4.5
80
90
100
110
120
130
140
150
Thickness (μm)

Figure 3-26 Control withWt11.76% with 204μm average thickness – Coated Specimen(Top), Cracks are clear in macroscopic image of the coated surface(Bottom Left), Thickness measurement distribution over coated area(Bottom Right).

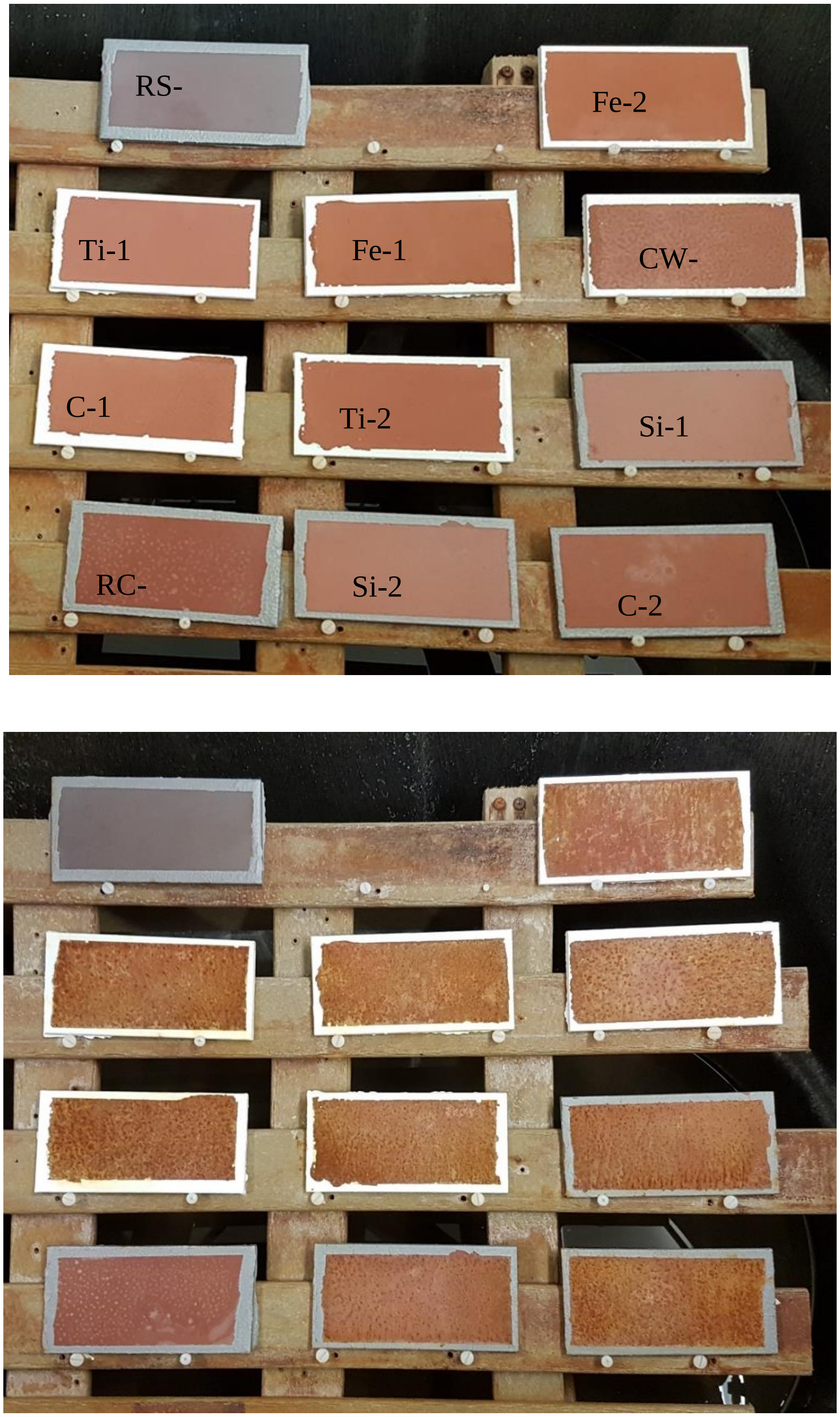
RS-
Fe-2
Ti-1
Fe-1
CW-
C-1
Ti-2
Si-1
RC-
Si-2
C-2

Figure 3-27 Batch-2 Specimens before Corrosion (Top), and after one month Accelerated Corrosion (Bottom).

Batch-2 of accelerated corrosion inluded 2 specimens from each of Control (C-1, C-2), Nano-Silica added(Si-1,Si-2), Titanum Oxide added(Ti-1,Ti-2), and Iron Oxide(Fe-1,Fe-2) added mixes. All of the mixes had 11.7% water content. One additional Control mix with 9.1% water content (CW-1.5) was also included in the test. One specimen with resin staurant on uncoated blasted steel(RS-1) and one specimen with resin on top of coated (control mix, RC-1) was also put in chamber. This makes total of 11 specimens for Batch 2 which is shown in Figure 3-27, top.

Examining the specimens in Batch-5 after corrosion cycle (see Figure 3-27 bottom) shows that still Silica added specimen shows overall best performance compared to other geopolymer coated specimens. The RC-1 and RS-1 specimens do not show any sign of corrosion which means the CFRP saturant does a good job of sealing the substrate. In addition RC-1 specimen shows emergence of white dots which did not existed early after applying saturant on top of coated steel (see Figure 3-27). These white dots were appeared on both samples in the chamber and outside of the chamber. This concludes that they were not result of corrosion cycle. Examining these dots showed that they were not air bubble and rather very small solid particle which could be result of continuous curing of geopolymer under confinement of saturant resin. Performing Pull off test on samples with appeared dots showed no reduction in pull off strength and same average value of 5MPa was observed.

4 CFRP-Substrate bond behavior

4.1 Modified Lap Shear Test Setups

Single joint and Double-joint lap shear tests are established methods of evaluating adhesive performance under shear loading. To evaluate bond behavior between uncoated and coated steel sheets and CFRP strips two test setups were investigated. Similar setups have been implemented in the research literature (Schnerch et al. 2004; Fawzia et al. 2006; Liu et al. 2009) to study adhesive bond behavior of CFRP laminates to steel.

4.1.1 SETUP 1- Single Lap Shear

This setup is a modified version of ASTM D1002-10. This test has been modified to include CFRP laminate as the mediator part which overlaps with steel sheets. The overlap length (bond length) on one of the metal sheets is held to be constant (maximum) while the bond length (b) is changed on the other steel sheet. The first goal is to investigate bond failure behavior with change of bond length on the coated steel sheet samples and uncoated steel sheet samples. Second goal is to determine minimum nominal bond length required to have rupture in CFRP rather than bond failure (delamination). A displacement control tensile loading with the rate of 0.05in (1.27mm)/min will be applied to the specimen till failure occurs. Figure 4-1 shows the details of the specimen in this setup.

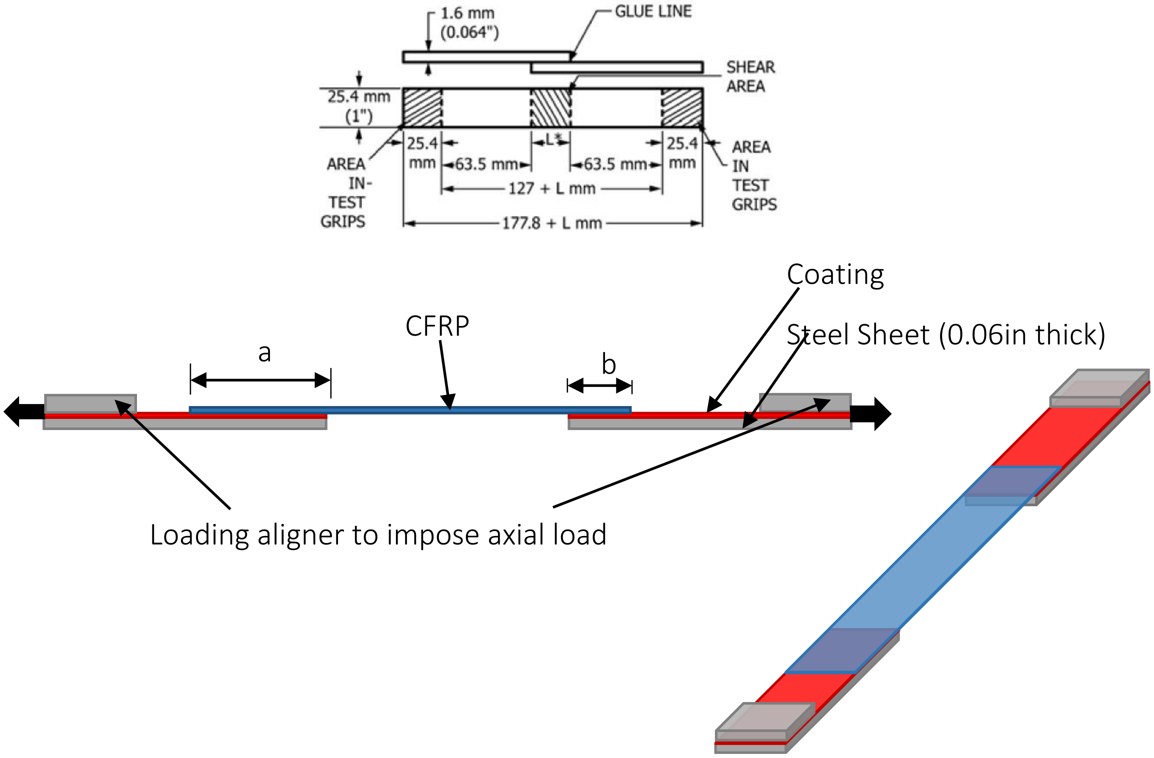

1.6 mm
(0.064")
GLUE LINE
SHEAR
AREA
25.4 mm
(1")
AREA
IN-
TEST
GRIPS
25.4
mm
63.5 mm
L*
63.5 mm
25.4
mm
AREA
IN
TEST
GRIPS
127 + L mm
177.8 + L mm
Coating
CFRP
Steel Sheet (0.06in thick)
a
b
Loading aligner to impose axial load

Figure 4-1 ASTM original specimen(top), SETUP 1 CFRP lap shear modified specimen (bottom).

4.1.2 SETUP 2 – Double Lap Shear (Double Strap)

This setup is a modified version of the ASTM D3528-96 Type B specimen. The "shear area" noted in Type B specimen in ASTM D3528-96 is where CFRP laminates are adhered to the metal sheets. Separate specimens are made for coated and uncoated metal sheets. This test follows the same goals as SETUP 1. Geometry of this setup satisfies axial loading without the need to use loading aligners. A displacement control tensile loading with the rate of 0.05in (1.27mm)/min will be applied to the specimen till failure occurs. Figure 4-2 shows the details of the specimen in this setup.

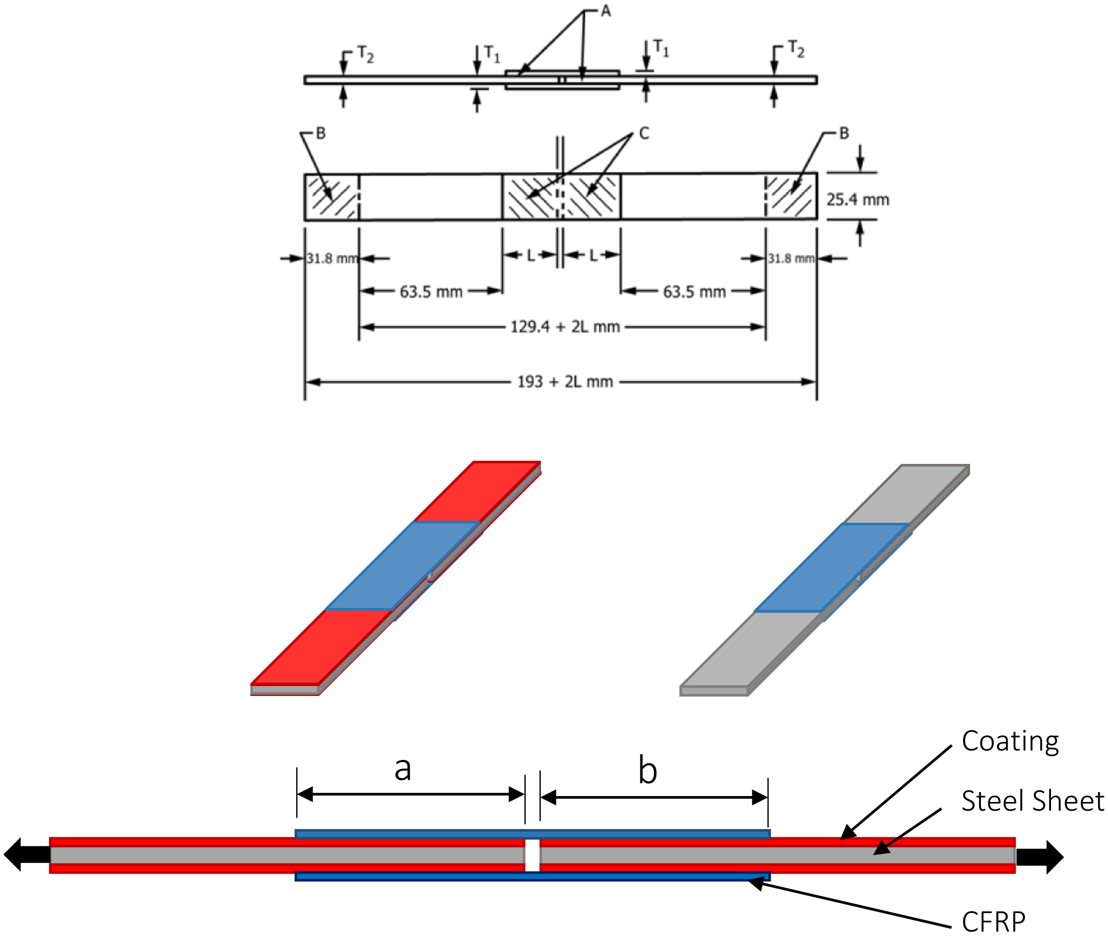
A
T2
T1
T1
T2
B
C
B
25.4 mm
31.8 mm
L
L
31.8 mm
63.5 mm
63.5 mm
129.4 + 2L mm
193 + 2L mm
a
b
Coating
Steel Sheet
CFRP

Figure 4-2 ASTM original type-B specimen(top), SETUP2 CFRP-STEEL lap shear test. coated and uncoated samples and Specimen details (bottom).

4.2 CFRP-Coating Interfacial properties

4.2.1 Pull Off Test (Mode-I Failure)

Prior to conduct Lap-Shear tests, bonding of CFRP saturant resin to the geopolymer coated surface was evaluated. Four specimens (P1, P2, P3, P4) were coated with geopolymer using spray gun and cured in the oven at 80°C (175°F) for 72 hours. Thickness measurements were performed on cured samples to investigate thickness distribution and evaluate average thickness. Average thickness of samples P1, P2, P3, and

P4 were 67, 59, 48, and 48µm, respectively. Coating thickness measurement distribution for 20 points on each sample is shown in Table 4-1 and Figure 4-3.

Table 4-1 Thickness data of coated samples for Resin-Coating bond evaluation.

Data No	Sample Thickness (µm)			
	P1	P2	P3	P4
1	76	38	48	49
2	83	53	54	64
3	76	50	55	57
4	84	62	53	51
5	33	70	39	38
6	56	52	37	56
7	50	61	37	35
8	60	45	32	46
9	58	49	30	44
10	75	61	31	39
11	74	48	44	49
12	70	63	48	47
13	84	73	54	46
14	77	55	62	70
15	57	38	70	54
16	63	42	58	55
17	66	70	48	51
18	59	91	45	44
19	69	86	49	34
20	70	72	58	35
Mean	**67**	**59**	**48**	**48**
STD	**12.8**	**14.8**	**10.9**	**9.6**

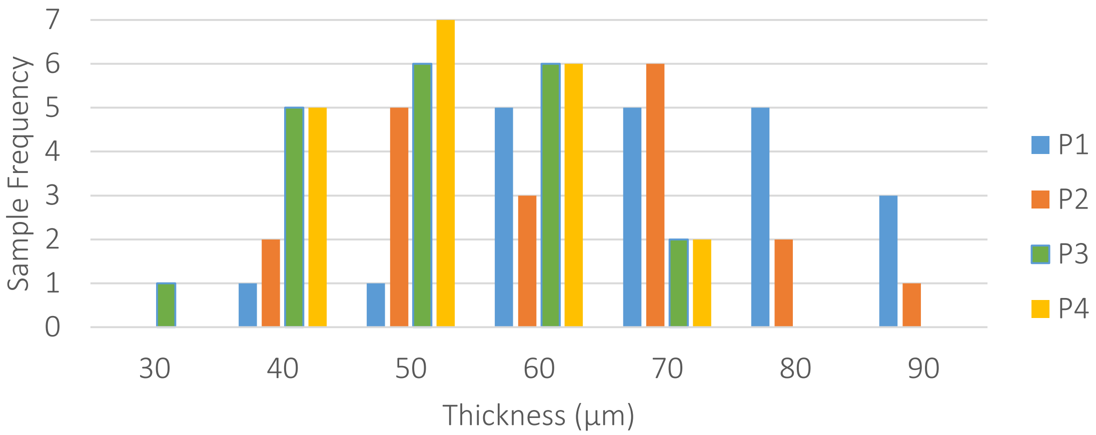

Figure 4-3 Thickness frequency distribution of coated samples for Resin-Coating bond evaluation.

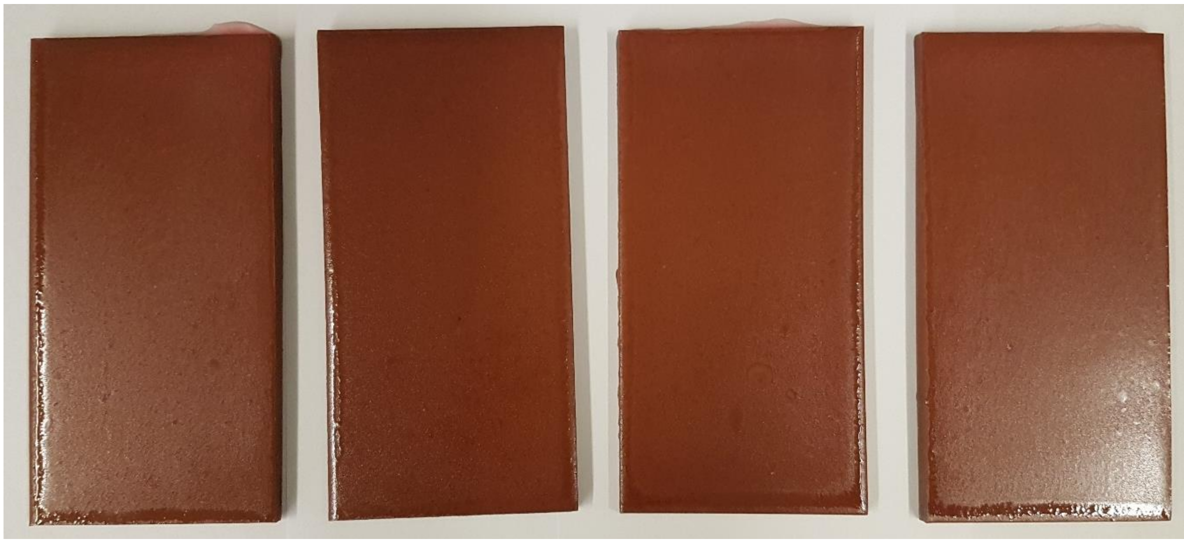

Figure 4-4 Resin Saturant applied and cured on coated samples.

Table 4-2 Resin thickness measurement data on the coated samples.

Data No	**Resin Thickness (µm)**			
	P1	**P2**	**P3**	**P4**
1	112	188	201	242
2	95	172	149	211
3	97	172	127	237
4	80	153	132	201
5	99	175	140	242
6	91	151	139	173
7	72	137	143	163
8	76	150	166	154
9	117	120	150	134
10	112	130	162	182
11	94	133	150	192
12	97	149	148	207
13	98	120	139	210
14	110	129	142	205
15	108	157	156	230
16	96	175	188	192
17	83	128	176	168
18	68	99	143	165
19	62	122	146	175
20	73	127	137	169
Mean	**92**	**144**	**152**	**193**
STD	**16.0**	**23.6**	**18.7**	**30.7**

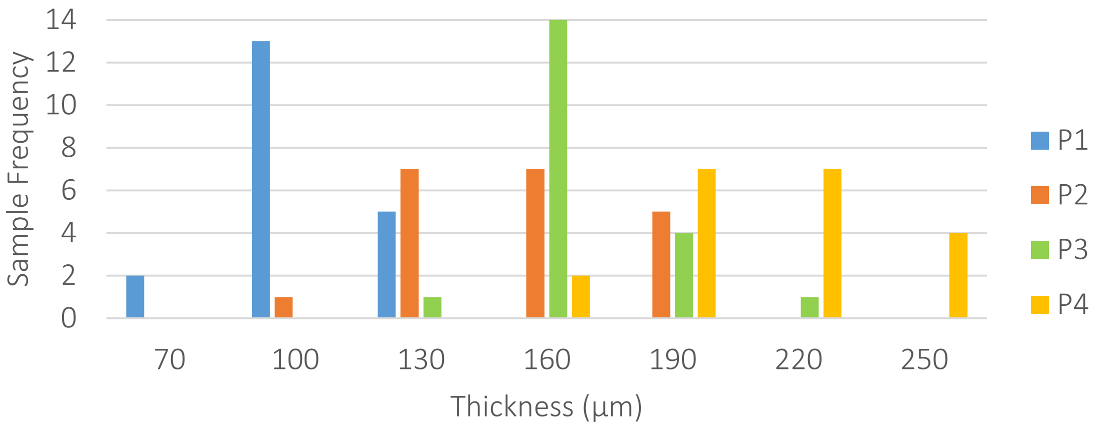

Figure 4-5 Resin thickness measurement distribution on coated samples.

DowAksa CarbonBond300H® saturant resin was applied on top of four cured geopolymer coated samples (Figure 4-4). Thickness measurements were repeated to calculated approximate resin thickness distribution on top of the coating. Measurement distribution from 20 measurements for each sample is shown in Table 4-2 and Figure 4-5. The average thickness of resin on top of specimens P1, P2, P3, and P4 were measured to be 92, 144, 152, and 193µm.

Table 4-3 Pull-Off strength of Saturant Resin on Geopolymer coated specimen

Sample	Pull Off Strength (MPa)			
	Dolly-1	Dolly-2	Dolly-3	Average
P2	5.4	5.1	NA	5.25
P3	5.2	4.6	5.2	5.03

Pull off test was conducted on two of the coated specimens topped with resin saturant. Test on P2 sample was performed one week after resin application and it was performed on P3 one month after resin application while samples were sitting in room temperature. Average pull off strength was measured to be 5MPa. Table 4-3 shows Pull

Off test values. Figure 4-6 shows the pull off test on a specimen before accelerated corrosion. It can be seen that clean failure occurs at the interface of resin and coating.

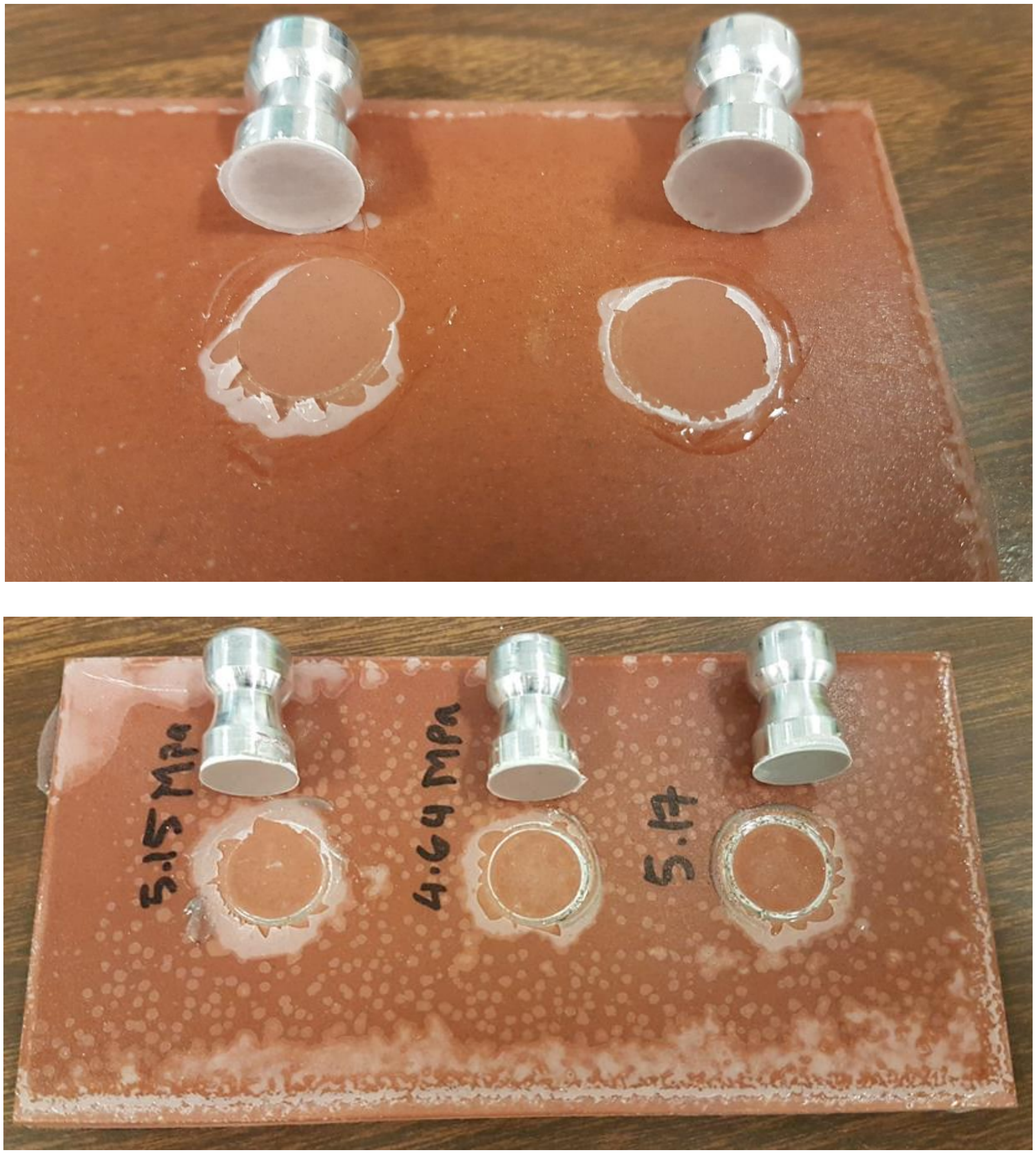

Figure 4-6 Pull off strength performed on geopolymer coated steel specimen topped with DowAksa CarbonBond 300H Saturant. P2 (Top), P3 (Bottom).

4.2.2 Lap-Shear Tests (Mode-II Failure)

The primary purpose of this test is to determine ultimate load capacity and average bond strength of CFRP repair. In addition, this test will help to calculate Mode II failure properties of the bond interface for simulation purposes. Three specimens of modified lap shear test of SETUP-1 type with CFRP laminates on coated steel sheet and bond length of 20mm were compared with three specimens of uncoated steel sheet and 20mm bond length (Figure 4-7). Lab tests were conducted using MTS machine with displacement control loading with 0.05in/min loading rate (Figure 4-8). Ultimate load capacity and average failure stress (Bond Strength) were compared in Table 4-4. Specimens before and after failure are shown in Figure 4-9. Coating on the steel sheets were performed using spray gun.

Table 4-4 Ultimate Load for coated and uncoated specimens

Specimen	Ultimate load (N)	Average Bond Stress (Bond strength) MPa	Average Bond Stress (Bond strength) MPa
Coated-20-2	3650	9.1	8.9
Coated-20-3	3440	8.6	
Uncoated-20-1	6836	17.1	17.6
Uncoated-20-2	7336	18.3	
Uncoated-20-3	6913	17.3	

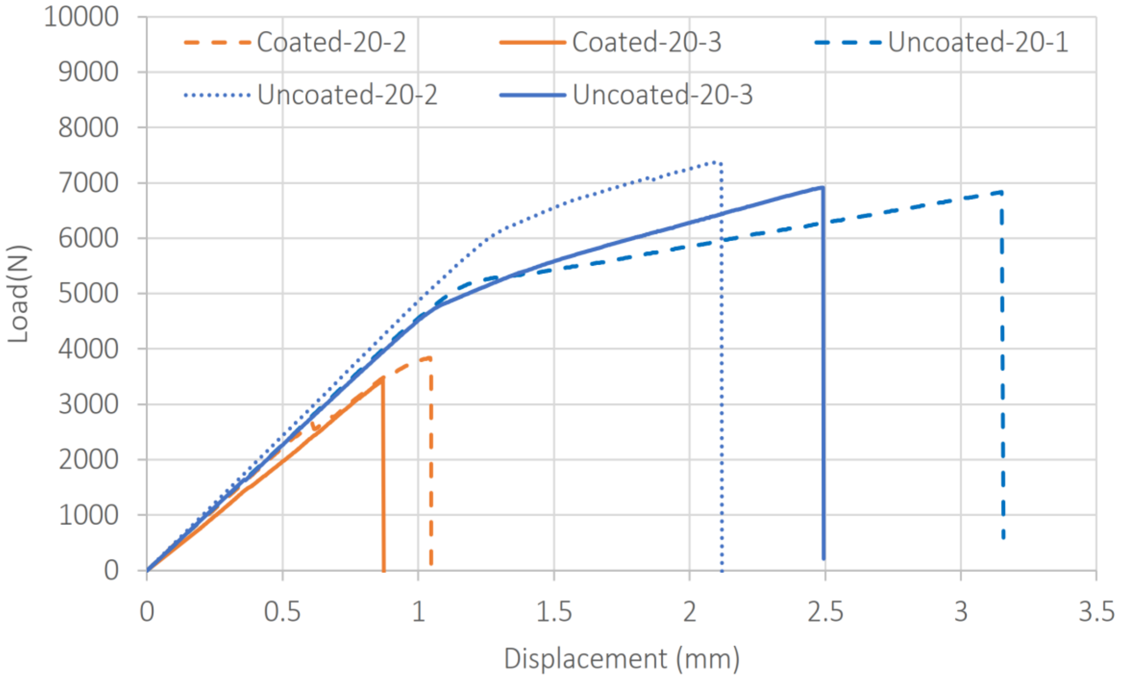

Figure 4-7 Load-Displacement Curve for Lap-Shear Specimens.

It should be noted that specimen Coated-20-1 was found to be defective due to fabrication quality. The reason that 20mm bond length was chosen as comparison basis is that due to shorter bond length peeling stresses at edge of CFRP are less severe and stress distribution along the bond is more uniform. In addition, it was found in prior FEM simulations that steel sheets will go into large yielding phase for bond lengths larger than 20mm.

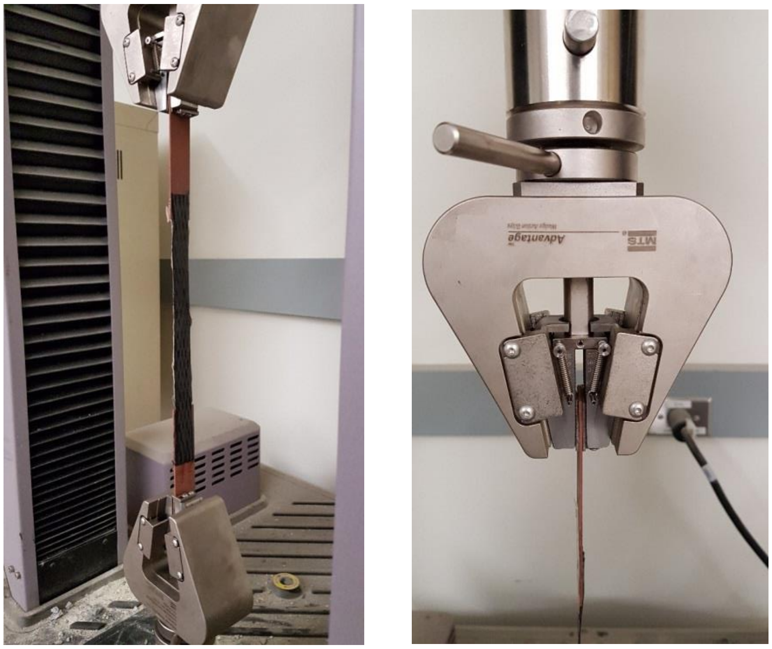

Figure 4-8 Performing tension test in MTS machine.

It should be noted that specimen Coated-20-1 was found to be defective due to fabrication quality. The reason that 20mm bond length was chosen as comparison basis is that due to shorter bond length peeling stresses at edge of CFRP are less severe and stress distribution along the bond is more uniform. In addition, it was found in prior FEM simulations that steel sheets will go into large yielding phase for bond lengths larger than 20mm.

Comparison between coated samples and uncoated samples for 20mm bond length shows that bond strength is reduced by about 50 percent duet application of coating. This reduction was expected due to earlier observations in saturant resin-geopolymer coating pull off strength results. Differences seen in displacement at failure for uncoated specimens could be the resulted minor manufacturing errors in sizing of CFRP carbon fabrics or bond overlap adjustments. In addition, excess of resin that may amalgamate at edges of the steel sheet could contribute to additional displacement before failure. Finally, variation in sand blasting extent on steel sheet could have very minor effect on failure displacement due to decrease of steel sheet thickness. This could result in yielding of steel at an earlier stage and contribute to more displacement before bond failure.

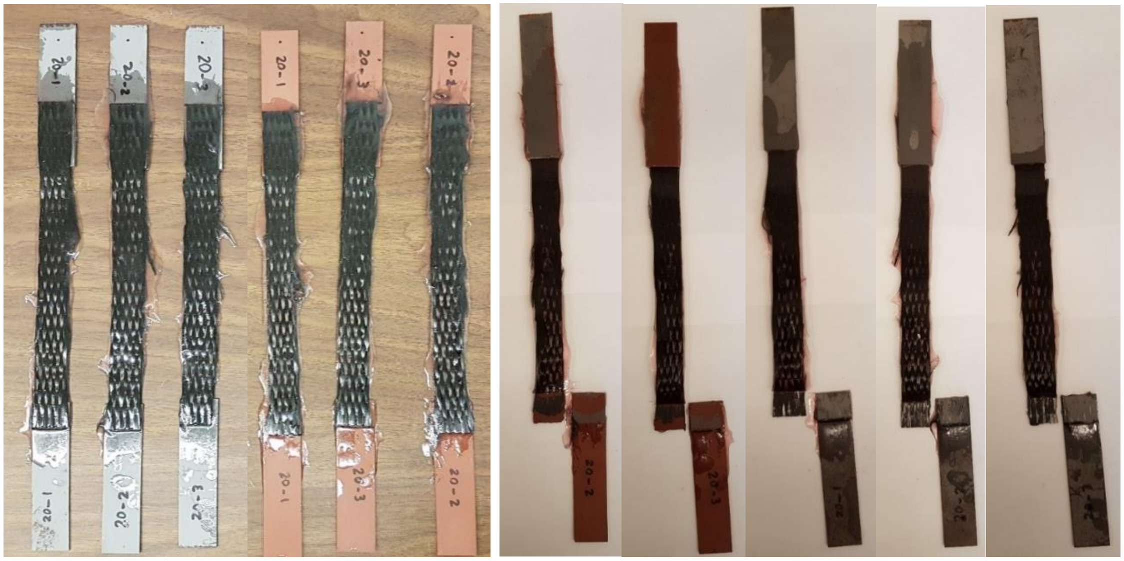

Figure 4-9 Modified Lap-Shear specimens before tension test (left), Specimens after Failure from left to right: Coated-20-2, Coated-20-3, Uncoated-20-1, Uncoated-20-2, Uncoated-20-3.

Observing Figure 4-10, it can be seen that there is a difference at the displacement point where 20mm bond length specimens start to change (about 1.1mm) the stiffness slope and the 40mm bond length specimens start to change (about 0.6mm) the stiffness slope. This difference is believed to be as result of plastic deformation (Liljedahl et al. 2006) due to adhesive interface behavior which is more engaged in the longer bond lengths.

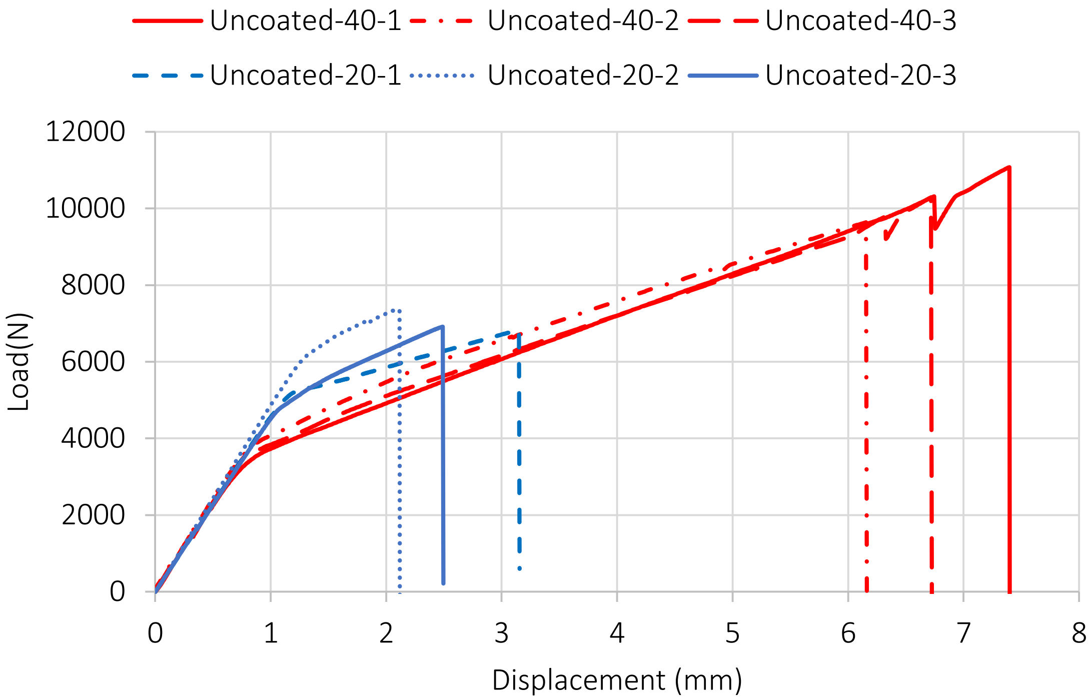

Figure 4-10 Comparison of uncoated experimental results with 20mm and 40mm bond lengths.

4.3 Finite Element Analysis

4.3.1 Model Geometry

Commercial software ABAQUS version 6.14 was used to model the modified lap shear joint specimens used in the lab tests. Steel sheets of 0.06” (1.524mm) were used as the metal substrate. The thickness of Carbon Fiber Reinforced Polymer (CFRP) laminate was measured with a caliper with an average of 0.055” (1.4mm) and length of 10.2” (260mm). The length of the steel sheets was chosen to be 4.5” (115mm). Specimen discussed here was primarily used to calibrate damage properties of the model. Surface-based cohesive behavior was implemented for bond behavior simulations.

In the primary stage material properties of steel were assumed to be linear elastic with Young’s modulus of 198GPa and Poisson’s ratio of 0.29. CFRP tensile modulus was adopted from manufacturer (DowAksa) to be 16.2Msi (111.7GPa) for medium weight carbon fabric (CFU20T).

Model is set up to have an overlap of 55mm at one end and 20mm at the other end, same as the actual specimen. Both steel and CFRP laminates were modeled as isotropic. This is an appropriate assumption as CFRP works only in tension along the fiber direction both in the lab test and in the model. A displacement control loading was applied with the rate of 0.05in/min (1.27mm/min) which is adopted from ASTM D1002. The model was evaluated at different mesh sizes (1-3mm). 2mm global mesh size was used as it has very close results to 1mm global mesh while saves considerable run time.

4.3.2 Cohesive Zone Model

To capture interfacial behavior and properties at the substrate-CFRP interface interaction module was used to define a surface based cohesive behavior between epoxy resin and substrate. This method is desirable in such cases were we have thin layer of interface (negligible thickness). The method follows traction separation laws to define constitutive behavior and damage initiation. Failure of cohesive bond is characterized by progressive degradation of cohesive stiffness driven by damage process. Failure mechanism comprises of two sections: damage initiation and damage evolution. In surface based cohesive behavior only one damage initiation and one damage evolution can be defined. Figure below shows a typical traction separation behavior.

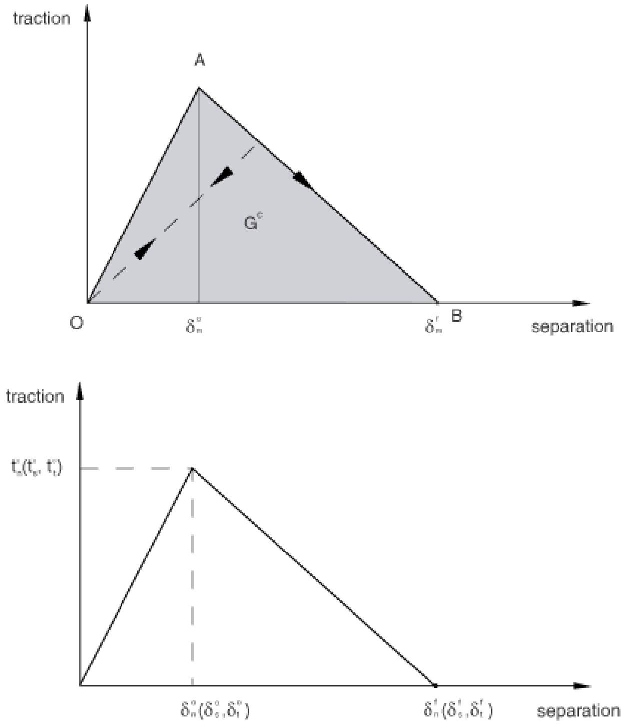
traction
A
G^c
O
δ_m^o
δ_m^f
B
separation
traction
t_n^o(t_s^o, t_t^o)
δ_n^o(δ_s^o,δ_t^o)
δ_n^f(δ_s^f,δ_t^f)
separation

Figure 4-11 Traction-Separation Behavior (After Dassault Systémes, 2015).

4.3.2.1 Damage Initiation

It refers to the initiation of bond degradation. For this model the Maximum Stress Criterion was used:

$$max\left\{\frac{\langle t_n\rangle}{t_n^o},\frac{t}{t_s^o},\frac{t_t}{t_t^o}\right\}=1 \qquad (4.1)$$

Where n, s, and t indices represent normal shear in first direction and shear in the second direction respectively. And *t* denotes contact stress while *t*° denotes peak values of contact stress.

4.3.2.2 Damage Evolution

Damage evolution can be defined as the energy dissipated as a result of damage process. In the FE simulation model Benzeggagh-Kenane (BK) form of damage evolution was used (Benzeggagh et al. 1996):

$$G_n^C + (G_S^C - G_n^C)\left\{\frac{G_S}{G_T}\right\}^{\eta} = G^c \qquad (4.2)$$

Where, $G_S = G_s + G_t$, $G_T = G_n + G_S$, and η is cohesive property parameter. The evolution was assumed to have linear degradation:

$$D = \frac{\delta_m^f(\delta_m^{max} - \delta_m^o)}{\delta_m^{max}(\delta_m^f - \delta_m^o)} \qquad (4.3)$$

Where, D is Damage variable. δ_m^o is separation at initiation of damage and $_{m}^{f}$ is separation at complete failure. G^c is the dissipated energy during the failure process Figure 4-12 shows the failure criteria of BK criterion in three dimenssions.

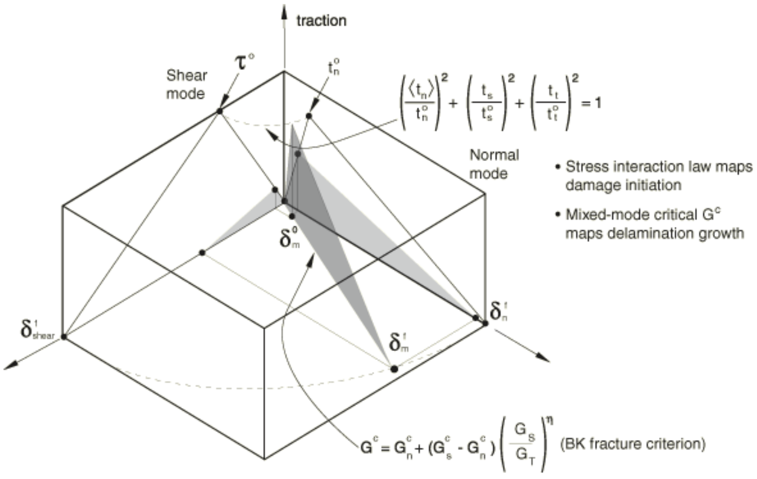
traction
Shear mode
τ^o
t_n^o
$\left(\frac{\langle t_n \rangle}{t_n^o}\right)^2 + \left(\frac{t_s}{t_s^o}\right)^2 + \left(\frac{t_t}{t_t^o}\right)^2 = 1$
Normal mode
• Stress interaction law maps damage initiation
• Mixed-mode critical G^c maps delamination growth
δ_m^o
δ_{shear}^f
δ_n^f
δ_m^f
$G^c = G_n^c + (G_s^c - G_n^c)\left(\frac{G_S}{G_T}\right)^{\eta}$ (BK fracture criterion)

Figure 4-12 BK Failure Criterion (After Dassault Systémes, 2015).

It should be noted that fracture energy is expressed by KJ.m^{-2} or J.m^{-2} units depending on selected system of units in the modeling.

4.3.3 Comparison between 2D and 3D Models

Multiple 2-Dimenssional FEM simulations of midfield Lap-Shear test was performed for different bonding lengths to establish guidelines for conducting lab tests. Initially the 2D simulations were performed with only elastic properties for steel. Validity of 2D results were verified by comparing a 2D vs 3D case results shown in Figure 4-13.

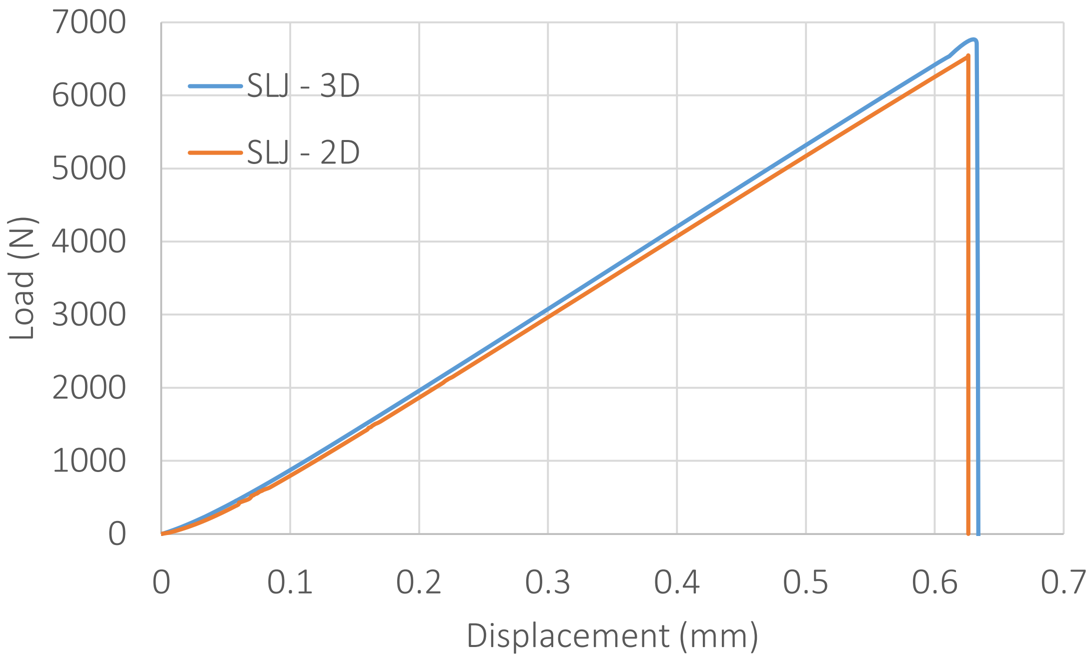

Figure 4-13 Comparison of 2D vs 3D simulation for a modified Lap-Shear test for uncoated steel sheet with 20mm Bond length.

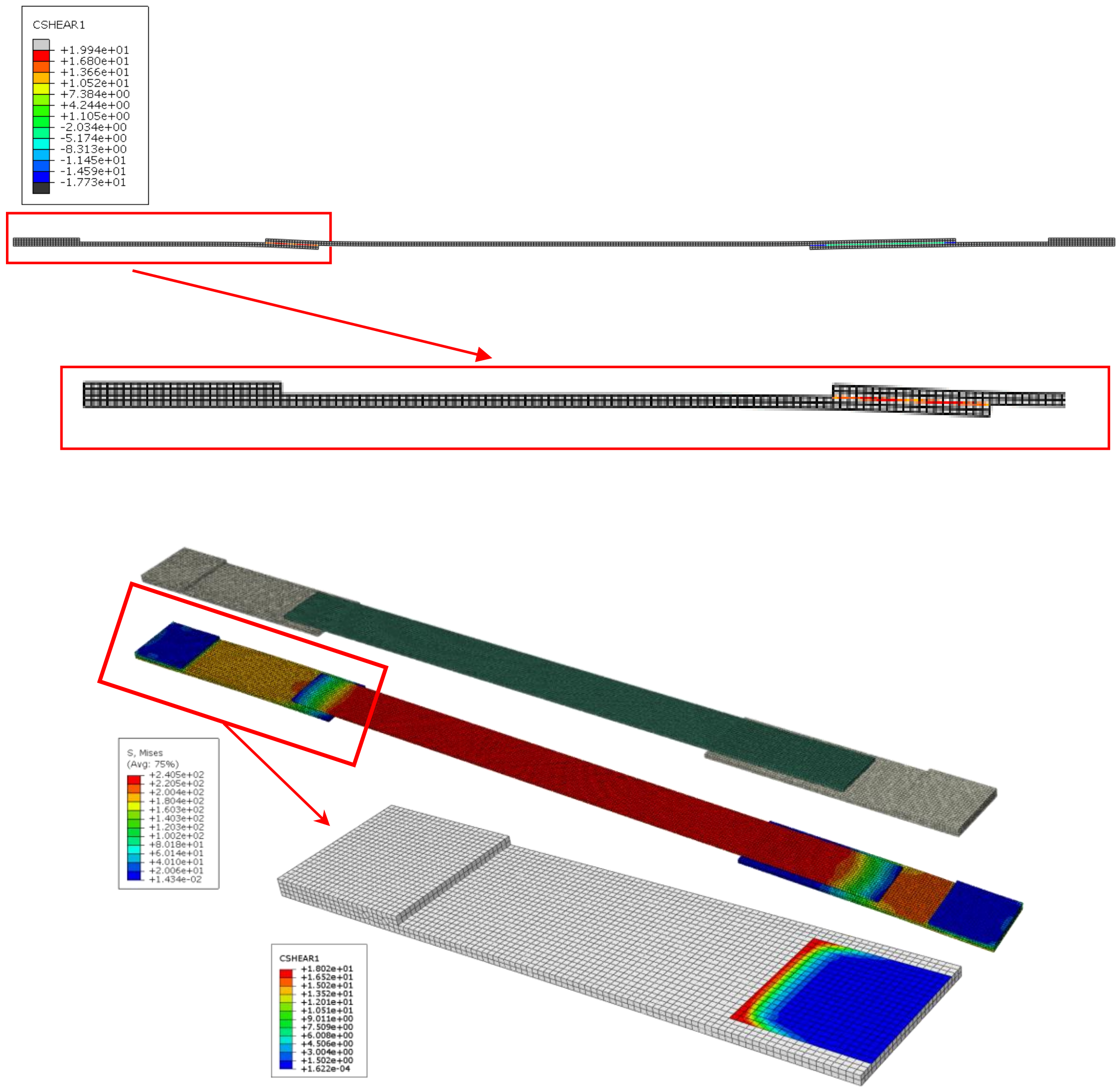
CSHEAR1
+1.994e+01
+1.680e+01
+1.366e+01
+1.052e+01
+7.384e+00
+4.244e+00
+1.105e+00
-2.034e+00
-5.174e+00
-8.313e+00
-1.145e+01
-1.459e+01
-1.773e+01
S, Mises
(Avg: 75%)
+2.405e+02
+2.205e+02
+2.004e+02
+1.804e+02
+1.603e+02
+1.403e+02
+1.203e+02
+1.002e+02
+8.018e+01
+6.014e+01
+4.010e+01
+2.006e+01
+1.434e-02
CSHEAR1
+1.802e+01
+1.652e+01
+1.502e+01
+1.352e+01
+1.201e+01
+1.051e+01
+9.011e+00
+7.509e+00
+6.008e+00
+4.506e+00
+3.004e+00
+1.502e+00
+1.622e-04

Figure 4-14 2D FE Model. Interface shear stress distribution at the onset of damage (Top Section). 3D FEM simulation. Mesh (top), Mises Stress (Middle), Interface stress distribution at the onset of damage (Bottom).

Figure 4-14 shows the FE model in 2D and 3D. Interface shear distribution is shown. As it can be seen, maximum shear stress develops at far edge and moves toward the close edge before complete delamination occurs. It can be seen that using 2D analysis for sensitivity of bond behavior with bond length is justified as the results of 2D and 3D simulations are very close. In addition, observed ultimate load (about 6800N) is in very good accordance with results from the lab test.

4.3.4 Effect of Bonding Length

Figure 4-15 shows Load-Displacement curves from simulation results for different bond lengths assuming elastic behavior for steel sheet. Properties of steel used in the mode are shown in Table 4-5. This helps to investigate different scenarios in 2D models which are considerably faster to run and establish basis to make more comprehensive 3D models to study local behavior in more detail. The results of 2D simulation with elastic property assumption are shown in Figure 4-15.

Table 4-5 Steel Properties used in the FE model.

Young Modulus (GPa)	Poisson Ratio, ν	Yield Stress (MPa)	Ultimate Strength (MPa)
205.7	0.2856	262	358

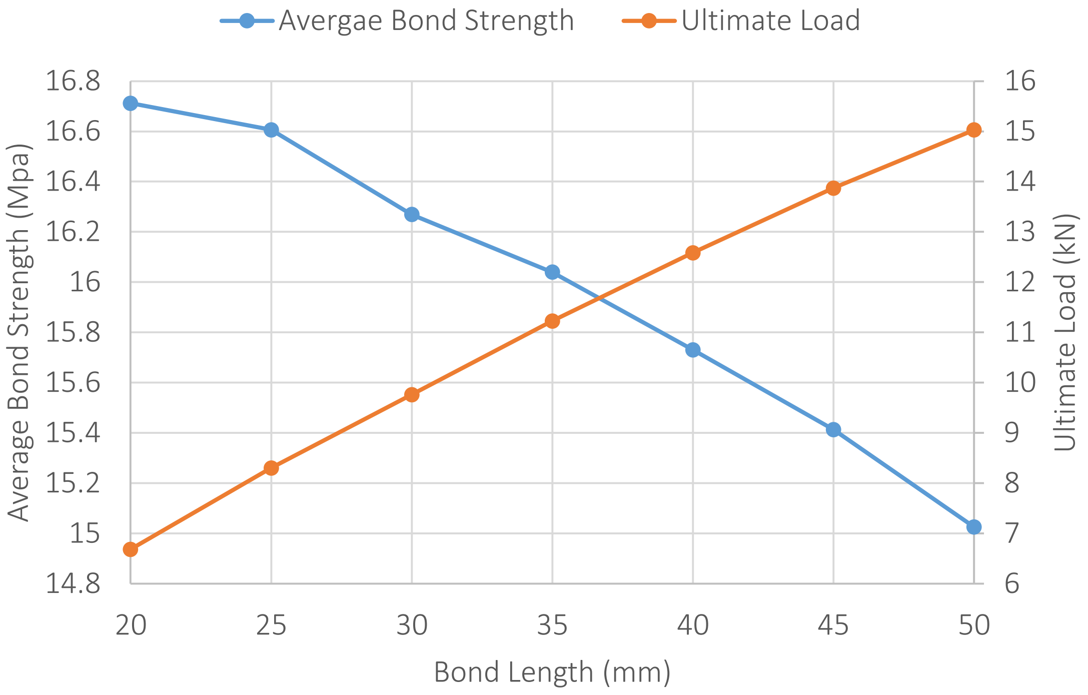

Figure 4-15 Bond Strength and Ultimate Load predictions using elastic 2D simulation.

4.3.5 Yielding Effect of Steel

Another set of 2D simulations were performed considering plastic behavior for steel sheets in the modified Lap-Shear specimens. A tension test was performed on a steel coupon to calculate steel plastic parameters in the simulation. Figure 4-16 shows the yielded steel model that was tested for tensile failure. The sample was 10” ×1”× 0.06”; same width and thickness as lap shear steel sheets but longer length. The plastic data acquired was then used to model the plastic failure in ABAQUS which is shown with yellow curve in Figure 4-17. It is clear the FE model follows the steel behavior very accurately up to 0.15 strain.

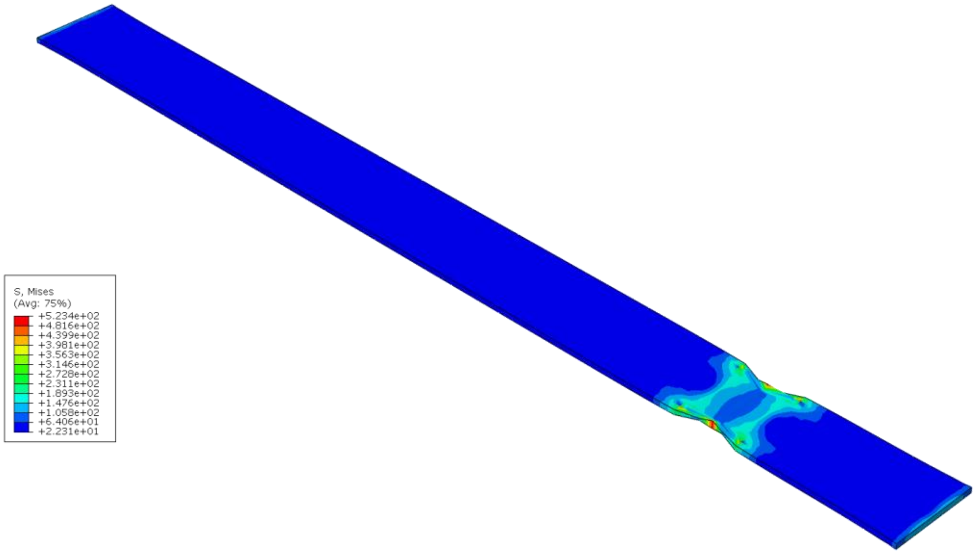
S, Mises
(Avg: 75%)
+5.234e+02
+4.816e+02
+4.399e+02
+3.981e+02
+3.563e+02
+3.146e+02
+2.728e+02
+2.311e+02
+1.893e+02
+1.476e+02
+1.058e+02
+6.406e+01
+2.231e+01

Figure 4-16 Yield occurred in the steel coupon tension simulation.

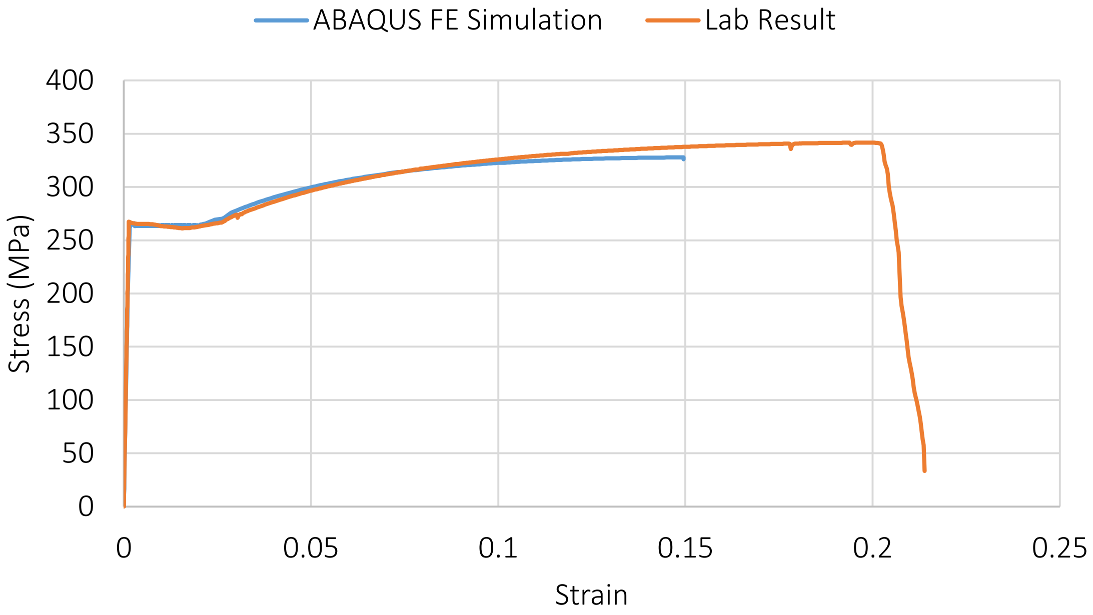

Figure 4-17 Comparison of ABQUS simulation for steel coupon tension test and Lab test.

Plastic parameters of the steel was used to run new series of different bond lengths of lap shear model with same bond lengths as elastic lap shear model. It was observed that even for the 20mm bond length steel reaches yield in very small areas before delamination occurs. Figure 4-19 shows the strain softening phase for bond lengths larger than 25mm. This behavior shows that the bond holds well after 25mm bond length and it is the steel which becomes the culprit for the failure in the joint.

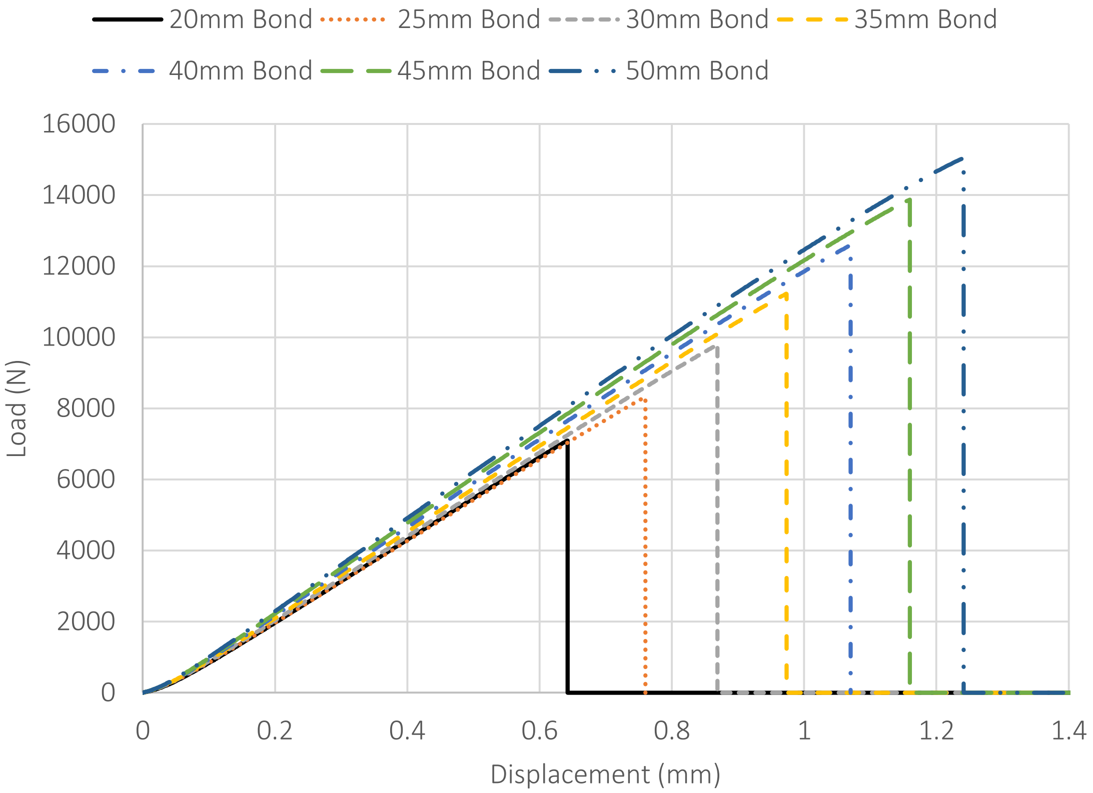

Figure 4-18 2D FE model results with elastic behavior assumption for steel.

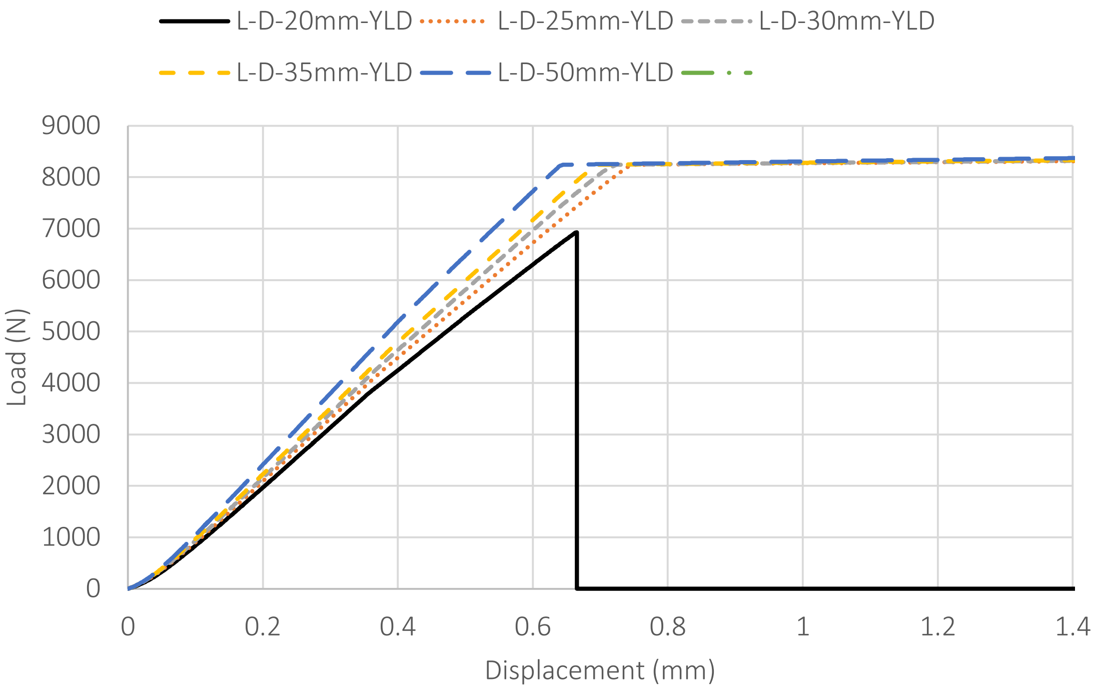

Figure 4-19 2D simulation of modified Lap-Shear test with plastic behavior for steel sheet.

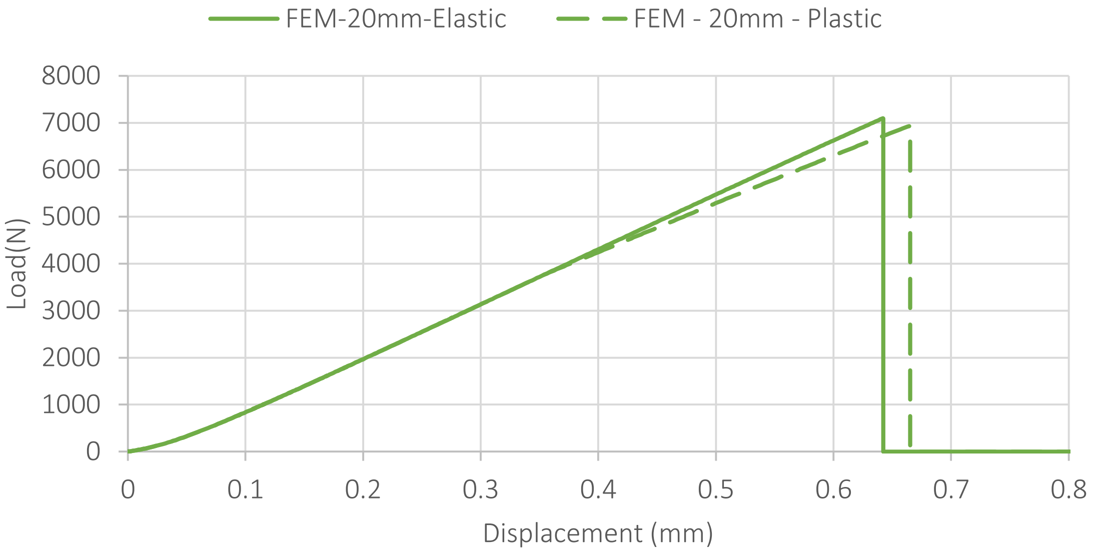

Figure 4-20 Elastic behavior versus Elastic-Plastic behavior for 20mm bond length Lap-Shear specimen simulation.

4.3.6 Comparison between Measurement and Modeling

Figure 4-23 shows that ultimate load after yielding occurs, is very close to the ultimate load for the 20mm bond length for elastic behavior. This suggests that assuming an elastic behavior for steel may give a good estimate for model to predict ultimate load bearing capacity. But this assumption would undermine realistic displacement behavior and energy dissipation of the repaired system. This especially would be of concern if plastic design is intended.

Previous plastic model verified that bond lengths studied beyond 20mm will cause the steel adherent to go into yielding phase. Assuming yielding of steel is not allowed, mentioned simulations suffice to verify adequate bonding. But they are not good enough to capture bond failure while adherent goes under plastic deformation. To observe effect of plastic deformation in steel adherent on bond failure, a full plastic behavior for steel was assumed in further simulations. These simulations can predict maximum load before bond failure between CFRP and steel. For the case of 40mm bond length, which lab tests are available, the simulation result demonstrated in Figure 4-21 shows good agreement between predicted maximum load and the average of maximum loads observed during the lab tests.

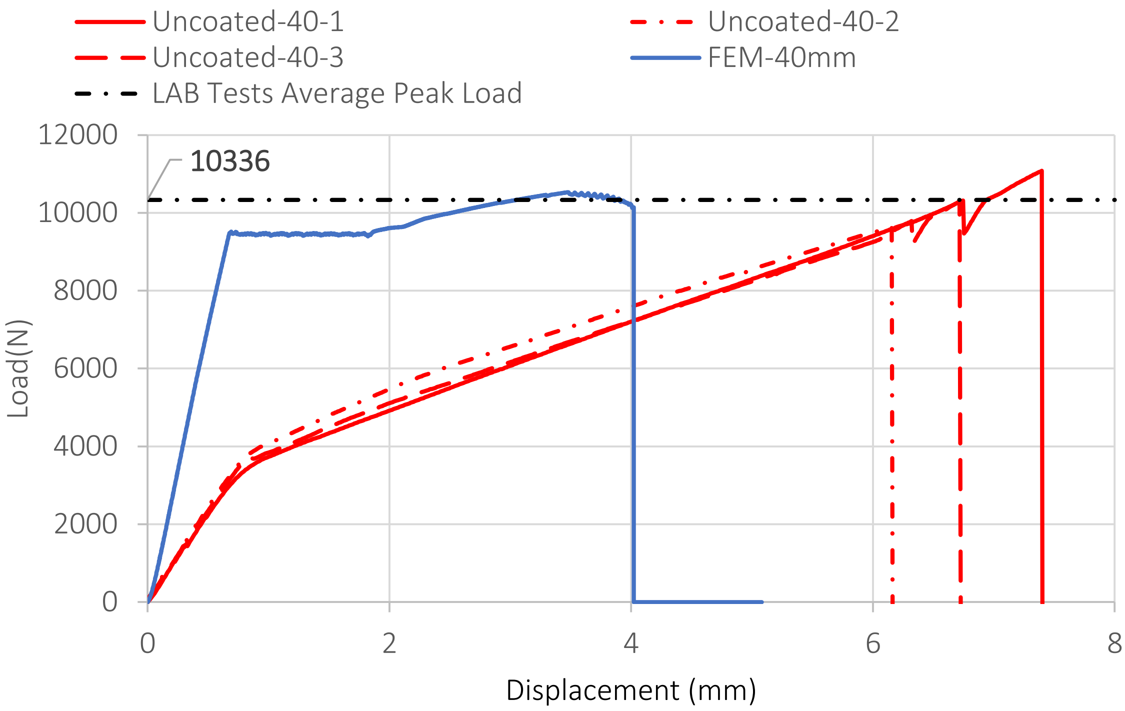

Figure 4-21 Comparison of FE simulation with Lab results for 40mm bond length.

Full range plastic simulation was performed for all bonding lengths. Investigating the results in Figure 4-22 shows that all bond lengths show the same behavior as in Figure 4-19. The longer the bond length the steeper the initial linear behavior which shows higher stiffness in the bond. All bond lengths except 20mm after yielding of steel will continue to yield up to 1.6 mm displacement point. Starting this point, failure behavior differences emerges. As with stiffness differences at the beginning of the curves, the maximum loads are very close but not the same.

The big difference between full range plastic behavior simulation results and the one shown in Figure 4-19 is that the failure of bond does not occur at the maximum load, but instead it happens during strain softening of steel adherent. This is very important as ductility of the adherent after the yield will regulate the failure.

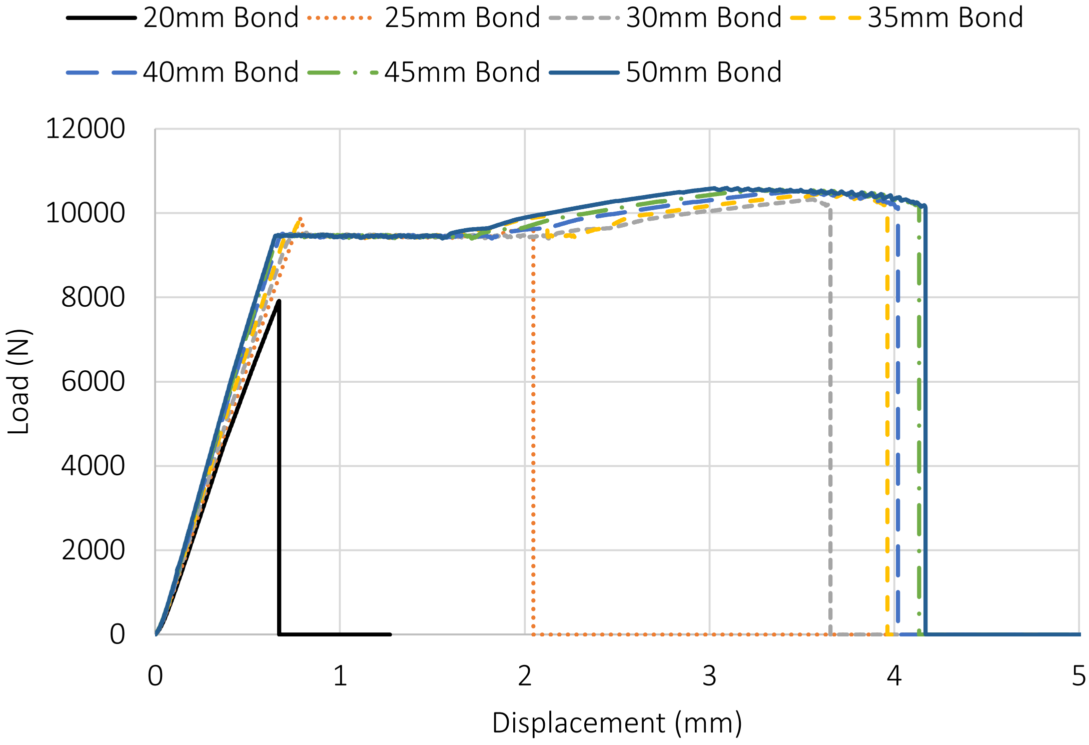

Figure 4-22 2D simulation of modified Lap-Shear test with full range plastic behavior for steel sheet.

Looking at Figure 4-22 it is clear that there is big jump at the failure displacement from 20mm to 25mm bond length, and 25mm to 30 mm bond length. In each case the displacement is almost doubled while the maximum bond capacity has increased only 20% and 10%, respectively. This shows that energy dissipated by increasing bond length has grown significantly without much change in the failure load. This is an important concept to help prevent sudden failure and provide buffer time before failure by choosing a higher bond length.

On the other hand, after 30mm bond length all other bond lengths (35mm, 40mm, 45mm, and 50mm) fail at a close load magnitude. In addition, they show close vicinity of failure displacement. This shows that bond lengths larger than 35mm will not improve neither maximum load bearing capacity of the bond, nor contribute to energy dissipation factor of the bond.

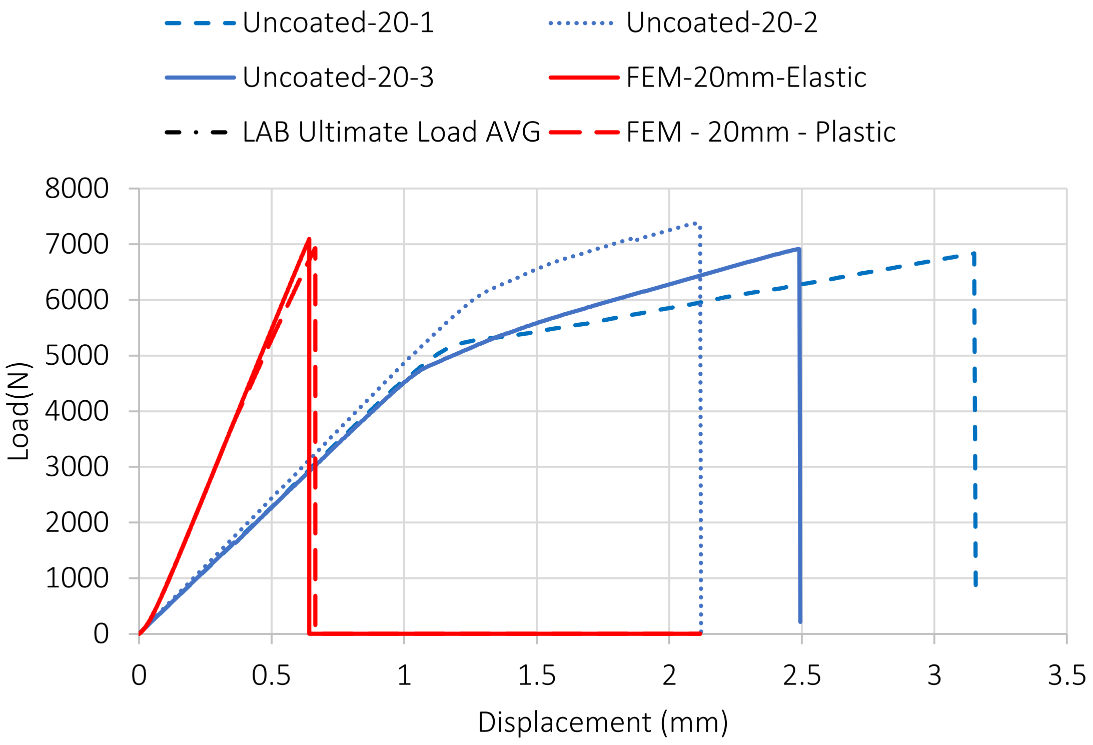

Figure 4-23 Comparison of uncoated steel lap shear test results for 20mm bond length between FE simulation and lab test.

Additionally looking at the Figure 4-23, a large discrepancy is observed between displacement in the simulation cases and experimental cases. This is believed to be due to actual properties of the specimen components and reported properties, and more importantly possible redundant displacements within customized MTS components after loads of higher than 5000N. This issue is under investigation to be addressed appropriately. This is expected to be achieved by implementing strain gauges to more accurately capture strain and displacement behavior along the bond length.

4.3.7 Bond Stress Distribution

Stress distribution along the bond length is an important parameter for defining maximum nominal stress while defining damage initiation in the FE model. The distribution is derived by calibrating fracture energies for mode I and Mode II failures, and maximum nominal stress for cohesive behavior failure.

Simulations with full range plastic behavior where used to demonstrate the stress distribution along the bond for all bond lengths. The stresses shown in Figure 4-24 to Figure 4-30 are interfacial stress between CFRP and steel. The values are shown at the onset of damage initiation. Stress distributions are relatively symmetric from bond length mid-point. This corresponds with common results observed in analytical methods of stress distribution derivation for single lap joints. Furthermore, slip along interface for all bond length are also shown. As discussed in section 4.3.2.1 bond-slip models are used to determine damage initiations in cohesive zone model.

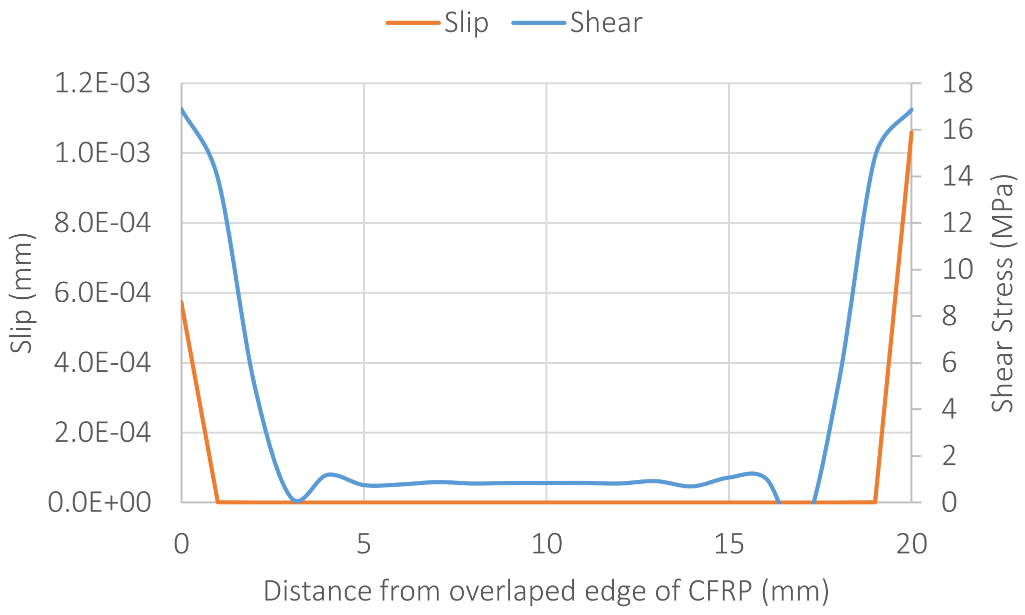

Figure 4-24 Shear and slip variations along 20mm bond length.

Observing Figure 4-24 to Figure 4-30, the maximum stress at the edges of bond do not change but the maximum slip from 20mm bond length to 50mm bond length doubles. This could mean that deboning rate is increased with bond length. In other words, damage evolves faster after initiation.

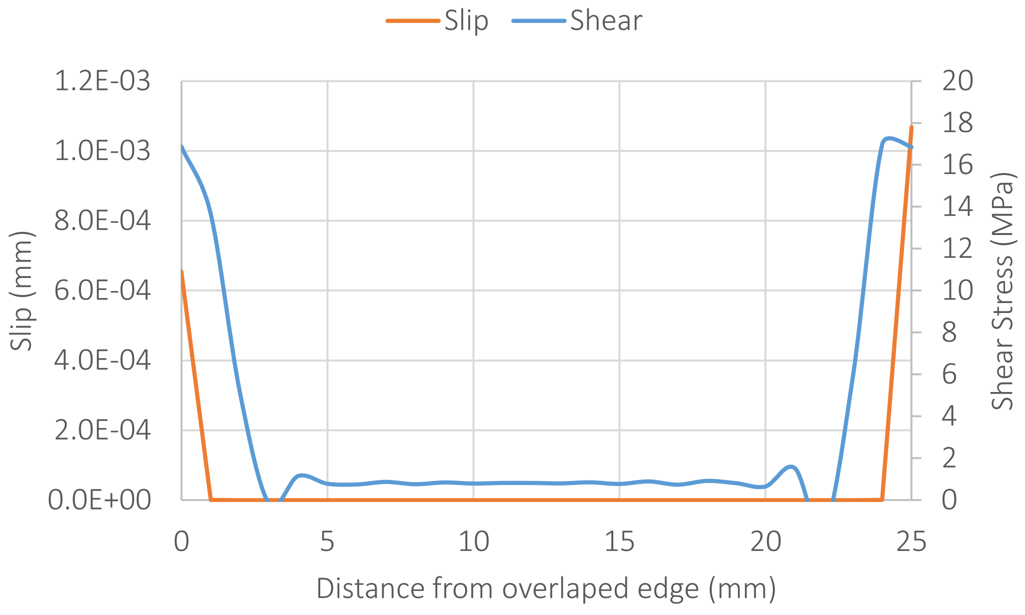

Figure 4-25 Shear and slip variations along 25mm bon length.

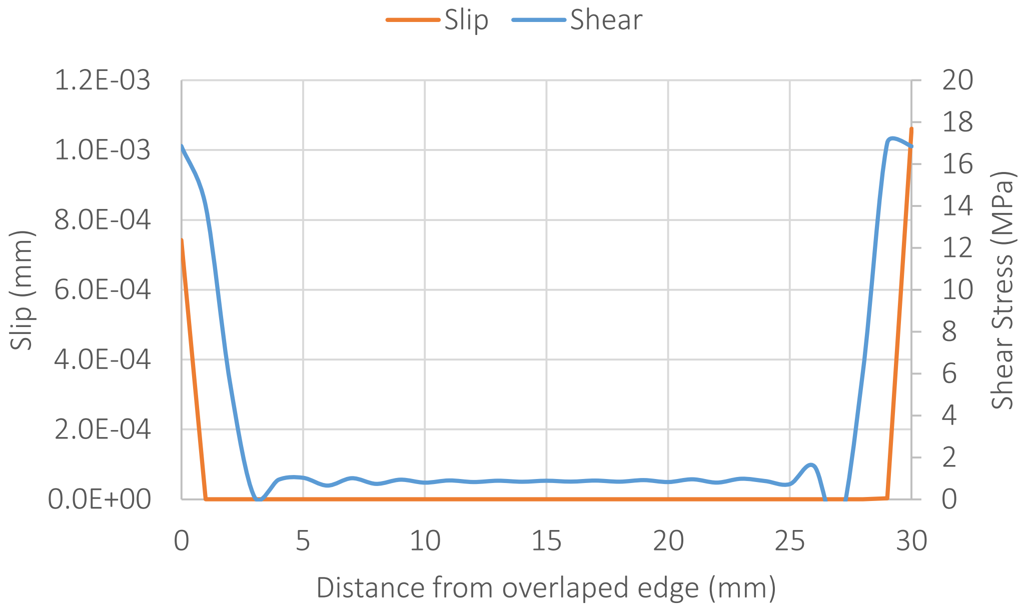

Figure 4-26 Shear and slip variations along 30mm bond length.

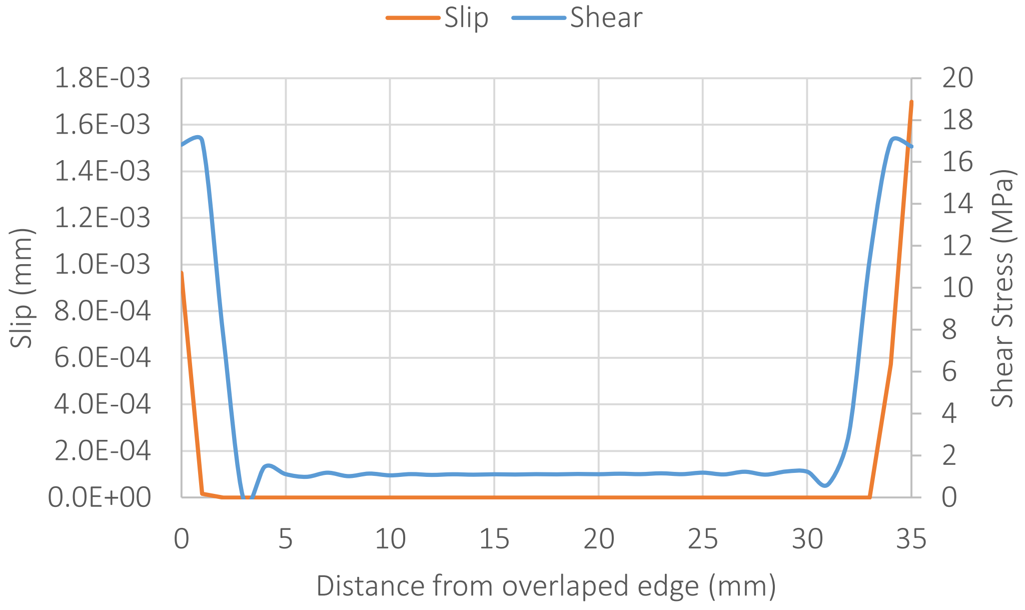

Figure 4-27 Shear and slip variations along 35mm bond length.

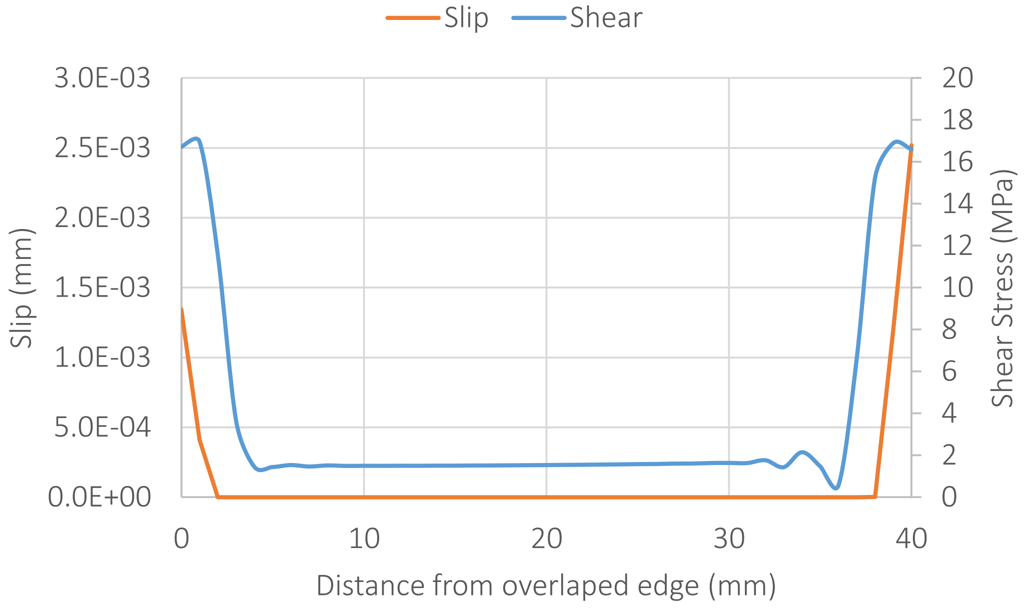

Figure 4-28 Shear and slip variations along 40mm bond length.

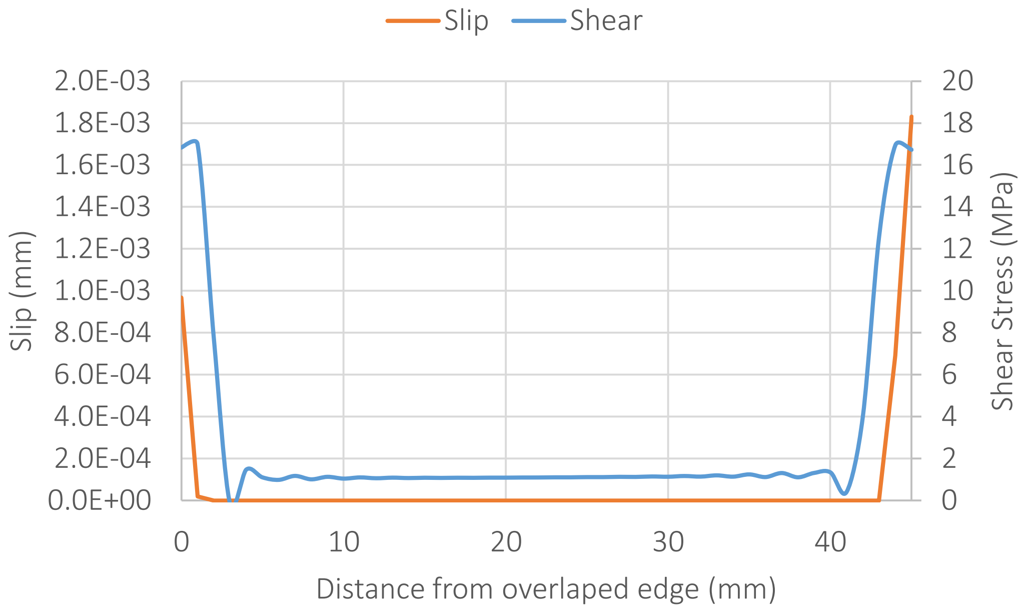

Figure 4-29 Shear and slip variations along 45mm bond length.

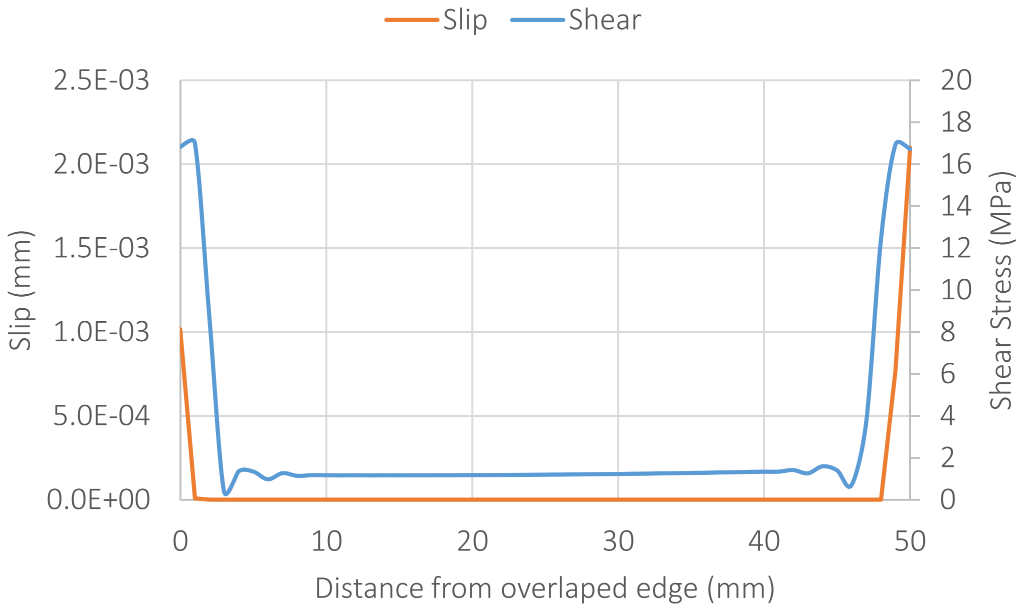

Figure 4-30 Shear and slip variations along 50mm bond length.

Strain in the adherent at bond length is one other parameter that is of interest for design purpose. Figure 4-31 shows the strain in the CFRP along the bond length at the onset of bond damage. It is clear that maximum strain occurs at the loaded end and it has minimum strain on the opposite edge. The 45-mm bond length has most critical strain at the loaded edge among all bond lengths.

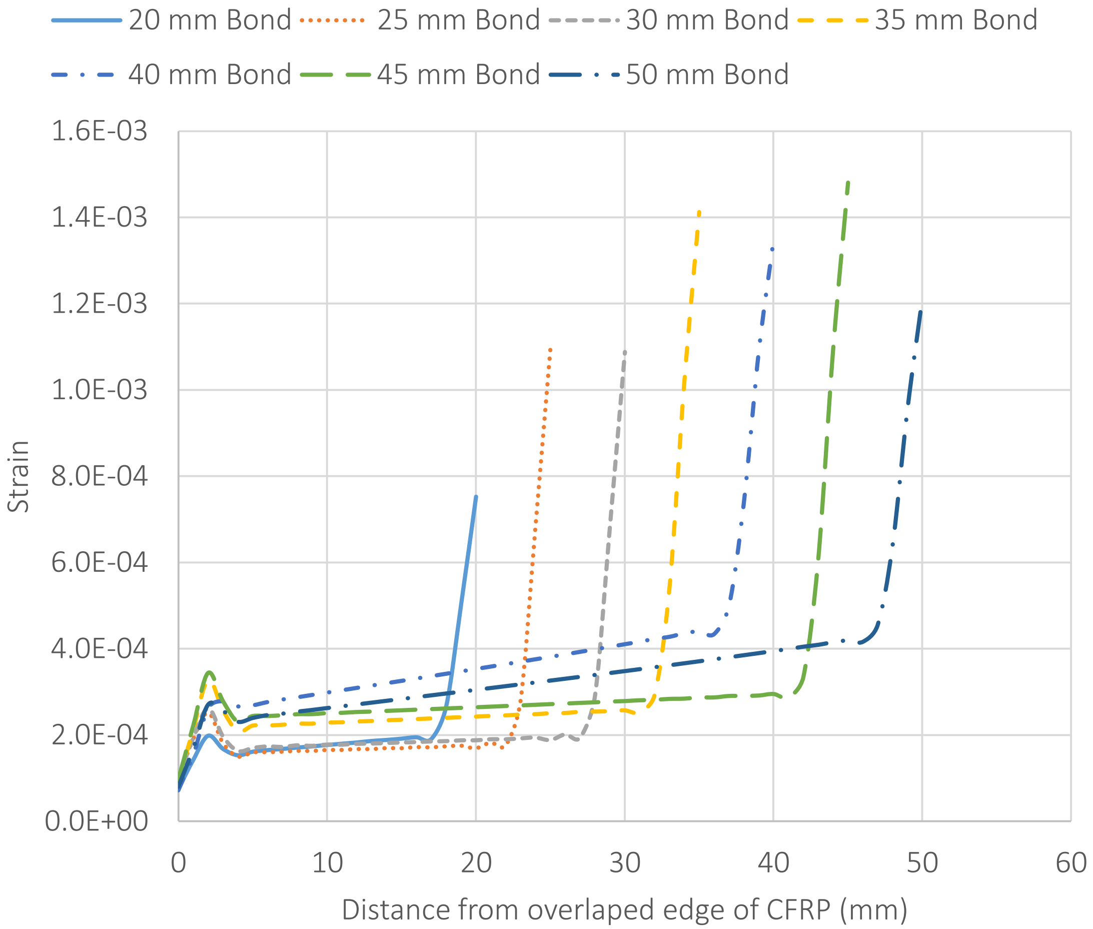

Figure 4-31 Simulation results for strain along bond lengths for modified single lap shear specimens.

5 Effect of Nano-additives on Lap-shear and steel coupon specimens

5.1 Lap-shear specimens

Application of various Nano-additives as corrosion inhibitor agents was investigated in chapter 3. Similar variations of mixture treatment with different Nano-additives in powder form such as Silicate (SiO_2), Titanium oxide (TiO_2), and in water-based form such as Graphene oxide, with various concentrations were evaluated for corrosion performance. In addition, these additives' effect on CFRP-Coated steel interface will be investigated. Interfacial mechanical property variations and bond behavior due to Nano-additive concentration were examined.

5.1.1 Specimen Preparation

Medium weight unidirectional carbon fabric pieces were cut into 250mmX20mm pieces. Some "wide" samples were also tested with 250mmX20mm dimensions. Two steel sheets used to prepare samples were 4.5in by 1in by 0.06 in. Each of the steel sheets at two ends of the specimens were sand blasted prior to fabrication of specimen. Sand blasted steel sheet at one end of the specimen was coated with geopolymer.

One of the concerns regarding preparation geopolymere mix was the source of water and their possible affect in the final performance of the cured coating. We experimented use of sparing water in comoarison to regular tap water in the base mix of geopolymer (without any nano additives). Two samples were prepared using spring water as water component and two other samples were prepared using tap water. We performed lap shear tests on cured specimens and results are shown in Figure 5-2. The results appear to favor use of spring water over tap water as on the average.

Various Nano-modified geopolymer mixes were tested. All the Nano-modified samples were prepared with spring water. The bond length on the coated steel sheet end was selected to be 30mm. The bond length at the opposite end on uncoated steel sheet was selected to be 50mm.

DowAksa Carbon300H resin was used to impregnate the carbon fabric pieces for specimen fabrication. The Specimens were cured for 10 days in room temperature and in the oven at 60°C. Figure 5-1 shows the specimens.

5.1.2 Testing and results

A total of 22 specimens were tested. The tension test on specimens were conducted using an MTS machine with 0.05in/min displacement control loading following the procedure discussed in 4.2.2. Figure 5-3 shows few samples after failure.

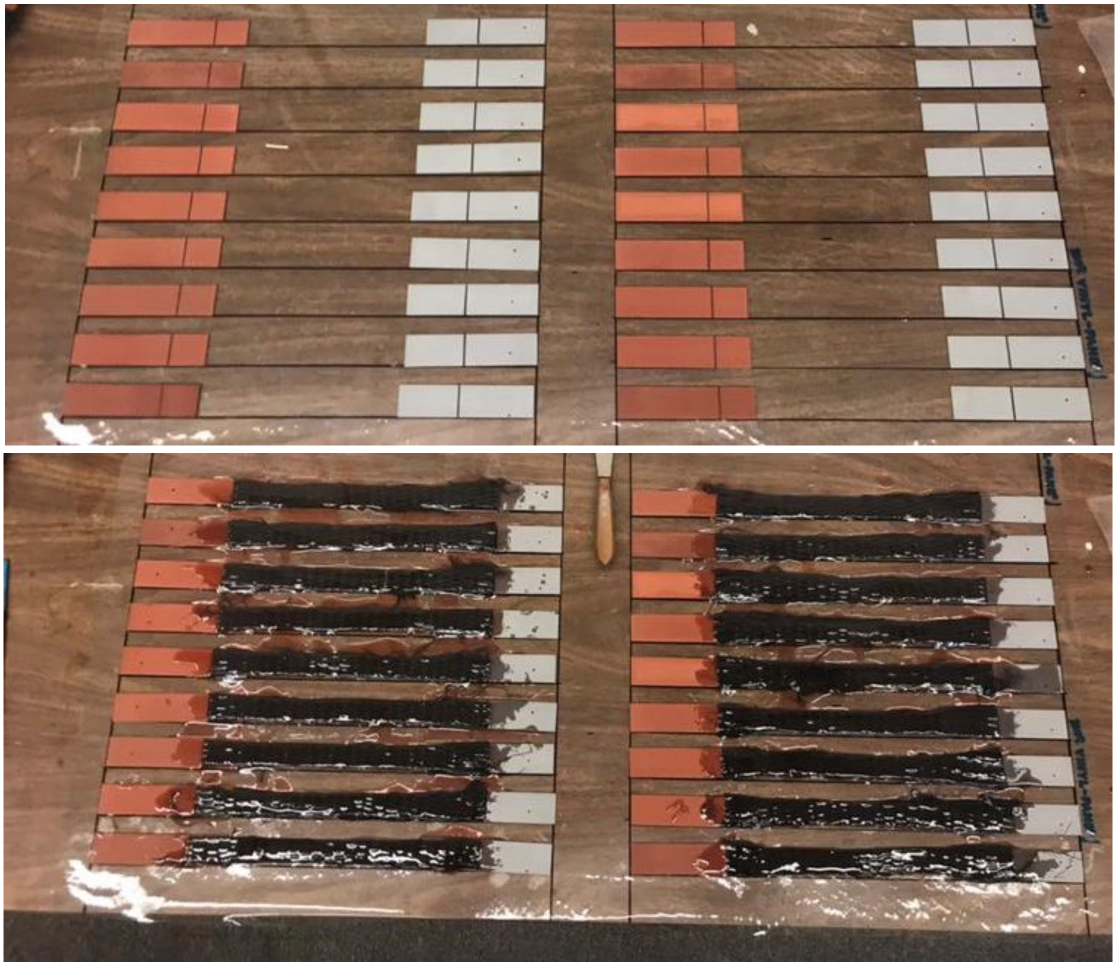

Figure 5-1 Specimen fabrication. Alignment and mark ups pf specimens where black lines show the extend of overlap on both ends of the specimen (top), laying CFRP in place (bottom).

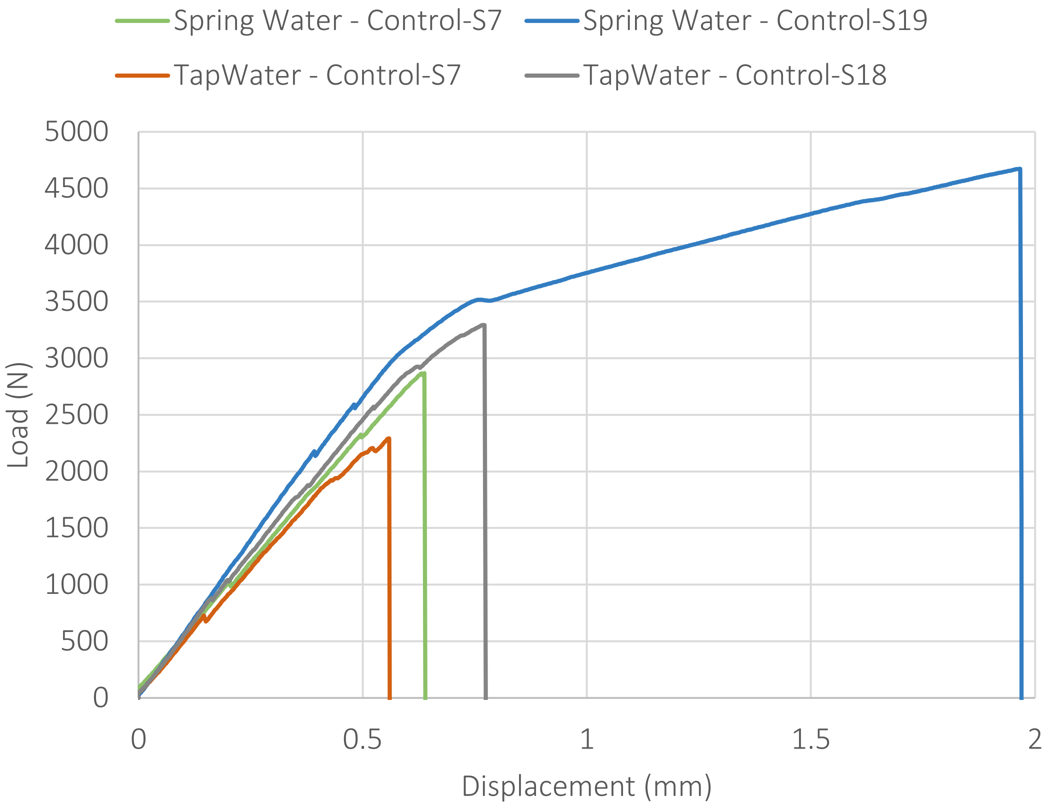

Figure 5-2 Water source effect on strength performance of geopolymer.

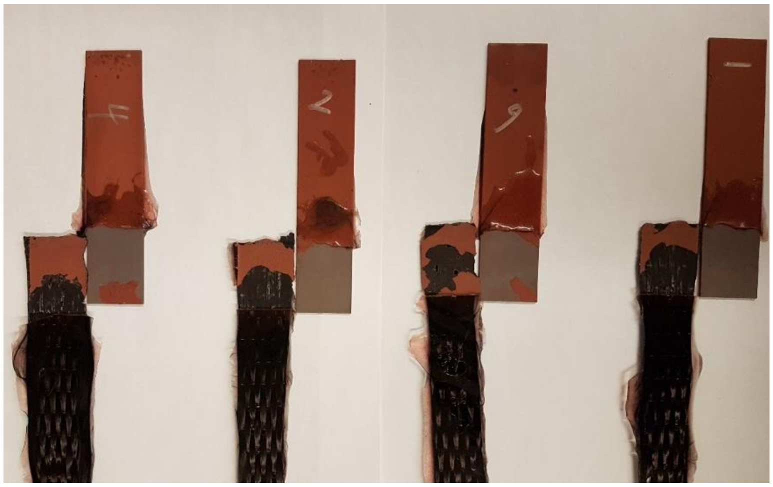

Figure 5-3 Bond failure at the end with coated steel sheet of the lap shear specimens.

Observing failure patterns as shown Figure 5-3, we can see almost all failures occurred at the steel sheet interface which indicates good adhesion of resin with geopolymer.

All lap-shear test results are summarized in Table 5-1.The SiO2 powder modified geopolymer in general performed the best in terms of bond strength. The second best performance observed was by TiO_2 powder samples.

Table 5-1 Summary of test results on all lap-shear specimens.

<table>
<tr><th rowspan="3">Nano-material</th><th colspan="5">Average Bond Strength (MPa)</th></tr>
<tr><th rowspan="2">Sample ID</th><th colspan="4">Nano-material Concentration (%)</th></tr>
<tr><th>1</th><th colspan="2">3</th><th>5</th></tr>
<tr><td rowspan="3">**Graphene Oxide**</td><td>**S1**</td><td>5</td><td colspan="2">5.5</td><td>5.5</td></tr>
<tr><td>**S2**</td><td>6.6</td><td colspan="2">6.5</td><td>5.8</td></tr>
<tr><td>**Average**</td><td>5.8</td><td colspan="2">6</td><td>5.65</td></tr>
<tr><td rowspan="4">**SiO2**</td><td>**S1**</td><td>8.7</td><td colspan="2">8.4</td><td>9.4</td></tr>
<tr><td>**S2**</td><td>5.8</td><td colspan="2">-</td><td>**11.7**</td></tr>
<tr><td>**S3**</td><td>7</td><td colspan="2">-</td><td>-</td></tr>
<tr><td>**Average**</td><td>7.17</td><td colspan="2">8.40</td><td>10.55</td></tr>
<tr><td rowspan="3">**TiO2**</td><td>**S1**</td><td>**3.7**</td><td colspan="2">6.4</td><td>7.7</td></tr>
<tr><td>**S2**</td><td>4.4</td><td colspan="2">6.5</td><td>5.6</td></tr>
<tr><td>**Average**</td><td>4.05</td><td colspan="2">6.45</td><td>6.65</td></tr>
<tr><td rowspan="4">**Control**</td><td></td><td colspan="2">**Spring Water**</td><td colspan="2">**Tap Water**</td></tr>
<tr><td>**S1**</td><td colspan="2">4.8</td><td colspan="2">3.8</td></tr>
<tr><td>**S2**</td><td colspan="2">7.8</td><td colspan="2">5.5</td></tr>
<tr><td>**Average**</td><td colspan="2">6.3</td><td colspan="2">4.65</td></tr>
</table>

Minimum average bond strength of 3.7MPa was observed in Nano-modified samples. Maximum average bond strength of 11.7MPa was observed in Nano-modified samples (5% Sio2 Powder). Among control samples minimum bond strength of 3.8 MPa for Tap water and maximum bond strength of 7.8MPa for spring water was observed. Table shows the average bond strength for all the tested samples. Highest and lowest values are shown in bold.

Furthermore, it was observed that the average bond strength was increased with increase of the percentage of the Nano-additive. As shown in Table 5-1 the bond strength variations for three group of Nano-additives used in the test. The only nano-additive that showed slight loss of average bond strength by increasing additive percentage was graphene oxide as it is shown in Figure 5-4. The observation for performance of Nano-additives in bond strength have general accordance with performance of same additives in previous accelerated corrosion test results. SiO2 powder modified samples in general had the best performance in corrosion protection of steel plates. The load-displacement results for all lap-shear tests are shown in Figure 5-5. The chart shows that majority of SiO2 modified specimens have at least 25% higher load capacity compared to all other specimens. Majority of SiO2 samples are on the right side of red dashed line. They also demonstrate higher strain capacity before failure at maximum load which reduces chances of sudden catastrophic failure. Results of each nano-modifier are presented in Figure 5-6, Figure 5-7, and Figure 5-8 and location of red dashed line is included for refrence.

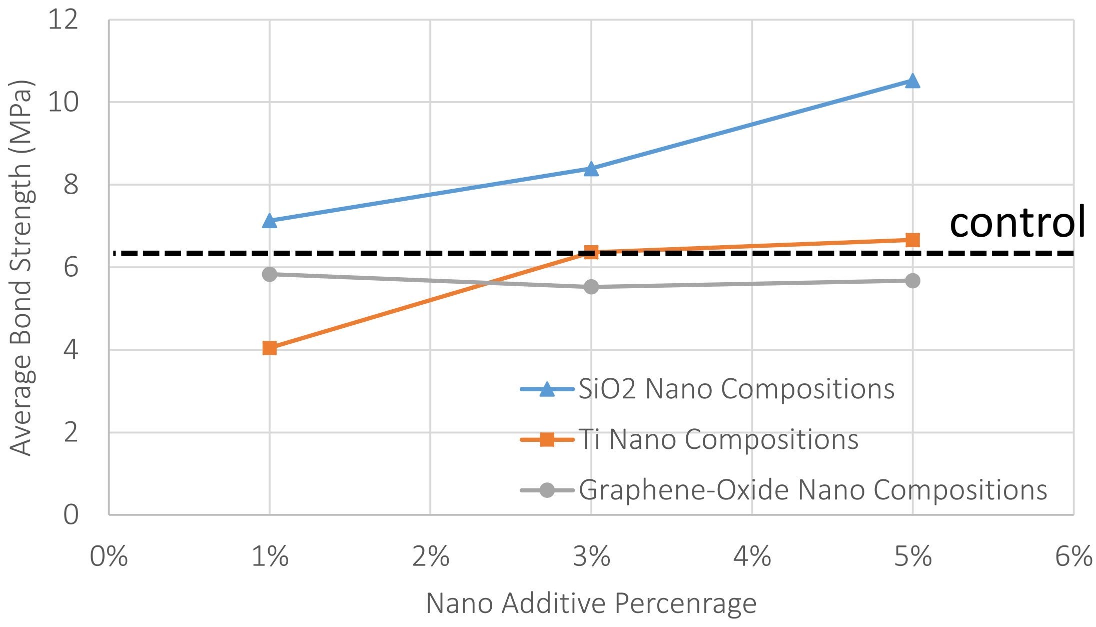

Figure 5-4 Bond strength trend versus Nano-additive concentration in the coating mixture.

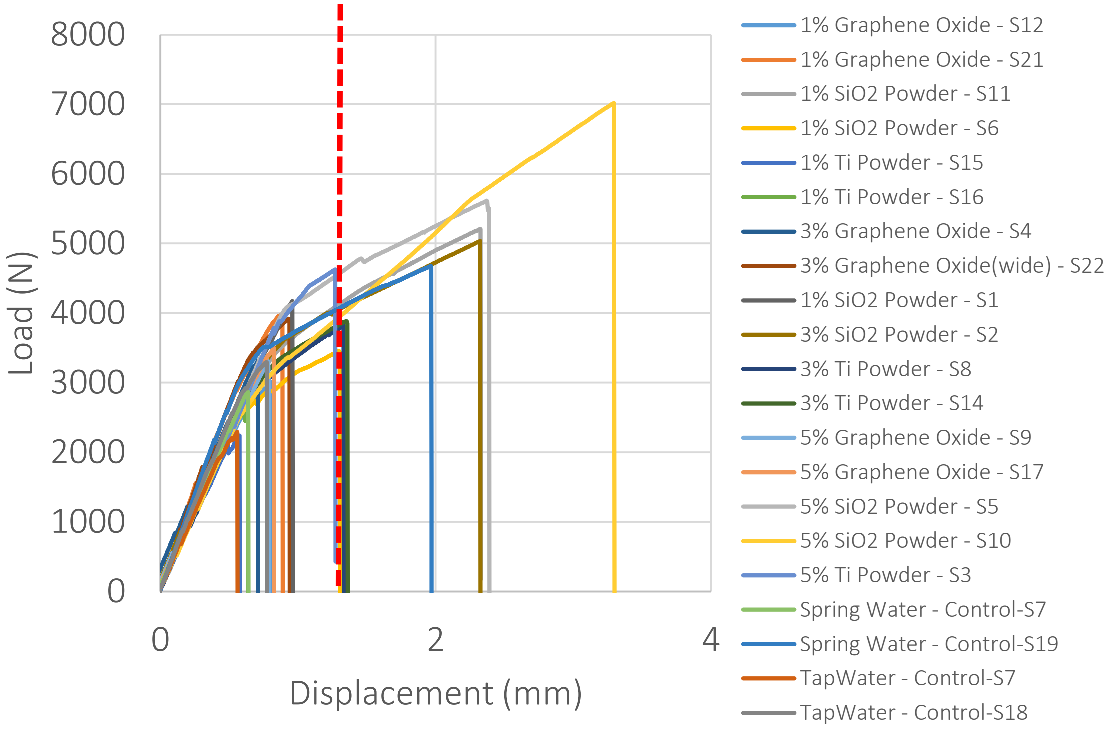

Figure 5-5 Summary of lap shear load-displacement test on coated specimens with various Nano-modifications.

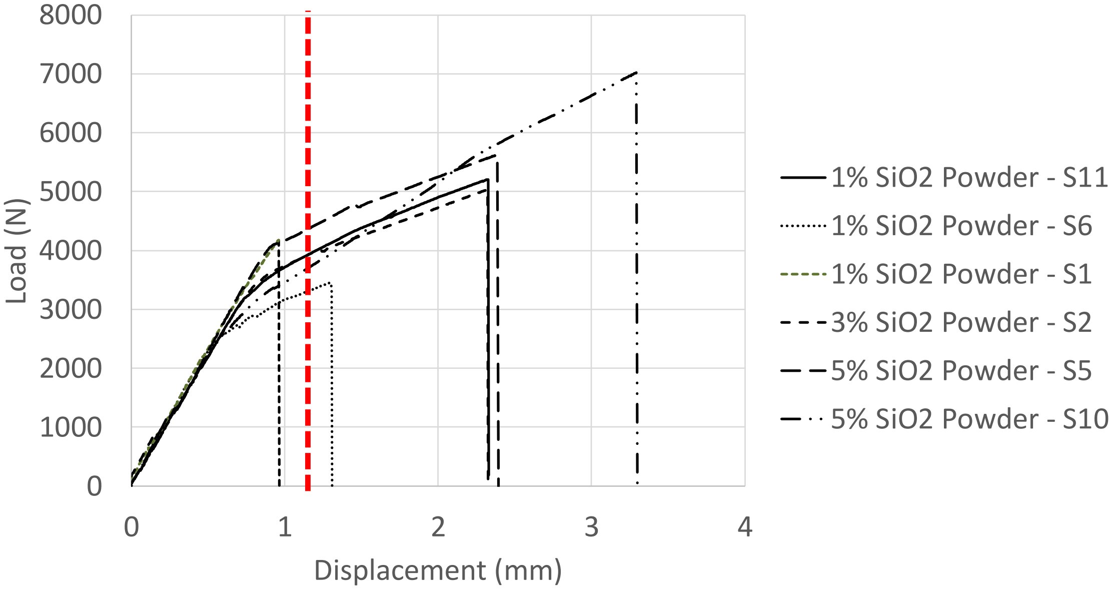

Figure 5-6 Summary of lap shear load-displacement test on coated specimens with SiO_2

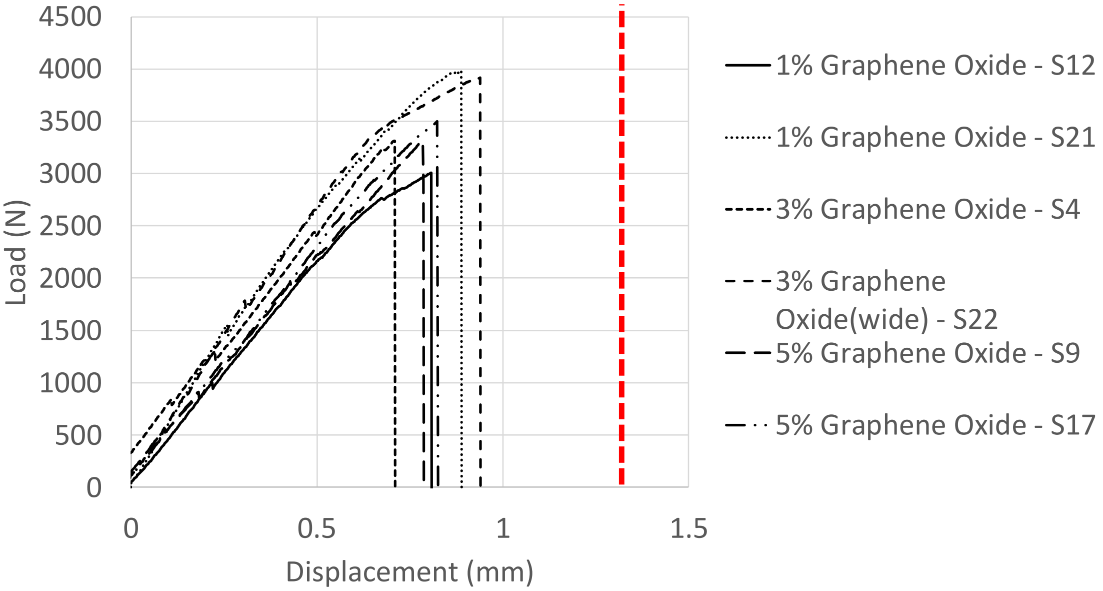

Figure 5-7 Summary of lap shear load-displacement test on coated specimens with Graphene oxide.

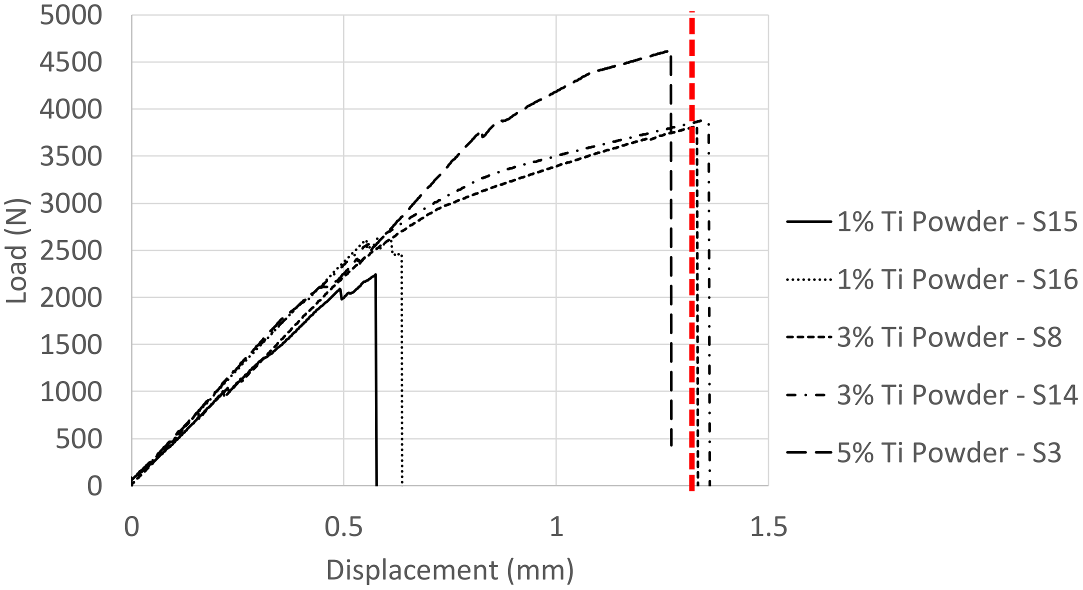

Figure 5-8 Summary of lap shear load-displacement test on coated specimens with Ti powder.

5.2 Steel Coupon Specimens

Various structures are in risk of different damages. Loss of part of the profile section due to impact, dents, and corrosion induced thickness loss are common potential defects in steel structures. It is of interest to address each defect with an appropriate repair procedure. To this end in this chapter we tested performance of specimens with damages in selected steel sheets are proposed to study repair effectiveness.

First, three undamaged steel specimens as control samples are failed under tensile force using MTS machine. Second, damaged samples are tested under tensile force. Finally, samples repaired with CFRP are tested under tensile force. Load–Displacement curves are compared to identify most severe type of damage and effectiveness of corresponding repair.

To examine strength capacity of repaired section with CFRP several rectangular shaped specimens were prepared according to guidelines recommended by ASTM E8/E8M (see Figure 5-9). Three type of damages were considered at the middle of specimens: linear damage along the width of the specimen, patch damage, and through hole. The damaged specimens were repaired with medium weight unidirectional carbon fabrics, impregnated with DowAksa H300 resin. Steel coupon surface was cleaned with acetone and sand blasted prior coating or CFRP application in case of uncoated specimens.

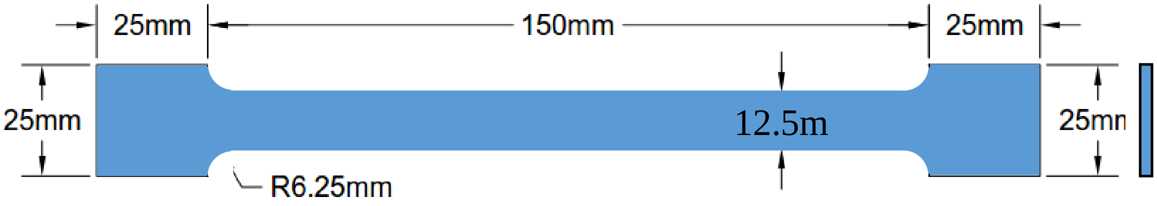

Figure 5-9 Schematics of steel coupon samples as per recommendations in ASTM E8/E8M.

Performance of repaired specimens with defined damages were observed. Study cases included CFRP repair over coated steel surface with geopolymer coating and uncoated steel surface. The goal was to examine load bearing capacity of repaired specimens compared to undamaged specimens in both coated and uncoated scenarios.

5.2.1 Linear damage

Scratches are common type damage that is done to the pipelines during transportation and installation. To simulate this type of damage in the test specimens, linear scribes are select as the emulation of this damage. Figure 5-10 shows the schematics of these specimens. Figure 5-11 shows a repaired specimen with CFRP. Linear damage was incurred using a 2mm diameter drill bit and two specimens were prepared by clamping two steel coupons firmly together and drilling through the width of specimen (12.5mm) to create a linear damage with the section of a half circle. This damage is shown in Figure 2. A total of for such specimens were prepared. Two for uncoated steel and two for coated steel with geopolymer.

Prepared specimens will be tested under tension with MTS machine. Loading rate will be same as the rate used for previous tests (1.27mm/min). The goal is to recover loading bearing capacity of the specimen at the repaired area to a higher value than the undamaged section. In other words the yield in the specimen is expected to occur at section out of bond length of CFRP repair. The required bond length will be determined and compared with minimum bond lengths suggested by the available codes.

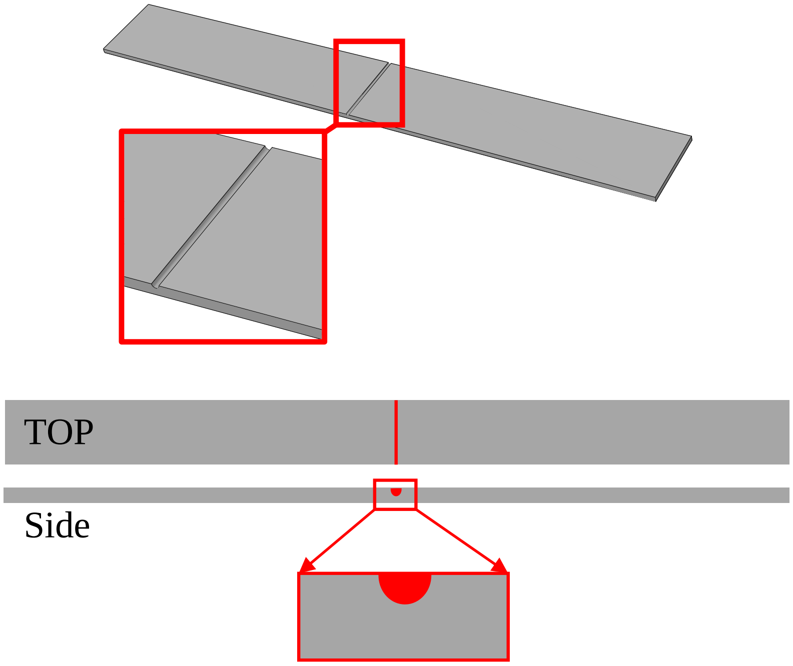

Figure 5-10 Scribes in the steel coupon. The damage is the filled red area.

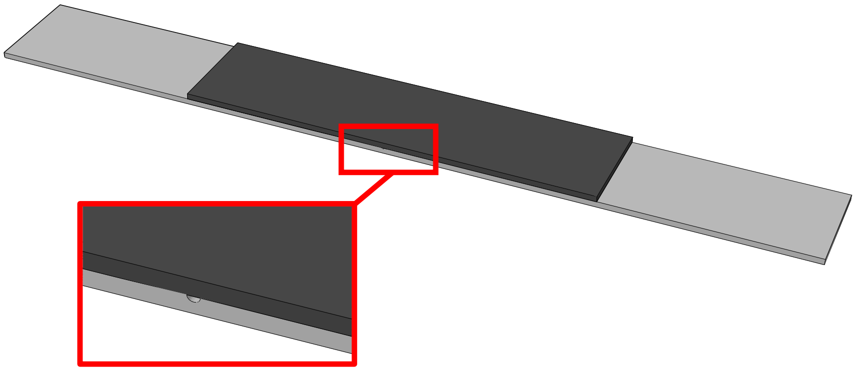

Figure 5-11 Figure 1.2 CFRP Repaired steel sheet specimen.

5.2.2 Through Thickness Hole Damage

Other potential type of damage to pipelines and sometimes bridge girders are partial loss of section due to an impact. These damages may be in the form of a puncture hole, torn flange, gouge and spot damage. Hole damage was incurred in the middle of the steel coupon. The whole extends through the thickness of the steel coupon (3mm). A 2mm diameter drill bit was used to drill the hole. A total of for such specimens were prepared. Two for uncoated steel and two for coated steel with geopolymer. Same repair procedure is followed as for the linear damage cases with CFRP. Figure 5-12 (bottom) shows this damage in a steel sheet specimen.

5.2.3 Patch Damage

This type of damage is specifically suitable to emulate section thickness loss due to corrosion and spreads over a larger area. Corrosive agents ingress and spread from an exposed spot to a larger area due to damages, ill inspection after coating application, coating deterioration, and cathodic disbondment. a patch shape damage was incurred in the middle of the steel coupon. The patch damage was prepared by using a 5mm diameter drill bit. Extent of drilling was defined by the following criteria: drilling was stopped when a drilled patch with a diameter equal to that of the drill bit was measured. Due to the fact that drill bit has an arrow shape the maximum depth of penetration was created in the center of the patch damage where the tip of the drill bit is located. Figure 5-12 (top) Shows schematics of this damage, incurred into the steel sheet specimen. Lab prepared samples are shown in Figure 5-13.

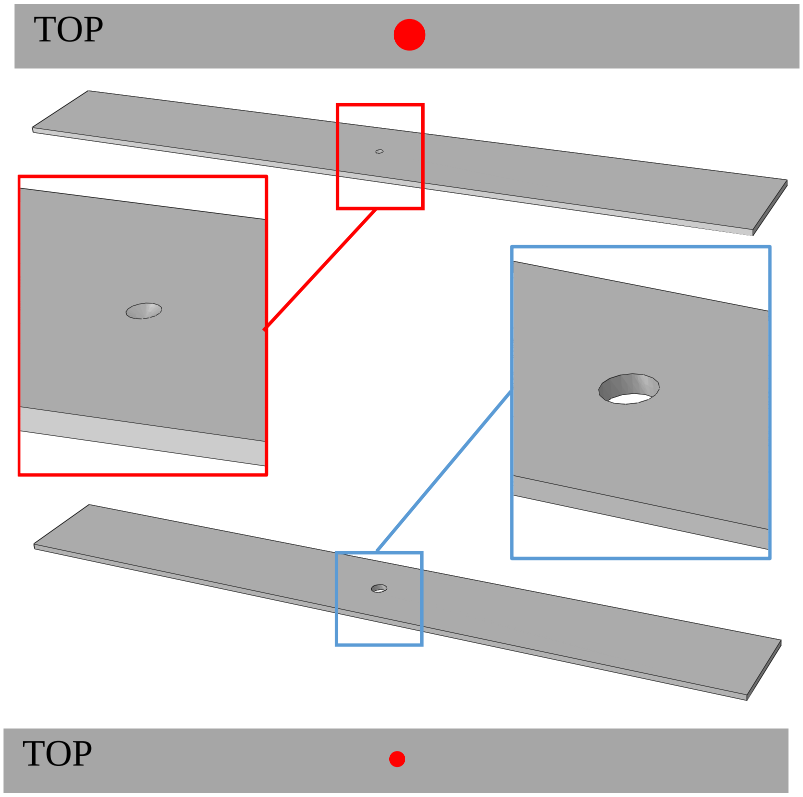

Figure 5-12 Patch section loss (top), and through thickness hole (bottom). Red dots indicate the damaged area.

5.2.4 Test results

Tension test was performed on all samples and the load displacement curves of repaired cases with and without use of coating as barrier layer were compared. For the specimens with the hole damage the Load-Displacement curves (Figure 5-14) show that the repaired specimens demonstrated higher or equal capacity before the yield point of steel. In addition no sample showed signs of bond failure (shown in red dotted circles in Figure 5-14) between CFRP and surface before reaching yielding stress of steel.

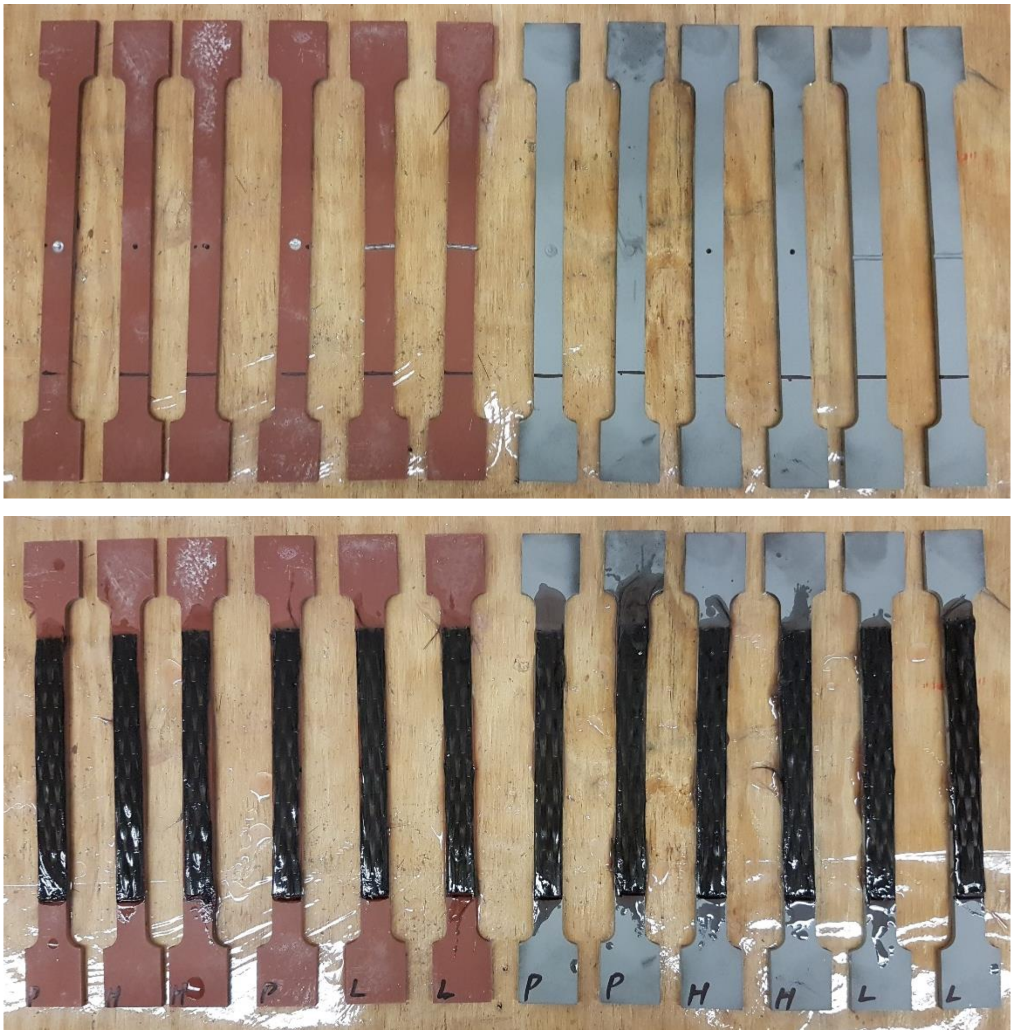

Figure 5-13 Types of damages (top) shown in the specimens, repaired specimens with CFRP.

Observation of displacement at fracture point of the repaired samples versus the control sample shows that the ductility of the repaired specimens was reduced greatly and consequently smaller energy is required to reach to fracture point in the repaired specimens.

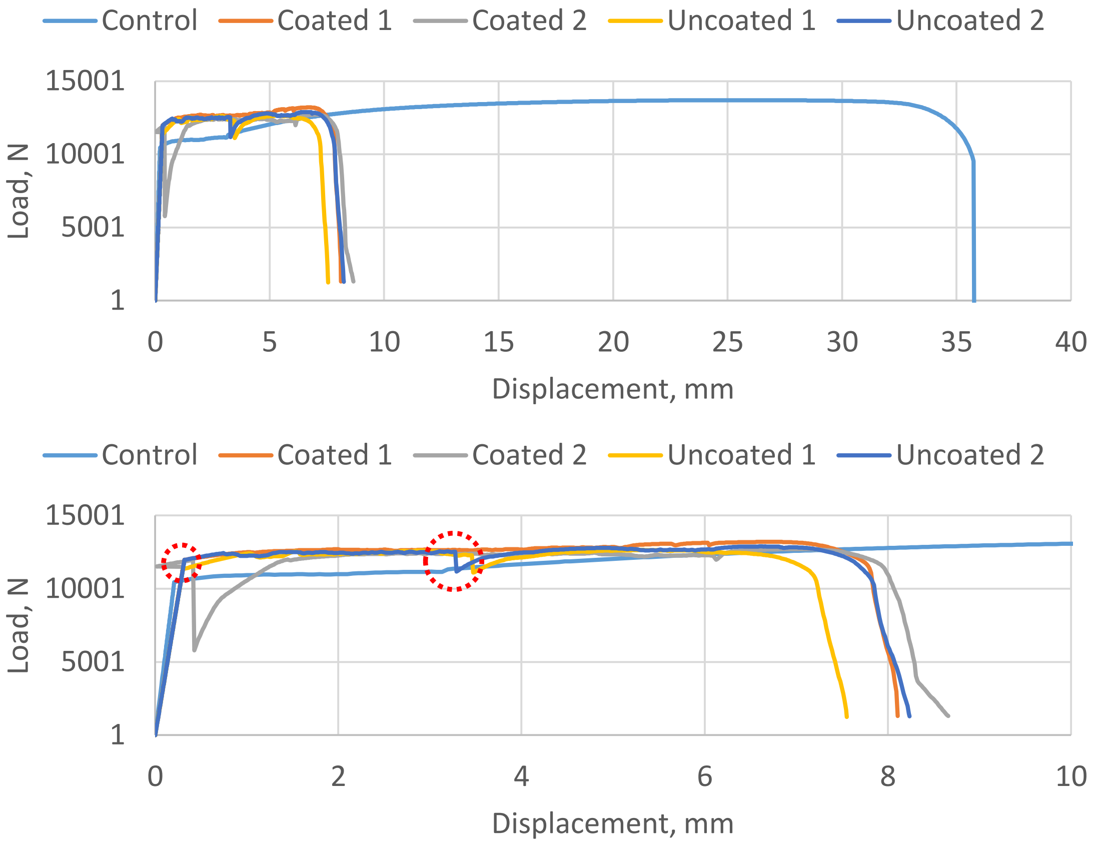

Figure 5-14 Load-Displacement curves for specimens tested with hole damage.

Similarly, the Load-displacement curves for linear damage (Figure 5-15) show that the repaired specimens demonstrated higher or equal capacity before the yield point of steel. Compared to the specimens with through thickness hole damage, linear damaged specimens after repair require less energy to reach break point and they fracture at smaller displacements. This is due to larger reduction of section area as a result of this type of damage.

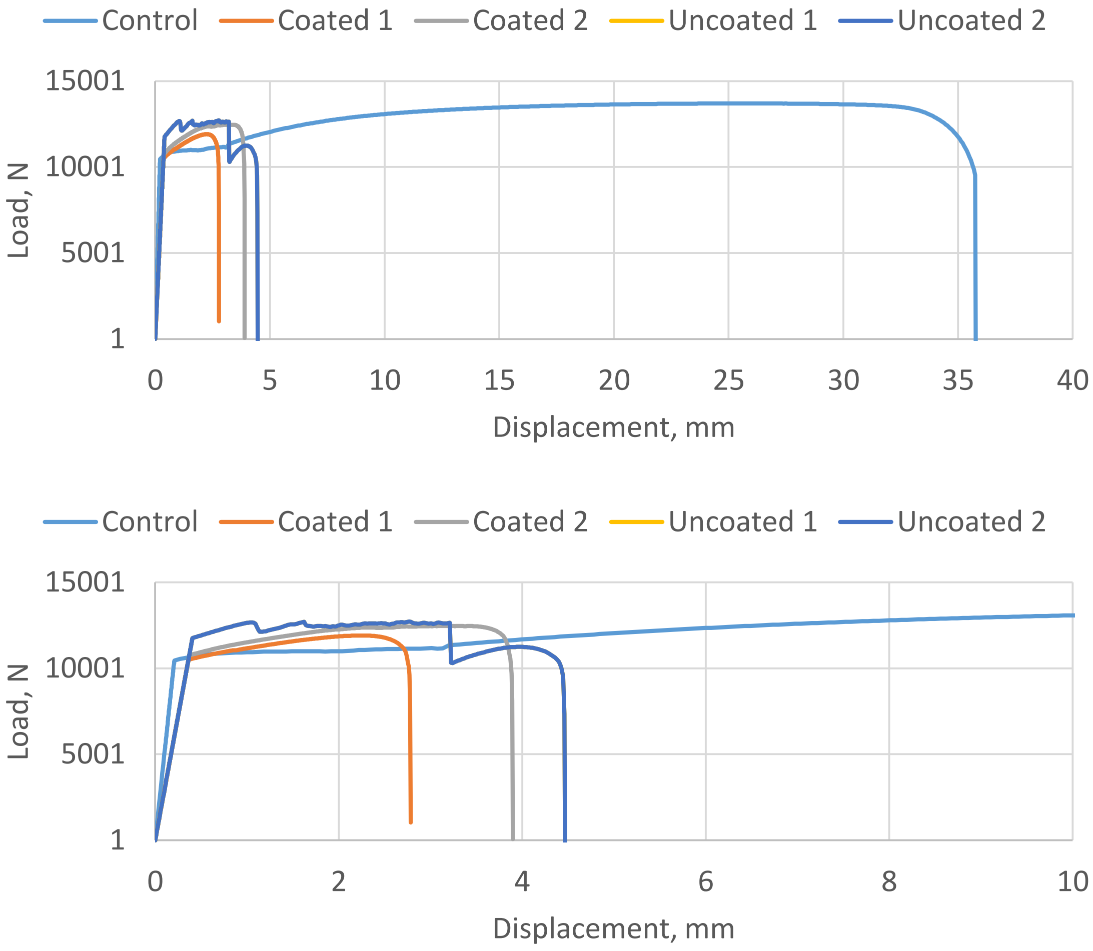

Figure 5-15 Load-Displacement curves for specimens tested with linear damage.

Finally, Figure 5-16 shows the load-displacement curves for repaired specimens with patch damage. This damaged showed to be least critical type of damage as expected due to least reduction of the section of the specimen. Repaired specimens demonstrated higher or equal capacity before the yield point of steel. Compared the specimens with through thickness hole damage, patch damaged specimens after repair require more energy to reach break point and they fracture at larger displacements.

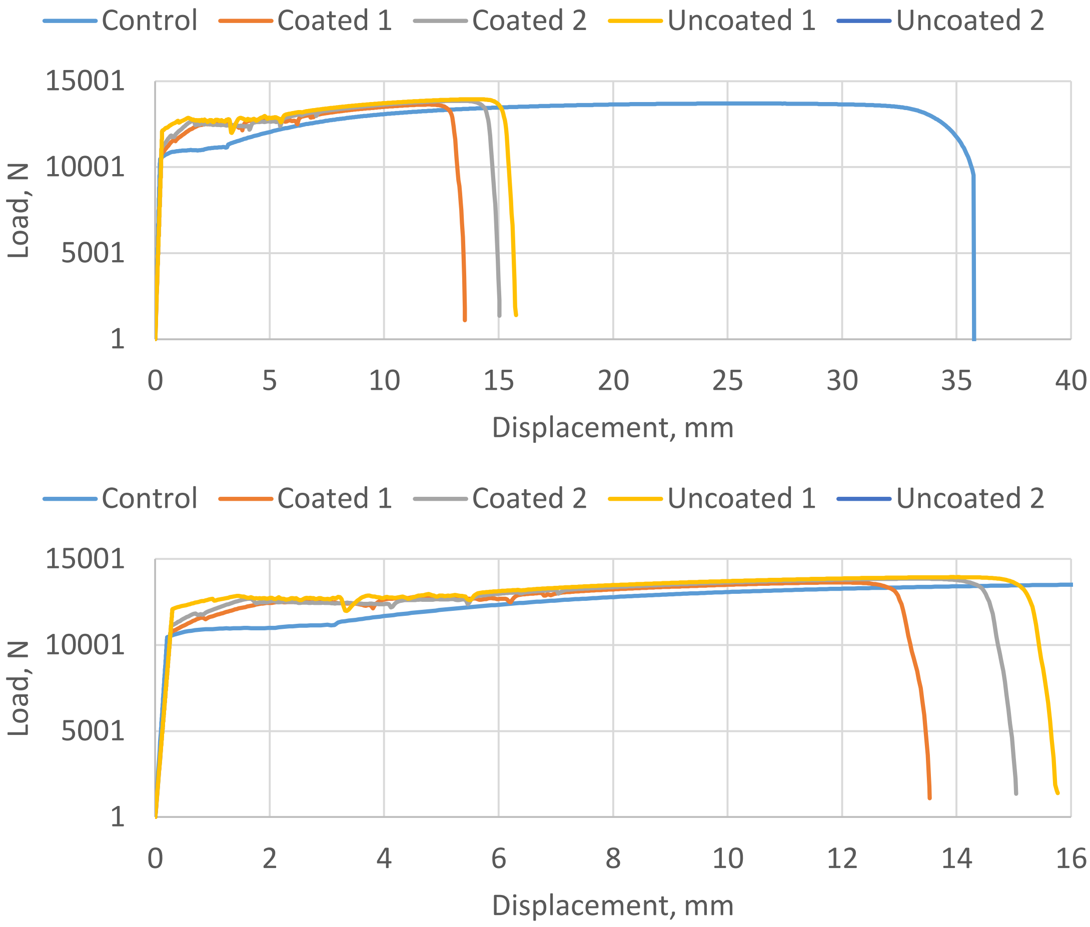

Figure 5-16 Load-Displacement curve for patch damaged specimens.

Comparing the results of all repair cases we can conclude that linear damage which could emerge in form of deep scratches or surface cracks may result in a more devastating failure or fracture as they tend to dissipate least energy before Fracture. This reduces alarming time before catastrophic failure and consequently more critical to be detected and repaired in time.

6 Finite Element Analysis Pipeline with Defect and Repair

In this chapter, FE simulations were performed on pipe model for several cases of crack length and depth in pipe wall thickness. Surrogate models were fitted to compute SIF for intermediary points among actual FE simulated SIF values. The proposed model predicts the failure based on 2-dimenssional crack growth in the pipe wall thickness.

6.1 Finite Element (FE) Modeling

The finite element modeling of this research includes 2D and 3D simulation to calculate at the crack tip. Commercially available multi-physics software ABAQUS was used to perform FE simulations (Dassault Systémes, 2015). For purpose of this study typical steel material properties (E=200 GPa, υ=0.3) were assumed for steel and it was assumed that steel has elastic behavior within the scope of SIF simulations.

6.1.1 Two Dimensional FE Model

In this model only cross section of pipe was modeled and various crack depths (a) were embedded in the model. The diameter of pipe was selected as $D = 863.6mm$ and pipe wall thickness of $t = 7.1mm$. These numbers were adopted from (Xie et al. 2018).

An internal pressure of $P = 4.5MPa$ was applied on the interior wall of the pipe section. As shown in Figure 6-1, the 2D FE model assumes the full depth of the crack is extended along the crack (perpendicular to this page) which is a simplified scenario in comparison to the realistic crack profile along the length of the crack. The figure also shows the SIF value for Mode-I SIF (K-I) for 5 different contours away from the crack tip and the stress distribution in the vicinity of crack tip. It can be seen from the section (d) of the figure that Mises stress confirms that that Mode-I fracture is dominant.

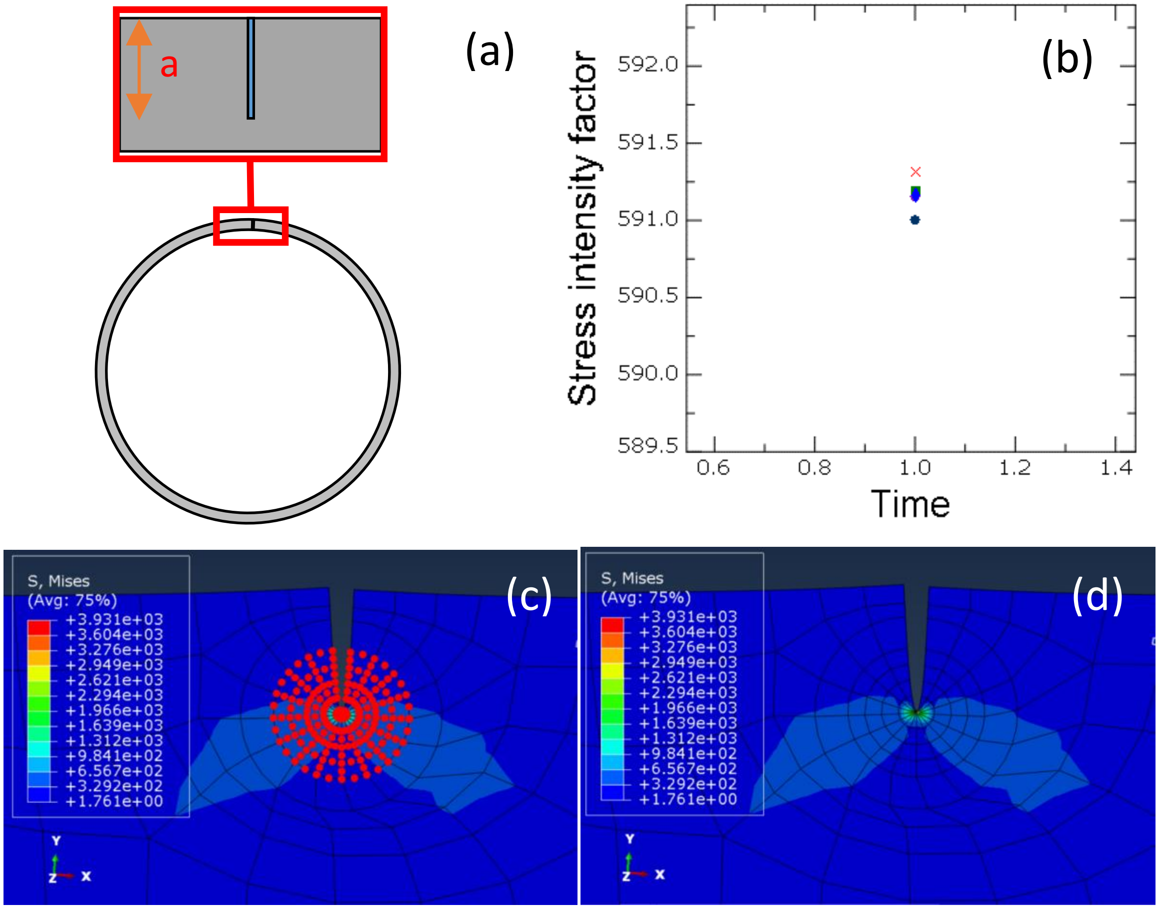

Figure 6-1 Example of calculated SIF for mode I fracture for a 1mm deep crack. (a) schematics of crack location, (b) SIF calculated at 5 counter integration points, (c) 5 contours shown at the crack tip, and (d) stress at the crack tip.

Plane strain condition for the 2D analysis is proper assumption as the pipeline length is many times larger than the thickness and diameter of the pipe almost in all cases. As it can be seen in Figure 6-1 (b) increasing number of contours centered at the crack tip does not change the SIF value significantly and the difference in values are negligible. Figure 6-2 illustrates the progression of intensified Mode-I SIF as the depth of the crack is increased. As expected the SIF is increased exponentially as crack depth is increased. In this case increasing number integration contours has negligible effect on increased accuracy of calculated SIF. Although not readily distinguishable in the shown scale the values of SIF for $a = 3.6mm$ shows a bit larger variance as we move from 2nd contour going forward. This is visible in Figure 6-3.

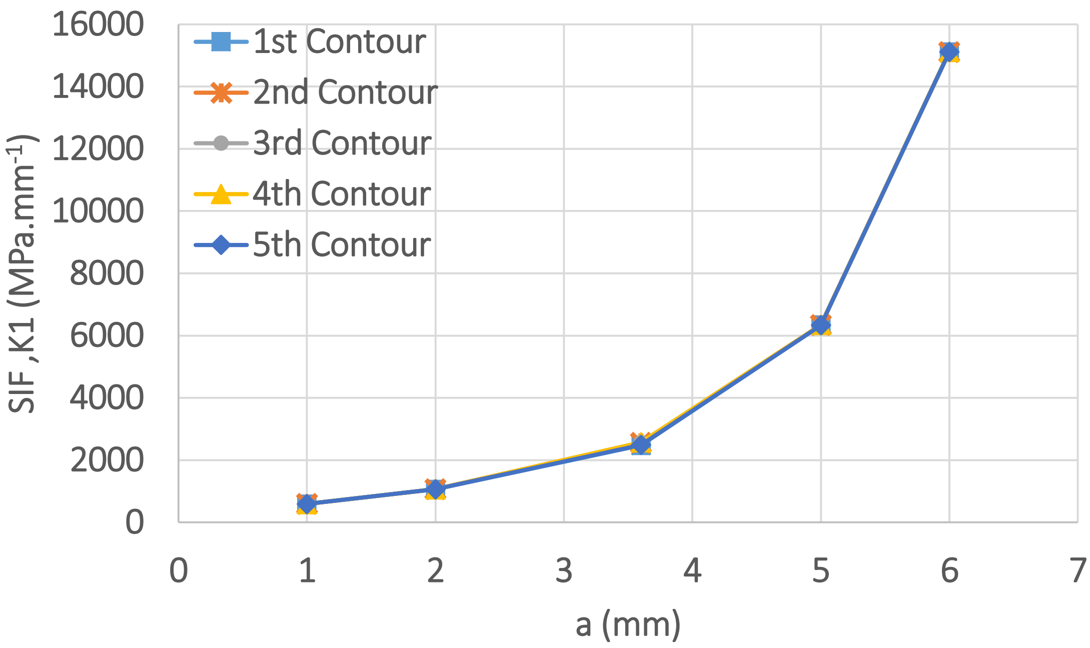

Figure 6-2 Variations of K1 SIF with increasing crack depth through pipe thickness for 5 different contour integration groups.

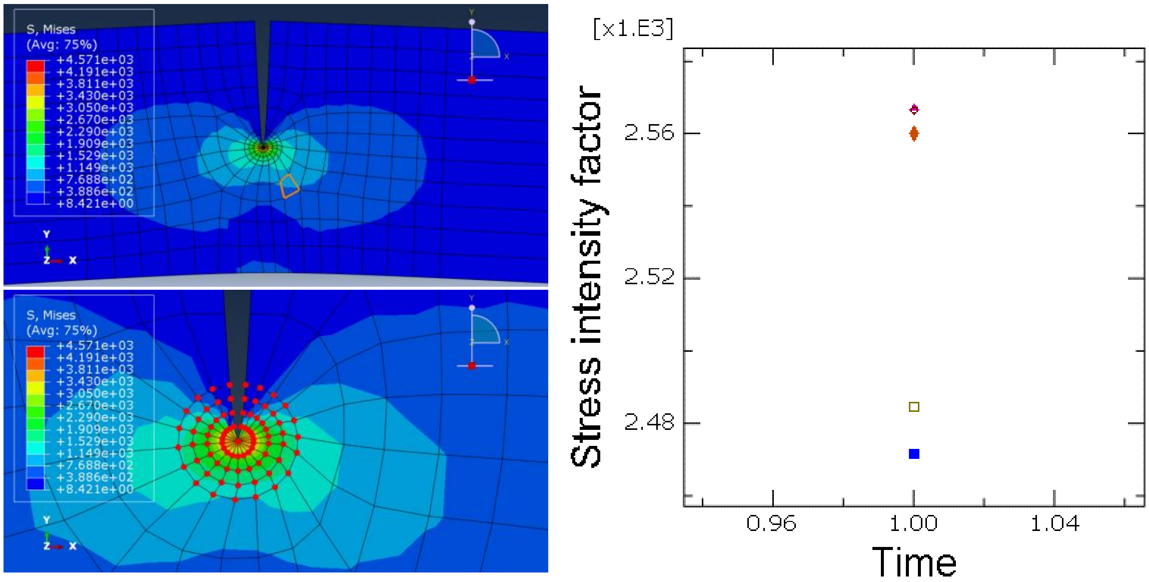

Figure 6-3 SIF values for Mode-I fracture at 3.6mm crack depth for 2D plane strain pipe model (blue square is 1st contour).

6.1.2 Three-Dimensional FE Model

To investigate crack growth and the respective SIF evaluation more accurately a 3D model was developed and a semi-elliptical (halved ellipse) shape was assumed for the crack shape as previously it was reported in the literature to emulate realistic crack shape more closely. The length of the pipe section model was chosen to be $1000mm$.

To reduce running time of each analysis case a preliminary mesh sensitivity analysis was performed to determine largest mesh size where solution reaches stable state and will not be improved by any further mesh size reduction at the vicinity of the crack. This analysis was performed for the crack with length of $L = 10mm$ and depth of $a = 1mm$. The analysis concluded that a mesh size of approximately $0.5mm$ (equivalent to 23 nodes) as shown in Figure 6-4 is small enough to produce the correct response.

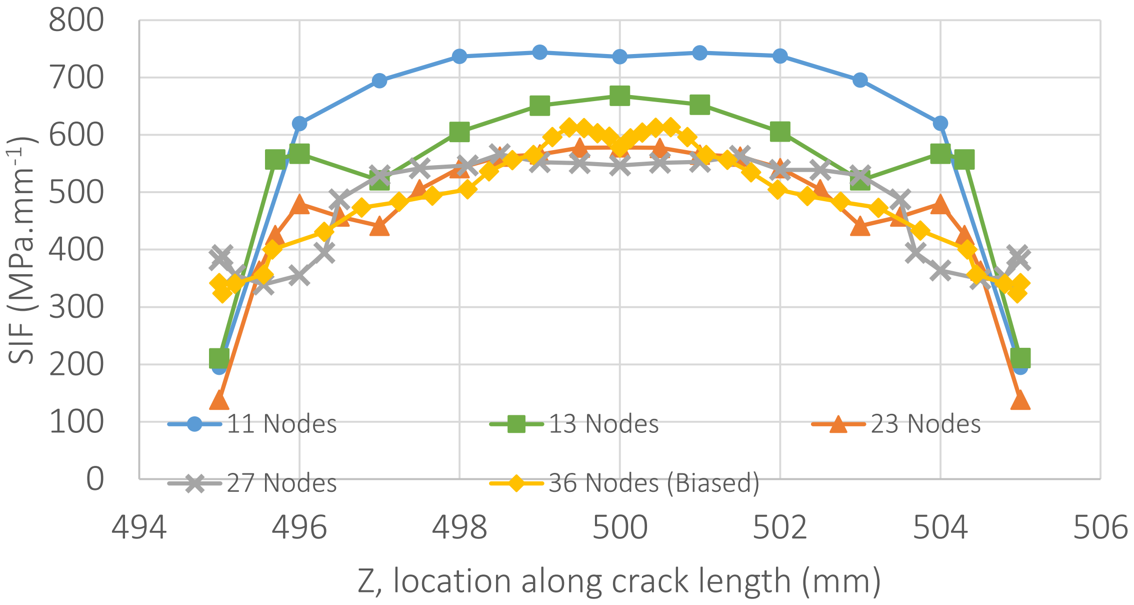

Figure 6-4 Mesh size sensitivity analysis results for an elliptical crack with length of $L = 10mm$ and depth of $a = 1mm$.

Additionally, to further optimize required running time for each analysis case, the symmetry of the model was taken advantage of, to reduce model size. To this end, as shown in Figure 6-5 , the full pipe model was once reduced in half due to symmetry along y axis (x-z plane) and a second time along z axis (x-y plane). In addition, bias mesh sizing was used to incrementally increase mesh size of the pipe as we go farther away from location of embedded crack.

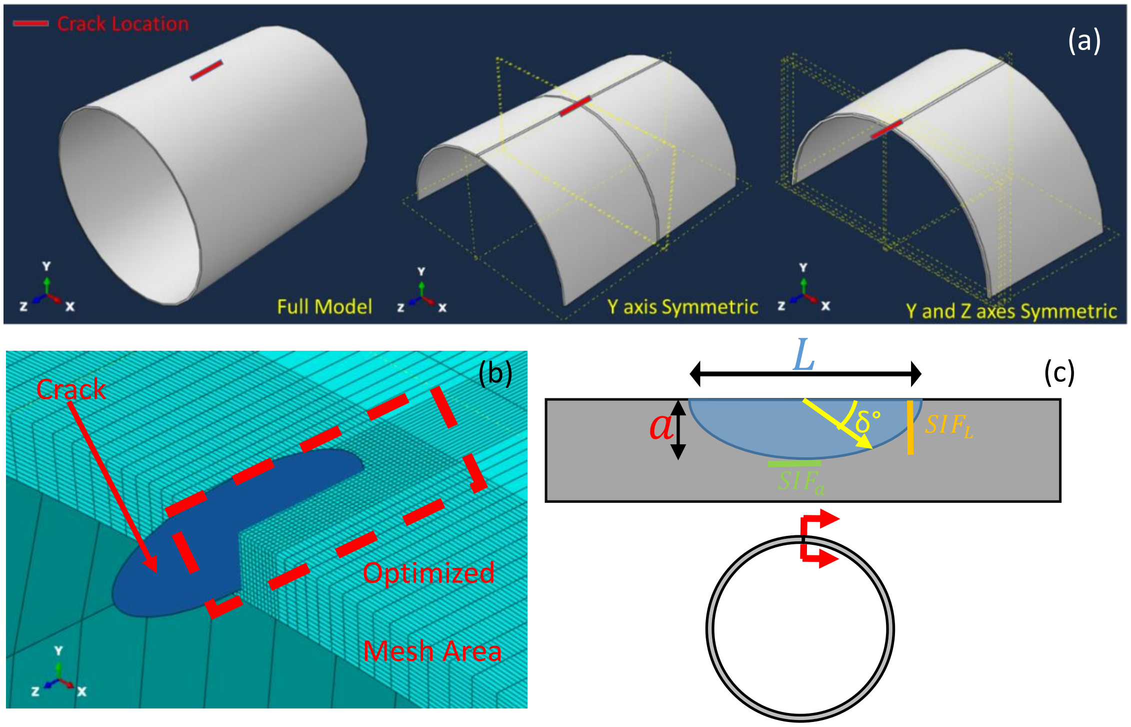
Crack Location
(a)
Full Model
Y axis Symmetric
Y and Z axes Symmetric
Y
Z
X
(b)
Crack
Optimized
Mesh Area
(c)
L
a
δ°
SIF_L
SIF_a

Figure 6-5 3D pipe model with three different representations for modeling.

It should be noted that the region where crack was embedded was always meshed uniformly in size and corresponding to the appropriate mesh size derived from mesh sensitivity analysis that was explained earlier. This incremental progression of mesh sizing can be observed in Figure 6-5 (b) where the elliptical crack is embedded in the quartile model(the model with symmetry along Y and Z axis) and mesh dimension along perimeter of pipe and long Z axis is increased as we go away from the crack region. To verify validity of this model reduction approach we have performed analysis for all models introduced in Figure 6-5 and the corresponding SIF calculations are presented in Figure 6-6. As it can be seen the quartile model is fully verified as an alternative to the full model.

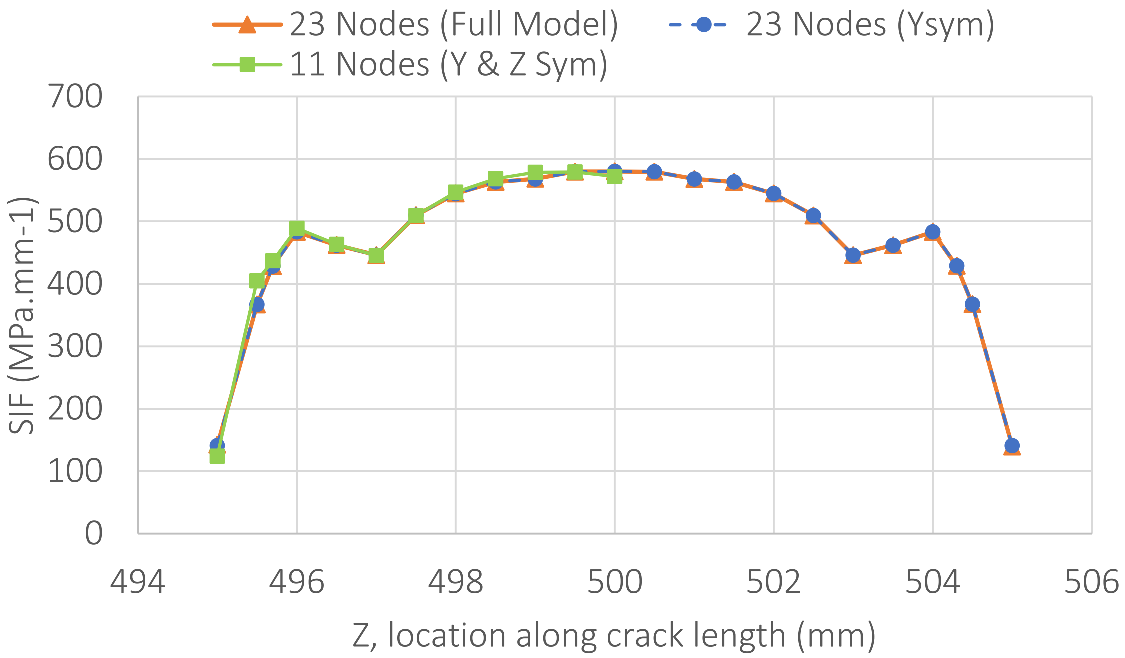

Figure 6-6 Verification of model size reduction by symmetry. Comparison of all three model results shows full accordance.

Figure 6-5 (c) shows a snippet of cross section of the pipe along Z axis where the crack is embedded (crack is positioned in the middle of the pipe). In this cross section we can calculate the SIF for Mode-I fracture along the perimeter of semi-elliptical crack. All combination crack length and depth that was simulated with FE model are summarized in Figure 6-7.

	a (mm)					
L (mm)	1	2	3	4	5	6
10	X	X	X	X	X	X
15	X	X	X	X	X	X
20	X	X	X	X	X	X
25	X	X	X	X	X	X
30	X	X	X	X	X	X
35	X	X	X	X	X	X
40	X	X	X	X	X	X

Figure 6-7 All FE modeled crack length-depth combination considered.

The result of the simulations reveals that at shorter crack lengths as the depth of crack increases the SIF becomes more critical at the endpoints along the crack length, as shown in Figure 6-9. As the length of the crack becomes longer the critical SIF remains at the deepest point of the crack. In other words, the longer the crack length becomes the more dominant crack depth becomes. This is the justification that crack depth is the main derive behind 2D crack growth progression when we discuss crack growth algorithm in the next chapter.

The cases illustrated in Figure 6-9 the critical points of stress intensity are clearly visible at red areas along crack perimeter. To further show the effect of crack length on the SIF results, the results for shortest and longest crack length cases along the crack length and crack perimeter (in polar system) are shown in **Error! Reference source not found.**. It can be seen that the variation of SIF is sensitive to crack length at a certain crack depth (see (a) and (b) of parts of the **Error! Reference source not found.**) for shorter crack lengths. On the other hand, at longer crack lengths the variations of SIF values are more sensitive to crack depth changes and does not change considerably along the length (see (c) and (d) of parts of the **Error! Reference source not found.**).

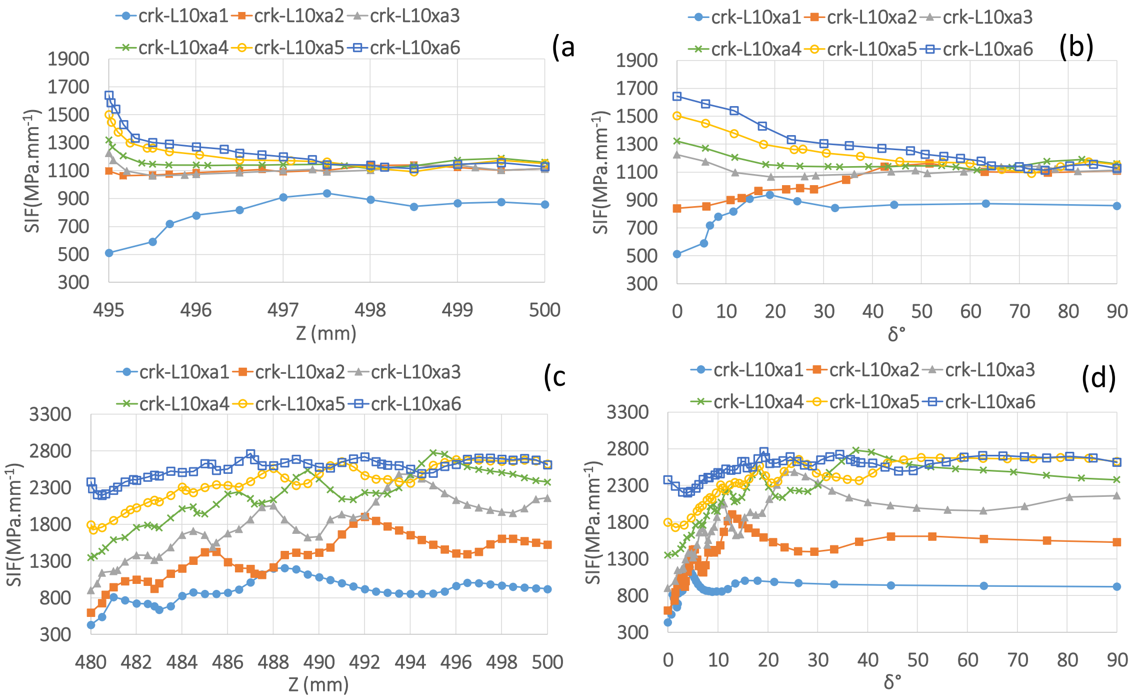

Figure 6-8 Comparison of SIF results from simulation. (a) results for crack length $L = 10mm$ along the length, (b) results for crack length $L = 10mm$ along the crack perimeter , (c) results for crack length $L = 40mm$ along the length, and (d) results for crack length $L = 40mm$ along the crack perimeter.

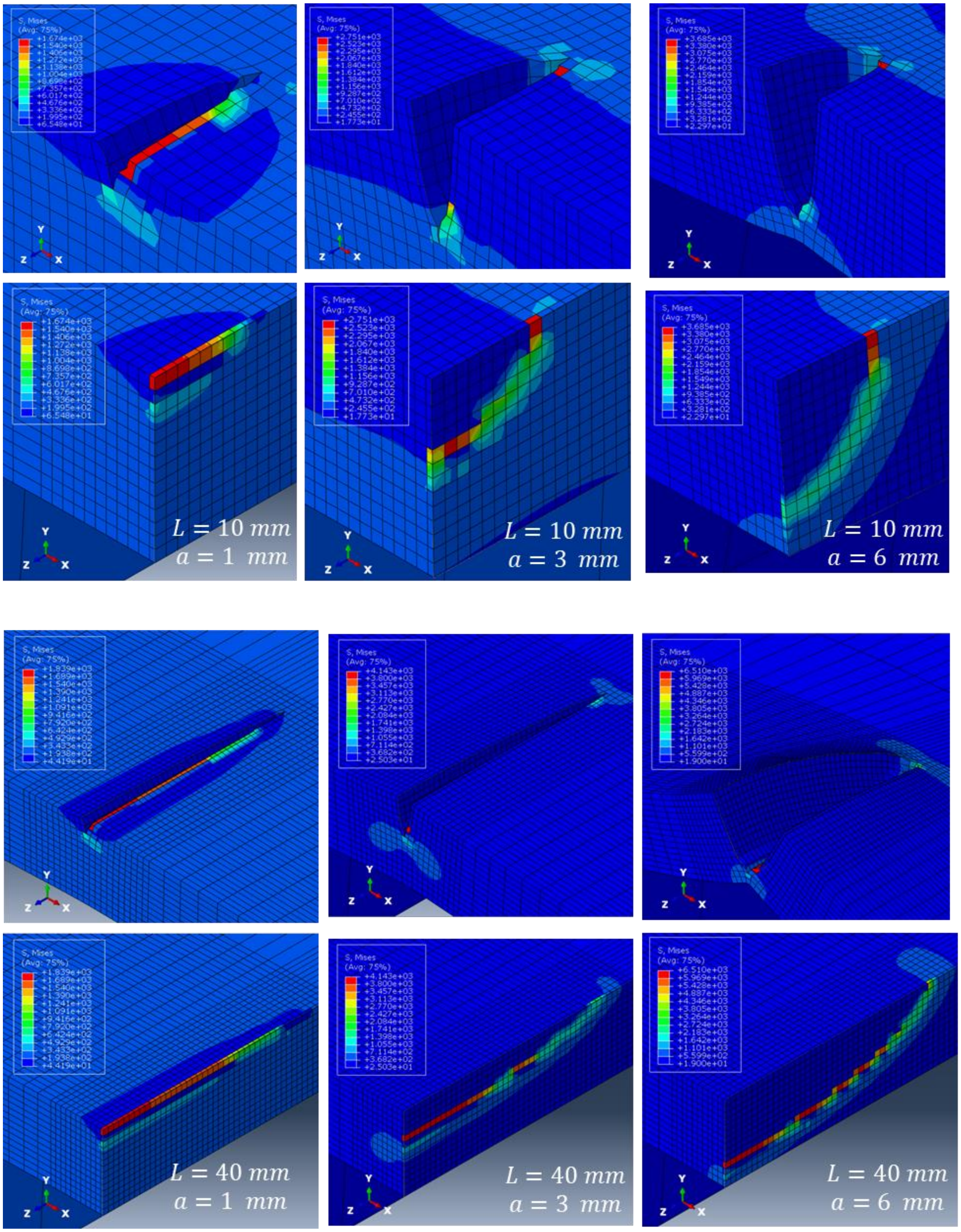
S, Mises
(Avg: 75%)
Y
Z
X
$L = 10\ mm$
$a = 1\ mm$
$L = 10\ mm$
$a = 3\ mm$
$L = 10\ mm$
$a = 6\ mm$
$L = 40\ mm$
$a = 1\ mm$
$L = 40\ mm$
$a = 3\ mm$
$L = 40\ mm$
$a = 6\ mm$

Figure 6-9 This figure shows variations of stress intensity along crack front in 6 scenarios of length-depth.

6.2 Surrogate Function of Stress Intensity Factor

Due to high computation cost and time, evaluating SIF values for all possible combinations of crack lengths and depths are not feasible. In a crack growth model and the flowchart shown in Figure 7-11 in each cycle we need to evaluate SIF for the updated L and a. To this end we need to define a function that can continuously compute SIF at any L and a within the lower and upper bounds of the crack length and depth that was evaluated in the FE model. This function in the literature is generally referred to as *surrogate function*.

The surrogate function forms a 3D surface. This surface can be estimated using various functions such as polynomial based functions or probabilistic based functions such as Gaussian process model. Here we will investigate both of these functions for the simulated cases and compare their fitting.

6.2.1 Polynomial Surface Fitting

We will use a bivariate polynomial function with variables L and a as inputs which are crack length and depth respectively. Consequently, the SIF value can be calculated as follows:

$$\widehat{IF}(a, L) = \sum_{i=0}^{\deg_L} \sum_{j=0}^{\deg_a} c_{i,j} L^i a^j$$

Where $\deg_a$ and $\deg_L$ are the highest degree for each variable (L and a) in the bivariate polynomial. Here we chose $\deg_a = \deg_L = 2$. In addition, $c_{i,j}$ are constant coefficients of the polynomial that will be evaluated using linear optimization. As we have two sets of SIF this function needs to be driven twice: once as SIF_a and second time as SIF_L ; which are SIF values at the front of the crack along the length and SIF values at the front of the crack along the depth, respectively. See Figure 6-5 (c) for visualized locations of crack fronts annotated with SIF_a and SIF_L.

6.2.2 Gaussian Process Fitting

In the Gaussian process fitting method each SIF data point is fitted to a normal distribution and the expected value of the distribution is chosen as fitted value at that point. Assuming input variables (L and a) in form of a vector $X_i = X_1, X_2, \dots, X_m$ for m data points, the output ,$\widehat{SIF}(a, L)$, would be I form of $Y(X_1), Y(X_2), \dots, Y(X_m)$. At each non training point , X^*:

$$K(X_i, X_j) = Cov\left(f(X_i), f(X_j)\right) = e^{-\frac{1}{2\ell^2}|X_i - X_j|^2}$$

$$\widehat{SIF}(a, L) = Y^*(X^*) = \mathbb{E}[Y^*(X^*)|X^*, X, Y] = K(X^*, X)K(X, X)^{-1}Y$$

$$\mathbb{V}ar[Y^*(X^*)|X^*, X, Y] = K(X^*, X^*) - K(X^*, X)K(X, X)^{-1}K(X, X^*)$$

Where, K is the kernel or covariance function, f is the process function , and ℓ is the characteristic length of the covariance function. In this study Radial-basis function (RBF) kernel (squared-exponential(SE) kernel) was used.

Too small ℓ values cause oscillatory behavior between training data points as result of faster variations of the function. For details on Gaussian process implementation refer to (Williams et al. 1996; Pedregosa et al. 2011).

There are 42 cases of FE simulations. These two surface fitting methods' accuracy with different number of training points will be evaluated and compared. We performed simulations at 6 crack depths and 7 crack length which in total yields 42 cases of simulation (see Figure 6-7). Figure 6-10 and Figure 6-11 illustrate results of fitting surface to the FE simulations.

In these figures the fitted surface is shown in blue and the all data points are shown in red circles. In both figures the left graph shows the fitted surface using Gaussian process method, and the middle graph was fit using a quadratic polynomial surface function. These methods were explained earlier. The graph shown on the right side of aforementioned figures shows the distribution of error for both methods side by side or performance graphs.

Although R-square which is shown on all the graphs is quick way to rate a fifing method in this case it is also worth looking and the ranges of error and their distributions we change training data size. The general finding from observing these graphs tells that for this particular problem polynomial fitting method has more consistent fitting than Gaussian process. That because according to performance graphs, the Gaussian process method tends to have more frequent larger errors.

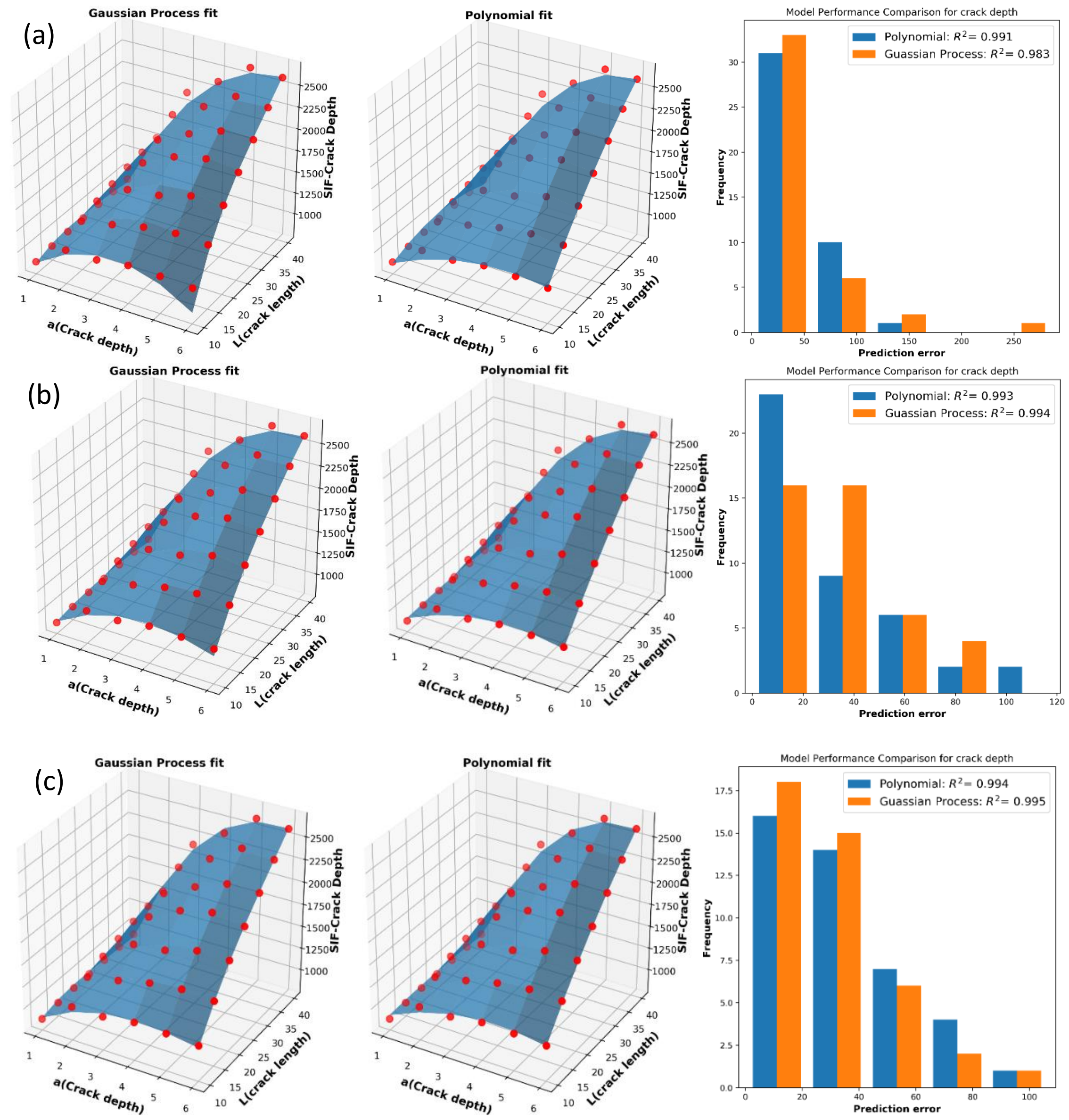

Figure 6-10 comparison of data fitting functions for SIF along crack depth with various training data sizes. Gaussian process fit (left), polynomial fit(middle), and R square score and fitting error distribution (right). (a) models fit with 13 training data, (b) model fit with 26 training data, and (c) model fit with 42 training data. Crack lengths are in mm and SIF in MPa.mm-1.

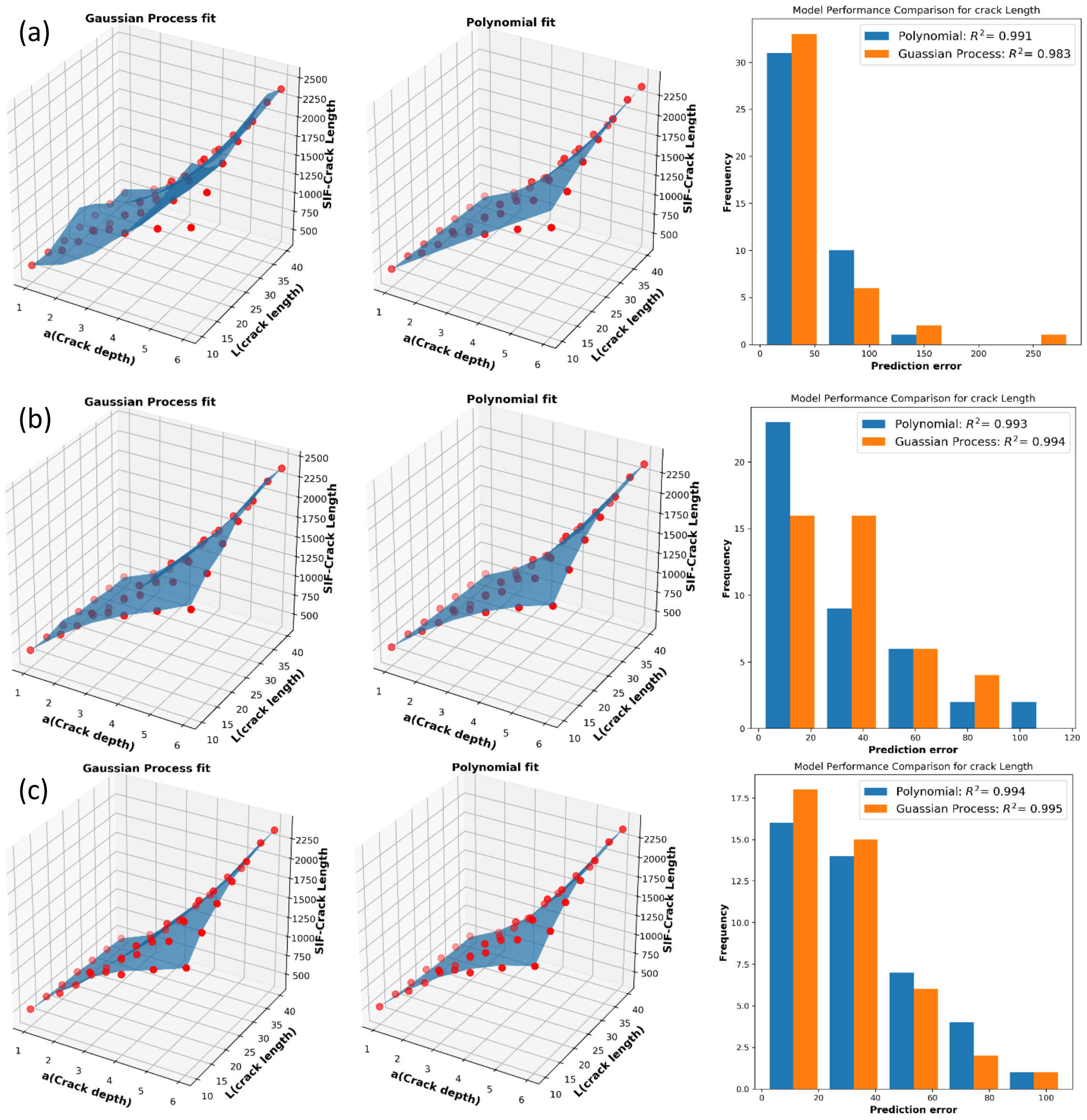

Figure 6-11 comparison of data fitting functions for SIF along crack length with various training data sizes. Gaussian process fit (left), polynomial fit(middle), and R square score and fitting error distribution (right). (a) models fit with 13 training data, (b) model fit with 26 training data, and (c) model fit with 42 training data. Crack lengths are in mm and SIF in MPa.mm-1.

Overall it can be said that both methods are performing very good with predictions. But cautions is needed when dealing with Gaussian process as the fitting in the method is very sensitive to the length scale parameter (ℓ). In addition, Gaussian process has a tendency of overfitting not tuned well with a good covariance function (kernel). The polynomial based fitting method shows that it consistently gets better as more training data is included in the fitting process. It is worth noting that neither of these methods (especially Gaussian process) are capable of having good extrapolated predictions so it is necessary to have as many boundary points as possible to make the fitted model more accurate.

Nevertheless, both these methods we incorporated in the developed algorithm that computes the SIF values for predicting number of cycles in the crack growth model.

6.3 Effect of Patch Repair on Stress Intensity Factor

To investigate performance of patch repaired pipe, all FE model cases discussed in section 6.1 were repaired using a patch repaired model. As advised by manufacturer's (DowAksa) datasheets the thickness of the patch was select to be $1mm$. Material behavior were assumed to be linear elastic in the model and material properties for CFRP sheet was adopted from datasheets. The manufacturer recommends $E = 102Gpa$ for CFRP laminate and 0.3 for Poisson ratio. An instance of one of the models is illustrated in Figure 6-13. In the ABAQUS software the enrichment region was not changed and addition of the patch will not interfere with crack instance and the corresponding enrichment region.

As we observed in section 5.2.4 the patch repaired steel coupons recovered the strength of the damaged section. Given this observation to model the patch part, tie constraint (no slip) was used to define interface of attached patch part to the pipe part.

The patch had $400mm$ extent along the pipe ($200mm$ is visible in Figure 6-13) and with coverage span equal to $\frac{1}{6}$ of the perimeter (equal to $60°$) as annotated in Figure 6-13.

Full SIF results for crack lengths of $10mm$ and $40mm$ is illustrated in Figure 6-12. Comparing the results with**Error! Reference source not found.** Figure 6-8 it is clear that the SIF along the length is now more uniform for shorter crack (10mm length), while for the longer cracks in the repaired model the SIF has decreasing trend as we move from crack front at $0°$ to crack front at $90°$ (deepest part), i.e. the intensity of SIF is shifted from predominantly promoting growth along crack length to a more length invariant scenario. One could compare this effect to a 2D model plane strain.

Observing the curves for 3,4,5, and 6mm deep cracks for 10mm crack length shown in Figure 6-12 (a) and (b) we can see that values of SIF are increased with the increase in the depth of crack (by depth here we mean maximum depth in the ellipse shape crack which occurs at $\delta = 90°$), shown in gray, green, yellow, and blue, respectively. But unlike the case for unrepaired pipe shown **Error! Reference source not found.** (a) and (b) the values of SIF along pipe (Z coordinate) remains relatively constant.

Similarly, Observing the curves for 3,4,5, and 6mm deep cracks for 40mm crack length shown in Figure 6-12 (c) and (d) we can see that values of SIF are show increasing trend as we approach to the deepest part of the crack at $\delta = 90°$. This is opposite of our observations in **Error! Reference source not found.** (a) and (b) where with the increase of crack depth SIF values tend to become invariant to crack length and again behaving close to a 2D plane strain model.

Furthermore, similar to the unrepaired case fitted surrogate functions for intermediary crack lengths and depths for patch repaired pipe model we fitted. Performance of both polynomial and GP models for SIF along depth and length of crack are shown in Figure 6-14 and Figure 6-15 , respectively.

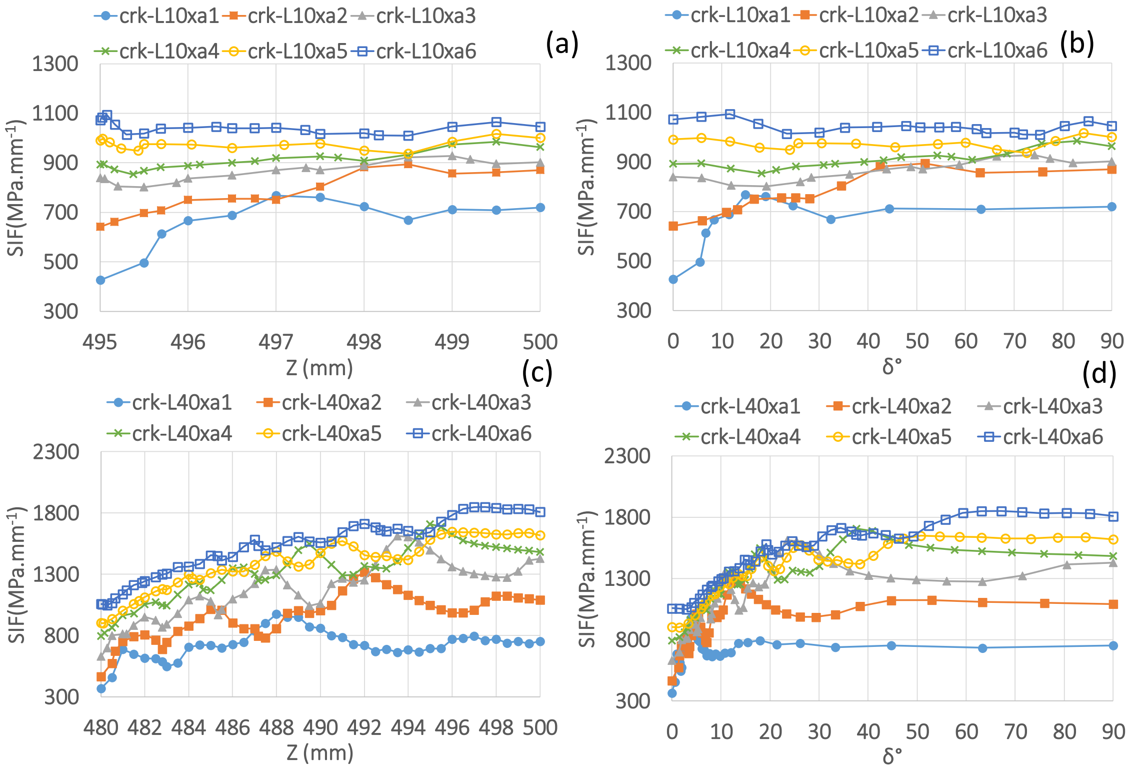

Figure 6-12 Comparison of SIF results from simulation for patch repaired pipe model. (a) results for crack length $L = 10mm$ along the length, (b) results for crack length $L = 10mm$ along the crack perimeter , (c) results for crack length $L = 40mm$ along the length, and (d) results for crack length $L = 40mm$ along the crack perimeter.

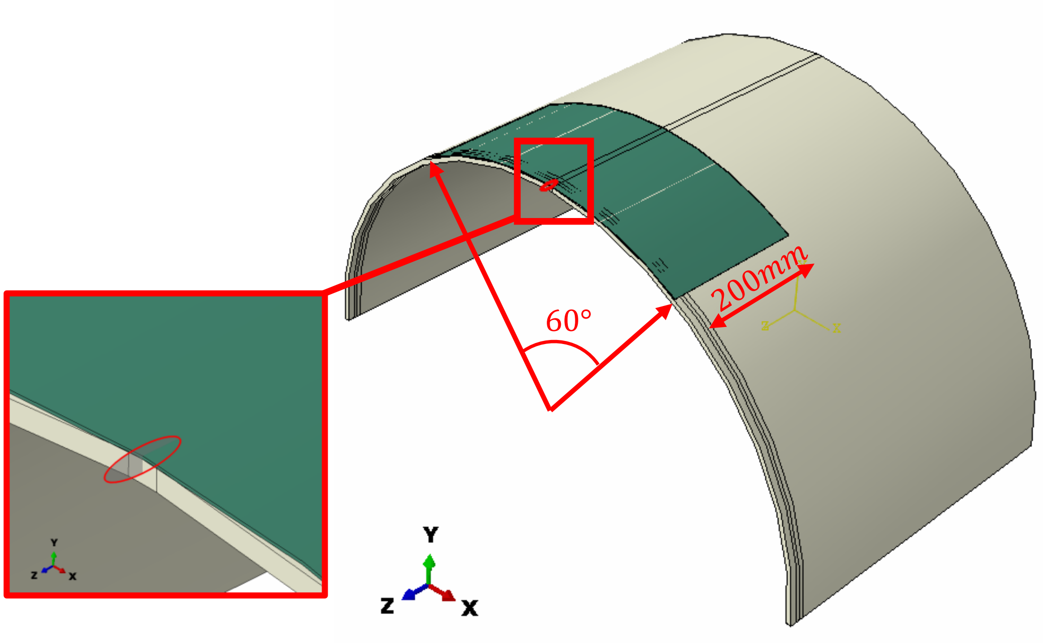

Figure 6-13 Symmetrical quartile model of patch repaired pipe.

Similar to the observations regarding performance of polynomial and Gaussian process model for unrepaired model, we can observe that the polynomial fit function performs well regardless of the number of training points that were used in the fitting process. While Gaussian process model reaches R-squared value of 0.99, it should be used with cautions as depending on the kernel size definition of the fitting process the model could tend to over-fit when the characteristic length is chosen to be very small value. A too large characteristic length also adversely affects the fitting of Gaussian process model and may cause oscillatory behavior between training points. Both fitting models do not perform well for extrapolations at the vicinity of boundary points. So it is important to include the boundary points in the FE simulations.

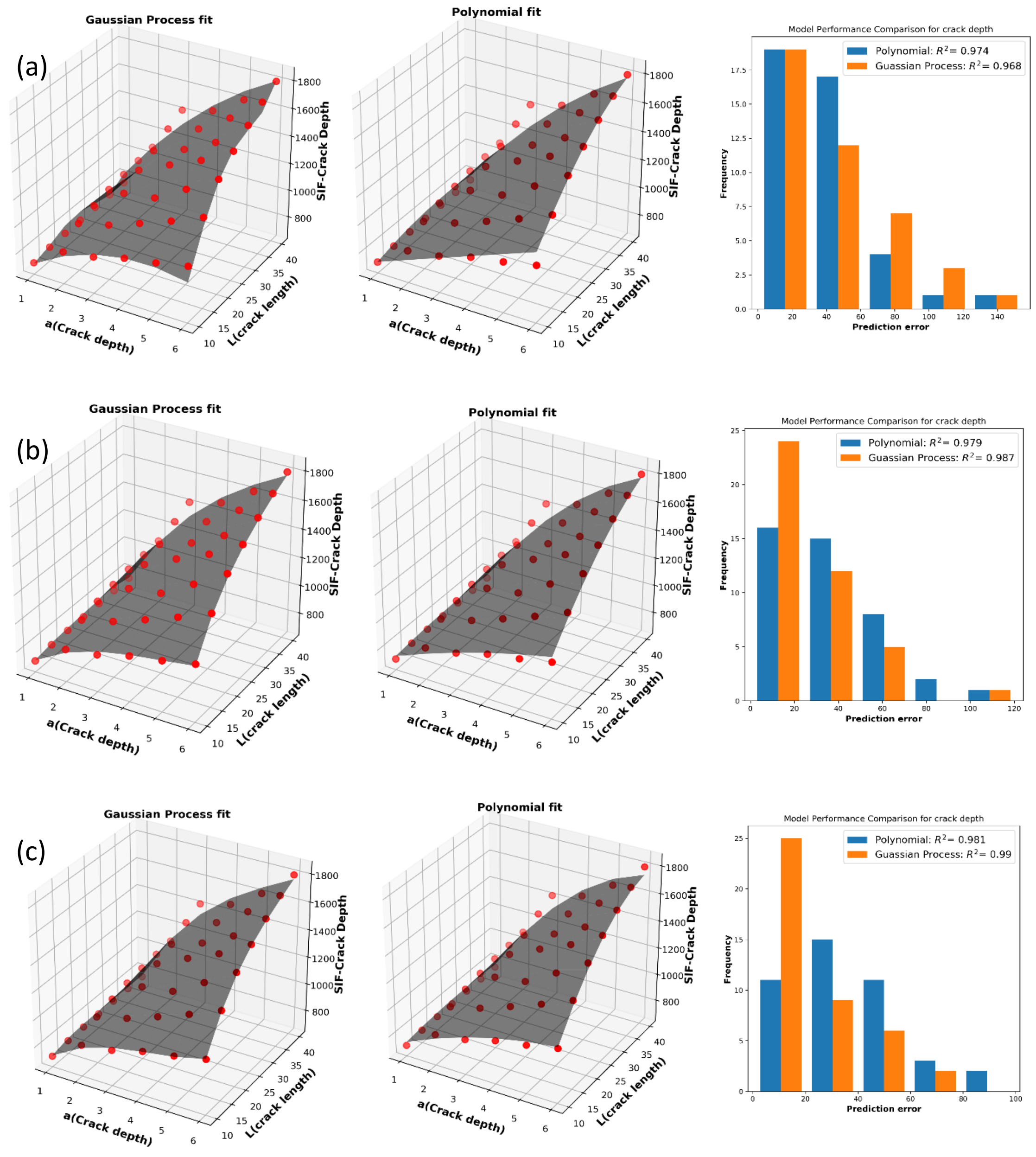

Figure 6-14 comparison of data fitting functions for SIF along crack depth with various training data sizes for patch-repaired pipe model. Gaussian process fit (left), polynomial fit(middle), and R square score and fitting error distribution (right). (a) models fit with 13 training data, (b) model fit with 26 training data, and (c) model fit with 42 training data. Crack lengths are in mm and SIF in MPa.mm-1.

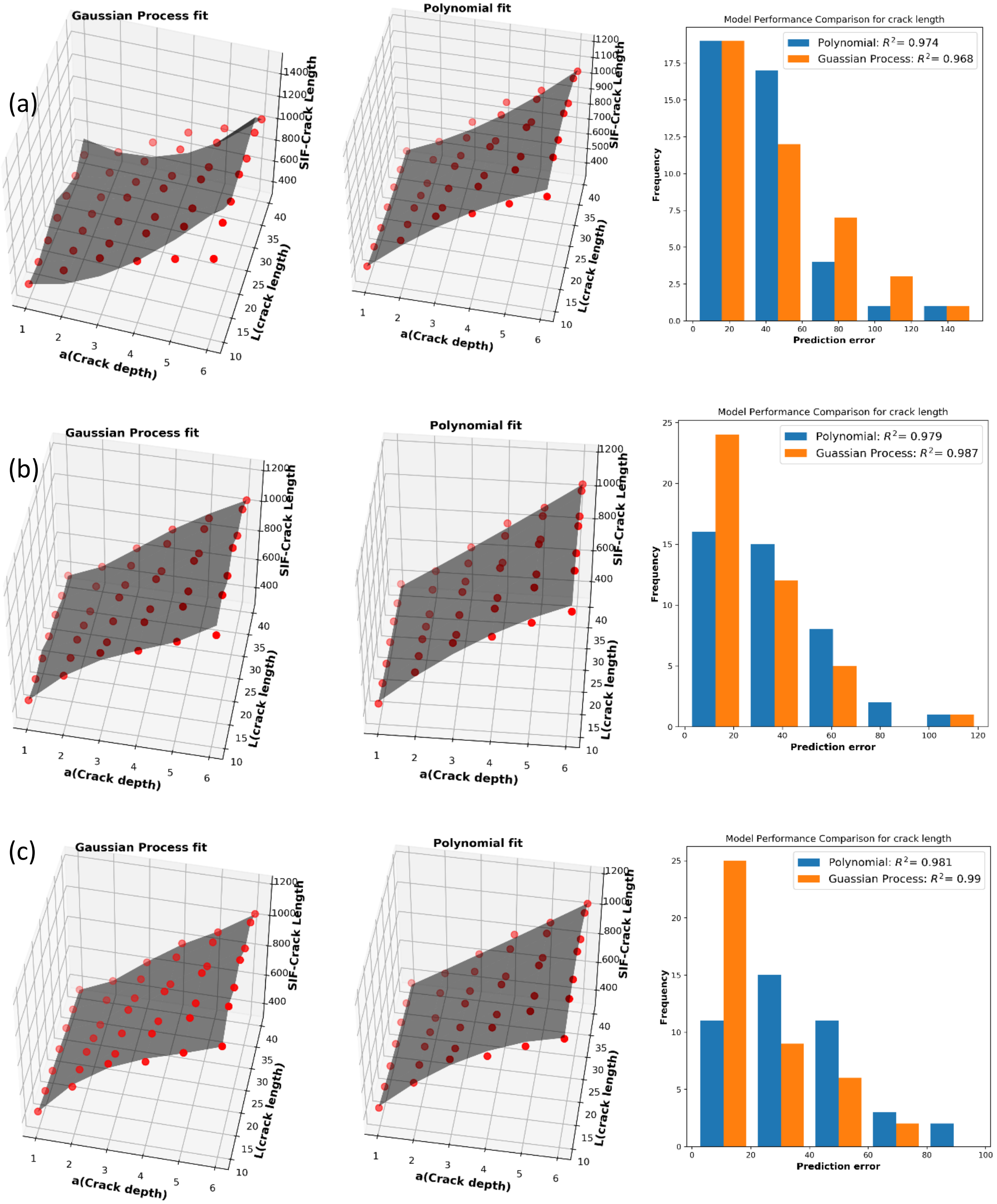

Figure 6-15 comparison of data fitting functions for SIF along crack length with various training data sizes for patch-repaired pipe model. Gaussian process fit (left), polynomial fit(middle), and R square score and fitting error distribution (right). (a) models fit with 13 training data, (b) model fit with 26 training data, and (c) model fit with 42 training data. Crack lengths are in mm and SIF in MPa.mm-1.

As discussed above, it was observed that patch repair significantly reduced the SIF along crack depth. This means under the same loading conditions larger number of cycles would be required to reach failure for the same crack size under repaired condition. Evolution of the crack followed by Paris's equation and computed SIF values are discussed in the next chapter.

7 Fatigue Life Prediction of Pipeline

This chapter establishes Bayesian model that improves its prediction for future state of pipeline condition as more inspection data is entered into the model. The model has backward and forward inference. At each addition of data point on number of cycle and crack size first the model infers the Equivalent Initial Flaw Size (EIFS) probability density function (PDF) and subsequently uses that to infer the PDF for number of cycles to failure. The model can be used to prioritize maintenance orders by isolating sections that are at greatest risk of failure. This is illustrated in as flowchart in Figure 7-1.

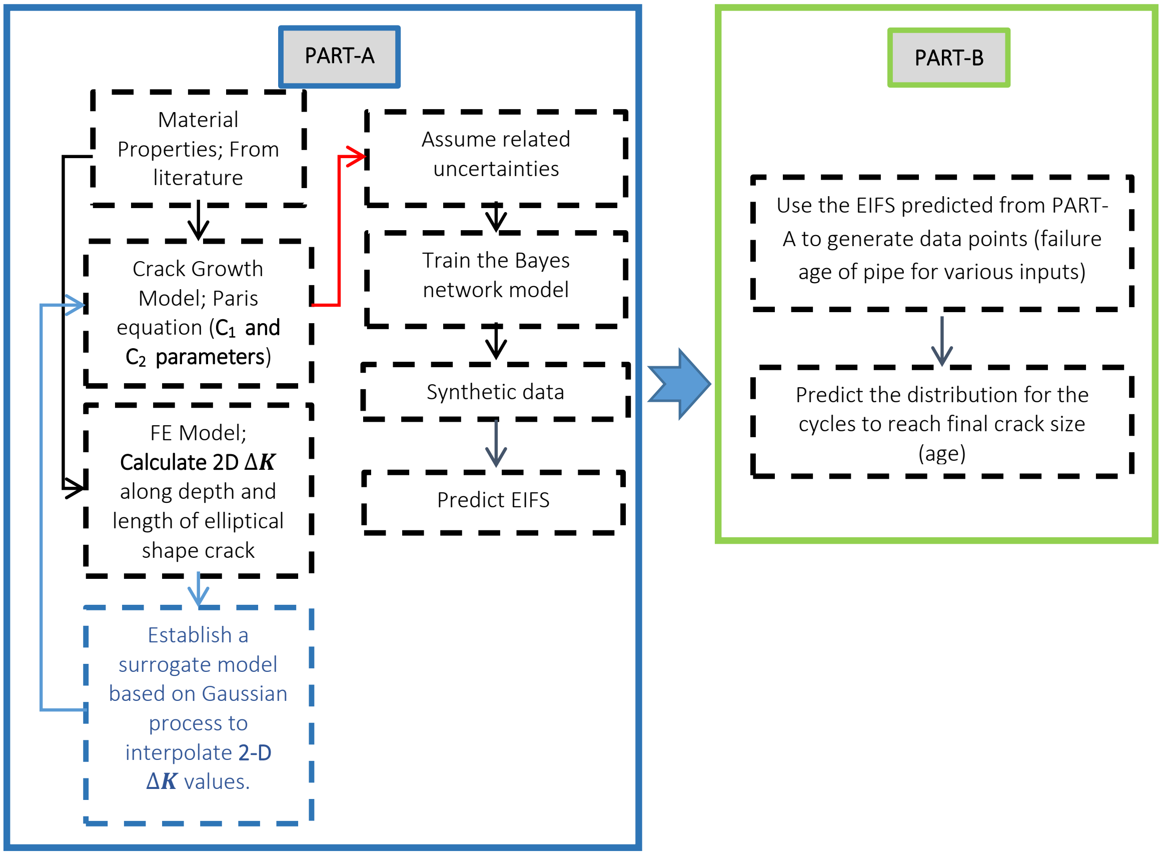
PART-A
Material Properties; From literature
Crack Growth Model; Paris equation (C_1 and C_2 parameters)
FE Model; Calculate 2D ΔK along depth and length of elliptical shape crack
Establish a surrogate model based on Gaussian process to interpolate 2-D ΔK values.
Assume related uncertainties
Train the Bayes network model
Synthetic data
Predict EIFS
PART-B
Use the EIFS predicted from PART-A to generate data points (failure age of pipe for various inputs)
Predict the distribution for the cycles to reach final crack size (age)

Figure 7-1 Flowchart of proposed model.

First, a base Bayesian framework model is established based on synthetically generated data sets generated from crack growth in steel plate from available equations in literature for edge crack in plates. Secondly, FE simulations were performed on pipe model for several cases of crack length and depth in pipe wall thickness. Surrogate models were fitted to compute SIF for intermediary points among actual FE simulated SIF values. The proposed model predicts the failure based on 2-dimenssional crack growth in the pipe wall thickness. Results of the proposed methodology are presented and ground truth values were compared with inferred values.

7.1 Equivalent Initial Flaw Size (EIFS) Concept

The initial flaw size (IFS) in fatigue analysis refers to the small flaws that exist in material’s grain scale. Such flaws do not necessarily follow crack growth regimes such as Paris regime which relates long crack propagation rates to material properties. The small crack growth rate exhibits oscillatory behavior compared to generally monotonic behavior in long crack growth rates.

The equivalent initial flaw size (EIFS) is the concept that allows interpretation of IFS into long crack analysis realm (FAWAZ, 2003; Johnson, 2010). EIFS concept assumes that from the very beginning there exist defects in grain size scale in the material (see Figure 7-2 (a) and (b)) whose growth does not follow crack growth models like Paris’. The EIFS concept allows implementation of long-crack based crack propagation models from the beginning life of a material undergoing cyclic loading (Liu et al. 2009). In other words, the number of cycles required to reach a certain crack length a_f

considering IFS and EIFS, and their respective short-crack and long-crack growth models $g_s(a)$ and $g_l(a)$ as follows:

$$N_f = \int_{IFS}^{a_f} \frac{da}{g_s(a)} = \int_{EIFS}^{a_f} \frac{da}{g_l(a)} \tag{7.1}$$

Are equal and this is illustrated visually in Figure 7-2 (c) and (d).

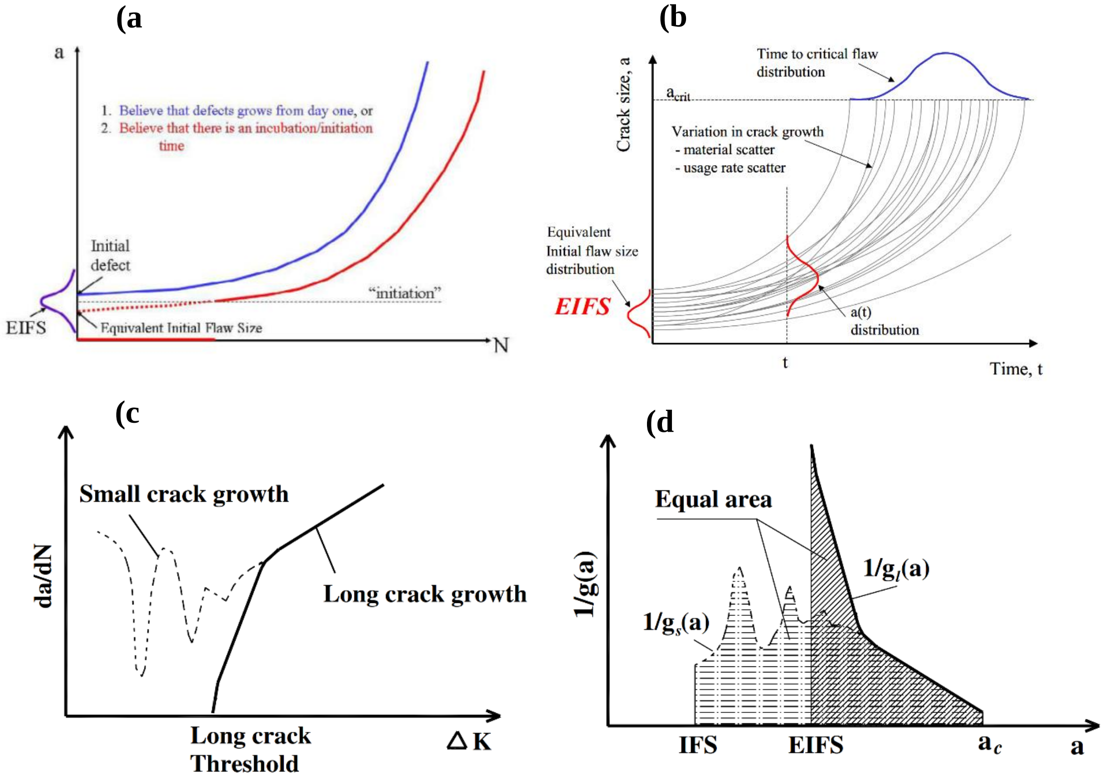

Figure 7-2 EIFS and IFS concept. Top: (a) Concept of crack growth with origination vs. crack existence and growth from day one, (b) Demonstration that how EIFS distribution affects distribution of number of cycles (time) at failure, (after Johnson 2010);Bottom: (c) crack growth behavior with growth rate, (d) equivalency of final cycle N_f with area under inverse growth functions,(after Liu et al. 2009).

7.2 Base Model Development – Steel Plate

Using the available empirical solution for crack propagation in plates with a single edge notch shown in Figure 7-3, in a load controlled boundary conditions (constant remote tensile stress) we establish the base model. To calculate stress intensity factor (SIF) at a given crack length we will use the equation proposed by (Tada et al. 1973) to calculate shape factor in the general SIF formula :

$$K_I = \sigma\sqrt{\pi a}F\left(\frac{a}{b}\right) \tag{7.1}$$

$$F\left(\frac{a}{b}\right) = \sqrt{\frac{2b}{\pi a}\tan\left(\frac{\pi a}{2b}\right)} \times \frac{0.752 + 2.02\left(\frac{a}{b}\right) + 0.37\left(1 - \sin\left(\frac{\pi a}{2b}\right)\right)^3}{\cos(\frac{\pi a}{2b})} \tag{7.2}$$

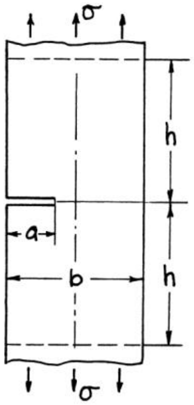

Figure 7-3 Schematics of plate with edge crack under uniform remote tensile stress.

Where, K_I is mode-I SIF, σ is applied nominal constant remote stress, a is crack length, b is plate width, and F is shape factor given by Tada's equation and is valid for any $\frac{a}{b}$ ratio.

The crack growth model will follow Paris' crack growth regime (Paris, 1963):

$$\frac{da}{dN} = C1(\Delta K)^{C2} \tag{7.3}$$

Where, $C1$ and $C2$ are martial properties calibrated based on experimental data, and ΔK is stress intensity factor range between minimum and maximum applied remote stress. $\frac{da}{dN}$ is the rate of crack growth with the change of loading cycle.

Combining the equation for SIF and Paris's regime:

$$N = \int_{c}^{a} \frac{da}{C1(\Delta K)^{C2}} \tag{7.4}$$

$$N = \int_{c}^{a} \frac{da}{C1(\sigma\sqrt{\pi a}F(\frac{a}{b}))^{C2}} \tag{7.5}$$

Where, c is initial crack length. This integral can be numerically calculated using Simpson's method.

The experimental data follows a general function in the form of:

$$N = f(a, \boldsymbol{\phi}) \tag{7.6}$$

Where, $\boldsymbol{\phi}$ is the vector of model parameters such as loading, material properties, and geometry. The elements of $\boldsymbol{\phi}$ are considered random variables in a probabilistic scheme. The parameters governing the distribution of each random variable in $\boldsymbol{\phi}$ are called hyper-parameters , $\boldsymbol{\alpha}$.

The probability of observing target cycle for a given data point of $(N, \boldsymbol{\phi})$ can be framed using a normal distribution:

$$p(N|a, \boldsymbol{\phi}, \beta) = \frac{1}{\sqrt{2\pi\beta^2}} \exp\left(-\frac{[N - f(a, \boldsymbol{\phi})]^2}{2\beta^2}\right) \tag{7.6}$$

Where, p is conditional probability of observing N cycle given model parameters $\boldsymbol{\phi}$, which includes EIFS, crack length a at cycle N, and associated noise in the crack growth model with standard deviation of β:

$$\log(\widehat{N}) = \log(N) \pm \beta \tag{7.7}$$

Where, $\widehat{N}$ is the noisy measurement of the cycle compared to the true cycle N .

Using Bayesian inference the joint probability of target data, N, given model for k number of data points can be derived as:

$$p(\boldsymbol{N}|\boldsymbol{a},\{\boldsymbol{\phi_k}\},\beta) = \prod_{k=1}^{m} p(N_k|a_k,\boldsymbol{\phi_k},\beta)$$

$$= \prod_{k=1}^{m} \frac{1}{\sqrt{2\pi\beta^2}} \exp\left(-\frac{[N_k - f(a_k,\boldsymbol{\phi_k})]^2}{2\beta^2}\right) \tag{7.8}$$

7.2.1 EIFS Direct Probability Density Inference - $\boldsymbol{p(\theta)}$

To develop and verify base model, it was assumed that all the uncertainties are the result of EIFS or initial crack length, θ. The modified distribution is as follows:

$$p(\boldsymbol{N}|\boldsymbol{a},\boldsymbol{\theta},\beta) = \prod_{k=1}^{m} p(N_k|a_k,\theta_k,\beta)$$

$$= \prod_{k=1}^{m} \frac{1}{\sqrt{2\pi\beta^2}} \exp\left(-\frac{[N_k - f(a_k,\theta_k)]^2}{2\beta^2}\right) \tag{7.9}$$

Where, now only EIFS, θ, is the only parameter whose distribution is directly inferred.

To solve for p for each data point, k, we have to solve for $\widehat{N}$ by solving for $f(a_k, c_k)$ following equation (7.5). To calculate the one dimensional integral in equation (7.5) Simpson's quadratic integration rule (Figure 7-4) can be employed which is discussed in detail in (Atkinson, 2008):

$$P(x) = f(a)\frac{(x-m)(x-b)}{(a-m)(a-b)} + f(m)\frac{(x-a)(x-b)}{(m-a)(m-b)}$$

$$+ f(b)\frac{(x-a)(x-m)}{(b-a)(b-m)} \quad (7.10)$$

$$\int_a^b P(x)\,dx \approx \frac{b-a}{6}\left[f(a) + 4f\left(\frac{a+b}{2}\right) + f(b)\right] \qquad (7.11)$$

Where, $P(x)$ is the estimate of function of interest, $f(x)$, and integration is performed within $[a, b]$ bounds. In the context of our problem the function to be estimated is $f(a) = \frac{1}{C1(\sigma\sqrt{\pi a}F(\frac{a}{b}))^{C2}}$ which is the function being integrated in equation (7.5).

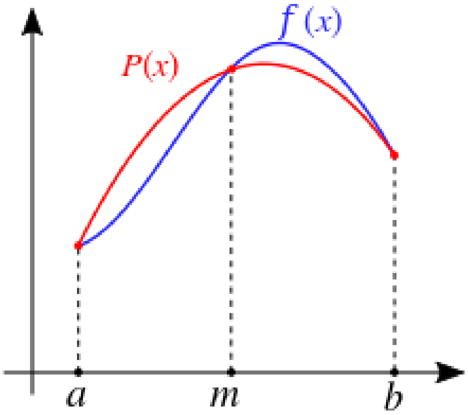

Figure 7-4 Simpson's quadratic integration rule is estimating $f(x)$ with $P(x)$ to perform integration from $x = a$ to $x = b$.

To evaluate the proposed base model, various sets of data points where generated and β=10% noise was added to the data to account for uncertainty within crack growth model. The training data were generated according to the following framework:

1- It was assumed that the initial flaw size, $\boldsymbol{\theta}$, follows a normal distribution with assumed mean and standard deviation. k samples were drawn from this distribution. In this study, it was assumed that the distribution of EIFS is around 1mm.

2- Uniform distributions was assumed for final crack size, a, and k samples were drawn from this distribution. The initial value of this uniform distribution was assumed to be at least 3 times of the assumed standard deviation of the normal distribution for c, larger than the mean assumed for c.

3- Given a and c for each data point the corresponding number of cycles, N, for that data point was calculated following equation (7.5) and using Simpson's quadratic numerical integration method.

4- A random noise with zero mean and β standard deviation was added to the calculated N.

5- It should be again noted that no fatigue lab test was performed and crack data was generated synthetically.

Figure 7-5 shows a sample of synthetically generated data points. In Figure 7-5(a) final crack size and its corresponding cycle number is visualized for k data point which for this example they are 20 data points.

Table 7-1 shows the selected properties and assumed parameters for crack growth in the base model for a steel plate with an edge crack.

Table 7-1 Material and model parameters used in the plate model.

Parameter	**Definition - Value**
C1	3.39e-13
C2	2.9
β	10%
σ	40 MPa
b (plate width/pipe wall thickness)	7.1 mm

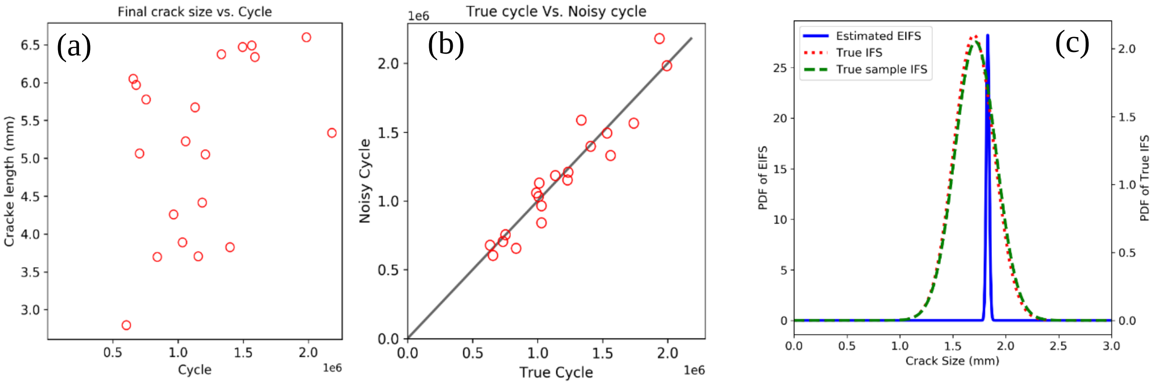

Figure 7-5 Synthetically generated data in plate model. (a) (N, a) pair data set sample, (b) True N versus noisy N, and (c) Comparison of inferred EIFS distribution and True EIFS distribution.

For each data point a likelihood probability density is calculated and the product of all data point likelihoods as shown in equation (7.9) will establish estimated probability density of EIFS. Figure 7-6 shows box plots for the data set containing 20 data points. The variation of the inferred EIFS distribution at each data point is clearly distinguishable.

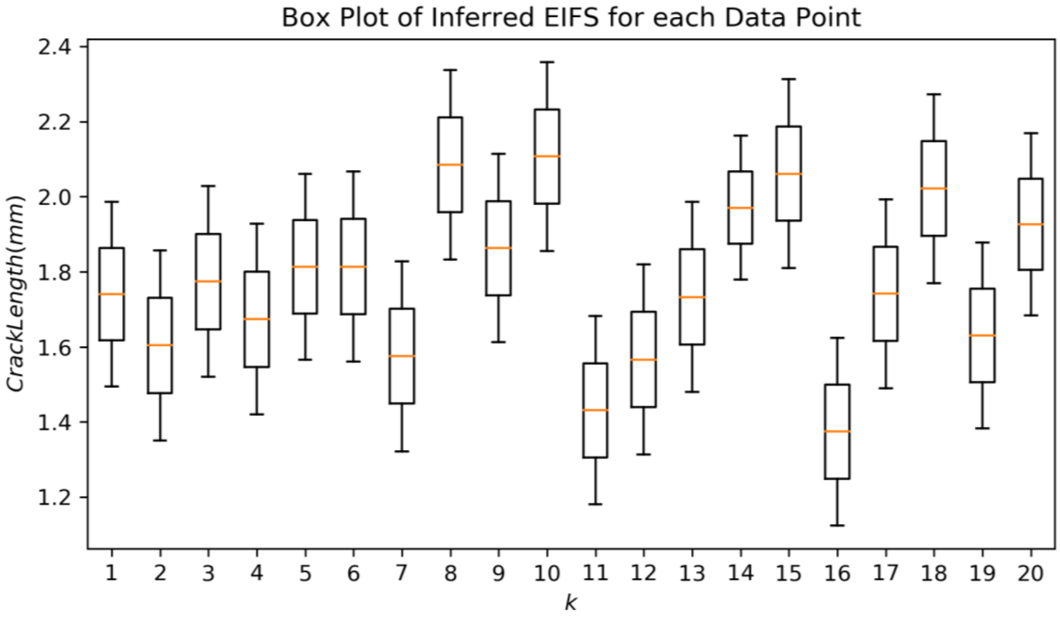

Figure 7-6 Box plot illustrating EIFS distribution for individual data points.

The final inferred EIFS distribution shown in Figure 7-5 (c) based on 20 data pints shows that the estimation for mean is very close to the mean of the true distribution but the standard deviation or spread is not captured very well. To improve the inferred distribution, we will try to infer the distribution parameters instead of distribution itself in the next section.

7.2.2 EIFS Probability Density Inference with Hyper parameters- $\boldsymbol{p(c|\alpha)}$

In this section instead of inference on EIFS itself, the parameters of the assumed governing distribution for EIFS conditioned on its distribution parameters will be inferred:

$$p(\boldsymbol{\theta}|\boldsymbol{\alpha}) = \prod_{k=1}^{m} p(\theta_k|\boldsymbol{\alpha}) \tag{7.12}$$

$$p(\boldsymbol{N}|\boldsymbol{a},\boldsymbol{\alpha},\beta) = \int p(\boldsymbol{N}|\boldsymbol{a},\boldsymbol{\theta},\boldsymbol{\alpha},\beta)p(\boldsymbol{c}|\boldsymbol{a},\boldsymbol{\alpha},\beta)\,d\boldsymbol{c} = \int p(\boldsymbol{N}|\boldsymbol{a},\boldsymbol{\theta},\beta)p(\boldsymbol{c}|\boldsymbol{\alpha})\,d\boldsymbol{\theta} \tag{7.13}$$

$$p(\boldsymbol{N}|\boldsymbol{a},\boldsymbol{\alpha},\beta) = \prod_{k=1}^{m} \int \frac{1}{\sqrt{2\pi\beta^2}} \exp\left(-\frac{[N_k - f(a_k,\theta)]^2}{2\beta^2}\right) p\,(\theta|\boldsymbol{\alpha})d\theta \tag{7.14}$$

Now in this equation where we have introduced a prior probability for EIFS, $p(\boldsymbol{\theta}|\boldsymbol{\alpha})$, which is conditioned on $\boldsymbol{\alpha}$ (Hoff, 2009). This is forms a hierarchical Bayes model shown in Figure 7-7 (b).

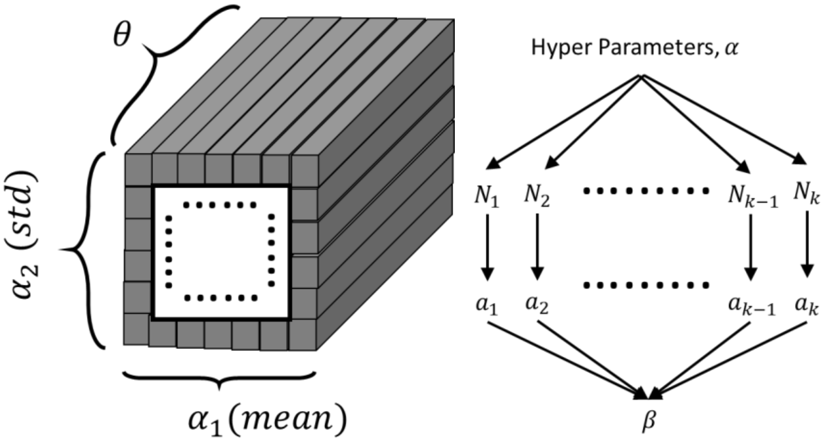

Figure 7-7 (a) Initialization of likelihood array. For a normal distribution the hyper parameters α_1 and α_2 , are mean and standard deviation. For each pair of hyper-parameters an $EIFS$ distribution which are indicated by long gray blocks are generated , shown with θ. (b) Bayes structure with hyper parameters.

In this approach an additional integration is introduced. This integration can be solved by applying Simpson’s quadratic integration twice.

Let us elaborate inference process of hyper-parameters of $EIFS$ distribution. We select some possible lower and higher bounds for both mean and standard deviation. Mathematically the bounds for mean can be from $-\infty$ to $+\infty$, and for standard deviation it can be from 0 to $+\infty$; but to save a huge computation cost especially if we are considering a finer step size or mesh, with a good guess based on engineering judgement, we can select appropriate bounds. The physics of the problem such as maximum possible crack depth and minimum possible crack depth, a non- negative value, would give initial intuition.

In the next step we select a small enough step size to capture a smooth outcome. This can be achieved by running few trial cases. After selecting the appropriate step size for both standard deviation range and mean range we can generate a θ distribution (we chose bounds of θ $(EIFS)$ from zero to close to maximum possible crack depth or plate thickness, b) and fill in all the θ blocks shown in Figure 7-7 (a).

Now, every time we loop over to a new data point we update all the θ blocks in the cubic array shown in Figure 7-7 (a). Every single result shown in Figure 7-9 is the solution of the nested integral in equation (7.14) and each of those are the joint likelihood probability of hyper-parameters, namely standard deviation and the mean. This process is summarized in a flowchart in Figure 7-8.

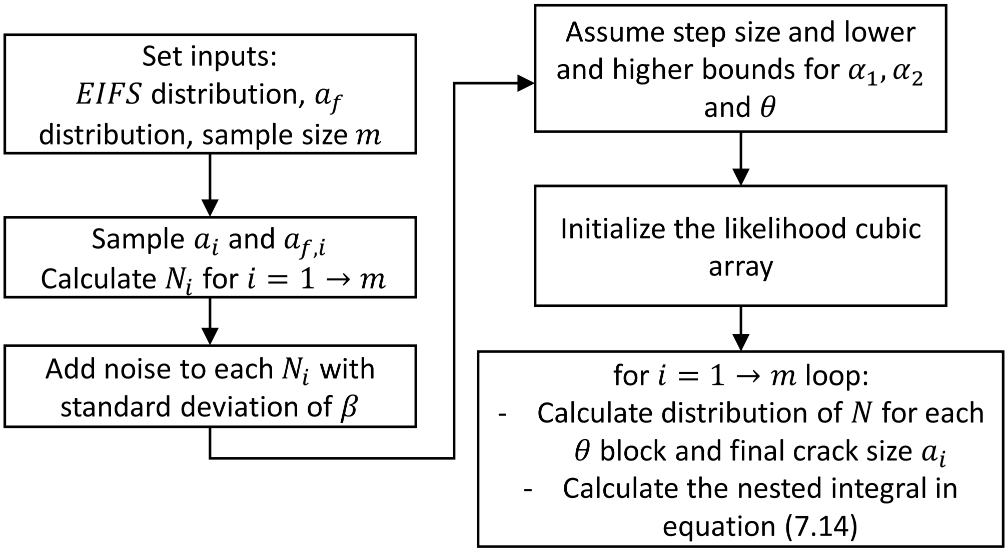
Set inputs:
$EIFS$ distribution, a_f distribution, sample size m
Sample a_i and $a_{f,i}$
Calculate N_i for $i = 1 \rightarrow m$
Add noise to each N_i with standard deviation of β
Assume step size and lower and higher bounds for α_1, α_2 and θ
Initialize the likelihood cubic array
for $i = 1 \rightarrow m$ loop:
- Calculate distribution of N for each θ block and final crack size a_i
- Calculate the nested integral in equation (7.14)

Figure 7-8 Flowchart of estimating the likelihood of $EIFS$ distribution hyper parameters.

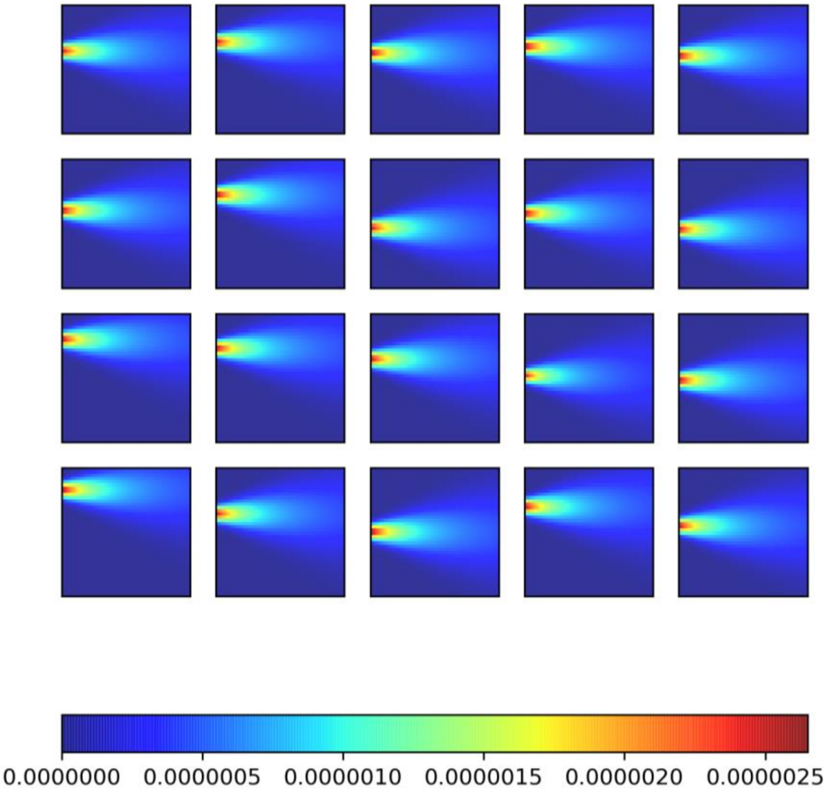

Figure 7-9 Joint likelihood of mean and standard deviation ($\boldsymbol{\alpha}$ parameters) of EIFS distribution for all 20 data points

Integrating the resulting joint probability density along mean and standard deviation separately yields the marginal probability densities of mean and standard deviation of the $EIFS$. As it can be seen from Figure 7-10(d) and Figure 7-5(c) the accuracy of $EIFS$ distribution estimation using hierarchical model and hyper-parameters has increased significantly.

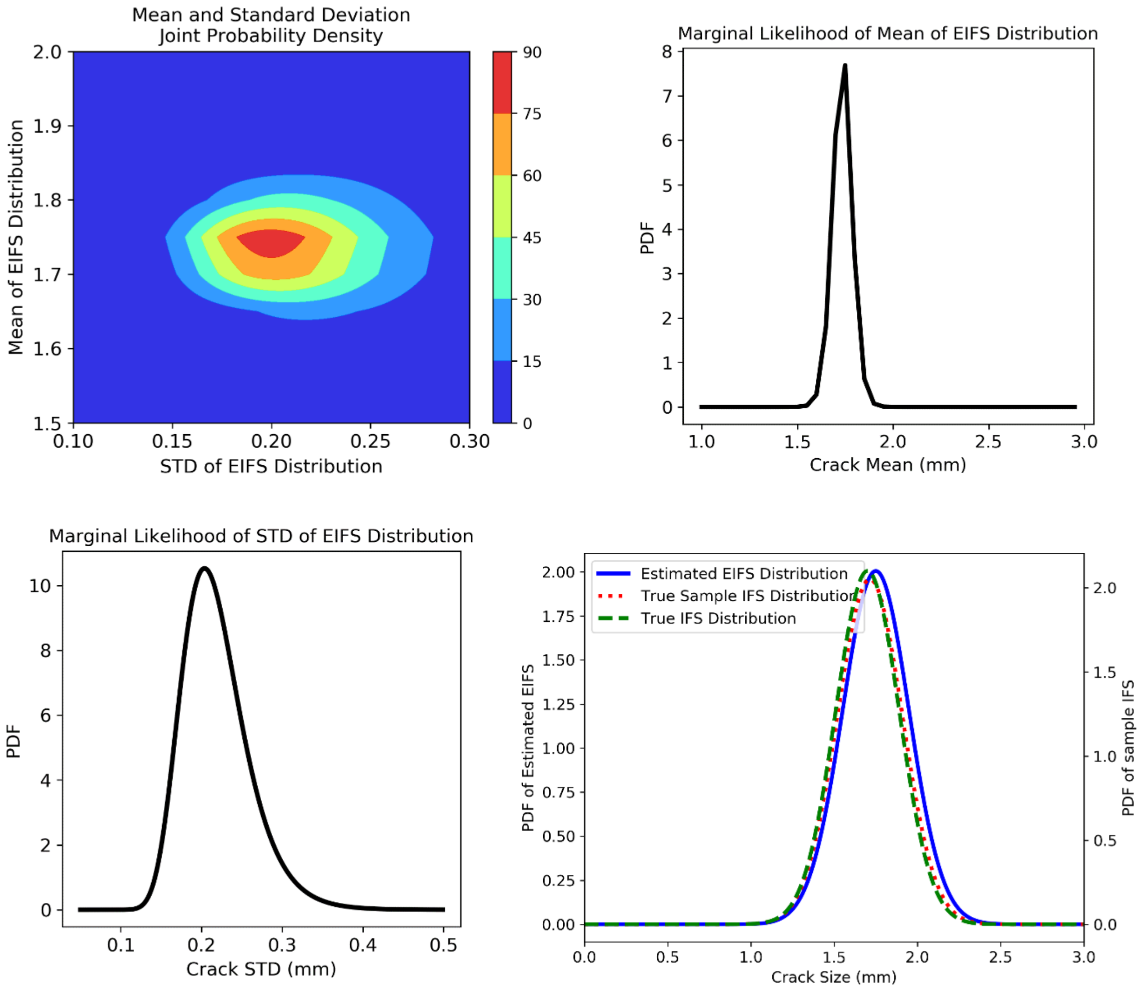

Figure 7-10 (a) Joint probability density function of mean and standard deviation of EIFS, (b) Marginal probability density of mean of EIFS, (c) Marginal probability density of standard deviation of EIFS. (d) Estimated EIFS density vs. True assumed density for EIFS.

It is clear that inference directly on EIFS distribution can estimate the mean within an acceptable range with less than $0.1\ mm$ error (less than 6%), but it fails to predict standard deviation and it has more than 90% error in standard deviation prediction. On the other hand, the hierarchical model was able to predict both mean and standard deviation with high accuracy. The error for estimating EIFS distribution mean was 2% and error for estimating standard deviation of EIFS distribution was 4.6%. Comparison of results between simple maximum likelihood (direct EIFS inference) and hierarchical Bayesian analysis are shown in Table 7-2.

Table 7-2 Comparison of EIFS inference results using discussed methods.

Parameters	**True Value**	**Inference on EIFS**	**Inference on Hyper Parameters**
Mean	1.715 mm	1.831	1.750 mm
Standard deviation	0.195 mm	0.014	0.204 mm

7.2.3 Estimating probability and cycle of the failure

To estimate probability of failure we need to set a failure crack length/depth criteria, a_f. This could be a percentage of the width in which crack is being propagated. From previous section we determined probability density of the EIFS for the plate problem. For the plate problem only a is the variable of crack that is growing and crack length does not apply.

Now, having the EIFS distribution we can proactively estimate distribution of number cycles required to reach failure as we gather inspection data over time. In the case of pipe problem, the inspection data could include length and depth of the cracks detected in the wall of pipe section.

To test this hypothesis, we need to generate synthetic inspection data points corresponding the number of cycles and respective crack length at that cycle (or time). We will use our crack growth model to progress crack length from the assumed initial size to assumed final crack size for each synthetically generated data point.

Initial crack length is randomly sampled from EIFS distribution that was estimated from section 2-3. As for the failure crack depth, a certain percentage of plate width, b, (and later pipe wall thickness in the pipe model) is assumed as the mean of failure crack depth (maximum allowable crack length). To include uncertainty for the failure crack length, a standard deviation is added to the assumed mean of failure crack depth to generate a normal distribution for the final crack length. In addition, for each randomly sampled EIFS, a corresponding failure crack depth is sampled from failure crack depth distribution and hence the number cycles are calculated as shown in the flow chart in Figure 7-11. The flow chart shown in this figure can be used in either plate problem or pipe problem. In the plate problem, being a 2D model, crack only grows in one dimension (one crack front), while in the pipe model crack grows along length and depth. Consequently, their corresponding SIF functions are single variate and bivariate, respectively.

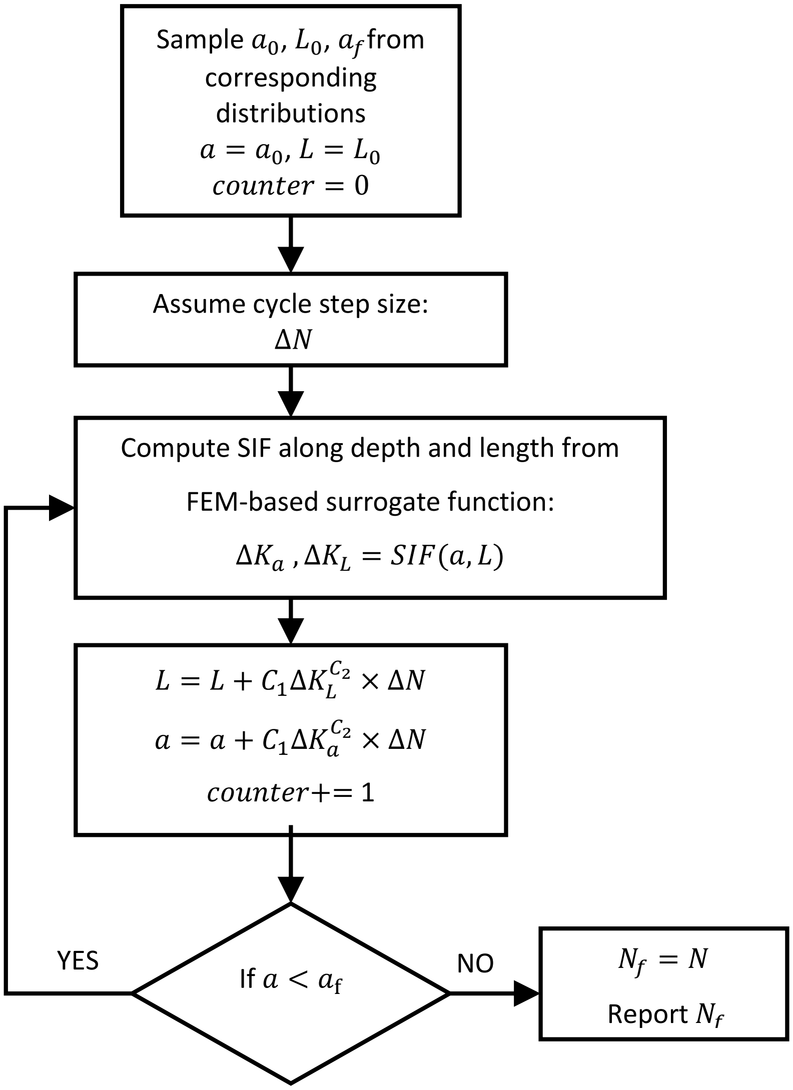
Sample a_0, L_0, a_f from corresponding distributions
$a = a_0, L = L_0$
$counter = 0$
Assume cycle step size: ΔN
Compute SIF along depth and length from FEM-based surrogate function:
$\Delta K_a, \Delta K_L = SIF(a, L)$
$L = L + C_1 \Delta K_L^{C_2} \times \Delta N$
$a = a + C_1 \Delta K_a^{C_2} \times \Delta N$
$counter += 1$
If $a < a_f$
YES
NO
$N_f = N$
Report N_f

Figure 7-11 Flow chart that shows derivation of number of cycles for at failure depth in generating synthetic data.

For each synthetic data point generated using the algorithm that was introduced earlier, the number of cycles to the failure point corresponding to the sampled EIFS and failure crack depth is estimated. Using Bayesian analysis two forecast scenarios are viable:

1- Estimating the distribution of number of loading cycles to failure (N_f) based on observed numbers of data points sampled from EIFS and failure crack depth distributions. This can only be done on the synthetic data or field data where data was collected after observing actual failure in the field or lab test.

2- Estimating the distribution of number of loading cycles to failure (N_f) based on observed numbers of data points sampled from EIFS and any random final crack depth that is sampled from a uniformly distributed final crack size from the sampled EIFS to any value smaller than assumed value for mean of failure crack depth. i.e. We will be able to predict probability distribution of number of loading cycles to failure from observed data (loading cycles vs crack depth) as new data points are added.

It should be mentioned the distributions resulted from scenario-1 may be used as an informative prior in the Bayesian process of estimating the distribution of number of cycles to failure in scenario-2. The mathematical expression is as follows:

$$p\left(\boldsymbol{N}\middle|\boldsymbol{N_{range}},\beta\right) = \prod_{k=1}^{m} p\left(N_k\middle|\boldsymbol{N_{range}},\beta\right)$$

$$= \prod_{k=1}^{m} \frac{1}{\sqrt{2\pi\beta^2}} \exp\left(-\frac{\left[N_k - \boldsymbol{N_{range}}\right]^2}{2\beta^2}\right) \qquad (7.15)$$

Where, $\boldsymbol{N_{range}}$, is a vector with lower bound and higher bound that covers the range of the number of cycles that may cause failure.

The upper bound of $\boldsymbol{N_{range}}$ can be calculated by assuming an extreme case of smallest possible EIFS and largest possible crack depth. The probability of such combination is very low in reality and even in case of synthetically generated data. For example, Figure 7-12, shows an illustration of possible failure cycle outcomes for a steel plate with an edge crack. This example includes 250,000 data points which was generated by sampling 500 $EIFS$ and 500 a_f from distributions $EIFS \sim N(1.5, 0.12)$ *and* $a_f \sim N(6, 0.1)$, respectively. As it can be seen in Figure 7-12, for this particular example the number of cycles does not reach 3 million. While calculating the number of cycles for the extreme case by considering $IFS = 0.1mm$, and $a_f = 6.99mm$, yields the maximum number of cycles at about 3.8 millions.

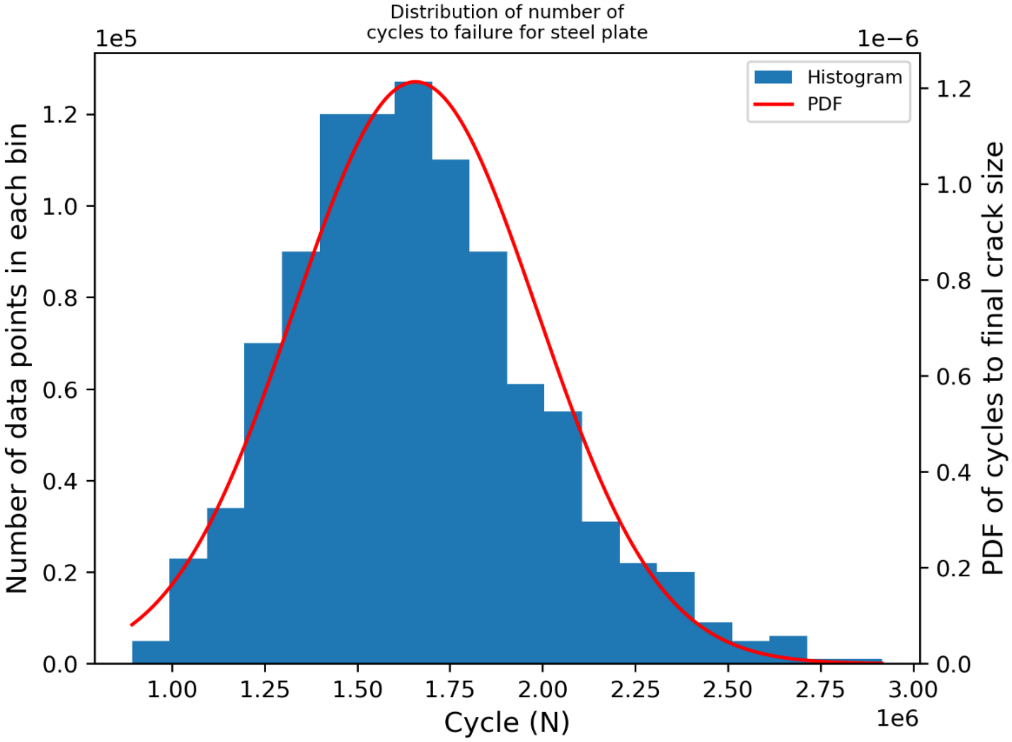

Figure 7-12 An illustrative example of possible distribution of number cycles to failure for a steel plate with thickness of 7mm. assumptions: $EIFS \sim N(1.5, 0.12)$, and $a_f \sim N(6, 0.1)$.

With this overview of methodology, we now investigate the estimations of number cycles to failure for various synthetic data sizes by directly estimating $\boldsymbol{N_{range}}$ distribution for the plate problem with edge crack. The following flowchart, shown in Figure 7-13 demonstrates the process for estimating the distribution of number of cycles to failure.

The non-informative prior was selected as unit integer. The informative prior may be a PDF generated the similar way as the example shown in Figure 7-12 by sampling from EIFS and an assumed failure crack length. In this particular method using a good informative prior will reduce the standard deviation of the final posterior PDF.

To demonstrate this methodology with example, results of various estimations for number of cycles to failure is shown in Figure 7-14 (top). In this example the inference was performed on four datasets comprising 5, 15, 30, and 50 data points.

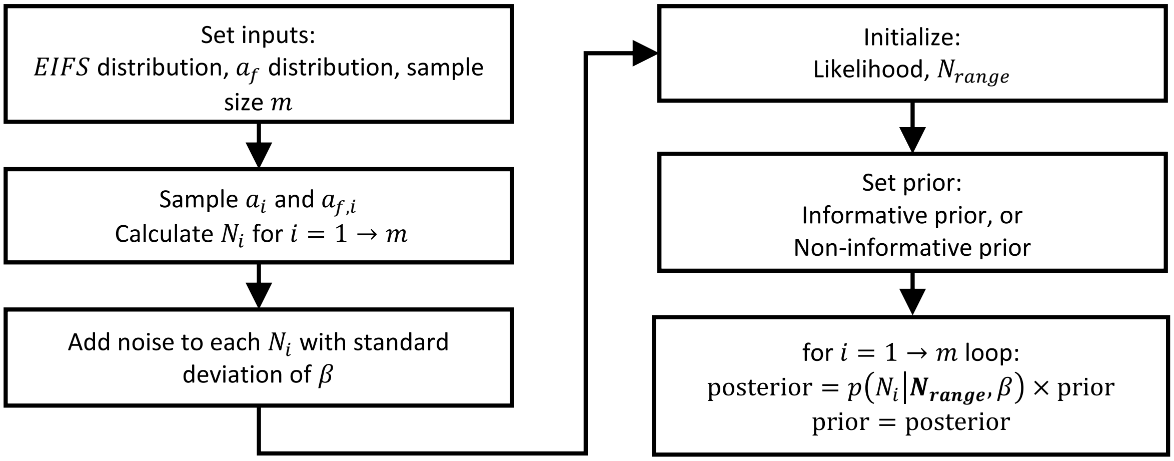
Set inputs:
$EIFS$ distribution, a_f distribution, sample size m
Sample a_i and $a_{f,i}$
Calculate N_i for $i = 1 \rightarrow m$
Add noise to each N_i with standard deviation of β
Initialize:
Likelihood, N_{range}
Set prior:
Informative prior, or
Non-informative prior
for $i = 1 \rightarrow m$ loop:
posterior $= p(N_i | \boldsymbol{N_{range}}, \beta) \times$ prior
prior = posterior

Figure 7-13 Flowchart of deriving estimated distribution for number cycles for final (or failure) crack size distribution.

From the Figure *7-14* (top) we can observe that as more data points are added (blue 5 samples and red 50 samples)the distribution becomes sharper at peak and closer to the mean of sample distribution shown in black dash lines. As we also in the case of $EIFS$ inference this method is better if only a single estimate is desired rather than the whole distribution. Table *7-3* Comparison of direct inference of $\boldsymbol{N_{range}}$ on different sample sizes. Table 7-3 lists the parameters of the distributions.

To have the standard deviation also represented in our inference process we will again resort to inferring hyper parameters of the $\boldsymbol{N_{range}}$ distribution as we did for $EIFS$. Figure 7-14 (bottom left) shows an example of resulting joint likelihood probability density for mean and standard deviation of the $\boldsymbol{N_{range}}$ distribution with 50 samples. To the right we can see progression of the $\boldsymbol{N_{rang}}$ distribution inference with 5 samples (blue curve) to 50 samples (red curve). The dashed black distribution is observed sample distribution. As it can be seen clearly there is very good match between predictions and observed samples. Table 7-4 summarizes the parameters of this distributions.

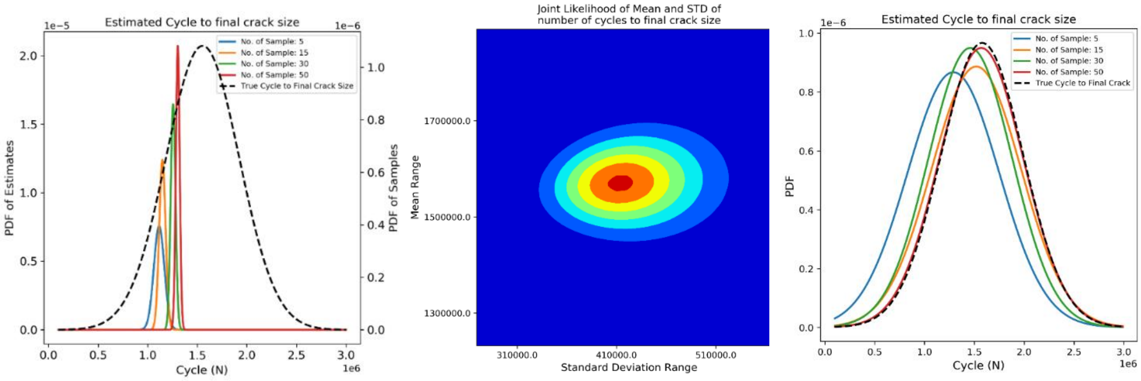

Figure 7-14 Estimating the distribution for number of cycles to reach final crack size. Inferring $\boldsymbol{N_{range}}$ likelihood density directly for various sample sizes(left), Inferring $\boldsymbol{N_{range}}$ hyper parameters' joint likelihood (middle), and likelihood densities of $\boldsymbol{N_{range}}$ for various sample sizes (right).

Table 7-3 Comparison of direct inference of $\boldsymbol{N_{range}}$ on different sample sizes.

No Samples	**STD**		**Mean**	
	True	**Estimate**	**True**	**Estimate**
5	515847	52757	1422988	1115177
15	530064	32175	1569746	1148483
30	425478	24247	1572589	1256449
50	368879	19258	1553850	1303446

Table 7-4 Comparison of inference of $\boldsymbol{N_{range}}$ with hyper parameters on different sample sizes.

No Samples	**STD**	**Mean**

	True	Estimate	True	Estimate
5	482924	460000	1318528	1290000
15	425447	450000	1516247	1520000
30	428778	420000	1493829	1460000
50	412633	420000	1578909	1570000

It is worth noting that final number cycles were more affected by the distribution of the $EIFS$ than the final crack size during process of generating synthetic data. This another instance that the exemplifies importance of $EIFS$ distribution inference.

7.3 Pipe Model Development

In this section we will infer EIFS for crack depth, length crack depth and use those inferred values to estimate the distribution for number of cycles to estimate cycle at final crack length. We introduced SIF computation procedure using FE simulations and surrogate function in Chapter 6.

7.3.1 EIFS Direct Probability Density Inference

Applying the aforementioned method to crack growth in pipeline brings a few more challenges. The case for crack growth in an edge crack in steel plate only assumes crack growth in single dimension while the crack growth in pipe wall is assumes as a semi-elliptical shape that has two growth fronts; along the depth and along the length of the crack. This property makes this problem similar to the problem of $EIFS$ distribution with hyper-parameters (introduced in the section 7.2.2) which would require cubic likelihood array. Applying the 2-dimmensional version of crack growth algorithm illustrated in Figure 7-11,we will generate 30 data points as shown in Figure 7-15. The finer the step size for cycles and mesh size for crack length and depth the longer it takes for the code to yield the results.

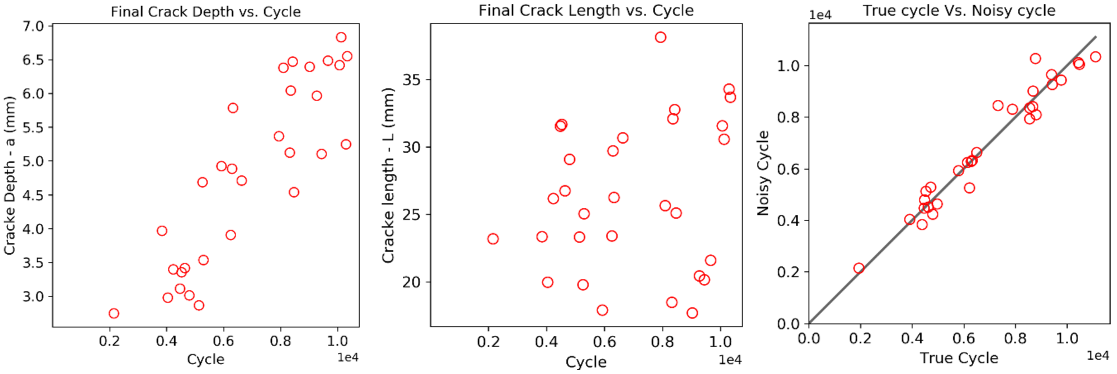

Figure 7-15 Synthetic data points generated for 2 dimensional crack growth in pipe wall. Crack depth vs. cycle(left), crack length vs. cycle (middle), and true cycle vs. noise added cycle (right).

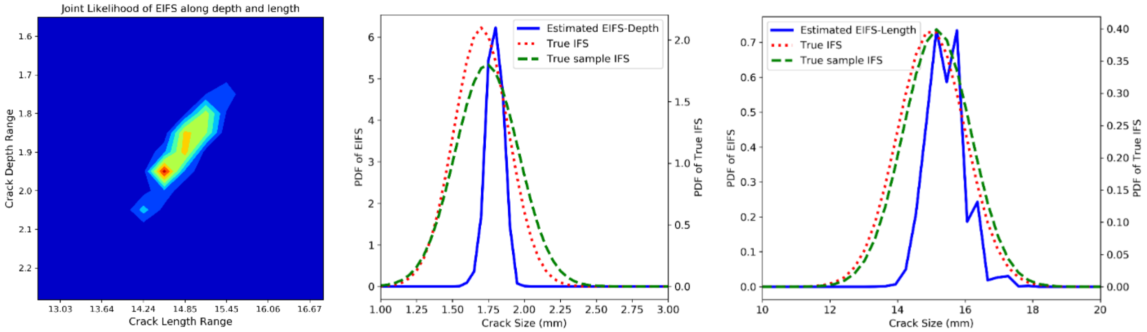

Figure 7-16 Comparison of estimated and true marginal $EIFS$ likelihood distributions. Joint likelihood distribution of crack length and depth (left), Crack depth distribution (middle), crack length (right). for 30 data points.

Consequently, there exists a likelihood distribution for every possible pair of crack length and crack depth. So, in the end we will find a joint likelihood distribution of $EIFS$ for crack length and crack depth. The example of such joint likelihood distribution is shown in Figure 7-16 (left). We can solve for marginal likelihoods of EIFS for crack length and crack depth by integrating out the other variable using Simpsons quadrature technique introduced earlier. Computed marginal likelihoods of crack length and depth are shown in in Figure 7-16 (middle and right). As it can be seen in the figure, the algorithm does very good job in estimating mean of the true distribution as we saw with plate problem with edge crack. Similar to the plate problem, standard deviation is not well estimated in this method.

To improve inference on standard deviation we could use hyper-parameter estimation as we did for plate problem. In comparison to the plate problem where crack growth was single dimensional, we only had to solve marginal likelihoods once for each data point. In the case pipe crack growth given we consider hyper parameters (mean and standard deviation) for both crack depth and crack length, we will have 4 hyper parameters to estimate. Solving this problem with Simpson's quadrature will be extremely expensive. To solve this problem Monte Carlo simulations will work more efficiently as also mentioned in (Makeev et al. 2007: Cross et al. 2007: Sankararaman et al. 2010). We chose to assume standard deviation for our problem in the section where we infer number of cycle to final crack size. This is because we did not perform hyper parameter estimates for mean and standard deviation of crack depth and length separately as we did in case of plate problem (see Figure 7-10, and Table 7-2 *Comparison of EIFS inference results using discussed methods.*). Such computation can be performed using Marcov Chain Monte Carlo (MCMC) (Geyer, 1991, 1992; Gilks et al. 1995).

The properties of estimates for EIFS are summarized in Table 7-5.The estimated values of standard deviation in this table are not capturing the variability compared to true values. The assumed values were selected based on many observations and engineering judgments. Values between 0.1 to 0.5 mm for depth and 0.5 to 1.5 mm can be considered good guess range for standard deviations according to author's observations. We will use these estimated values as input for the model to do inference of the likelihood distribution for the number of cycles to failure in the next section.

Table 7-5 Estimated vs. true distribution values for $EIFS$ along depth and length.

$EIFS$	Mean		STD		
	True	**Estimate**	**True**	**Estimate**	**Assumed**
Depth	1.74	1.794	0.222	0.052	0.19
Length	15.166	15.429	1	0.555	1

7.3.2 Estimating probability and cycle of the failure

Here we will follow the similar steps as we did for plate problem to estimate the distribution for the number of cycles to failure, $\boldsymbol{N_{range}}$. Using the methodology discussed in section 7.2.3 for plate problem we will estimate the distribution of number cycle to failure. As shown in Figure 7-17(top) the direct inference on $\boldsymbol{N_{range}}$ distribution is shown for various sample sizes. We can see the progressive approach of the predictions towards the true sample distribution from 5 samples (blue) to 50 samples (red). The ground truth of the sample distribution is shown in black dashed line. As with previous observation using direct inference we can see that while the standard deviation is not accurately captured the mean or expected value of number of cycles to final crack size is very well captured. The summary of data for this model is presented in Table 7-6.

Table 7-6 Comparison of direct inference of $\boldsymbol{N_{range}}$ on different sample sizes.

No Samples	STD		Mean	
	True	**Estimate**	**True**	**Estimate**

5	836	321	8240	7080
15	898	202	8455	7732
30	1039	147	8626	7986
50	1000	116	8580	8165

Using hyper parameters to perform estimations we will have the joint marginal likelihood distribution of mean and standard deviation of number of cycles to failure, shown in Figure 7-17 (bottom left).

Integrating along mean and standard deviation separately we have marginal distribution for mean and standard deviation of number of cycles to failure separately. Using the expected value of the latter distributions we construct the distribution for number of cycles to failure. These distributions for various number data points or samples are shown in Figure 7-17 (bottom right). We can see that as more data points are added to the model, from samples (blue curve) to 50 samples (red curve), the estimated distribution very closely matches the true sample distribution shown in black dashed line. The results for various sample sizes are summarized in Table 7-7.

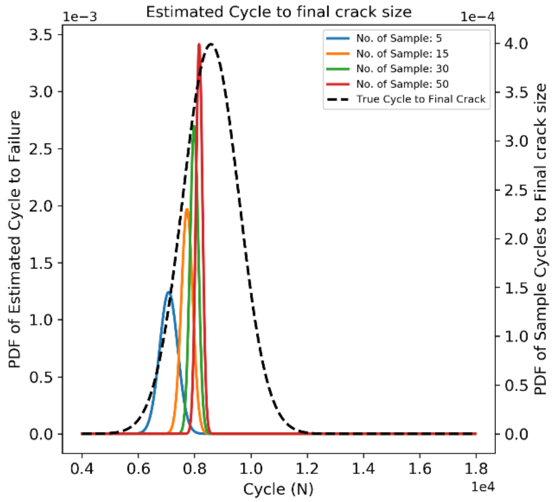

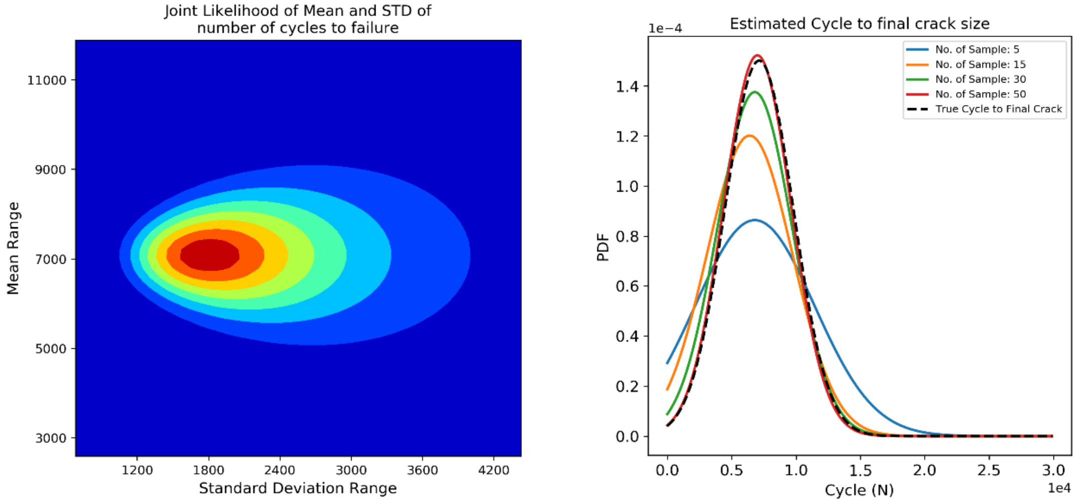

Figure 7-17 Estimating the distribution for number of cycles to reach final crack size. Inferring $\boldsymbol{N_{range}}$ likelihood density directly for various sample sizes(top), Inferring $\boldsymbol{N_{range}}$ hyper parameters' joint likelihood (bottom left), and likelihood densities of $\boldsymbol{N_{range}}$ for various sample sizes (bottom right).

Table 7-7 Comparison of inference of $\boldsymbol{N_{range}}$ with hyper parameters on different sample sizes.

No Samples	**STD**		**Mean**	
	True	**Estimate**	**True**	**Estimate**
5	3885	4620	6966	6800
15	3195	3320	6363	6400
30	2876	2900	6918	6800
50	2657	2620	7136	7000

8 Conclusions and Recommendations

8.1 Conclusions

A corrosion chamber was developed and built to emulate accelerated corrosion environment. Saltwater spray, heat, UV exposure, and freezing cycles were used to test durability of inorganic, organic, and hybrid coatings and compare their performance. Various specimens and exposure time periods were experimented. Different methods of coating application such as foam brush, bristle brush and, HVLP sprayers were used to observe effect of applications methods. We performed pull-off strength tests on various coating systems before and after corrosion cycles to investigate extent of deterioration of coating adhesion to steel substrate.

It was demonstrated that the developed chamber and designed cycle effectively induced corrosion in test specimens. It was observed that due to inherent porous surface of geopolymer coating, very thin coating thickness layers (on average smaller than 100µm) has more susceptibility to premature corrosion. In addition, overly thick (on average larger than 200μm) proved to show poor pull off strength were prone to cohesive failure within coating thickness. While inorganic-organic hybrid system with inorganic as base layer and organic coating as top layer, were observed to have good performance both in corrosion prevention and pull-off strength of the coating, sandwich systems where organic coating was used as intermediary layer showed dissatisfactory performance as the median layer becomes the culprit for inter-layer adhesive failure in a pull-off test. For the coating application procedure, it was observed that due to general larger grain size of geopolymer and its consistency, HVLP sprayer resulted in best coating finish followed by foam brush, and lastly bristle brush. In particular bristle brush showed the worst outcomes as it usually leaves brush marks on the coated surface and creates longer travel path for corrosive liquid to ingress into the substrate. Finally, in this chapter, in Batch-5 of tests, it was observed that longer exposure time in the corrosion chamber did not have linear relationship to reduction in pull-off strength. As it was observed some specimens demonstrated increased pull-off strength after on month exposure, continued by a reduction of pull-off strength after exposure for to contentious months.

A modified single-lap-shear specimen was proposed to test bonding of CFRP laminates to coated and un-coated steel substrate. The goal was to investigate use of geopolymer as barrier between steel substrate and CFRP laminate. The results revealed that use of geopolymer reduces the bond strength between CFRP and substrate by up to 50%. Nevertheless, the bond strength was still acceptable. Observed bond strength property was used to perform FE analysis in both 2D and 3D models. Result of the models successfully emulated the ultimate load as observed in the experimental test results.

The load bearing capacity of damaged steel coupons were evaluated and effectiveness of CFRP as patch repair for various types of damages was investigated. Linear damage, patch damage, through thickness hole damage were studied. It was observed that the repaired specimens can fully recover their ultimate strength but they lose ductility and consequently they will dissipate less amount of energy before rupture. In this chapter effect of various nano-additives on shear strength between CFRP and geopolymer coating and steel substrate and geopolymer coating were investigated. silicate, graphene oxide and titanium oxide nano-powders were evaluated. In these observations, silicate powder showed best performance in lap-shear test results.

In chapter 6 Finite Element (FE) Modeling was employed to calculate stress intensity factor (SIF) at finite points of crack length and depth combinations for an elliptical crack embedded into wall thickness of the pipe. We introduced two surrogate models, namely polynomial and Gaussian process, to further expand calculation of SIF at the intermediary points where FE simulations were not computed. FE simulations of crack in non-repaired and repaired pipe cases highlighted insightful observation about SIF values. In the non-repaired model SIF results along the crack length showed that for shallow and long cracks the critical SIF is at depth front of the crack i.e. promoting the crack growth through pipe thickness. As crack depth grows and ratio of crack depth to its length increased, SIF becomes more critical along the length of the crack. For the case of repaired pipe model in addition to general reduction of the SIF at all length-depth combinations, for given crack length SIF along crack length remains relatively constant. This affirmed the role that the patch repair is supposed to have, which is to prevent furthered opening of crack by preventing generation of stress concentration at crack front.

On part of fitted surrogate models, it was observed that the polynomial SIF fit demonstrated better performance in capturing trend of SIF values regardless of data training size. Polynomial model consistently had larger frequency for smaller error values specially when fewer samples were used as training. While Gaussian process model showed higher R-squared values as more training data were used, the surface generated by this method followed all points too closely and it is more prone to overfitting.

A Bayesian inference methodology was introduced to accurately estimate the time (cycle) when the structure (pipe or plate) has the most probability of failure based on observed crack growth measurements and cycle data (equivalent to field inspection) which was generated synthetically. We first introduced a methodology to estimate Equivalent Initial Flaw Size (EIFS) and then used that data to predict the distribution for number of cycles to failure. We initially developed a base model based on edge crack growth in a steel plate and verified the methodology. Then the method was expanded to model predictions for two-dimensional crack growth in pipe wall thickness. Comparison of estimation and true values showed that the proposed Bayesian methodology has very strong grounds for accurately predicting most critical time (cycle) when the structure may become susceptible to failure as more inspection data is collected and fed into the model.

8.2 Recommendation for Future Work

There are many possibilities in developing new mixes for geopolymer coating. Variety in availability of Nano-materials, development procedure, curing procedure before and after application of the coating, method of the application. There are many parameters in the process of geopolymer production, application, and curing that can be tuned to improve certain properties in the geopolymer body. Similar to cement, geopolymer is susceptible to shrinkage, as a result curing of coted specimens in lower temperatures could be examined to see if that affects micro-cracks observed under the microscope.

It is recommended to use strain gauge at the interface of the CFRP and substrate to measure strains and stress along the bond length accurately. Furthermore, use of extensometer may be used to quantify strain in CFRP and steel substrate. On the FE modeling part, it is encouraged to incorporate use of rupture in the model to be able to simulate the failure up to the fracture point.

Due to difficulties that were face with sprayer application of coating, it is worth investigating possibility of further reducing size of particles in the powder part of the geopolymer mix (for example fly ash and other constituents).

In analysis of crack propagation in pipeline, large scale pipe test can be performed to evaluate effectiveness of patch repair on various types of damages that pipes may experience during installation or operation.

Bayesian methods are very powerful tools for performing inference on many parameters involved in a problem with the exponential increase in the power of computers. In this study only single peak loading cycle was investigated as pressure in pipelines do not change peak in short periods. The effect of multi peak loading cycles on fatigue life of pipelines can be further investigated. The introduced Bayesian methodology can be further customized and more variables can be inferred simultaneously. Consequently, the more variables of the model to be inferred, the more complex and certainly more computationally expensive it becomes. Real field data can be collected and performance of model can be evaluated. In addition, customized Paris crack models may be employed in the algorithm. In the FE model, effect of area loss in the vicinity of crack may be considered.

It is also recommended that laboratory fatigue tests on steel specimens in controlled environment for plate with edge crack are conducted and microscopic flaws measured in the specimen and compared with predicted EIFS using the Bayesian approach.

9 References

[1] Hollaway, L. C., & Cadei, J. (2002). Progress in the technique of upgrading metallic structures with advanced polymer composites. Progress in Structural Engineering and Materials, 4(2), 131-148.

[2] Tavakkolizadeh, M., & Saadatmanesh, H. (2001). Repair of cracked steel girder using CFRP sheet. In Creative Systems in Structural and Construction Engineering, Proceedings of the 1st International Structural Engineering and Construction Conference, Amarjit Singh, ed., Honolulu, Hawaii (pp. 461-466).

[3] Tavakkolizadeh, M., & Saadatmanesh, H. (2001). Galvanic corrosion of carbon and steel in aggressive environments. Journal of Composites for Construction, 5(3), 200-210.

[4] Tavakkolizadeh, M., & Saadatmanesh, H. (2003). Fatigue strength of steel girders strengthened with carbon fiber reinforced polymer patch. Journal of Structural Engineering, 129(2), 186-196.

[5] Bambach, M. R., Jama, H. H., & Elchalakani, M. (2009). Axial capacity and design of thin-walled steel SHS strengthened with CFRP. Thin-Walled Structures, 47(10), 1112-1121.

[6] Khoramishad, H., Crocombe, A. D., Katnam, K. B., & Ashcroft, I. A. (2010). Predicting fatigue damage in adhesively bonded joints using a cohesive zone model. International Journal of fatigue, 32(7), 1146-1158.

[7] Liljedahl, C. D., Crocombe, A. D., Wahab, M. A., & Ashcroft, I. A. (2006). Damage modelling of adhesively bonded joints. International journal of fracture, 141(1), 147-161.

[8] Zhu, Y., & Kedward, K. (2005). Methods of analysis and failure predictions for adhesively bonded joints of uniform and variable bondline thickness. Office of Aviation Research, Federal Aviation Administration.

[9] Khoramishad, H., Crocombe, A. D., Katnam, K. B., & Ashcroft, I. A. (2010). Predicting fatigue damage in adhesively bonded joints using a cohesive zone model. International Journal of fatigue, 32(7), 1146-1158.

[10] Nozaka, K., Shield, C. K., & Hajjar, J. F. (2005). Effective bond length of carbon-fiber-reinforced polymer strips bonded to fatigued steel bridge I-girders. Journal of Bridge Engineering, 10(2), 195-205.

[11] Sen, R., Liby, L., & Mullins, G. (2001). Strengthening steel bridge sections using CFRP laminates. Composites Part B: Engineering, 32(4), 309-322.

[12] Miller, T. C., Chajes, M. J., Mertz, D. R., & Hastings, J. N. (2001). Strengthening of a steel bridge girder using CFRP plates. Journal of Bridge Engineering, 6(6), 514-522.

[13] Teng, J. G., & Hu, Y. M. (2007). Behaviour of FRP-jacketed circular steel tubes and cylindrical shells under axial compression. Construction and Building Materials, 21(4), 827-838.

[14] Shanafelt, G. O., & Horn, W. B. (1984). Guidelines for evaluation and repair of damaged steel bridge members (No. HS-037 759).[NCHRP Report 271]

[15] Zhao, X. L., & Zhang, L. (2007). State-of-the-art review on FRP strengthened steel structures. Engineering Structures, 29(8), 1808-1823.

[16] Yuan, H., Teng, J. G., Seracino, R., Wu, Z. S., & Yao, J. (2004). Full-range behavior of FRP-to-concrete bonded joints. Engineering structures, 26(5), 553-565.

[17] Wu, Z., Yuan, H., & Niu, H. (2002). Stress transfer and fracture propagation in different kinds of adhesive joints. Journal of Engineering Mechanics, 128(5), 562-573.

[18] Toutanji, H., & Dempsey, S. (2001). Stress modeling of pipelines strengthened with advanced composites materials. Thin-Walled Structures, 39(2), 153-165.

[19] Duell, J. M., Wilson, J. M., & Kessler, M. R. (2008). Analysis of a carbon composite overwrap pipeline repair system. International Journal of Pressure Vessels and Piping, 85(11), 782-788.

[20] Mazurkiewicz, L., Tomaszewski, M., Malachowski, J., Sybilski, K., Chebakov, M., Witek, M., ... & Dmitrienko, R. (2017). Experimental and numerical study of steel pipe with part-wall defect reinforced with fibre glass sleeve. International Journal of Pressure Vessels and Piping, 149, 108-119.

[21] American Society of Mechanical Engineers (2015). Repair of Pressure Equipment and Piping (ASME PCC2).

[22] Sen, R., Liby, L., & Mullins, G. (2001). Strengthening steel bridge sections using CFRP laminates. Composites Part B: Engineering, 32(4), 309-322.

[23] Balaguru, P. (1998). Geopolymer for protective coating of transportation infrastructures (No. FHWA NJ 1998-12,).

[24] Lyon, R. E., Balaguru, P. N., Foden, A., Sorathia, U., Davidovits, J., & Davidovics, M. (1997). Fire-resistant aluminosilicate composites. Fire and materials, 21(2), 67-73.

[25] Chong, S. L. (1997). A Comparison of Accelerated Tests for Steel Bridge Coatings in Marine Environments. Journal of Protective Coatings & Linings, 14(3).

[26] Kodumuri, P., & Lee, S. K. (2012). Federal Highway Administration 100-Year Coating Study (No. FHWA-HRT-12-044).

[27] Schnerch, David, et al. "Strengthening Steel Structures and Bridges with High-Modulus Carbon Fiber-Reinforced Polymers Resin Selection and Scaled Monopole Behavior." Transportation Research Record: Journal of the Transportation Research Board 1892 (2004): 237-245.

[28] Fawzia, Sabrina, Riadh Al-Mahaidi, and Xiao-Ling Zhao. "Experimental and finite element analysis of a double strap joint between steel plates and normal modulus CFRP." Composite structures 75.1 (2006): 156-162.

[29] Liu, Hongbo, et al. "Prediction of fatigue life for CFRP-strengthened steel plates." Thin-Walled Structures 47.10 (2009): 1069-1077.

[30] Romano, M., Dabiri, M., & Kehr, A. (2005). The ins and outs of pipeline coatings: Coatings used to protect oil and gas pipelines. Journal of protective coatings & linings, 22(7).

[31] Bahadori, A. (2015). Essentials of Coating, Painting, and Lining for the Oil, Gas and Petrochemical Industries. Gulf Professional Publishing.

[32] Ossai, C. I., Boswell, B., & Davies, I. J. (2015). Pipeline failures in corrosive environments–A conceptual analysis of trends and effects. Engineering Failure Analysis, 53, 36-58.

[33] Roche, M., Melot, D., & Paugam, G. (2006). Recent experience with pipeline coating failures. JOURNAL OF PROTECTIVE COATINGS AND LININGS, 23(10), 18.

[34] Papavinasam, S., Attard, M., & Revie, R. W. (2006). External polymeric pipeline coating failure modes. Materials performance, 45(10), 28-30.

[35] Wasserman, K. (2012). Durability of an inorganic polymer concrete coating. Rutgers The State University of New Jersey-New Brunswick.

[36] Farrag, K. (2013). Selection of pipe repair methods (No. GTI Project Number 21087).

[37] Jaske, C. A., Hart, B. O., & Bruce, W. A. (2006). Pipeline repair manual. Pipeline Research Council International. Inc. Virginia.

[38] Dassault Systémes (2015). ABAQUS 6.14 Documentation–Theory Guide. Providence, RI.

[39] Alexander, C., & Francini, B. (2006, September). State of the art assessment of composite systems used to repair transmission pipelines. In Proceedings of IPC2006 (Paper No. IPC2006-10484), 6th International Pipeline Conference.

[40] Freire, J. L. F., R. D. Vieira, J. L. C. Diniz, and L. C. Meniconi. "Part 7: effectiveness of composite repairs applied to damaged pipeline." Experimental Techniques 31, no. 5 (2007): 59-66.

[41] Shamsuddoha, M., Islam, M. M., Aravinthan, T., Manalo, A., & Lau, K. T. (2013). Effectiveness of using fibre-reinforced polymer composites for underwater steel pipeline repairs. Composite Structures, 100, 40-54.

[42] Alexander, C. R., & Worth, C. (2006, September). Assessing the use of composite materials in repairing mechanical damage in transmission pipelines. In Proceedings of the 6th International Pipeline Conference, Paper No. IPC2006-10482, Calgary, Alberta, Canada.

[43] Dahlberg, E. P., & Bruno, T. V. (1985). Analysis of Gas Pipeline Failures. JOM Journal of the Minerals, Metals and Materials Society, 37(1), 71-73.

[44] Ayaz, Y., Çitil, Ş., & Şahan, M. F. (2016). Repair of small damages in steel pipes with composite patches. Materialwissenschaft und Werkstofftechnik, 47(5-6), 503-511.

[45] Saeed, N., Ronagh, H., & Virk, A. (2014). Composite repair of pipelines, considering the effect of live pressure-analytical and numerical models with respect to ISO/TS 24817 and ASME PCC-2. Composites Part B: Engineering, 58, 605-610.

[46] Balaguru, P., & Lee, K. W. (2001). Effectiveness of High Strength Composites as Structural & Protective Coatings for Structural Elements (No. NETCR 28).

[47] Zhang, Y. J., Li, S., Wang, B. Q., Xu, G. M., Yang, D. F., Wang, N., ... & Wang, Y. C. (2010). A novel method for preparation of organic resins reinforced geopolymer composites. Journal of materials science, 45(5), 1189-1192.

[48] Liyana, J., & Kamarudin, H. (2013). Reviews on Fly Ash based Geopolymer Materials for Protective Coating Field Implementations. Australian Journal of Basic and Applied Sciences, 7(5), 182-186.

[49] Salwa, M. S., Al Bakri, A. M., Kamarudin, H., Ruzaidi, C. M., Binhussain, M., & Zaliha, S. S. (2013). Review on current geopolymer as a coating material. Australian Journal of Basic and Applied Sciences, 7(5), 246-257.

[50] Balaguru, P. N. (2012). U.S. Patent No. 8,197,593. Washington, DC: U.S. Patent and Trademark Office.

[51] Davidovits, J. (1991). Geopolymers: inorganic polymeric new materials. Journal of Thermal Analysis and calorimetry, 37(8), 1633-1656.

[52] Xie, M., Bott, S., Sutton, A., Nemeth, A., & Tian, Z. (2018). An integrated prognostics approach for pipeline fatigue crack growth prediction utilizing inline inspection data. Journal of Pressure Vessel Technology, 140(3), 031702.

[53] Williams, C. K., & Rasmussen, C. E. (1996). Gaussian processes for regression. In Advances in neural information processing systems (pp. 514-520).

[54] Pedregosa, F., Varoquaux, G., Gramfort, A., Michel, V., Thirion, B., Grisel, O., ... & Vanderplas, J. (2011). Scikit-learn: Machine learning in Python. Journal of machine learning research, 12(Oct), 2825-2830.

[55] Makeev, A., Nikishkov, Y., & Armanios, E. (2007). A concept for quantifying equivalent initial flaw size distribution in fracture mechanics based life prediction models. International journal of fatigue, 29(1), 141-145.

[56] Cross, R., Makeev, A., & Armanios, E. (2007). Simultaneous uncertainty quantification of fracture mechanics based life prediction model parameters. International journal of fatigue, 29(8), 1510-1515.

[57] Sankararaman, S., Ling, Y., & Mahadevan, S. (2010). Statistical inference of equivalent initial flaw size with complicated structural geometry and multi-axial variable amplitude loading. International Journal of Fatigue, 32(10), 1689-1700.

[58] Liu, Y., & Mahadevan, S. (2009). Probabilistic fatigue life prediction using an equivalent initial flaw size distribution. International Journal of Fatigue, 31(3), 476-487.

[59] Sankararaman, S., Ling, Y., & Mahadevan, S. (2011). Uncertainty quantification and model validation of fatigue crack growth prediction. Engineering Fracture Mechanics, 78(7), 1487-1504.

[60] Zarate, B. A., Caicedo, J. M., Yu, J., & Ziehl, P. (2012). Bayesian model updating and prognosis of fatigue crack growth. Engineering Structures, 45, 53-61.

[61] Newman Jr, J. C., & Raju, I. S. (1984). Stress-intensity factor equations for cracks in three-dimensional finite bodies subjected to tension and bending loads.

[62] Atkinson, K. E. (2008). An introduction to numerical analysis. John Wiley & Sons. p. 203.

[63] Tada, H., Paris, P. C., & Irwin, G. R. (1973). The stress analysis of cracks. Handbook, Del Research Corporation.

[64] Schütz, W. (1996). A history of fatigue. Engineering fracture mechanics, 54(2), 263-300.

[65] Schijve, J. (2003). Fatigue of structures and materials in the 20th century and the state of the art. International Journal of fatigue, 25(8), 679-702.

[66] Smith, R. (1990). The versailles railway accident of 1842 and the first research into metal fatigue.(retroactive coverage). Fatigue 90, 2033-2041.

[67] Griffith, A. A. (1921). VI. The phenomena of rupture and flow in solids. Philosophical transactions of the royal society of london. Series A, containing papers of a mathematical or physical character, 221(582-593), 163-198.

[68] Paris, P., & Erdogan, F. (1963). A critical analysis of crack propagation laws.

[69] Newman Jr, J. C., & Raju, I. S. (1984). Prediction of fatigue crack-growth patterns and lives in three-dimensional cracked bodies. In Fracture 84 (pp. 1597-1608). Pergamon.

[70] Newman Jr, J. C., & Raju, I. S. (1981). An empirical stress-intensity factor equation for the surface crack. Engineering fracture mechanics, 15(1-2), 185-192.

[71] FAWAZ, S. A. (2003). Equivalent initial flaw size testing and analysis of transport aircraft skin splices. Fatigue & Fracture of Engineering Materials & Structures, 26(3), 279-290.

[72] Johnson, W. S. (2010). The history, logic and uses of the Equivalent Initial Flaw Size approach to total fatigue life prediction. Procedia Engineering, 2(1), 47-58.

[73] Fujii, H., DJC, M., & HKDH, B. (1996). Bayesian neural network analysis of fatigue crack growth rate in nickel base superalloys. Isij International, 36(11), 1373-1382.

[74] Hoff, P. D. (2009). A first course in Bayesian statistical methods (Vol. 580). New York: Springer.

[75] Irwin, G. R. (1958). Handbuch der Physik, vol. 6.

[76] Geyer, C. J. (1992). Practical markov chain monte carlo. Statistical science, 473-483.

[77] Gilks, W. R., Richardson, S., & Spiegelhalter, D. (1995). Markov chain Monte Carlo in practice. Chapman and Hall/CRC.

[78] Geyer, C. J. (1991). Markov chain Monte Carlo maximum likelihood.

[79] Benzeggagh, M. L., & Kenane, M. J. C. S. (1996). Measurement of mixed-mode delamination fracture toughness of unidirectional glass/epoxy composites with mixed-mode bending apparatus. Composites science and technology, 56(4), 439-449.